



HAL
open science

Etude expérimentale du bruit de combustion dans un foyer de type aéronautique

Marek Mazur

► **To cite this version:**

Marek Mazur. Etude expérimentale du bruit de combustion dans un foyer de type aéronautique. Autre. Université Paris Saclay (COmUE), 2017. Français. NNT : 2017SACLC034 . tel-01580180

HAL Id: tel-01580180

<https://theses.hal.science/tel-01580180>

Submitted on 1 Sep 2017

HAL is a multi-disciplinary open access archive for the deposit and dissemination of scientific research documents, whether they are published or not. The documents may come from teaching and research institutions in France or abroad, or from public or private research centers.

L'archive ouverte pluridisciplinaire **HAL**, est destinée au dépôt et à la diffusion de documents scientifiques de niveau recherche, publiés ou non, émanant des établissements d'enseignement et de recherche français ou étrangers, des laboratoires publics ou privés.

Etude expérimentale du bruit de combustion dans un foyer de type aéronautique

Thèse de doctorat de l'Université Paris-Saclay
préparée à CentraleSupélec

École doctorale n°579 sciences mécaniques et énergétiques,
matériaux et géosciences (SMEMAG)
Spécialité de doctorat: combustion

Thèse présentée et soutenue à Châtenay-Malabry, le 11/07/2017, par

Marek Alojzy Mazur

Composition du Jury :

Aimee Morgans Professeur, Imperial College London	Président
Friedrich Bake Ingénieur de Recherche, DLR Berlin	Rapporteur
Stéphane Moreau Professeur, Université de Sherbrooke	Rapporteur
Maxime Huet Ingénieur de Recherche, ONERA Châtillon	Examineur
Sébastien Ducruix Directeur de Recherche, CNRS EM2C	Directeur de thèse
Franck Richecoeur Professeur, CentraleSupélec	Co-Directeur de thèse
Philippe Scouflaire Ingénieur de Recherche, CNRS EM2C	Co-Directeur de thèse

Remerciements

Tout d'abord je voudrais remercier mes encadrants qui ont supervisé mon travail : Philippe qui m'a encadré surtout au niveau pratique à la salle de manip et qui m'a autant appris sur les diagnostics laser. Merci aussi pour nos discussions et conseils nombreux aussi sur des sujets dehors la thèse. Un grand merci aussi à Franck pour son encadrement, pour me pousser de chercher plus loin que ce que je vois dans le travail expérimental et surtout pour la patience et l'aide précieuse pendant ma phase de rédaction. Finalement, merci beaucoup à Sébastien pour m'avoir donné l'opportunité de travailler sur un sujet si passionnant et enrichissant. Merci aussi pour le guidage tout au long de cette thèse et aussi à la confiance pour me laisser tester des idées et approches qui n'étaient pas prévus dès le début.

Je souhaite aussi remercier Aimee Morgans pour avoir été la présidente de mon jury et pour ses remarques pendant ma soutenance. Aussi un grand merci aux deux rapporteurs, Friedrich Bake et Stéphane Moreau pour avoir consacré autant de temps sur ma thèse et pour leurs remarques pertinentes qui m'ont aidé à raffiner ce manuscrit. Egalement merci à Maxime Huet pour ses remarques intéressantes et pour ses corrections et suggestions d'améliorations de ce manuscrit.

Je remercie aussi très chaleureusement l'ensemble du personnel administratif et technique. Merci surtout à Brigitte, Nathalie, Noi et Anne-Cécile pour leur présence et leur aide tout au long de la thèse. Un grand merci pour le personnel de l'atelier, Erica et Yannick qui m'ont aidé avec des différents montages avec une énorme réactivité et volonté. Merci aussi à Jérôme et Dédit pour leur aide pendant la conception du banc et du système électrique. Merci aussi à David pour nos riches discussions sur des diagnostics différentes.

Je souhaite également remercier les chercheurs du laboratoire qui ont toujours partagé leur expérience pendant des discussions informelles et qui contribuent à la bonne ambiance du laboratoire EM2C. Un merci spécial à Wenjie et Nancy avec qui j'ai pu travailler sur notre projet. Aussi aux partenaires européens avec qui j'ai pu travailler, notamment aux thésards Corentin, Kilian et Wolfram, mais également aux autres gens avec qui j'ai pu échanger et travailler

pendant ce temps.

Finalement merci aux doctorants de notre bureau et au labo avec qui j'ai pu passer du temps merveilleux pendant le travail et aussi dehors pendant des occasions différentes à Paris et ailleurs : Yann, Benjamin, Gilles, Erwan, Melody, Kimmo, Shiyun, Nico. Aussi aux motivés avec qui j'ai pu participer au Raid : Antoine, Wenjie, Nico, Aymeric, Matthieu, Théa, Adam, Abigail, Robin, Quentin). Aussi à Nicolas, Cédric, Milan, Claire, Lorella, Giunio, Kévin, Amanda, Davy, Paul, Florence, Benoit, Léo, Thomas, Clément, Laurent, Marien, Aurélien...enfin à tous les doctorants ! Parce que vous avez toutes et tous supportés mes blagues (et même rigolés de temps en temps !) et en général contribués que ces trois ans étaient inoubliables !

Enfin un grand merci pour mes plus proches : A mes parents et à mon frère et à ma copine Katia. C'est grâce à votre amour, votre patience et votre soutien que je suis arrivé où je me trouve maintenant et que j'ai pu surmonter tous les défis qui sont apparus sur le chemin.

Abstract

Combustion noise has become an increasing contributor of overall aircraft engine noise. It consists of two major parts, direct and indirect combustion noise. The former is generated by the heat release fluctuations of the flame itself. The latter is generated by the temperature inhomogeneities in the burnt gases, which are accelerated in the turbine stages or nozzle following the combustion chamber. Various works have been done in the past in order to describe direct and indirect combustion noise generation experimentally. However no quantification has been done yet where a combustion system generates direct and indirect combustion noise simultaneously. The aim of this thesis is to narrow this gap and to design and build a pressurized lean swirling combustor test bench, which generates high quantities of indirect combustion noise. The entropy waves are to be accelerated by a choked exhaust nozzle. It is necessary to characterize this combustor, determine its acoustic boundary conditions and to find means to determine the contributions of direct and indirect combustion noise quantitatively.

The first part of the thesis is focusing on a presentation of the new combustor test bench, as well as of an experimental description of its velocity fields and flame dynamics. The mean and RMS velocity and OH* chemiluminescence fields are determined and used to identify the areas of strongest dynamics. The time resolved local velocity, heat release and pressure are obtained by high speed diagnostics. The results are used to put forward the existence of a combustion instability in the combustor. Furthermore, the eigen modes of the system are found by a combined experimental and analytical approach. The second part is dealing with two optical diagnostics that were worked on during this thesis. One of the diagnostics is a new high speed PIV technique that was developed during this thesis and is applied for the velocity field measurements. It is based on the use of a continuous laser source and allows for sampling frequencies of up to 100 kHz. The other technique is used for the visualization of the density fluctuations. This is done by applying a focussing Schlieren technique, which allows to obtain 2D images of the density gradients at high sampling frequencies. Due to the application of a particular installation, the densities are shown on a field of view of only a few millimetres. The technique allows to visualize wave-like phenomena in the burnt gases that are probably related to entropy

waves. Both techniques give qualitatively correct results however, work is still necessary in order to validate these techniques. Nevertheless, they are supposed to be of interest for future studies of combustion dynamics and noise. Finally, in the third part of the thesis, the experimental determination of direct and indirect combustion noise is treated. Two different approaches were worked on and are presented. The first approach is based on the determination of direct combustion noise from the global heat release rate. The second approach is based on the measurement of high-speed line-of-sight averaged temperature fluctuations by Laser Interferometric Vibrometry. The measurements are conducted simultaneously and synchronized with pressure measurements. From these results, the different combustion noise contributions are calculated. Both approaches show that indirect combustion noise exists in this combustor, however its contribution is small compared to direct combustion noise.

The test bench is thus able to generate a non-negligible quantity of indirect combustion noise. Furthermore, techniques were found to characterise the combustor and to determine its direct and indirect combustion noise contributions. It is now necessary to improve the test bench in order to increase indirect combustion noise generation.

Résumé

Résumé: Le bruit de combustion est devenu un contributeur de plus en plus important dans le bruit total de moteur d'avion. Ce bruit global a deux composantes: Le bruit direct et le bruit indirect. Le premier est issu des fluctuations de dégagement de chaleur dans la flamme elle-même. Le deuxième a pour origine les inhomogénéités de température dans les gaz brûlés accélérés par les étages de turbine ou une tuyère. Des travaux différents ont été faits dans le passé pour décrire le bruit direct et indirect en utilisant les moyens expérimentaux. Mais aucune quantification n'a été faite encore sur un système de combustion qui génère le bruit direct et indirect simultanément. L'objectif de ce travail est la conception d'un banc de combustion sous pression avec une flamme pauvre, prémélangée swirlée dont les paramètres d'injection permettront d'obtenir des grandes quantités de bruit indirect. Les ondes entropiques sont accélérées par une tuyère amorcée. Il est nécessaire de caractériser ce banc et d'établir quelle est la part du bruit direct et de l'indirect afin d'identifier les sources de ces contributions. Pour cette caractérisation il est nécessaire d'utiliser différents diagnostics, de prendre en compte la résolution temporelle. Ces diagnostics à haute cadence permettent de caractériser les champs de vitesse et les dynamiques de flamme, les instabilités de combustion dans le système et ainsi évaluer les contributions du bruit direct et indirect.

La première partie de la thèse se concentre sur la présentation du nouveau banc d'essai ainsi que sur une description expérimentale des champs de vitesse et de la dynamique de flamme. Les champs moyens et RMS de la vitesse et de l'émission spontanée du radical OH^* sont déterminés et utilisés pour identifier les régions avec les plus fortes dynamiques. Des mesures résolues en temps de vitesse, dégagement de chaleur et pression sont obtenus par des diagnostics à haute cadence. Les résultats sont utilisés pour mettre en évidence une instabilité de combustion dans l'installation. Aussi, les modes propres du système sont déterminés par une approche combinée expérimentale et analytique. La deuxième partie est consacrée au travail sur deux diagnostics optiques. Un des diagnostics est une nouvelle technique rapide du type PIV et est utilisée pour mesurer les champs de vitesse. La technique est basée sur l'utilisation d'un laser continu et permet d'obtenir des fréquences d'acquisition jusqu'à 100 kHz. La deuxième technique est utilisée pour visualiser les fluctuations de densité. Ceci

est fait en utilisant un Schlieren focalisé, qui permet d'acquérir des images 2D des gradients de densité en haute cadence. Grâce à un montage particulier, les densités sont montrées sur un champ avec une épaisseur de seulement quelques millimètres. La technique permet de visualiser des effets de type onde dans les gaz brûlés probablement liées aux ondes entropiques. Les deux diagnostics donnent des résultats qualitativement correctes, mais il reste du travail à fournir afin de les valider. Néanmoins ces techniques semblent prometteuses pour des futures études des dynamiques de combustion et du bruit. La troisième partie traite la détermination expérimentale du bruit direct et indirect. Deux approches différents ont été abordées. La première approche est basée sur la détermination du bruit direct à partir du taux de dégagement de chaleur de la flamme. La deuxième démarche est basée sur les mesures en haute cadence des fluctuations de température moyennées sur une ligne de vue. Ceci est fait par la Vibrométrie Laser. Les mesures sont prises simultanément et synchronisées avec les mesures de pression. À partir de ces résultats, les différentes contributions du bruit de combustion sont calculées. Les deux approches montrent qu'il y a du bruit indirect dans le brûleur, mais que sa contribution est faible par rapport à celle du bruit direct. Ceci est probablement lié à la forte instabilité de combustion.

Le banc est donc capable de produire une quantité non-négligable de bruit indirect et des moyens ont été trouvés afin de le caractériser et de quantifier les deux contributions du bruit de combustion. Il est maintenant nécessaire de modifier l'installation pour augmenter la contribution du bruit indirect.

Contents

Abstract	v
Résumé	vii
Nomenclature	xxv
Introduction	1
I Presentation and characterisation of the CESAM-HP test bench	23
1 Design of a test bench for combustion noise studies	27
1.1 Design of the combustor test bench	27
1.2 In-chamber diagnostics	36
1.3 The operating conditions	42
1.4 Conclusion	47
2 Statistic flame and flow characterization	49
2.1 Motivation	49
2.2 Diagnostics	50
2.3 Experimental results	51
2.4 Conclusion	66
3 Modal analysis of the test bench	67
3.1 Introduction	67
3.2 Procedure to identify the acoustic eigenmodes	68
3.3 Results of the experimental and analytical study	76
3.4 Conclusion	80
4 Time and spatially resolved analysis of the combustion instability	81
4.1 Introduction	81
4.2 Methodology for the spatially resolved observation of combustion instabilities	83

4.3	Experimental results	90
4.4	Conclusion	97
II	Development of optical diagnostics	101
5	Development of a high speed planar velocimetry technique	105
5.1	Introduction	105
5.2	Presentation of the new velocimetry technique	107
5.3	Experimental procedure for validation	112
5.4	Results	116
5.5	Conclusion	122
6	Visualization of the density fluctuations with focusing Schlieren	125
6.1	Presentation of focusing Schlieren as a technique to visualize density fluctuations	125
6.2	Experimental results	135
6.3	Conclusion	157
III	Determination of direct and indirect combustion noise	159
7	Estimation of direct combustion noise	163
7.1	Introduction	163
7.2	Theoretical approach to determine direct combustion noise	164
7.3	Applied diagnostics	166
7.4	Experimental results	167
7.5	Conclusion	177
8	Quantitative determination of direct and indirect combustion noise contributions	179
8.1	Introduction	179
8.2	Experimental procedure	180
8.3	Temperature fluctuations of the burnt gases	186
8.4	Determination of direct and indirect combustion noise contribution	196
8.5	Conclusion	203
	Conclusion	205
A	Potential improvements of the test bench	211
A.1	Proposed modifications of the test bench	211
A.2	Experimental procedure to verify the effectiveness of the modi- fications	213
A.3	Measurements in the fully premixed case without secondary air	215
A.4	Effects of flame stabilisation by a flame holder rod in the injector	219

CONTENTS

xi

A.5	Effects of flame stabilisation by a flame holder rod in the injector and partially premixed operation due to separate fuel injection . . .	223
A.6	Effects of secondary air injection through the chamber walls . . .	230
A.7	Analysis of the PSD of measured and theoretical pressure for all tested configurations	238
A.8	Conclusion	243
	References	256
	Index	257

List of Tables

1.1	Technical specifications of the KISTLER 4045A pressure sensor	37
1.2	Technical specifications of the KISTLER 701A pressure sensor	37
1.3	Technical specifications of the Bruel & Kjaer 4938 microphone	39
1.4	Technical specifications of the PM	42
1.5	Positions of the applied pressure sensor and PMs	42
1.6	General operating conditions of the CESAM-HP test bench	43
1.7	Chosen operating points for the experimental study	46
2.1	Calculation of the geometric swirl number for the three operating points. The mass flow rates include air and fuel mass flows	66
3.1	Summary of the acoustic modes obtained experimentally and analytically	76
3.2	Summary of the mode interpretations for n=1 to 7. Frequencies found experimentally are also indicated	79
4.1	Chosen regions where the PSD is determined. The coordinates of the regions studied by OH* chemiluminescence indicate the central point of a 1.02 mm × 1.02 mm square. The coordinates of the regions studied by PCMV indicate the interrogation window in which the point is located. They indicate the center of a 0.97 mm × 0.97 mm square	89
5.1	Comparison of the present laser system with existing systems from literature. c: Continuous laser source, p: Pulsed laser source, LS: low speed, F_s : Sampling frequency, $E_{per-image}$: Energy per image, t_{laser} : Laser opening duration per image, w: Laser sheet width, t: Laser sheet thickness, I_{norm} : Normalized Intensity. 1: Providakis et al. (2013). 2: Boxx et al. (2009). 3: Willert (2015). 4: Letty et al. (2013)	112
6.1	Summary of the Schlieren system parameters	129

6.2	overview of the regions at the injector, where the Intensity PSD of the Schlieren images was calculated. $y = 0$ mm for all regions. The indicated x and z coordinate correspond to the central point of the $2 \text{ mm} \times 2 \text{ mm}$ region.	138
7.1	Positions of the applied pressure sensor and PMs	167
8.1	Calculation of the Mach values for the three operating points	201

List of Figures

1	Trend of the specific fuel consumption for aircraft turbo engines (Gröenstedt et al. (2013))	2
2	Relation of Specific fuel consumption, NO_x emissions and pressure ratio. (created by Lapeyre (2015), based on Suder (2012)). The overall pressure ratio is directly linked with the thermal efficiency and the turbine entry temperature of the engine (Jeschke (2012))	3
3	Typical flow structure in a Swirl stabilized aircraft combustor (Bräunling (2015))	4
4	Reduction of aircraft engine noise in the last decades (Neise and Enghardt (2003))	5
5	Breakdown of the different engine noise contributions and their predicted development until 2025 (Sensiau (2013))	5
6	Breakdown of the different engine noise contributions in their typical spectra (Sensiau (2013))	6
7	Schematic drawing of an aircraft combustion chamber with illustrations of direct combustion noise, entropy noise and vorticity noise (Ullrich and Sattelmayer (2016))	7
8	Schematic drawing of the key processes that are connected to combustion noise (Morgans and Duran (2016))	10
9	Comparison of the effects of the Mach number in the combustion chamber and at the nozzle exit on combustion noise generation (Dowling and Mahmoudi (2015), based on the simulations of Leyko et al. (2009))	15
10	Schematic drawing of the CESAM testbench of EM2C Laboratory (Lamraoui (2011))	17
1.1	Schematic drawing of the CESAM-HP test bench	29
1.2	Geometry of the tangential injection system	29
1.3	Schematic drawing of the injection stage (light blue) and the ICS with the bias air flow (green arrow). The figure also includes the axial fuel injection (blue arrow).	30
1.4	CESAM-HP test bench with the layout of the feeding lines	31

1.5	Geometry of the Combustion Chamber (Drawing made by Combustion Bay One (F. Giuliani)	32
1.6	Geometry of the Instrument Port (Drawing made by Combustion Bay One (F. Giuliani)). The left image shows a 3D view of an instrument port. It includes three locations for pressure sensors and one for a spark plug. The right image shows a section of the same piece together with its dimensions.	33
1.7	Sketch of the cooling system. The pressure sensor is protected by a 10 mm thick wall with an orifice of 2 mm diameter. The walls are cooled by an open water cooling circuit.	34
1.8	Geometry of the Exhaust Nozzle	34
1.9	Geometry of the Exhaust Nozzle Cooling Circuit. The left image shows the nozzle from outside with the water feeding lines and the right image shows the cooling water pipes inside the nozzle.	36
1.10	Mass-spring model of the orifice and the gap between protective wall and the pressure sensor. This geometry corresponds to the installation of the pressure sensors and was developed by KISTLER. (Figure based on drawing from KISTLER (2013))	37
1.11	Schematic drawing and photograph of the ITHACA acoustic test bench. A loudspeaker is located at the bottom of the tube. At the top, the tube contains various ports in order to mount microphones and pressure sensors.	38
1.12	Pressure spectra of the KISTLER 701A sensor with different installation arrangements, compared to microphone signal. The upper figure corresponds to an excitation frequency of 120 Hz (140 dB) and the lower one of 480 Hz (154 dB).	40
1.13	Pressure spectra of the KISTLER 701A and the KISTLER 4045A sensors. The upper figure corresponds to an excitation frequency of 120 Hz (140 dB) and the lower one of 480 Hz (154 dB).	41
1.14	Examples of a) detached flame, b) flash backed flame and c) conical flame	43
1.15	Operation map of the CESAM-HP test bench. Both axial mass flow rates are zero.	45
1.16	Pressure spectra of the three chosen operating points, measured by a wall-mounted sensor. The spectra show particular differences in the low frequency region. This difference justifies the choice of these operating points.	47
2.1	Abel transformed mean OH* chemiluminescence fields of the three operating points. Top figure: Op16-0-2 ; Middle figure: Op16-2-0 ; Bottom figure: Op13.4-4.6-0	52
2.2	Abel transformed RMS OH* chemiluminescence fields of the three operating points. Top figure: Op16-0-2 ; Middle figure: Op16-2-0 ; Bottom figure: Op13.4-4.6-0	54

2.3	Top left figure: Mean vector field of Op16-0-2 ; Top right figure: Mean vector field of Op16-2-0 ; Bottom figure: Mean vector field of Op13.4-4.6-0	56
2.4	Mean velocity fields in x and z direction of Op16-0-2	57
2.5	Mean velocity fields in x and z direction of Op16-2-0	57
2.6	Mean velocity fields in x and z direction of Op134-46-0	58
2.7	RMS velocity fields in x and z direction of Op16-0-2	58
2.8	RMS velocity fields in x and z direction of Op16-2-0	59
2.9	RMS velocity fields in x and z direction of Op134-46-0	59
2.10	Mean velocity profiles in x-direction for different x-positions for the three operating points	60
2.11	Mean velocity profiles in z-direction for different x-positions for the three operating points	61
2.12	RMS velocity profiles in x-direction for different x-positions for the three operating points	62
2.13	RMS velocity profiles in z-direction for different x-positions for the three operating points	63
2.14	RMS velocity profiles in z-direction for different x-positions for the three operating points	64
3.1	Positions of the installed sensors in the combustion chamber	68
3.2	Schematic drawing of the Pressurized Impedance Measurement System (PIMS), adapted from Lamraoui et al. (2010)	69
3.3	Coherence of the PIMS pressure sensors. The diagram shows that the coherence drops for frequencies above 500 Hz.	71
3.4	PSD of the pressure sensors in the PIMS, the premixer and the combustion chamber	72
3.5	Modelling of the burner as a) two and b) five cavities. The main dimensions and boundary conditions are also indicated.	73
3.6	Reflection coefficient in the feeding line measured at a radial distance of 60 mm from the premixing tube axis. In red: 10th order polynomial fit	78
3.7	Structure of the modes $f^1 = 116$ Hz, $f^5 = 592$ Hz and $f^7 = 2935$ Hz. Lines: analytical modes. Symbols: experiments. Circle: 116 Hz; Triangle: 592 Hz; Square: 2935 Hz. ($x_2 = 75$ mm). The mode for $f^5 = 592$ Hz has a similar shape for both models.	79
4.1	Applied coordinate system. Keep in mind that the coordinate system is right-handed. The y-coordinate is therefore showing away from the reader.	83
4.2	Time resolved plot of the streamlines together with the RMS OH* chemiluminescence for Op16-0-2	86

4.3	Image of the RMS OH* chemiluminescence of Op16-0-2 with the regions that are listed in table 4.1. The image is not Abel transformed and very low values are shown as gray. Further descriptions of the mean and RMS OH* chemiluminescence fields can be found in chapter 2.	87
4.4	PM and total OH* chemiluminescence imaging spectra of the three chosen operating points for the entire combustion chamber. The figures show that the spectra for both diagnostics have the same peaks.	90
4.5	The pressure spectra of the three chosen operating points show strong pressure fluctuations in the low frequency region. Op16-0-2 and Op16-2-0 feature their strongest peak at 120 Hz and also the harmonics of that frequency. Op13.4-4.6-0 is characterized by a more broadband peak with its maximum frequency at around 80 Hz.	91
4.6	PSD of the OH* and velocity fluctuations in regions 1 to 4 for Op16-0-2 and Op16-2-0	92
4.7	PSD of the OH* and velocity fluctuations in regions 1 to 4 for Op13.4-4.6-0	93
4.8	Summary of the identified combustion instability mechanisms. The blue text corresponds to the experimental indications that presented in this chapter. p : Pressure, Q : Heat release, v : Velocity, Ω : Vorticity, Φ : Equivalence ratio, A : Flame surface . . .	97
5.1	Description of PCMV with continuous laser source and the different timing parameters of the technique	108
5.2	Left: Displacement of a particle that is captured as a dot by classic PIV. Right: Displacement of a particle that is captured as a trace by PCMV	109
5.3	Different time steps that are relevant for PIV and PCMV	110
5.4	Schematic drawing of the CESAM-HP combustor also showing the position of the PIV laser sheet	113
5.5	Left: Example of the instantaneous Mie scattering at the studied operating point. The images are taken at 8 bits and the maximum intensity is thus 255. Right: Example of the instantaneous velocity vectors of the studied operating point at the same time step.	116
5.6	Example of the instantaneous velocity field in x-direction and z-direction for the studied operating point	117
5.7	Mean velocity profiles in x direction for different axial positions for PCMV and PIV	118
5.8	Mean velocity profiles in z direction for different axial positions for PCMV and PIV	119

5.9	RMS velocity profiles in x direction for different axial positions for PCMV and PIV	119
5.10	RMS velocity profiles in z direction for different axial positions for PCMV and PIV	120
6.1	Schematic drawing of the focusing Schlieren technique (based on Floryan et al. (2012))	126
6.2	Layout of the source grid and the cut-off grid (Weinstein (1993)). The dimensions of the source grid are chosen freely and are oriented on the optical complement of the cut-off grid, thus taking into account the zoom of the camera lens.	127
6.3	Different stages of pre-processing of the Focusing Schlieren visualization. The image is taken at the burner lip of the CESAM-HP combustor for Op16-0-2 . Top: Raw image, Middle: Image after background subtraction, Bottom: Image after background subtraction and spatial filtering	132
6.4	Validation experiment for the focusing Schlieren system. Both jets come from a choked tube of 2 mm diameter. While one jet is kept in the focal plane of the Schlieren system, the other is displaced on the Schlieren system axis. In this image dx corresponds to the distance from the focal plane.	134
6.5	Results of the validation experiment for the focusing Schlieren system. The results are equal for a positive or negative displacement.	134
6.6	Schematic drawing of the CESAM-HP test bench with the applied coordinate system. The system is a right-hand coordinate system, thus the y coordinate is showing away from the reader. The figure also includes the two regions where the Schlieren imaging is applied.	135
6.7	Focusing Schlieren visualization taken at the burner lip of the CESAM-HP combustor for Op16-0-2 (top), Op16-2-0 (middle) and Op13.4-4.6-0 (bottom). The images were pre-processed for a better visibility of the density gradients.	136
6.8	PSD of the Focusing Schlieren visualization taken at the burner lip of the CESAM-HP combustor for Op16-0-2 , Op16-2-0 and Op13.4-4.6-0 in region 1. The fourth diagram corresponds to a reference point taken at no combustion. It can be seen that the low frequency fluctuations associated with the combustion instability are well represented. The 4.2 kHz frequency, which is detected in the 2D Schlieren images, seems to be masked by other phenomena.	139

6.9	PSD spectra of the Focusing Schlieren visualization taken at the burner lip of the CESAM-HP combustor for Op16-0-2 , Op16-2-0 and Op13.4-4.6-0 in region 2. The fourth diagram corresponds to a reference point taken at no combustion.	140
6.10	2D PSD of the Focusing Schlieren visualization taken at the burner lip of the CESAM-HP combustor for Op16-0-2 . The top image corresponds to the 127 Hz mode and the bottom image to the 4.2 kHz mode.	141
6.11	2D PSD of the Focusing Schlieren visualization taken at the burner lip of the CESAM-HP combustor for Op16-2-0 . The top image corresponds to the 127 Hz mode and the bottom image to the 4.2 kHz mode.	142
6.12	2D PSD of the Focusing Schlieren visualization taken at the burner lip of the CESAM-HP combustor for Op13.4-4.6-0 . The top image corresponds to the 98 Hz mode and the bottom image to the 4.2 kHz mode.	143
6.13	Focusing Schlieren visualization taken at the exit of the CESAM-HP combustor for Op16-0-2 (top), Op16-2-0 (middle) and Op13.4-4.6-0 (bottom)	144
6.14	Focusing Schlieren visualization taken at the exit of the CESAM-HP combustor for Op16-0-2 (top), Op16-2-0 (middle) and Op13.4-4.6-0 (bottom) with an increased contrast	145
6.15	PSD spectra of the Focusing Schlieren visualization taken at the exit of the CESAM-HP combustor for Op16-0-2 , Op16-2-0 and Op13.4-4.6-0 . The fourth diagram corresponds to a reference point taken at no combustion.	147
6.16	2D PSD of the Focusing Schlieren visualization taken at exhaust of the CESAM-HP combustor for Op16-0-2 . The top image corresponds to the 127 Hz mode and the bottom image to the 4.2 kHz mode.	149
6.17	2D PSD of the Focusing Schlieren visualization taken at the exhaust of the CESAM-HP combustor for Op16-2-0 . The top image corresponds to the 127 Hz mode and the bottom image to the 4.2 kHz mode.	150
6.18	2D PSD of the Focusing Schlieren visualization taken at exhaust of the CESAM-HP combustor for Op13.4-4.6-0 . The top image corresponds to the 98 Hz mode and the bottom image to the 4.2 kHz mode.	151
6.19	PSD spectra of the Schlieren and Vibrometry measurements for Op16-0-2 at $x = 95$ mm and $z = 0$ mm. Top: Focusing Schlieren measurements; Bottom: LIV measurement	154
6.20	PSD spectra of the Schlieren and Vibrometry measurements for Op16-2-0 at $x = 95$ mm and $z = 0$ mm. Top: Focusing Schlieren measurements; Bottom: LIV measurement	155

6.21	PSD spectra of the Schlieren and Vibrometry measurements for Op13.4-4.6-0 at $x = 95$ mm and $z = 0$ mm. Top: Focusing Schlieren measurements; Bottom: LIV measurement	156
7.1	Applied coordinate system including the regions described in table 7.1. The coordinate system is right-handed. The y-coordinate is therefore showing away from the reader.	167
7.2	Top: Measured pressure and PM signal for Op16-0-2 . Bottom: PSD pressure and PSD PM signal for the same operating point.	168
7.3	Top: Measured pressure and PM signal for Op16-2-0 . Bottom: PSD pressure and PSD PM signal for the same operating point.	169
7.4	Top: Measured pressure and PM signal for Op13.4-4.6-0 . Bottom: PSD pressure and PSD PM signal for the same operating point.	170
7.5	Comparison of calculated and measured pressure for Op16-0-2 and the deduced PSD pressure	173
7.6	Comparison of calculated and measured pressure for Op16-2-0 and the deduced PSD pressure	174
7.7	Comparison of calculated and measured pressure for Op13.4-4.6-0 and the deduced PSD pressure	175
7.8	Coherence of p_{calc} and p_{meas} for Op16-0-2 , Op16-2-0 and Op13.4-4.6-0	176
8.1	Functioning of LIV (Li (2012); Kings et al. (2015))	180
8.2	Schematic Drawing of the CESAM-HP test bench with the applied coordinate system	181
8.3	Temperature distribution on the y-z-plane at $x = 122.5mm$, calculated by LES (Tao (2015))	182
8.4	Top: Raw density spectrum of Op16-0-2 measured by LIV, including the contribution of the measurements system vibrations. Bottom: Density fluctuations calculated from in-chamber pressure fluctuations and the temperature fluctuations	187
8.5	Top: Raw density spectrum of Op16-2-0 measured by LIV, including the contribution of the measurements system vibrations. Bottom: Density fluctuations calculated from in-chamber pressure fluctuations and the temperature fluctuations	188
8.6	Top: Raw density spectrum of Op13.4-4.6-0 measured by LIV, including the contribution of the measurements system vibrations. Bottom: Density fluctuations calculated from in-chamber pressure fluctuations and the temperature fluctuations	189
8.7	Temperature spectrum of Op16-0-2 measured by LIV	190
8.8	Temperature spectrum of Op16-2-0 measured by LIV	191
8.9	Temperature spectrum of Op13.4-4.6-0 measured by LIV	191

8.10	Entropy related temperature spectrum of Op16-0-2 measured by LIV	192
8.11	Entropy related temperature spectrum of Op16-2-0 measured by LIV	192
8.12	Entropy related temperature spectrum of Op13.4-4.6-0 measured by LIV	193
8.13	Time signal of the pressure and the temperature for Op16-0-2 . The red horizontal line shows the phase shift between the two signals.	194
8.14	Time signal of the pressure and the temperature for Op16-2-0 . The red horizontal line shows the phase shift between the two signals.	195
8.15	Time signal of the pressure and the temperature for Op13.4-4.6-0 . The red horizontal line shows the phase shift between the two signals.	195
8.16	Representation of the approach to determine direct and indirect combustion noise contributions (<i>Kings et al. (2015)</i>). The reflections at both ends are neglected.	196
8.17	Spectra of the pressure oscillations of the up- and downstream propagating acoustic wave as well as of the downstream propagating entropy wave in the combustion chamber for Op16-0-2 .	198
8.18	Spectra of the pressure oscillations of the up- and downstream propagating acoustic wave as well as of the downstream propagating entropy wave in the combustion chamber for Op16-2-0 .	199
8.19	Spectra of the pressure oscillations of the up- and downstream propagating acoustic wave as well as of the downstream propagating entropy wave in the combustion chamber for Op13.4-4.6-0	200
8.20	Direct, indirect and total combustion noise spectra of Op16-0-2	202
8.21	Direct, indirect and total combustion noise spectra of Op16-2-0	202
8.22	Direct, indirect and total combustion noise spectra of Op13.4-4.6-0	203
A.1	PSD of the pressure signal recorded in the CESAM-HP test bench with the three operating points Op16-0-2 , Op16-2-0 and Op13.4-4.6-0 . The highest activity can be observed in the low frequency region below 1000 Hz with distinct peaks that are associated with a combustion instability and a high direct combustion noise contribution.	212
A.2	RMS pressure map of the fully premixed case	215
A.3	PSD at 0 g/s axial air flow through the perforated plate of the measured pressure (top image) and the theoretically calculated pressure (middle image) for the different configurations. The bottom image shows the coherence of these two pressures. . . .	217
A.4	Mean injector PM intensity map of the fully premixed case . .	218

A.5	RMS injector PM intensity map of the fully premixed case . . .	218
A.6	Modified injector with the flame holder rod	219
A.7	RMS pressure in dependence from the ICS bias air flow rate for fully premixed combustion with and without flame holder rod . . .	220
A.8	PSD at 0 g/s axial air flow through the perforated plate of the measured pressure (top image) and the theoretically calculated pressure (middle image) for the different configurations. The bottom image shows the coherence of these two pressures. . . .	221
A.9	Mean injector PM signal in dependence from the ICS bias air flow rate for fully premixed combustion with and without flame holder rod	222
A.10	RMS injector PM signal in dependence from the ICS bias air flow rate for fully premixed combustion with and without flame holder rod	222
A.11	Modified injector including the separate fuel injection. The fuel injection is installed in the last element before the combustor. The drawing also includes the flame holder that stabilizes the flame.	223
A.12	Schematic drawing of the fuel injector element including the flow directions of the fuel.	224
A.13	Flame shape of Op16-0-2 at fully premixed and partially premixed functioning	225
A.14	RMS pressure in dependence from the ICS bias air flow rate for fully premixed and the partially premixed case	226
A.15	PSD at 0 g/s axial air flow through the perforated plate of the measured pressure (top image) and the theoretically calculated pressure (middle image) for the different configurations. The bottom image shows the coherence of these two pressures. . . .	228
A.16	Mean injector PM signal in dependence from the ICS bias air flow rate for fully premixed and the partially premixed case . . .	229
A.17	RMS injector PM signal in dependence from the ICS bias air flow rate for fully premixed and the partially premixed case . . .	229
A.18	Schematic drawing of the CESAM-HP testbench updated by the secondary air injection through the chamber walls.	230
A.19	RMS pressure map of the fully premixed case with secondary air injection	232
A.20	PSD at 0 g/s axial air flow through the perforated plate of the measured pressure (top image) and the theoretically calculated pressure (middle image) for the different configurations. The bottom image shows the coherence of these two pressures. . . .	233
A.21	Mean injector PM intensity map of the fully premixed case with secondary air injection	234
A.22	RMS injector PM intensity map of the fully premixed case with secondary air injection	234

A.23	RMS pressure in dependence from the ICS air flow rate for the different configurations	236
A.24	Mean injector PM signal in dependence from the ICS air flow rate for the different configurations	237
A.25	RMS injector PM signal in dependence from the ICS air flow rate for the different configurations	237
A.26	PSD at 0 g/s axial air flow through the perforated plate of the measured pressure (top image) and the theoretically calculated pressure (middle image) for the different configurations. The bottom image shows the coherence of these two pressures. . . .	240
A.27	PSD at 1 g/s axial air flow through the perforated plate of the measured pressure (top image) and the theoretically calculated pressure (middle image) for the different configurations. The bottom image shows the coherence of these two pressures. . . .	241
A.28	PSD at 2 g/s axial air flow through the perforated plate of the measured pressure (top image) and the theoretically calculated pressure (middle image) for the different configurations. The bottom image shows the coherence of these two pressures. . . .	242

Nomenclature

The following file gives the nomenclature :

Latin Characters :

A	Surface	p'	Pressure fluctuations
A	Camera aperture	q	Heat release rate
c	Sound speed	\bar{q}	Heat release rate fluctuations
c_p	Specific heat	q'	Heat release rate fluctuations
c_v	Specific heat	R	Gas constant
d	Diameter	R	Reflection coefficient
e	Internal energy	r	Specific gas constant
f	Frequency	s	Entropy
f_s	Sampling frequency	\bar{s}	Mean entropy
C	Coherence	s'	Entropy fluctuations
G	Cross/Auto spectral density	St	Strouhal number
G	Gladstone Dale index	t	Time
H	Transfer function	T	Temperature
k	Thermal conductivity	\bar{T}	Mean temperature
k	Wave number	T'	Temperature fluctuations
\dot{m}	Mass flow rate	u	Velocity
l	Length	\bar{u}	Mean velocity
L	Length	u'	Velocity fluctuations
M	Mach number		
p	Pressure		
\bar{p}	Mean pressure		

Greek Characters :

γ	Isentropic coefficient	$\bar{\rho}$	Mean density
λ	Wave length	ρ'	Density fluctuations
Φ	Equivalence ratio	τ	Viscous stress
ρ	Density		

Abbreviations :

CESAM	"Combustion Etagée Swirlée Acoustiquement Maitrisée - Haute Pres- sion" - "Staged Swirled Acoustically Controlled Combustion - High Pressure")
EWG	Entropy Wave Generator
FFT	Fast Fourier Transform
ICS	Impedance Control System
ITHACA	Impedance Test bench for High ACoustic Amplitudes
LES	Large eddy simulation
LIV	Laser interferometric Vibrometry
PCMV	Planar Continuous laser-based Mie scattering Velocimetry
PM	Photomultiplier
PIMS	Pressurized Impedance Measurement System
PSD	Power Spectral Density
PIV	Particle Image Velocimetry
RECORD	Research on CORE noise reDuction
RMS	Root mean square
SNR	Signal to noise ratio

Introduction

State of art in the development of combustion in aircraft engines

With rising world population and economic growth, air traffic is supposed to increase and thus also the amount of aircrafts. [Vedantham and Oppenheimer \(1998\)](#) predicted an increase of air traffic by a factor of around 10 from the year 2000 to 2050, with the highest growth around 2030. The consequence is an increase in exhaust emissions. In the same work, the CO_2 emissions are predicted to rise by a factor of 8 and the NO_x emissions by a factor of five until the year 2100, even when taking into account reductions due to technological progress. [Woody et al. \(2011\)](#) obtained similar results, predicting NO_x emissions to double from 2005 to 2025. Another consequence of the increasing air traffic is the increased aircraft noise, especially close to airports.

The increasing emissions are the motivation for the continuous improvements of aircraft engines. Indeed, the emissions of CO_2 are considered a major contributor of global warming and the associated environmental effects ([EPA \(2010\)](#)). NO_x emissions on the other hand are responsible for phenomena such as acid rain, which also leads to environmental damages. Besides, air pollution contributes to health issues such as respiratory problems or heart diseases. Aircraft noise on the other hand can lead to hearing loss and disturbances in sleep, in particular for the population living close to airports ([enHealth \(2004\)](#)).

Due to these aspects, but even more due to economical motivations, reductions in these emissions are especially linked to the reduction of the specific fuel ratio ([Gröenstedt et al. \(2013\)](#)). In particular the introduction and the increase of bypass flow lead to a significant decrease in fuel consumption, as shown in figure 1.

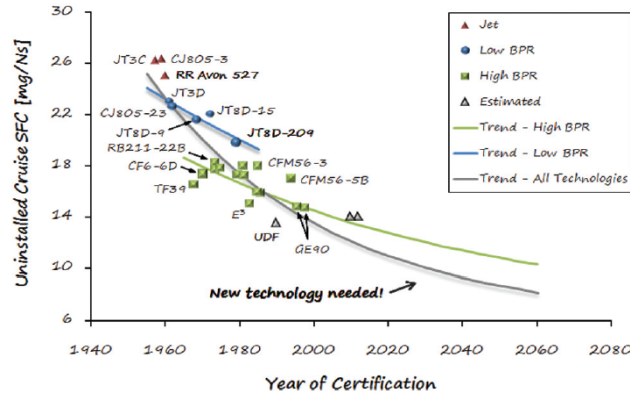


Figure 1: Trend of the specific fuel consumption for aircraft turbo engines (Grönstedt et al. (2013))

As can be seen in the figure the technological development is converging towards a plateau. According to Grönstedt et al. (2013), ruptures in technology are needed for further reductions in fuel consumption. Possible examples would be advanced cycles, such as pulse detonation combustors (Wintenberger2004), open rotors (Hendricks (2011)) or even attempts to integrate the combustion in the first stator stages of the engine (Schobeiri and Ghoreyshi (2014); Schobeiri and Ghoreyshi (2015)).

All these technologies lead to a decrease in CO_2 emissions as a consequence of a decreased fuel consumption. However they are based on the use of improved, more compact combustors, which lead to higher temperatures. But already the first studies of combustion have shown that an increase in combustion temperature leads to an increase of NO_x emissions (Zeldovich (1946)). Indeed, Suder (2012) showed the direct link between the reduction of specific fuel consumption and the increase of NO_x emissions, as presented in figure 2.

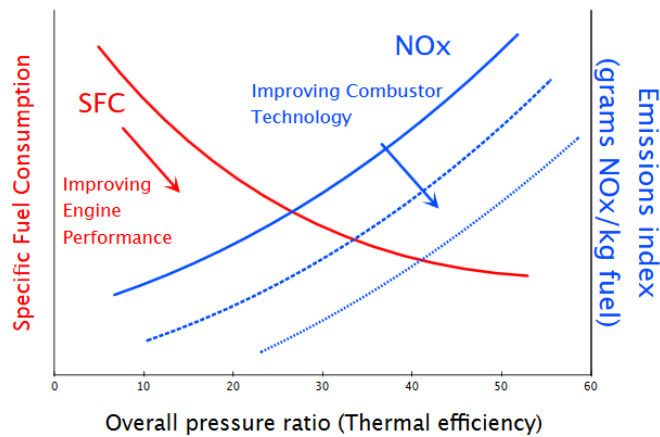


Figure 2: Relation of Specific fuel consumption, NO_x emissions and pressure ratio. (created by Lapeyre (2015), based on Suder (2012)). The overall pressure ratio is directly linked with the thermal efficiency and the turbine entry temperature of the engine (Jeschke (2012))

The typical solution for this issue is the application of lean premixed combustion. Previous works show that this arrangement significantly reduces NO_x emissions (Correa (1998)). However this causes new issues in terms of stabilization of the flame:

- Due to the low equivalence ratio, the risk of extinction exists and is problematic especially due to issues of re-ignition. (Stöhr et al. (2011))
- With the premixing, the flame has the tendency to flash back into the injector. This condition is dangerous, since it can damage the entire system due to overheating. (Fritz et al. (2004); Lapeyre et al. (2016))
- The next issue is the existence of combustion instabilities, which can be explained by a positive feedback circle. The geometric eigen modes lead to pressure fluctuations. These perturb the flow field, which then perturbs the local heat release rate. Finally, these generated fluctuations of heat release directly influence the pressure fluctuations. The possible consequences of these are system ruptures due to premature fatigue and excessive vibrations, as well as increased noise nuisance. (Candel (2002); Ducruix et al. (2003))

The first issue can be resolved by the Swirl stabilization. In this arrangement the premixture is injected either via tangential injection or an axial swirler in order to create a rotational motion. (Candel et al. (2014); Bräunling (2015)) The consequence is a compact flame, which can be operated under lower equivalence ratios. The typical flow structure of a swirling flame is shown in figure 3.

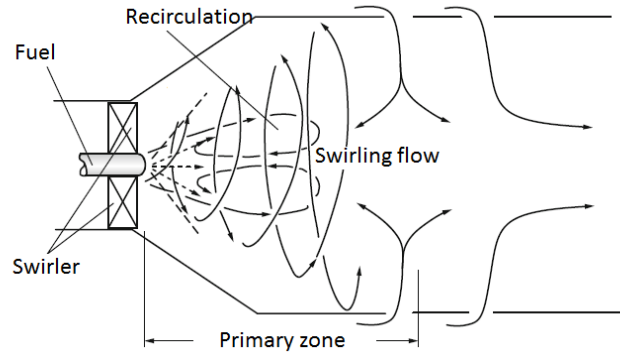


Figure 3: Typical flow structure in a Swirl stabilized aircraft combustor (*Bräunling (2015)*)

The issue of flashback can be resolved by constructive choices, as was shown in previous works. For example, the injection of a small axial air flow can counterbalance the flashback tendency and the installation of a bluff body can block the flame from flashing back into the injector (*Fritz et al. (2004)*; *Reichel et al. (2015)*; *Sattelmayer et al. (2015)*).

The third issue, the combustion instabilities are still of high actuality and are being studied extensively. Combustion instabilities occur in combustors where the flame is highly turbulent and confined. The interactions between the flame and the chamber walls as well as the vortices lead to fluctuations in heat release rate of the flame and thus in pressure. These pressure oscillations perturb the flame itself. This positive feedback circuit is typical for combustion instabilities and can even lead to damages of the combustor. A state of art about the research in instabilities can be found in different works (*Candel (2002)*; *Ducruix et al. (2003)*; *Lieuwen and Cho (2005)*).

Another issue of actuality is combustion noise. Aircraft engines can be a great noise nuisance, especially close to airports. In 2013 the International Civil Aviation Organization ICAO agreed on a global standard for further aircraft noise reductions (*FAA (2016)*). As combustion noise is a contributor to overall aircraft engine noise, its understanding and reduction is of high actuality. The state of art of the research on combustion noise is presented in the following section.

Combustion noise

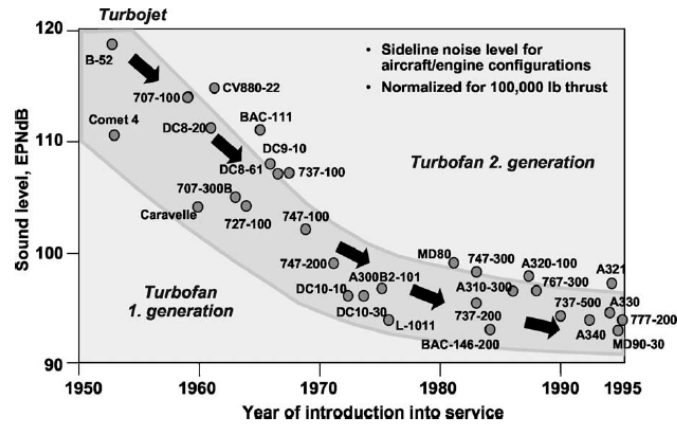


Figure 4: Reduction of aircraft engine noise in the last decades (Neise and Enghardt (2003))

The noise of aircraft engines has continuously been reduced as shown by Neise and Enghardt (2003). The diagram shows that after rapid decreases of aircraft noise in the 1960s and 70s, it has become more and more difficult to obtain significant noise reductions. In these first periods, the noise reduction has been achieved due to advances in different engine elements such as the exhaust jet or the fan, where for example the blade shape has been optimized. Sensiau (2013) shows that major improvements were achieved in particular for the rotating part and the exhaust jet, as can be seen in figure 5.

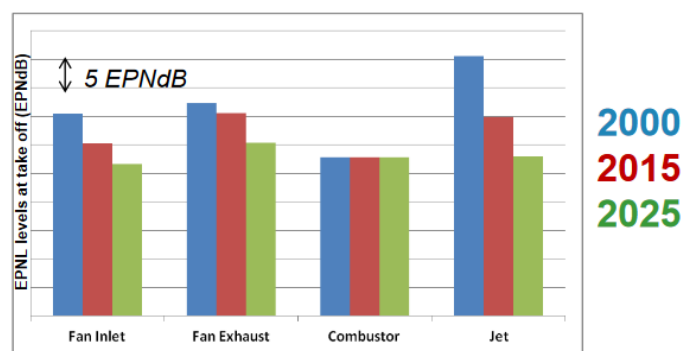


Figure 5: Breakdown of the different engine noise contributions and their predicted development until 2025 (Sensiau (2013))

Figure 5 shows another interesting aspect: While the noise of the fan, the turbine and the jet were continuously decreased, only few work was done on

the combustor. This is due to the fact that in the past, combustion noise did not play a major role compared to the other contributors. However, with the reductions in noise of the different engine components to come, combustion noise will equally become a major contributor of overall engine noise. This is especially the case in approach and taxiing, where the jet velocity is low, while combustion noise stays relatively high. Combustion noise is characterized by a low frequency, as shown in figure 6. Its frequency is usually below 1.5 kHz and it has a broadband spectrum (Sensiau (2013); Leyko (2010); Silva (2010)).

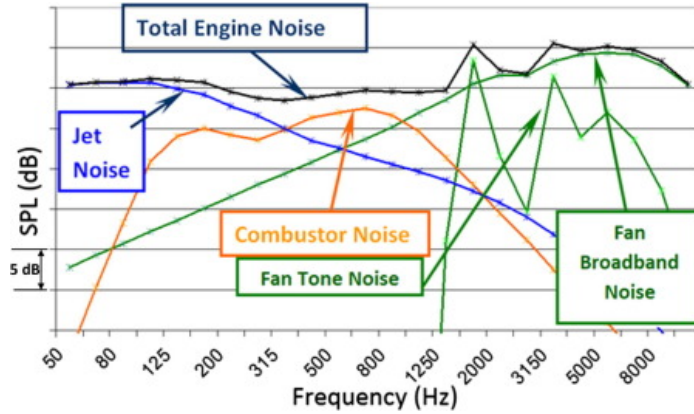


Figure 6: Breakdown of the different engine noise contributions in their typical spectra (Sensiau (2013))

Combustion noise can be described by noise emissions which are generated by enhanced system resonances as explained by Candel et al. (2009) and can be separated into the following contributions, as presented in figure 7

- Direct combustion noise is noise generated from the heat release fluctuations from the flame itself
- Indirect combustion noise results from the inhomogeneities in vorticity and entropy in the burnt gases, which are generated by the turbulent flame. These are accelerated in the engine parts downstream of the combustor, such as an exhaust nozzle or the first turbine stages.

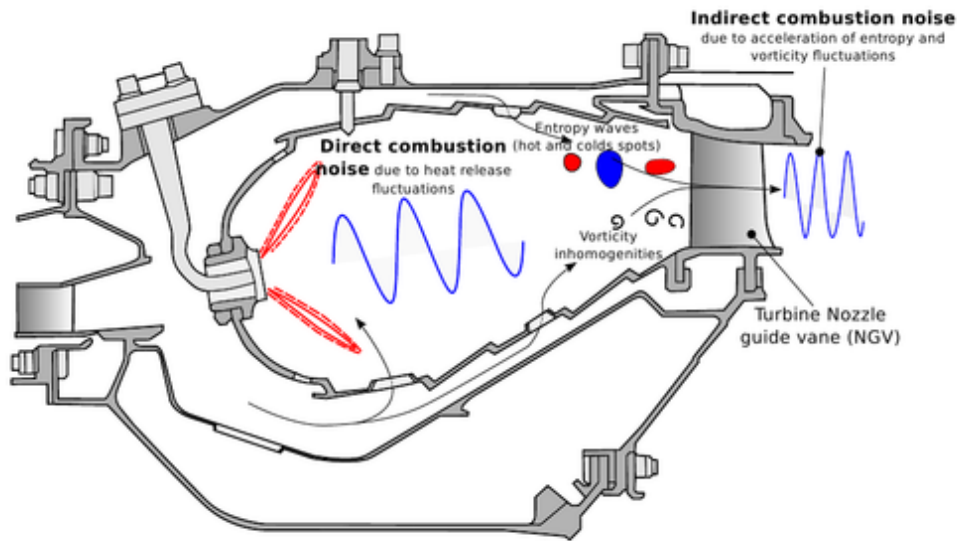


Figure 7: Schematic drawing of an aircraft combustion chamber with illustrations of direct combustion noise, entropy noise and vorticity noise (Ulrich and Sattelmayer (2016))

The mechanisms which generate direct and indirect combustion noise have been described in various reviews (Strahle (1978); Crighton et al. (1992); Candel et al. (2009); Dowling and Mahmoudi (2015); Morgans and Duran (2016)).

Since the focus of this thesis is the experimental study of combustion noise, a detailed presentation of the different experimental works is provided. The description concentrates on gas turbine combustors. The aim is also to show the questions which stay open and the motivations for the present work. Finally, the most relevant mechanisms of direct and indirect combustion noise are described.

Overview of the experimental studies of combustion noise in gas turbine combustors

The first experimental studies of combustion noise in aero engines were conducted already in the 1970s and 80s. The aim was to identify the contribution of combustion noise in industrial gas turbines and to compare it with other contributors, such as turbine or jet noise.

The first tests were conducted by Karchmer and Reshotko (1976) on an AVCO-Lycoming YF-102 turbofan engine, where several microphones were mounted on different positions. The total engine noise was measured by mounting micro-

phones in the far-field of the engine. The contributions of the different engine parts were then obtained by calculating the correlation and coherence between the different microphones. It could be shown that the combustor contributes with broadband noise in frequencies below 200 Hz. [Karchmer and Reshotko \(1976\)](#) also concluded that combustion noise is the main contributor when the engine is operated at low loads.

Similar observations were made by [Shivashankam \(1978\)](#) on an iResearch GTC P 85 series gas turbine, which is used as an Auxiliary Power Unit (APU) in aircraft, and by [Guédel and Ferrando \(1986\)](#) on a TM 333 turboshaft engine. Both identified combustion noise as a low frequency broadband contributor that is dominant in low load operating points. Besides, [Guédel and Ferrando \(1986\)](#) compared the acoustic signal downstream of the combustor with that within and saw that the former one is dominating. This result suggests the high importance of indirect combustion noise.

More recently, [Harper-Bourne et al. \(2008\)](#) tested the contribution of combustion noise on a Rolls-Royce Trent 500 engine in the framework of the European SILENCE(R) program and obtained similar findings.

The technique of using correlations and coherences is also applied in first attempts to separate direct from indirect combustion noise. This is done by adding high-speed thermocouples at different positions in the gas turbine. By calculating the correlation between the thermocouple signals and the different microphone signals, first conclusions could be made about the importance of entropy noise. This approach was applied by [Muthukrishnan et al. \(1978\)](#) on a Boeing 502-7D gas turbine, by [Pickett \(1975\)](#) on a JT3D engine from Pratt and Whitney and equally by [Strahle and Muthukrishnan \(1980\)](#) on different aero engines. These works confirm the previous observations that combustion noise is a broadband phenomenon at low frequencies. With the help of the thermocouple spectra they could also show that entropy noise is a more important contributor for noise in industrial gas turbines than direct combustion noise. With raising interest on combustion noise, the technique was applied on recent aero engines.

In the framework of the European TEENI project ([Duran et al. \(2014\)](#)), [Livebardon \(2015\)](#) conducted experiments on a turbo-shaft engine from Turbomeca. This engine has the advantage that jet noise is low, thus the contribution of combustion noise is easier to detect. The signals of in-chamber microphones and high speed thermocouples are compared with those of far-field microphones in order to identify the contributions of direct and indirect combustion noise. However, the study is limited by the response time of the thermocouples, which only allows for correct measurements up to 300 Hz ([Childs \(2003\)](#)).

While all these studies allowed to identify the strong contribution of entropy noise to total combustion noise, a quantification still needs to be done. For this purpose, different laboratory scale experiments were developed, where entropy

waves are accelerated in a nozzle. [Zukoski and Auerbach \(1976\)](#) made first attempts to generate periodic temperature fluctuations in flows. In a more recent experiment created by [Bake et al. \(2009\)](#), the so-called Entropy Wave Generator (EWG), air is periodically heated by an electric heating module. It is accelerated through a choked nozzle and the pressure fluctuations are measured by microphones on different positions upstream and downstream of the nozzle. The results in general correspond to theory and show in particular that the entropy noise generation increases with a decreasing Mach number at the nozzle entry and an increasing Mach number at the nozzle exit. Differently said, the more the nozzle is accelerating the flow (and thus the density fluctuations), the more entropy noise is generated.

Studies of combustion noise were also made on laboratory scale. The analysis of direct combustion noise is straightforward due to the link of the pressure and the heat release rate of the flame, as shown by [Schuller et al. \(2002\)](#). An example is the experiment of [Bender et al. \(2009\)](#), who measured the sound emission from a confined swirling combustor with modifiable geometry. The experiments showed indeed the link between the pressure fluctuations and the spatially resolved fluctuations of the heat release rate of the flame.

First attempts were also made to use laboratory scale combustors, where the entropy waves are generated by the flame and accelerated through an exhaust nozzle. Examples of such chambers are presented by [Bake et al. \(2008\)](#), [Bake et al. \(2009\)](#), where a combustor with a nozzle is examined. By varying the nozzle geometry, the Mach number at the nozzle exit is varied as well. The experiments show that combustion noise generation increases with increasing nozzle exit Mach number. The experiments thus confirm the findings on the EWG.

The EWG allows to generate entropy fluctuations artificially and the experiments on laboratory scale show the importance of their acceleration for entropy noise generation. However, no test bench exists yet, where direct and indirect combustion noise are studied and quantified with a turbulent flame as a source. The aim of this thesis is to narrow this gap and to design and build a pressurized lean swirling combustor test bench, which generates high quantities of indirect combustion noise. Similarly to the previous works, the entropy waves are to be accelerated by an exhaust nozzle. The difficulties of this objectives are the high pressure which needs to be attained and the thermal load on the walls. Furthermore, the right dimensions need to be found, leading to high quantities of indirect combustion noise while avoiding the existence of a strong combustion instability. Also, the acoustic boundary conditions must be well-known and controllable.

The second aim is then to characterize this combustor, determine its acoustic boundary conditions and to find means to determine the contributions of direct and indirect combustion noise. This is however not trivial, due to the harsh

environment in the combustor and the high needs for spatial and temporal resolution. It also has to be added that in this thesis, vorticity noise is not taken into account. Thus when speaking of Indirect combustion noise, only the entropy noise is meant.

In this thesis, the design of the combustor is based on the most important theoretical findings concerning direct and indirect combustion noise generation. They are summarized in the next section and then used to suggest different design objectives for the combustor built and used in this work. A good summary of the key processes that are connected to entropy noise was recently made by [Morgans and Duran \(2016\)](#) and is recapitulated here and combined with a description of the direct combustion noise generation.

Theoretical framework on combustion noise generation

First it needs to be considered that indirect combustion noise can be separated into two contributors, vorticity noise and entropy noise. The noise generated by vorticity fluctuations has been theoretically described by [Howe \(2003\)](#). In a numerical simulation of a vortex propagating through a nozzle, [Hulshoff et al. \(2001\)](#) found that the main factors that influence the amplitude of vorticity generated noise are the vortex circulation, the initial position of the vortex and the mean flow Mach number. In an experimental approach [Kings et al. \(2011\)](#) generated vorticity waves artificially by pulsed alternating circumferential air-injections and found that an increasing intensity of the swirling flow also increases noise generation in the nozzle.

However in this thesis the focus is put on entropy noise, while vorticity noise is not taken into account. Thus when speaking of indirect combustion noise, only the entropy noise contribution is meant.

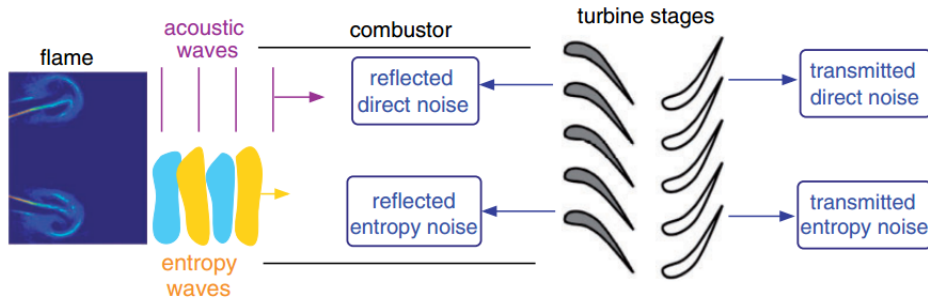


Figure 8: Schematic drawing of the key processes that are connected to combustion noise ([Morgans and Duran \(2016\)](#))

These key processes, identified by [Morgans and Duran \(2016\)](#) and summarized

in figure 8, are following (extended by the generation of direct combustion noise):

- Generation of acoustic waves in the flame
- Generation of entropy waves in the flame
- Propagation of entropy waves through the combustor
- Acceleration of the entropy wave and generation of entropy noise
- Propagation of the entropy wave through the turbine
- Effects of the reflected entropy noise on the combustion instability

Generation of acoustic waves in the flame

Many studies were conducted about the generation of acoustic waves in the flame, thus direct combustion noise. The first ones were conducted on free flames. These experiments have shown the link between the heat release fluctuations of the free flame and the resulting noise emission in the far field (Smith and Kilham (1963); Thomas and Williams (1966); Shivashankara et al. (1975)). This phenomenon has been expressed mathematically by Strahle (1978) and corrected by Crighton et al. (1992). In a review of these works, Candel et al. (2009) describe the link between the flame heat release fluctuations and the far field noise by the following equation:

$$p'(r, t) = \frac{\gamma - 1}{4\pi c_0^2 r} \int_{V_c} \frac{\partial \dot{Q}}{\partial t} \left(r_{0,t} - \frac{r}{c_0} \right) dV(r_0) \quad (1)$$

with c_0 the ambient speed of sound, \dot{Q} the global heat release rate, γ the specific heat release ratio, V_c the volume of the combustion zone and $\frac{r}{c_0}$ the time span for the generated sound to propagate between flame and far field observer.

This equation has been based on the approach, that sound is generated in a quantity of monopole sound sources, which corresponds to Lighthill's analogy for aerodynamic sound (Lighthill (1952)). These sources are generated by the heat release fluctuations of the flame. The source term in this equation includes the interactions between turbulent flow and the pressure field, for example convection, refraction or diffraction (Bogey et al. (2003); Bailly et al. (2010)). Abugov and Obrezkov (1978) and later Clavin and Siggia (1991) could demonstrate experimentally the link between far field pressure fluctuations and the fluctuations of flame surface, putting forward the relation between the surface changing due to turbulence and sound generation. However, the approach of eq. 1 is only valid under the precondition that the length scale L of the flame is well below the acoustic wavelength λ , which itself is well below the distance

between flame and observer r : $L \ll \lambda \ll r$

The preconditions mentioned for the theory below are not valid in an industrial combustion chamber, where the pressure is measured close to the flame. Furthermore, the confinement by the chamber walls is not taken into account. Nevertheless the equation is sufficient to explain the generation of direct combustion noise.

Generation of entropy waves in the flame

The next aspect that is mentioned by [Morgans and Duran \(2016\)](#) is the generation of entropy waves in the flame. This phenomenon can be explained based on the calculations presented in [Dowling and Stow \(2003\)](#) and [Dowling and Williams \(1983\)](#) and stated in the following.

The energy conversion in a compressible flow can be described by the following equation:

$$\rho \frac{D}{Dt} \left(e + \frac{1}{2} u^2 \right) = -\nabla \cdot (pu) + q + \nabla(k\nabla T) + \frac{\partial}{\partial x_j} (\tau_{ij} u_i) \quad (2)$$

with ρ the fluid density, e the internal energy, u the velocity, p the pressure, q the heat release rate, k the thermal conductivity, T the temperature and τ_{ij} the viscous stress tensor. This equation can be combined with Gibb's equation $Tds = dh - dp/\rho$, where s is the entropy and h is the enthalpy. This operation results in the following equation:

$$\rho T \frac{Ds}{Dt} = q + \nabla(k\nabla T) + \tau_{ij} \frac{\partial u_i}{\partial x_j} \quad (3)$$

The left side of this term shows the entropy advection. The three terms on the right hand side are either entropy sources or entropy sinks. The first one corresponds to the generation of heat, the second to thermal gradients and the third to heating due to friction.

Another classical entropy definition is $s = c_v \ln(p/p^\gamma)$. If this is decomposed into a mean and fluctuating part and the perturbations are supposed to be small, one obtains $s' = c_v p'/\bar{p} - c_p \rho'/\bar{p}$. Combined with the ideal gas law, this leads to the equation:

$$\frac{s'}{c_p} = \frac{T'}{\bar{T}} - \frac{\gamma - 1}{\gamma} \frac{p'}{\bar{p}} \quad (4)$$

When this equation is combined with eq. 3, assuming constant k and linearising, one obtains following:

$$\frac{\bar{D}s'}{Dt} = \frac{R}{\bar{p}} \left[q' + \nabla(k\nabla T') + \bar{\tau}_{ij} \frac{\partial u'_i}{\partial x_j} + \tau'_{ij} \frac{\partial \bar{u}_i}{\partial x_j} \right] - \left(\frac{p'}{\bar{p}} + \frac{u'_i}{\bar{u}_i} \right) (\bar{q} + \nabla(k\nabla \bar{T}) + \bar{\tau}_{ij} \frac{\partial \bar{u}_i}{\partial x_j}) \quad (5)$$

It is often assumed, that the flow is non-diffusive. The viscous effects and temperature gradients are thus neglected. Furthermore, it is assumed that for low frequencies the acoustic waves are plane and one-dimensional. In this case, the equation simplifies to the following ([Dowling et al. \(1988\)](#)):

$$\frac{\bar{D}s'}{Dt} = \frac{R\bar{q}}{\bar{p}} \left(\frac{q'}{\bar{q}} - \frac{p'}{\bar{p}} - \frac{u'}{\bar{u}} \right) \quad (6)$$

Eq. (6) shows that the generated entropy fluctuations depend principally on the heat release fluctuations. These need to be high in order to generate strong entropy fluctuations. However, as already explained in this section, these heat release fluctuations ultimately also generate direct combustion noise. The consequence on the practical design of a combustor for combustion noise research is, that a compromise needs to be found between strong entropy fluctuations and low direct combustion noise generation.

Propagation of entropy waves through the combustor

Once generated at the flame, the entropy waves propagate downstream in the combustion chamber. This corresponds to the next process, which [Morgans and Duran \(2016\)](#) states.

The propagation of entropy in the combustor is described by Eq. (3). Since the entropy waves have left the flame in this stage, the heat addition term is zero. The equation becomes thus following:

$$\rho T \frac{Ds}{Dt} = \nabla(k\nabla T) + \tau_{ij} \frac{\partial u_i}{\partial x_j} \quad (7)$$

In this equation, the entropy fluctuations depend on the temperature gradients and on friction losses. This means that the entropy waves lose their strength while propagating in the combustion chamber. This was also observed in the experimental works of [Sattelmayer \(2002\)](#) and [Eckstein et al. \(2004\)](#). They showed in their combustor test benches that the entropy waves have almost disappeared in the combustor exit. On the other hand, the LES simulations of

combustors in actual engines show that the entropy fluctuations survive until their arrival to the chamber exit (Franzelli et al. (2012); Leyko et al. (2009); Livebardon (2015); ?). As stated by Morgans and Duran (2016), no stronger conclusions can be made on this topic and further research needs to be done.

Nevertheless, different conclusions on combustion system design can be drawn from the existing findings and from Eq. (7). In general it is desirable, that the combustion chamber is as short as possible in order to minimize losses due to friction or heat losses (However care needs to be taken as the higher confinement can decrease the flame stability). A possibility to even increase entropy fluctuations could be the addition of a secondary air flow through the chamber walls, as done in industrial aero engine combustors (Jeschke (2012)). These would increase the temperature gradients in the burnt gases and thus possibly also the entropy fluctuations.

Acceleration of the entropy wave and generation of entropy noise

The next mechanism mentioned by Morgans and Duran (2016) is the generation of entropy noise due to the acceleration of the entropy noise in a nozzle or a turbine stage.

The interactions between pressure fluctuations and flow homogeneities were already observed in the 1950s. Tsien (1952) developed an analytical expression for the response of a nozzle to an excitation in velocity and pressure. Furthermore, Crocco (1951) studied the effects of nozzles on combustion instabilities. Based on pressure and velocity measurements at the nozzle inlet, they obtained an analytical solution for the response of the nozzle on the entire frequency range. In a later work Bell et al. (1973) used an impedance tube facility in order to determine the admittance of a nozzle experimentally.

The results of these first studies led to the suggestion that the acoustic impedance of the nozzle has an influence of the sound generated by flow inhomogeneities. In order to test the contribution of each, Chu and Kovaszny (1958) synthesized the flow homogeneities from the burnt gases of a turbulent flame into its acoustic, vorticity and entropy modes. They then examined the interaction between each of these modes with a nozzle (as treated by Marble and Candel (1977); Moase et al. (2007)) or a turbine stage (as shown by Cumpsty (1979)). They could show that acoustic modes propagate the nozzle or turbine blade at speed of sound, while entropy and acoustic waves do so at flow velocity. When the mean flow velocity increases, the fluctuations in entropy or vorticity are then transformed into sound emission.

The generation of entropy noise due to acceleration of the flow homogeneities is described in a simplified way by Marble and Candel (1977). The nozzle is

considered as compact and its length is thus negligible compared to the wave length of the acoustic and the entropy wave. The density perturbations are considered one-dimensional. In this work the sound generation due to the entropy wave could be calculated analytically. The results show that while the acoustic wave is reflected and transmitted, another acoustic wave is transmitted that is associated with the accelerated entropy wave. The work has also shown the importance of the Mach number. Entropy noise generation is highest when the Mach number of the flow is low at the nozzle entry and high at the nozzle exit. Differently said, the more the flow (which contains the entropy fluctuations) is accelerated, the more noise is generated in the nozzle. These findings are also illustrated in figure 9.

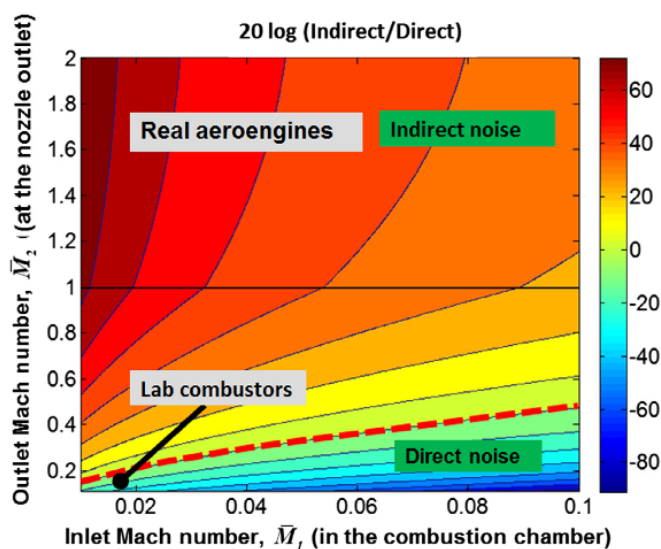


Figure 9: Comparison of the effects of the Mach number in the combustion chamber and at the nozzle exit on combustion noise generation (Dowling and Mahmoudi (2015), based on the simulations of Leyko et al. (2009))

Concerning combustor design, these findings mean that the burnt gases need to be accelerated as much as possible in order to generate large quantities of indirect combustion noise. For the sake of simplicity this is done in a nozzle. In the presented theoretical works (Marble and Candel (1977); Leyko et al. (2009)) the flow even attains velocities that are higher than the speed of sound. Therefore, the exhaust nozzle is choked and the in-chamber pressure increases. As a consequence, higher mechanical and thermal stresses are put on the structure, which needs to be taken into account during the combustor design process.

These findings are however valid only under the assumption of a compact nozzle. ? went a step further and developed an analytical solution for any exhaust

nozzle and are thus able to calculate the generated direct and indirect combustion noise for more general cases.

Propagation of the entropy wave through the turbine

In industrial scale gas turbines, the entropy waves do not propagate through one turbine stage or nozzle, but through a series of blades. The process which leads to the generation of indirect combustion noise is similar to what was described in the previous section. Moreover, this problematic is not relevant for this laboratory scale project. Therefore, this point is not detailed further. A detailed theoretical description can be found in [Morgans and Duran \(2016\)](#).

Effects of the reflected entropy noise on the combustion instability

The acoustic waves that are generated in the exhaust nozzle propagate downstream and upstream towards the flame. As explained by [Morgans and Duran \(2016\)](#), these acoustic waves can interact with a possible combustion instability that can be found in the burner.

The different mechanisms of combustion instabilities are explained by [Ducruix et al. \(2003\)](#). A typical mechanism is the impact of the flame on the chamber walls, which leads to periodic changes of the flame surface, thus fluctuations of the heat release rate and finally pressure fluctuations. Another mechanism is the flame vortex interaction, where vortices lead to a periodic roll-up of the flame, leading to fluctuations of heat release rate and thus pressure. Besides, [Ducruix et al. \(2003\)](#) explains different mechanisms, in which the pressure fluctuations act on the flame. This leads to a positive feedback circuit, as described by [Candel \(2002\)](#). The pressure fluctuations can for example lead to flow rate fluctuations in the feeding lines, which leads to oscillations in equivalence ratio and thus finally to heat release fluctuations. Furthermore, the pressure fluctuations also act on the vortices which interact with the flame, or on the flame-wall interaction.

In the same way, the generated entropy noise, which is propagating upstream, can also have an influence of the different mechanisms that were described before. However it is difficult to predict the effects beforehand. [Goh and Morgans \(2013\)](#) have shown in an analytical study the effects of entropy noise on the strongest eigen modes of a model combustor. They observed various possible effects: Entropy noise could destabilize stable modes but also stabilize unstable ones. It could also lead to mode switching or cause proper acoustic-entropic instabilities. Due to this variety, no conclusions can be made on combustor design. But what has been shown by ? and ? is that the reflection coefficient from the first stage of the high pressure turbine is low.

Motivation of this thesis

As shown in the previous sections, various works have been done in order to describe direct and indirect combustion noise generation experimentally. However no work has been done where a combustion system generates direct and indirect combustion noise simultaneously. The aim of this thesis is to narrow this gap and to design and build a pressurized lean swirling combustor test bench, which generates high quantities of indirect combustion noise. Similarly to the previous works, the entropy waves are to be accelerated by an exhaust nozzle. The second aim is then to characterize this combustor, determine its acoustic boundary conditions and to find means to determine the contributions of direct and indirect combustion noises.

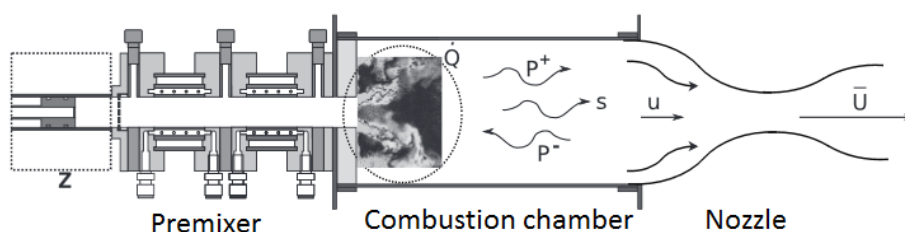


Figure 10: Schematic drawing of the CESAM testbench of EM2C Laboratory (*Lamraoui (2011)*)

The thesis is using and integrating the rich experience of EM2C Laboratory about gas turbine model combustors and their acoustics. The architecture of the combustor is shown in figure 10 and is based on the work of *Dioc (2005)* who in her work designed a combustor test bench featuring lean premixed swirling combustion at atmospheric pressure. In following works, methods were developed in order to fix and to determine the acoustic boundary conditions of the test bench. *Tran (2009)* developed an impedance control system (ICS) which is able to damp oscillations at a chosen frequency range and determined its acoustic impedance. The ICS was later modelled and optimized by *Scarpato (2014)*. *Lamraoui (2011)* enhanced the test bench by developing a technique to measure feeding line impedances on the fly. This technique allowed to conduct a modal analysis of the atmospheric combustor. He also made first attempts to examine the effects of an exhaust nozzle on acoustic sound generation, however the nozzle was not choked. Together with the explained techniques, the acoustic modelling and the optimization of the exhaust nozzle by *Giauque et al. (2012)*; *Giauque et al. (2013)* opened a way to design a combustor test bench with all acoustic boundary conditions being well defined.

Apart from advances in test bench design, knowledge was also obtained in the diagnostics which allow to determine of direct and indirect combustion noise.

With the application of Laser Interferometric Vibrometry on flows (Mayrhofer and Woisetschläger (2001); Giuliani et al. (2009); Li (2012)), a technique is available which allows to obtain temperature fluctuations at sampling frequencies above that of thermocouples, which are limited to 300 Hz (Childs (2003)). In a next step, Tao (2015) developed a technique to separate direct and indirect combustion noise, based on simultaneous high speed measurements of temperature and pressure fluctuations on different positions. These approaches, together with classic diagnostics, such as PIV for the measurement of velocity fields or high speed imaging of OH* chemiluminescence, allow to characterize the test bench and to determine its direct and indirect combustion noise contributions.

Structure of this thesis

From the motivation described in the previous, the following research questions emerge:

How to design a combustor test bench that generates a high quantity of indirect combustion noise?

What are the main characteristics of the flame and the flow of this combustor?

Which diagnostics can be used to obtain information about combustion noise and how do they need to be worked on in order to do so?

What are the contributions of direct and indirect combustion noise in this combustor?

In order to answer these research questions, this thesis has been structured in the following parts and chapters:

In the first part of the thesis, the new combustor test bench, as well as the velocity and flow fields and dynamics are described. While this part is not directly linked to combustion noise, it is necessary in order to know the main properties of flame and flow in the burner.

- In chapter **Chapter 1** the design of the new combustor test bench CESAM-HP is presented. The main architecture is explained and justified in terms of combustion noise generation. Furthermore, the operating conditions are described and three operating points are chosen for the entire thesis.
- **Chapter 2** is focussing on the statistics of flame and aerodynamic in

the combustor. For this the mean and RMS flame visualizations are obtained by OH* chemiluminescence. The aerodynamics are obtained by the mean and RMS velocity fields determined by PIV. Finally, the areas with the strongest dynamics are identified.

- In **Chapter 3** a modal analysis of the test bench is conducted by combined experimental and analytical approaches. In this approach, the combustor geometry is modelled as two/five cavities and the acoustic boundary conditions are determined analytically and experimentally by pressure measurements. This study helps to interpret the main acoustic modes of the test bench and finally indicates the existence of a combustion instability.
- **Chapter 4** is dedicated to the main combustion instability. In this chapter, the fluctuations of local velocity, heat release and pressure are obtained by high speed measurements with PIV, OH* imaging and pressure sensors respectively. The existence of the combustion instability is put forward by comparing the FFT of the different measurements at different locations in the combustion chamber.

The second part is dealing with optical diagnostics that were worked on during this thesis. While work is still necessary in order to validate and/or quantify the techniques, they are supposed to be of interest for the studies of combustion dynamics and noise in the future.

- In **Chapter 5** a new high speed PIV technique is presented that was developed during this thesis and is applied for the velocity field measurements. It is based on the use of a continuous laser source and allows for sampling frequencies of up to 100 kHz. The validity of the technique is tested and discussed for the use on this thesis by comparing its mean and RMS velocities with the results obtained by a classic pulsed PIV technique.
- In **Chapter 6**, the visualization of the density fluctuations are presented. They are conducted by a focussing Schlieren technique, which allows to obtain 2D images of the density gradients at high sampling frequencies. Due to the application of a particular installation, the densities are shown on a field of view of only a few millimetres. Fourier analysis is conducted on the resulting images and suggestions are made to extend the approach to a technique which allows for a quantitative determination of temperature fluctuations.

Finally, in the third part of the thesis, the experimental determination of direct and in direct combustion noise is treated. Two different approaches were worked on and are presented here.

- **Chapter 7** presents a theoretical determination of direct combustion noise contributions. For this purpose the global heat release rate is obtained experimentally by photomultiplier measurements. From these results, the theoretical pressure fluctuations are calculated by using a simplified wave equation. The high contribution of direct combustion noise is finally suggested by determining the coherence between the theoretical and measured pressures.
- **Chapter 8** presents the separation of direct and indirect combustion noise contributions on the CESAM-HP test bench. For this, high speed line-of-sight averaged temperature fluctuations are measured with Laser Interferometric Vibrometry. The measurements are conducted synchronously with pressure measurements. From these results, the different combustion noise contributions are calculated.

In the end, Annex A describes two potential modifications, which have the aim to increase indirect combustion noise contributions. (1) The fuel injection system is changed with an aim to verify the effects of premixing on combustion noise. (2) Secondary air injection through the chamber wall is applied in order to add inhomogeneities to the burnt gases. The modifications are compared at different operating points in terms of pressure fluctuations, direct combustion noise contributions and flashback into the injector.

Publications

In the framework of this thesis, the following publications were made until the moment of submission of the manuscript:

M. Mazur, W. Tao, P. Scouffaire, F. Richecoeur, S. Ducruix. Experimental and analytical study of the acoustic properties of a gas turbine model combustor with a choked nozzle. GT2015-43013. ASME Turbo Expo 2015, June 2015, Montréal, Canada

M. Mazur, P. Scouffaire, F. Richecoeur, S. Ducruix. High speed PIV measurements in reactive flows using a continuous wave laser, Poster presentation. Gordon Research Conference Laser Diagnostics in Combustion, August 2015, Waterville Valley, NH, USA

N. Kings, M. Mazur, W. Tao, P. Scouffaire, F. Richecoeur, S. Ducruix. Experimental and numerical investigation on combustion noise sources in a model gas turbine combustor. XNOISE Workshop 2015, September 2015, La Rochelle, France

M. Mazur, N. Kings, P. Scouffaire, F. Richecoeur, S. Ducruix. Combustion

noise studies of a swirled combustion chamber with a choked nozzle using high-speed diagnostics. X-NOISE Workshop 2015, September 2015, La Rochelle, France

M. Huet, F. Vuillot, N. Bertier, M. Mazur, N. Kings, W. Tao, P. Scouffaire, F. Richecoeur, S. Ducruix, C. Lapeyre, T. Poinsot. Recent improvements in combustion noise investigation: from combustion chamber to nozzle flow. Journal AerospaceLab Issue 11, June 2016, AL11-10

C. Lapeyre, M. Mazur, P. Scouffaire, F. Richecoeur, S. Ducruix, T. Poinsot. Acoustically induced flashback in a staged swirl-stabilized combustor. Flow, Turbulence and Combustion, June 2016

M. Mazur, P. Scouffaire, F. Richecoeur, L. Cunha Caldeira Mesquita, A. Vié, S. Ducruix. Planar Velocity Measurements at 100 kHz in Gas Turbine Model Combustors with a Continuous Laser Source. Proceedings of ASME Turbo Expo 2017: Turbomachinery Technical Conference and Exposition GT2017-64597, June 26-30, 2017, Charlotte, NC, USA

Part I

Presentation and characterisation of the CESAM-HP test bench

Summary

This part of the thesis has two aims: (1) It has the aim to present the design of the test bench which is used during this work, (2) It has the goal to present its flame and flow dynamics as well as its eigenmodes.

The design of the test bench, named CESAM-HP (“Combustion Etagée Swirlée Acoustiquement Maitrisée - Haute Pression” - “Staged Swirled Acoustically Controlled Combustion - High Pressure”) in the following, is presented in chapter 1. It is designed with the the aim to generate a high quantity of combustion noise, to be close to an aeronautic configuration and to have adequate access for different measurement techniques. In order to fulfil these objectives, the burner features a lean premixed swirling combustion and has pressures of up to 2.5 bar. Apart from the combustor design, the chapter also describes the operating range, basic in-chamber diagnostics and finally the operating points that are chosen for this thesis.

The mean and rms velocity fields and flame visualizations are presented and discussed in chapter 2. This is done in order to obtain first insight about the flame shape and dynamics and also in order to identify the regions with the strongest velocity and heat release oscillations.

In the following chapter, a modal analysis is conducted in order to determine the eigen modes of the CESAM-HP combustor. This is done by applying a combined analytical and experimental approach. In this approach, the combustor is modelled in 1D as different cavities and the acoustic boundary conditions are determined partially experimentally.

Finally, in chapter 4 these eigen frequencies are investigated further. With the help of time and spatially resolved diagnostics, the PSD of velocity, heat release and pressure are obtained in different regions in the chamber. These experiments show that these eigen frequencies are associated with a low frequency combustion instability. The instability is put into evidence by describing different driving and coupling mechanisms that can be suggested from the observations that are made.

Chapter 1

Design of a test bench for combustion noise studies

In this chapter, the design of the CESAM-HP test bench is presented. This test bench is designed to study direct and indirect combustion noise for aeronautical applications. This framework results in a set of design objectives, which are stated in the first part of the chapter. This is followed by a presentation of the test bench architecture and the choices, which were made in order to fulfil these objectives. The design of each element is explained in detail, with the focus on the generation of combustion noise. Then, the diagnostics used to find and verify the operating points are presented. Finally, the operating conditions are elaborated and three operating points are chosen and justified for the rest of this project.

1.1 Design of the combustor test bench

The CESAM-HP test bench has been designed with the aim to study direct and indirect combustion noise at a laboratory scale for an application to aircraft engines. For this purpose, the design choices need to fulfil the following objectives: (1) The combustor architecture and the physical behaviour inside the burner need to be close to those of aircraft combustion chambers; (2) The burner needs to be designed in a way, that entropy noise generation is observable; (3) The design needs to be simple enough to perform reproducible experiments in a safe way; (4) The design needs to be simple enough to allow for numerical simulations in the framework of the RECORD project; (5) The acoustic boundary conditions need to be measured and eventually controllable. The aim of this chapter is to present the chosen test bench design and to justify the choices made with regards to the stated objectives. It is also put forward how the experiments and results from previous work at EM2C laboratory are used to fulfil these design objectives. Furthermore, the operating limits are explained and operating points are chosen for the following of the thesis.

1.1.1 The architecture of the test bench

The CESAM-HP test bench features a lean premixed swirling combustion. This is similar to most of the aeronautical configurations, where the swirl stabilizes the flames and allows for lower NO_x emissions. Furthermore, the combustion chamber corresponds to a can-shaped model (Jeschke (2012)). However, the shape of the combustion chamber is rectangular which allows an easier design and a high modularity. The combustor is fuelled with propane instead of kerosene in order to exclude multiphase phenomena in this study, which is focussed on acoustic phenomena. Besides, the combustion chamber is pressurized with the help of a choked exhaust nozzle to pressure levels up to 2.5 bar.

Various design choices were made in order to ensure the desired acoustic behaviour. The choked exhaust nozzle pressurizes the combustion chamber and has been shaped in order to favour the generation of indirect combustion noise (Giauque et al. (2012); Giauque et al. (2013)). The impedance control system as well as the choked nozzle allow to control the acoustic boundary conditions upstream and downstream of the combustor (Tran et al. (2009a)). The simplicity and modularity of the design allow the application of various diagnostics. The combustion chamber includes large optical access for the application of optical diagnostics and the test bench contains various ports for pressure sensors and thermocouples. The rectangular combustion chamber shape results in straight windows, which avoids optical distortions.

The data acquisition system is of type NI Compact DAQ. It permits to capture physical quantities, such as pressures or temperatures, synchronously with the applied optical diagnostics. It has also been chosen to isolate signals in order to avoid interferences between the different measurements. Its maximal sampling frequency is 50 kHz and it is connected to the control computer via USB 2.0. This assures that the data transfer is sufficiently rapid even at these high sampling frequencies.

The main elements of the test bench are shown in figure 1.1 and are the following:

- An injection system containing a tangential injection of an air-propane premixture, an axial injection and an Impedance Control System (ICS)
- A square-shaped combustion chamber with large optical access
- A choked exhaust-nozzle with an optimized shape

These elements are described in more detail in the following sections.

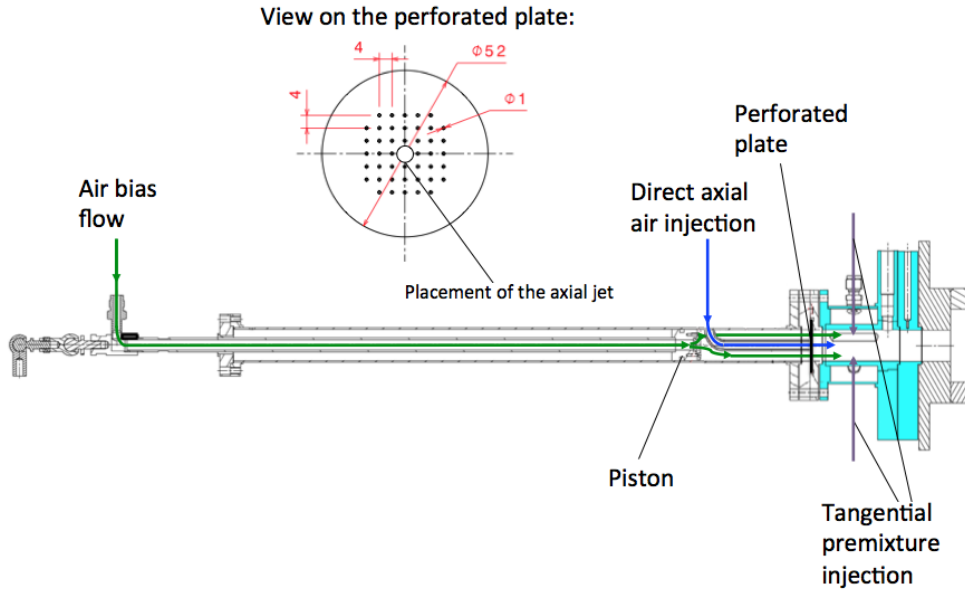


Figure 1.3: Schematic drawing of the injection stage (light blue) and the ICS with the bias air flow (green arrow). The figure also includes the axial fuel injection (blue arrow).

The axial injection system is shown in figures 1.1 and 1.3. The system is constituted from two elements: The ICS, which is a perforated plate with bias flow backed by a cavity of adjustable length, and a direct axial air injection of 4 mm diameter. The system has been designed, tested and modelled at EM2C (Tran et al. (2009a); Tran et al. (2009b); Scarpato et al. (2012); Scarpato et al. (2013)) and aims at the following objectives.

- (1) The ICS controls the upstream acoustic impedance due to the combination of the perforated plate, the bias flow and the cavity. The cavity length determines the frequency range in which the acoustic waves are damped. It is set to its longest length (500 mm) in order to attenuate frequencies below 200 Hz, as described by Scarpato et al. (2012).
- (2) Both the bias flow and the direct axial injection counterbalance the natural flashback tendency of the combustor by pushing the flame downstream, decreasing the swirl number and thus decreasing this tendency (Reichel et al. (2015); Sattelmayer et al. (2015); Lapeyre et al. (2016)). Indeed, Fritz et al. (2004) show that flashback can be caused by vortex breakdown induced by the sudden expansion present in burners with similar structures. The addition of a small axial flow reduces the circumferential velocity gradient and helps in preventing flashback.
- (3) The direct axial jet allows to inject axial air of high velocities into the combustor. Supposing equal air mass rate, it injects air with a velocity over 50 times higher than the bias flow through the perforated plate. This

axial jet has the aim to attenuate the main instability frequencies of the test bench and give a broadband shape to the acoustic spectrum. Both effects will be shown later in this chapter.

The fuel and air repartition influences the acoustic spectra measured in the combustion chamber as will be shown in section 1.3. Between 70 and 90 % of the total air flow is injected through the tangential stage to ensure a high swirl value. The axial air flow is smaller and distributed between the high velocity central jet from the direct injection and the low velocity flow through the perforated plate. No fuel is injected axially in order to ensure the counterbalancing impact on the flame flashback. The fuel is therefore exclusively injected through the tangential stage.

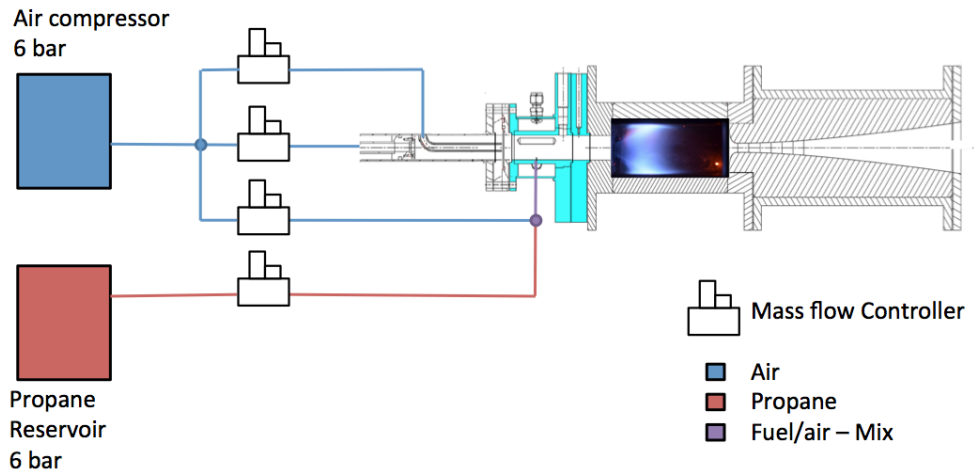


Figure 1.4: CESAM-HP test bench with the layout of the feeding lines

The feeding lines of the test bench can be seen in figure 1.4. The pressurized fresh air is supplied at 6 bar and 300 K, and the fuel is supplied at 3 bar and 300 K. The mass flow rates are controlled via Brockhorst EL-FLOW Select mass flow controllers and a constant humidity is ensured by appropriate filters. As it can be seen in figure 1.4, premixing already starts in the feeding lines, about 1 m upstream from the tangential injection stage. While this does not guarantee perfect premixing, the long premixing distance as well as the existence of the plenum in the swirler are both contributing to the premixing quality.

1.1.3 The combustion chamber

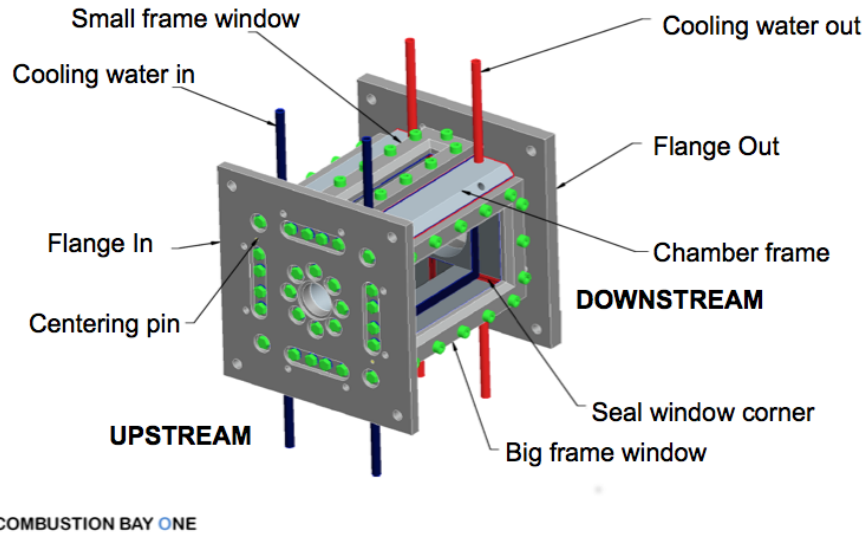


Figure 1.5: *Geometry of the Combustion Chamber (Drawing made by Combustion Bay One (F. Giuliani))*

The combustion chamber is the region where the flame is observed. It is shown in figure 1.5 and its dimensions are indicated in figure 1.1. It has a length of 140 mm and a squared cross-section of 70 mm x 70 mm. The length has been chosen to be sufficiently long so that the flame does not impinge the exhaust nozzle but short enough to avoid a complete dissipation of the entropy waves. The chamber cross section was chosen large enough to avoid a perturbation of the rotational motion of the flame by excessive wall impact. This corresponds to a ratio of surfaces $S_{chamber}/S_{injector} \approx 7$, which was elaborated in the previous versions of the burner (Dioc (2005); Lamraoui (2011)) and leads to a flame which fulfils the mentioned requirement. The chamber shape in general is based on these; however for CESAM-HP it was also taken into account that the chamber pressurization will lead to a more compact flame. The combustion chamber dimensions are hence smaller in this test bench than what would be expected from the previous studies carried out at atmospheric pressure.

During the design process, it was important to ensure a test bench which features reproducible and durable operation and allows for the use of different measurement techniques. The chamber structure is cooled by an open water circuit. Therefore the combustor can be operated safely for long durations at constant thermal conditions. The squared shape of the chamber is a simplification compared to industrial applications but it allows for a high modularity.

Indeed the chamber walls can be chosen either to be instrumented ports or windows for observation. The chamber windows have a thickness of 30 mm, which permits safe operation also at high pressures. The instrument ports can be mounted with the spark plug for ignition, thermocouples and pressure sensors. The design of the instrument ports can be seen in figure 1.6. The safe and durable operation of the pressure sensors is insured by a combined system of thermal protection and water cooling and shown in figure 1.7. The installation of the piezo-sensors was a major design driver in this work. Hence their functioning as well as their installation will be described in detail in section 1.2.1

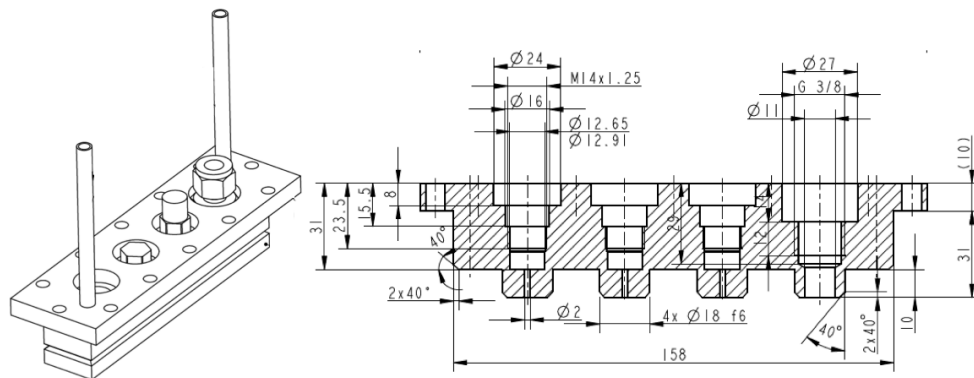


Figure 1.6: Geometry of the Instrument Port (Drawing made by Combustion Bay One (F. Giuliani)). The left image shows a 3D view of an instrument port. It includes three locations for pressure sensors and one for a spark plug. The right image shows a section of the same piece together with its dimensions.

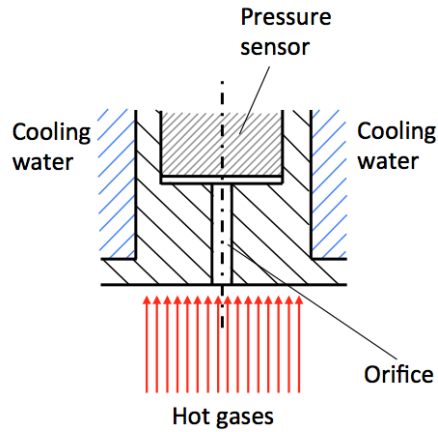


Figure 1.7: Sketch of the cooling system. The pressure sensor is protected by a 10 mm thick wall with an orifice of 2 mm diameter. The walls are cooled by an open water cooling circuit.

1.1.4 The exhaust nozzle

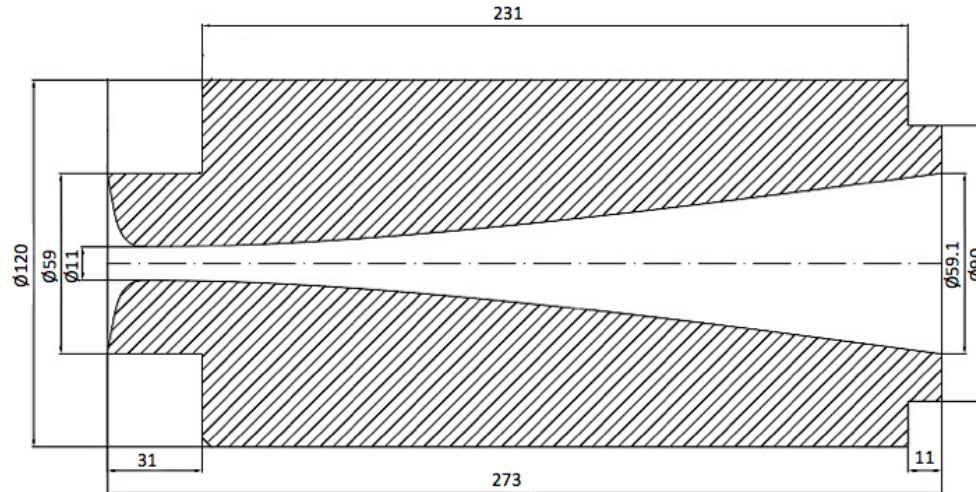


Figure 1.8: Geometry of the Exhaust Nozzle

The exhaust nozzle is a classical de Laval nozzle with the geometry shown in figure 1.8. It has a throat diameter of 11 mm and its converging part is very short compared to the entire length, which will be explained later on. The nozzle has two functions in the test bench:

- (1) Due to its small throat diameter, the nozzle is choked at total mass flows above 15 g/s. This leads to an increase of the total chamber pressure up

to 2.5 bars. It also prevents the upstream propagation of acoustic waves from sources downstream the chamber, such as the exhaust jet.

- (2) The nozzle shape has been optimized in previous works in order to favour the generation of indirect combustion noise (Giauque et al. (2012); Giauque et al. (2013)). For this, the nozzle shape is expressed as Bezier splines and the acoustic behaviour is expressed via a thermoacoustic model. The shape is then optimized using a genetic algorithm. As can be seen in figure 1.8, the convergent part converges rapidly, while the divergence is very smooth. The reason for the geometry of the converging part can be deduced from the set of equations, developed by Marble and Candel (1977):

$$\left[\frac{\partial}{\partial t} + \bar{u} \frac{\partial}{\partial x}\right] \left(\frac{p'}{\gamma \bar{p}}\right) + \bar{u} \frac{\partial}{\partial x} \left(\frac{u'}{\bar{u}}\right) = 0 \quad (1.1)$$

$$\left[\frac{\partial}{\partial t} + \bar{u} \frac{\partial}{\partial x}\right] \frac{u'}{\bar{u}} + \frac{\bar{c}^2}{\bar{u}} \frac{\partial}{\partial x} \left(\frac{p'}{\gamma \bar{p}}\right) + \left(2 \frac{u'}{\bar{u}} - (\gamma - 1) \frac{p'}{\gamma \bar{p}}\right) \frac{d\bar{u}}{dx} = \frac{d\bar{u}}{dx} \frac{s'}{C_p} \quad (1.2)$$

The source term on the right hand side of the second equation shows that the pressure fluctuations increase when the entropy waves are accelerated. Hence a shape was chosen, which accelerates the flow as much as possible and hence generates as much indirect combustion noise as possible. The considerations for the divergent shape were different. The diameter increases over a long distance above 100 mm in order to avoid stall of the accelerated flow.

First versions of the nozzle were made of graphite. This material has the advantage of easy and inexpensive manufacturing, but erodes and become porous during operation, which leads to an increasing throat diameter and changes the convergent shape. As explained with Eq. (1.2), this leads to decreased entropy noise generation. The final version of the nozzle is thus made of stainless steel and has a water cooling circuit (Figure 1.9) in order to ensure safe operation with a constant nozzle shape and under constant thermal conditions.

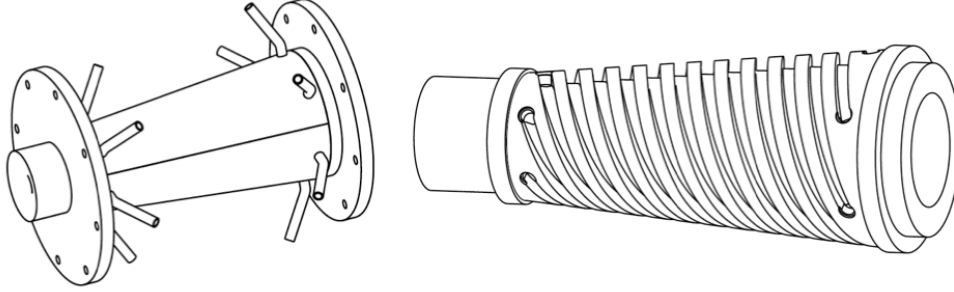


Figure 1.9: *Geometry of the Exhaust Nozzle Cooling Circuit. The left image shows the nozzle from outside with the water feeding lines and the right image shows the cooling water pipes inside the nozzle.*

1.2 In-chamber diagnostics

In this section the basic in-chamber diagnostics are presented. The static pressure and dynamic pressure fluctuations are measured with pressure probes of piezo type. Their functioning and installation is described in section 1.2.1. The global heat release rate fluctuations are monitored with a photomultiplier probe (PM), which is presented in detail in section 1.2.2.

1.2.1 Sensors for pressure measurement and their installation

The static pressure and the pressure fluctuations of the CESAM-HP test bench are measured with two types of pressure sensors, the 4045A and the 701A from KISTLER. Their specifications are summarized in tables 1.1 and 1.2. Sensors of the type KISTLER 4045A are installed in the combustor walls. They are of piezo-resistive type and measure static pressure and dynamic pressure fluctuations simultaneously. Their installation in the combustor walls requires a combined system of thermal protection and cooling, which was presented in figure 1.7. In the injector, a sensor of the type KISTLER 701A is installed. It is piezo-electric and measures dynamic pressure fluctuations. The 701A sensor does not need to be cooled because it is installed in the premixer and thus in contact with the fresh air/fuel premixture.

As explained before, the in-chamber pressure sensors are installed in a combined set of water cooling and thermal protection. The system is inspired from previous works (Brouckaert et al. (2008); Mersinligil et al. (2010); Mersinligil et al. (2011)) and was developed in collaboration with the engineers from KISTLER and F. Giuliani.

Table 1.1: *Technical specifications of the KISTLER 4045A pressure sensor*

Specification	
Name	KISTLER 4045A pressure sensor
Measuring principle	Piezo-resistive
Application	Absolute pressure, static and dynamic
Pressure range	0 to 5 bar
Amplifier	KISTLER 4618A0

Table 1.2: *Technical specifications of the KISTLER 701A pressure sensor*

Specification	
Name	KISTLER 701A pressure sensor
Measuring principle	Piezo-electric
Application	Dynamic pressure fluctuations
Pressure range	0 to 250 bar, calibrated for 0 to 2.5 bar
Amplifier	KISTLER 5011A

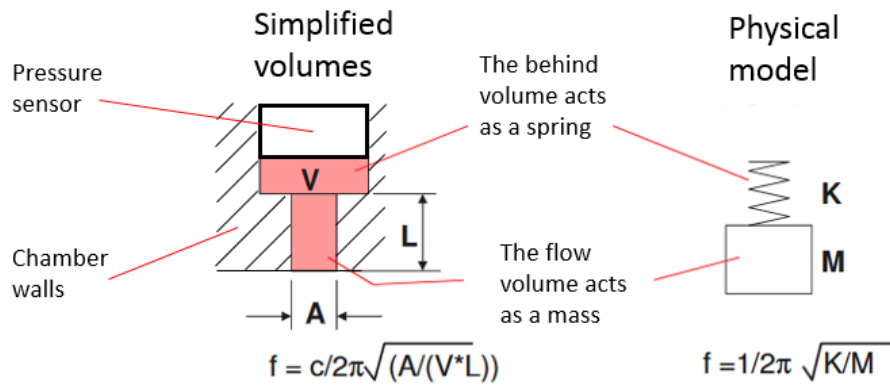


Figure 1.10: *Mass-spring model of the orifice and the gap between protective wall and the pressure sensor. This geometry corresponds to the installation of the pressure sensors and was developed by KISTLER. (Figure based on drawing from KISTLER (2013))*

The in-chamber pressure sensors are placed behind a wall of 10 mm thickness (L in figure 1.10) with an orifice of 2 mm diameter (A in figure 1.10). The instrument port is water cooled via an open water circuit. The basic layout of this arrangement is shown in figure 1.7. It can be modelled as a combined mass-system, as shown in figure 1.10. In this model, the orifice and the cavity between chamber wall and pressure sensor act as a Helmholtz resonator. Its

resonance frequency can be calculated by the following equation:

$$f = \frac{c}{2\pi} \sqrt{\frac{A}{V \cdot L}} \quad (1.3)$$

with c the speed of sound, A the section of the orifice, L the thickness of the protecting wall and V the volume between protecting wall and pressure sensor. The variables are also specified in figure 1.10. At an orifice length of 10 mm, an orifice diameter of 2 mm and a cavity depth of below 0.5 mm, the resulting frequency has a value of 6 kHz. This value is above the vast majority of the phenomena observed in this work thus it will not interfere with the in-chamber pressure measurements. Thus the chosen arrangement is suitable for this test bench in terms of resonance frequency.

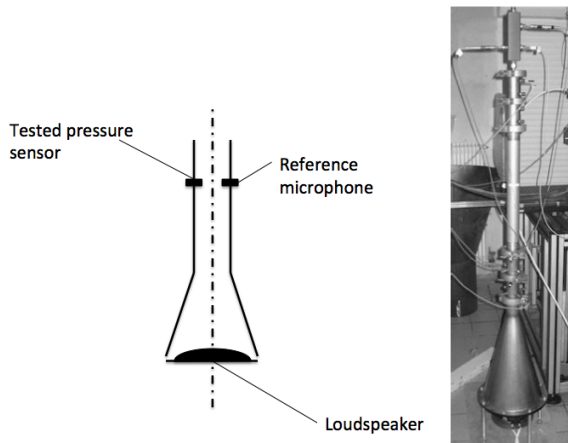


Figure 1.11: *Schematic drawing and photograph of the ITHACA acoustic test bench. A loudspeaker is located at the bottom of the tube. At the top, the tube contains various ports in order to mount microphones and pressure sensors.*

In a second step, the sensors as well as their installation are validated experimentally. The test are conducted with the ITHACA acoustic test bench, which was developed at EM2C (Tran et al. (2009a)). A schematic drawing as well as a photograph are shown in figure 1.11. The ITHACA test bench can be considered as a Kundt tube and consists of a loudspeaker for acoustic excitation and different microphone and pressure sensor ports. These ports are installed on the same longitudinal position on a tube with an open end.

As a first test, the KISTLER 701A sensor is mounted behind different protecting walls and its signal is acquired and compared with a microphone signal. In this test, the loudspeaker is modulated at 120 Hz and 480 Hz and with an amplitude of around 150 dB. The pressure measurements are acquired at 40 kHz

Table 1.3: *Technical specifications of the Bruel & Kjaer 4938 microphone*

Specification	
Name	Bruel & Kjaer type 4938 microphone
Measuring principle	Condenser microphone
Application	Dynamic pressure fluctuations
Dynamic range	30 to 174 dB
Frequency range	4 Hz to 70 kHz
Amplifier	Type 2670 preamplifier

during 1 s and their PSD is obtained by applying Welch’s algorithm with Hamming windows of 8192 elements per window and a 50 % overlap.

The KISTLER 701A sensor is mounted behind walls of different thicknesses (see L in figure 1.10) and an orifice of 2 mm diameter (see A in figure 1.10) each. In parallel, a Bruel & Kjaer type 4938 microphone (for specifications see table 1.3) without protective wall is mounted as a reference. The resulting pressure spectra are shown in figure 1.12. Four configurations are compared: (1) The flush-mounted microphone, (2) a wall thickness of 1.5 mm and a cavity depth of 0.5 mm, (3) a wall thickness of 1.5 mm and a cavity depth of 1.5 mm and (4) a wall thickness of 10 mm and a cavity depth of 1.5 mm. For both excitation frequencies, the main excitation frequency and its main harmonics are well captured by all pressure sensors. For the lower harmonics the frequencies are equal to that of the microphones, while for higher harmonics it decreases slightly. Besides, the 701A signals feature a higher white noise, yet it stays far below the main frequencies. It also has a 50 Hz peak and its harmonics. These peaks are probably linked to the electric system, as will be shown later. Another aspect is a broadband phenomenon around 3000 Hz. While it is not negligible, it does not interfere with the main frequencies.

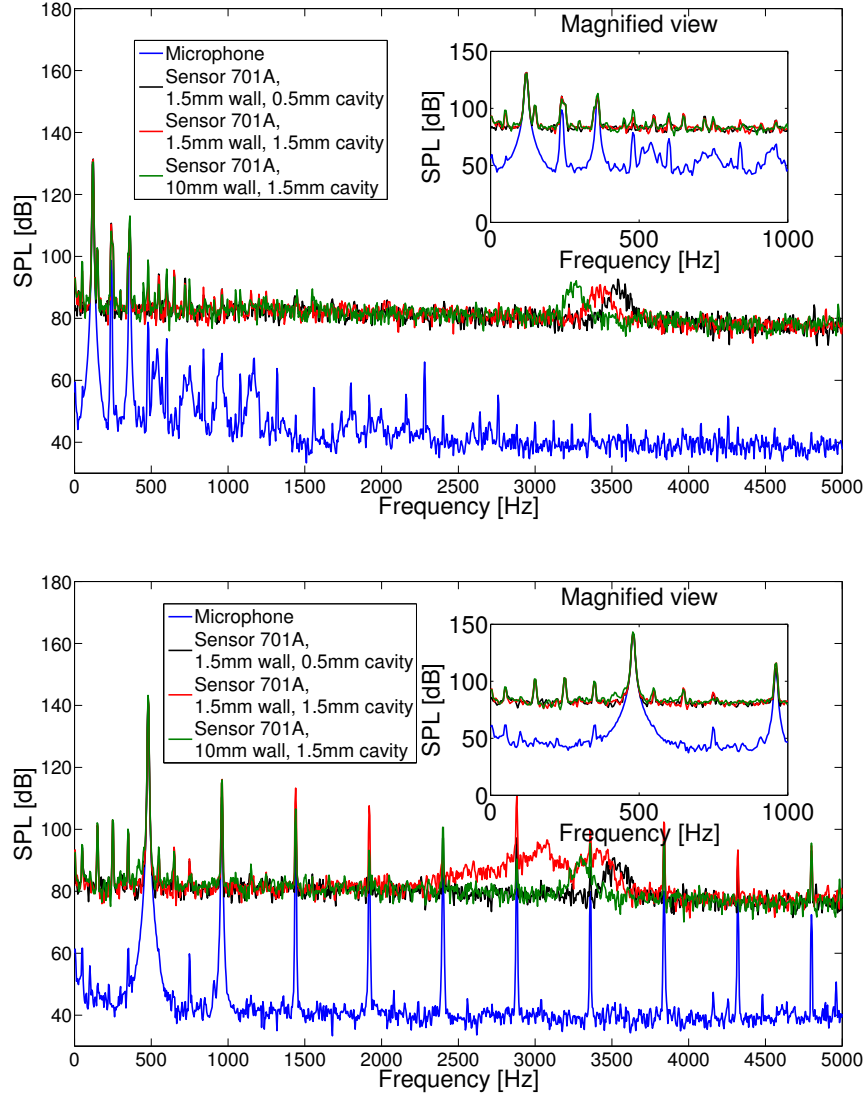


Figure 1.12: Pressure spectra of the KISTLER 701A sensor with different installation arrangements, compared to microphone signal. The upper figure corresponds to an excitation frequency of 120 Hz (140 dB) and the lower one of 480 Hz (154 dB).

In the second test, the KISTLER 701A and the KISTLER 4045A sensors are compared with each other. No protecting wall is used here. As in the previous study the loudspeaker is modulated at 120 Hz and 480 Hz and around 150 dB. The pressure measurements are acquired at 40 kHz during 1 s and their PSD is obtained by applying Welch's algorithm with Hamming windows of 8192 elements per window and 50 % overlap. The resulting spectra are shown in figure 1.13. For both sensors, the main excitation frequency and its harmonics are equally captured in terms of frequency and amplitude. The white noise is

slightly higher for the 4045A measurement. The 701A spectrum on the other hand features the same 50 Hz peak with its harmonics as well as the broad-band phenomenon around 3 kHz. The former is probably linked to the electric system. Indeed, the 701A sensor is powered by 230 VAC (at 50 Hz), while the 4045A sensor is driven by 24 VDC.

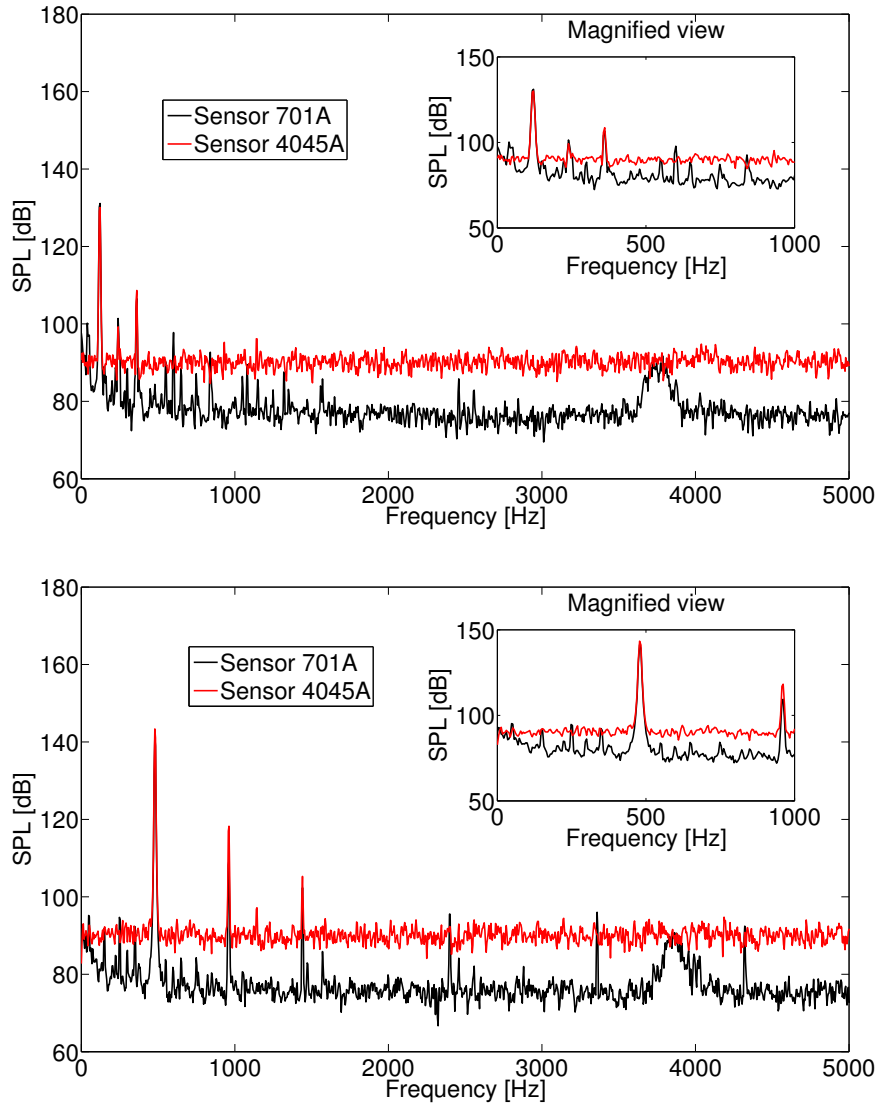


Figure 1.13: Pressure spectra of the KISTLER 701A and the KISTLER 4045A sensors. The upper figure corresponds to an excitation frequency of 120 Hz (140 dB) and the lower one of 480 Hz (154 dB).

The experiments on the ITHACA test bench validate the use of the 701A

Table 1.4: *Technical specifications of the PM*

Specification	
Name	Photosensor module
Packaging	Metal package photomultiplier tube
Type	H5784-06
Spectral Response	185 nm to 650 nm
Conversion factor	1 V/ μ A
Power Supply	C7169
Applied filter	313 nm with 10 nm spectral width

Table 1.5: *Positions of the applied pressure sensor and PMs*

Sensor	x [mm]	y [mm]	z [mm]
OH* photomultiplier - total	0 to 110	line-of-sight	-35 to 35
OH* photomultiplier - nozzle	117.5 to 127.5	line-of-sight	5 to 15

and the 4045A sensor and their installation. Both sensors correctly detect the acoustic excitation in terms of frequency and also in terms of amplitude. The protecting installation has little influence on these results. The only irregularities observed are the 50 Hz peak and its harmonics as well as the broadband phenomena around 3 kHz, however these are specific to the 701A sensor and show a far weaker amplitude than the observed phenomena. In total, it can be concluded that both the pressure sensors as well as the installation can be applied on the CESAM-HP test bench.

1.2.2 In-chamber OH* measurements

The global heat release rate is obtained by using photomultiplier probes (PM) with a 313 nm filter with 10 nm spectral width. They hence capture the chemiluminescence of OH*. The properties of the PM are summarized in table 1.4. The two regions observed with the help of the PM are shown in table 1.5. The sensor named "total" aims at observing the entire combustion chamber. The sensor named "nozzle" focuses on the downstream region, which is not included in the first probe measurement zone. Its region of interest is reduced by using a tube.

1.3 The operating conditions

The combustion chamber is fed with fresh air and fuel at 300 K as well as 3 bar and 6 bar reservoir pressure respectively. The total air mass flow rate can be varied from 3 to 20 g/s. The air mass flow rates through the ICS and the central

Table 1.6: *General operating conditions of the CESAM-HP test bench*

Property	
$p^{a,u}$	6 bar
$p^{f,u}$	3 bar
$T^{a,u}$	300 K
$T^{f,u}$	300 K
Φ^{global}	0.85
$p^{chamber}$	2.45 bar
Power	45.0 kW

a: air, f: fuel, u: unburnt, b: burnt

jet are limited to 2 g/s and 5 g/s respectively. The total fuel mass flow rate is injected exclusively through the tangential injection and can be chosen to up to 1 g/s. The fuel is propane, which has a lower heat capacity of 46.4 MJ/kg. This leads to a maximum power of 46.4 kW. The main operating conditions are summarized in table 1.6.

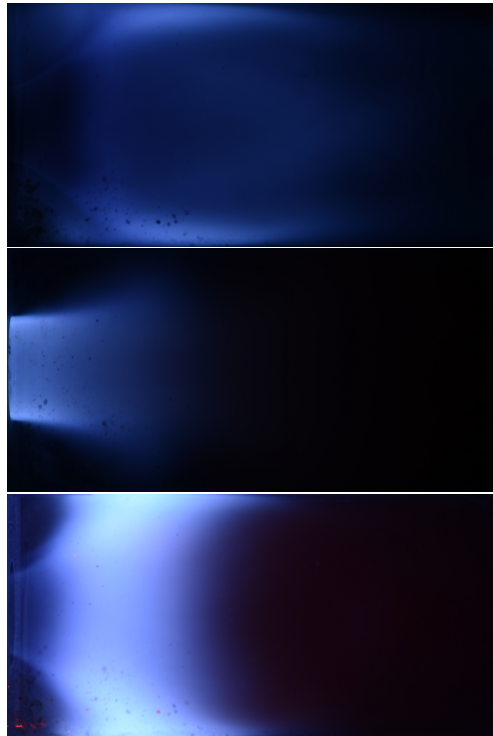


Figure 1.14: *Examples of a) detached flame, b) flash backed flame and c) conical flame*

The combustor can be operated in a stable and durable manner for a wide

range of operating conditions. The flame can have different forms, depending on the global equivalence ratio as well as the chosen air repartition between the tangential and the two axial air injections. The possible flame types are presented in figure 1.14. Three types are identified:

- Particularly lean flames are detached from the injector and characterized by strong contact with the chamber walls. An example is shown in figure 1.14a. The detached flame is very close to the blowoff limit, especially at higher air mass flows.
- Particularly rich flames have the tendency to be located entirely in the injector, as can be seen in figure 1.14b. The flashbacked flame leads to overheating of the injection stage and cannot be observed using optical diagnostics.
- A flame with a shape between the two others leads to a flame which is presented in figure 1.14c. The flame is robust to small modifications of mass flow rates and equivalence ratios.

The different operating regions and boundaries are presented in the operation map shown in figure 1.15. In this figure the axial mass flow rates are chosen zero for the sake of simplicity. The addition of axial flow rates does not greatly impact the operating boundaries, thus this operating map is suitable and applicable in general. The diagram shows two operating boundaries: (1) The lean boundary indicates the region of the lowest possible equivalence ratio for a given total air mass flow rate. The choice of a leaner flame leads to flame blow off. (2) The upper equivalence ratio limit has been chosen to be 0.9. While it would be physically possible to operate under richer conditions, the limit of 0.9 was set in order to limit NO_x and soot emissions. Two other limits can be observed in the operation map, the flame detachment limit and the flashback limit, corresponding to the transition between the different flame types of figure 1.14.

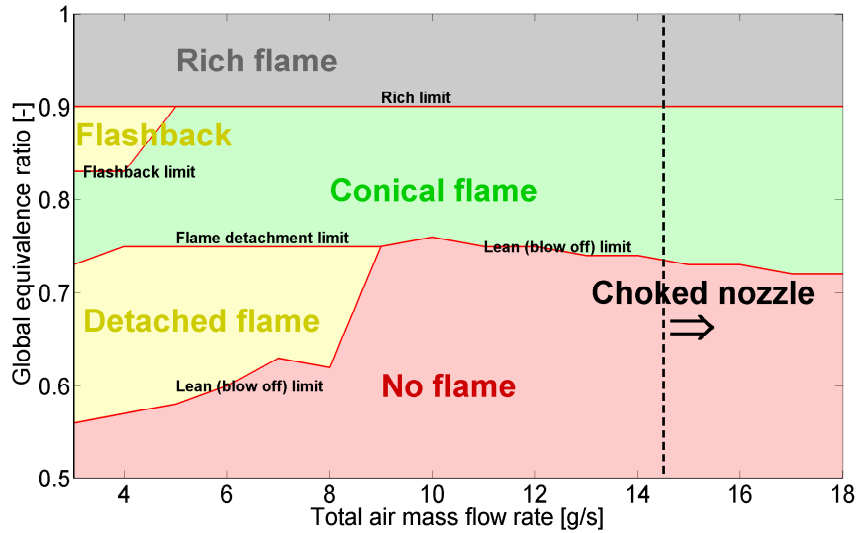


Figure 1.15: Operation map of the CESAM-HP test bench. Both axial mass flow rates are zero.

For the choice of operating points from this map the following criteria are taken into account:

- (1) Ignition
- (2) Path of access
- (3) Stability
- (4) Acoustic spectra

The ignition can be only made in a very restricted region of the operating map. The air mass flow must come exclusively from the tangential injection stage and needs to be between 2 g/s and 2.5 g/s. The equivalence ratio needs to be around 0.63. At lower equivalence ratios or air flow rates no ignition takes place. At higher equivalence ratios or air flow rates the flame is not able to stabilize itself. Instead, only a succession of failed ignitions can be observed and heard. After successful ignition the flame is detached from the injector due to the low equivalence ratio.

When the flame is ignited, the air mass flows and the equivalence ratio need to be increased in order to reach high power regimes. This is first done by simultaneously increasing tangential air mass flow to 6 g/s and the equivalence ratio to 0.8. At this point the flame corresponds to the shape shown in figure 1.14c. It is robust and the equivalence ratio and mass flow rates can be quickly and safely increased. Also, from this point on, air can be added by the axial injections.

The stability of the flame depends on the chosen flame type and whether the

Table 1.7: Chosen operating points for the experimental study.

	Op16-0-2	Op16-2-0	Op13.4-4.6-0
$\dot{m}^{a,stage}$	16 g/s	16 g/s	13.4 g/s
$\dot{m}^{a,jet}$	0 g/s	2 g/s	4.6 g/s
$\dot{m}^{a,ICS}$	2 g/s	0 g/s	0 g/s
\dot{m}^f	0.97 g/s	0.97 g/s	0.97 g/s
Φ^{global}	0.85	0.85	0.85
$p^{chamber}$	2.45 bar	2.45 bar	2.45 bar
Power	45.0 kW	45.0 kW	45.0 kW

a: air, f: fuel

operating point is close to the operating limits. Especially when the flame is close to the lean limit it experiences strong oscillations and is prone to be blown off. When the rich limit is reached the flame flashes back into the injector. While the flame stays stable, this position is not suitable because the flame overheats the injector and cannot be observed by the in-chamber sensors. The consequence of these observations is that the chosen operating points must be located in the region between the rich and the lean limit.

Taking into account the three mentioned criteria, the operating points were chosen based on their acoustic spectra. Three operating points were chosen for this study. These points are presented in table 1.7. The operating points are named **Op16-0-2**, **Op16-2-0** and **Op13.4-4.6-0**. The first number corresponds to the tangential air flow rate, the second to the central jet flow rate and the third to the ICS flow rate all of them being expressed in g/s. The three operating points have a total air mass flow of 18 g/s and an equivalence ratio of 0.85. This choice leads to a choked exhaust nozzle and a chamber pressure over 2.4 bar and hence fulfils the requirements stated at the beginning of this chapter.

The difference between these operating points lies in the repartition of the axial flow, which influences their acoustic behaviour. This effect is depicted in the in-chamber pressure spectra of the three chosen operating points in figure 1.16. The pressure was measured with an in-chamber KISTLER 4045A sensor during 4 s at a sampling frequency of 25 kHz. From these measurements the PSD spectra were calculated using Welch's algorithm with Hamming windows with 2048 points each window and 50 % window overlapping.

The pressure spectra are described and analysed in detail in chapters 3 and 4. Here, the focus is put on the difference between the spectra in the region below 1 kHz. While the dynamics of **Op16-0-2** are dominated by a sharp peak around 120 Hz and its harmonics, **Op13.4-4.6-0** has one very broad peak with

no visible harmonics. The point **Op16-2-0** shows a behaviour in-between. In this last case, the low frequency harmonics are partly attenuated.

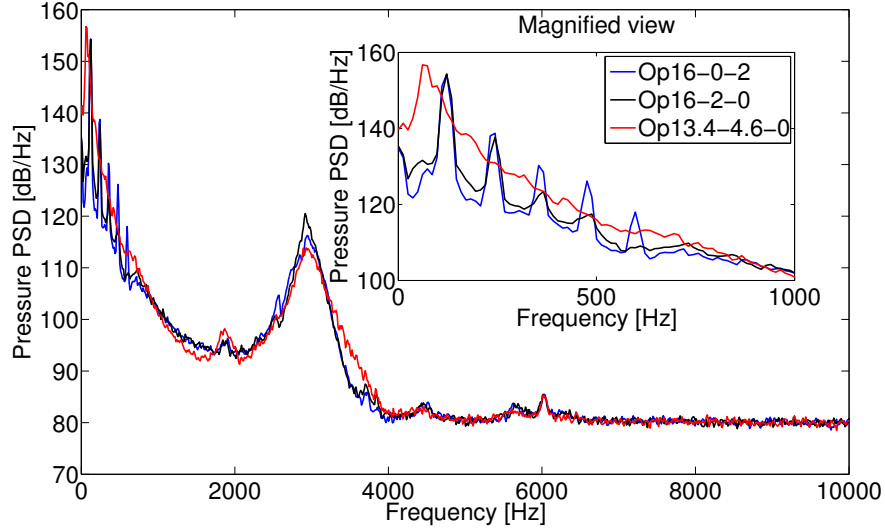


Figure 1.16: Pressure spectra of the three chosen operating points, measured by a wall-mounted sensor. The spectra show particular differences in the low frequency region. This difference justifies the choice of these operating points.

The comparison of the spectra allows to create a hypothesis concerning the acoustic behaviour on these operating points. **Op16-0-2** shows a very strong low frequency peak with its harmonics, possibly belonging to a combustion instability. The high amplitude of this instability leads to the assumption that this phenomenon is dominating, hence leading to a high amount of direct combustion noise. This operating point should thus be dominated by direct combustion noise.

The contrary is observed for **Op13.4-4.6-0** with a large broadband part and a far lower dominance of the low frequency peak. This behaviour allows to assume that this operating point has a higher contribution of indirect combustion noise. With the same logic, **Op16-2-0** is assumed to have shown a behaviour in-between.

1.4 Conclusion

The CESAM-HP test bench has been developed with the aim to study direct and indirect combustion noise. To do so, the combustor needs to fulfil a variety of constraints: It needs to feature a pressurized premixed swirling combustion, it needs a design which favours the generation of indirect combustion noise and allows for easy experimental observation and numerical simulations, it needs to

have well defined and controllable acoustic boundary conditions.

The test bench has been designed to take into account these requirements. The tangential injection allows for a lean swirling and compact flame. The use of an optimized exhaust nozzle leads to a pressure above 2 bar. This nozzle, together with the impedance control system upstream, allows to obtain well defined acoustic boundary conditions. The rectangular shape and the modularity of the combustion chamber permit to apply a large variety of diagnostics in order to observe the physical phenomena in the combustor. The test bench can be operated safely for long durations due to a water cooling system, which protects the combustion chamber, the exhaust nozzle and the in-chamber instruments. The pressure is measured by piezo sensors, which need a combined system of cooling and thermal protection. This system as well as the sensors themselves are validated on an acoustic test bench.

The designed test bench allows for a large variety of operating conditions. From these, three operating points were chosen with regards to their acoustic behaviour: One point is estimated to be dominated by direct combustion noise. A second operating point is assumed to contain a larger indirect combustion noise contribution. The third point is supposed to show a behaviour between that of the other two. Therefore this project features a test bench optimized for the generation and study of direct and indirect combustion noise, together with operating points with various acoustic spectra.

Chapter 2

Statistic flame and flow characterization

In this chapter, the statistics of the flow field and the flame are analysed with the help of Particle Image Velocimetry and OH chemiluminescence imaging. The aim is to obtain first insight about the topology of the flame as well as its size, shape and position. The experiments are conducted for the three chosen operating points in order to show the differences and similarities in their flow fields and flame shapes. The mean position of the flame as well as its topology are described by the mean fields. The areas of strongest flow and flame dynamics are identified with the help of the RMS fields of velocity and OH* chemiluminescence. Finally these results allow to estimate the regions that will be of highest importance for the following work in this thesis.*

2.1 Motivation

This chapter has the aim to describe the statistics of the flame and the aerodynamics of the CESAM-HP test bench. This is done experimentally by two techniques: (1) The velocity fields are obtained with Planar velocimetry (PCMV). (2) The flame shape is determined experimentally by the acquisition of OH* chemiluminescence images of the flame.

The velocity field and the OH* chemiluminescence are regarded at the entry zone of the combustion chamber because of the presence of the flame in this region. The OH* signal further downstream is too weak to be detected with an intensified camera, therefore this region is not taken into account here.

This chapter is focussing on the mean and RMS fields. This allows to describe the shape of the flow field and the flame. It also gives a first insight about the regions with the strongest dynamics.

2.2 Diagnostics

Two diagnostics are used in this part of the project: OH* visualization is used since the radical OH* indicates the position of the flame front and is directly linked to the heat release rate (Schuller et al. (2002)). The velocity fields are obtained by performing Planar velocimetry (PCMV), which is based on PIV, a standard technique for measuring 2D velocities (Adrian (1991); Adrian (2005)).

The mean and RMS fields of OH* chemiluminescence are determined by the application of a high-speed camera with a filter for OH*. This diagnostic allows to visualize the flame front, as previous works have shown (Higgins et al. (2001)).

The images are acquired with a Photron SA-X2 high speed camera with a sampling frequency of 10 kHz and an exposure time of 99 μ s per image. The signal intensity is increased by a Hamamatsu intensifier unit. The intensifier has the same gain for all experiments in order to be able to compare the result. The comparison is possible because the intensifier gain is linear to the detected intensity. The pixel resolution of the acquisition is 410×590 covering an area of $70 \text{ mm} \times 100 \text{ mm}$ thus an image resolution of $5.9 \text{ px}/\mu\text{m}$. The camera is equipped with a Nikkor 105 mm UV-lens and a narrow-band filter centred at 313 nm and a bandwidth of 10 nm. With the chosen alignment, the camera does not cover the entire combustion chamber but only the region where the signal is strong enough. The OH* signal in the chamber exit region cannot be detected because it is very weak.

In PCMV (see Adrian (1991); Adrian (2005) for more details), the flow is seeded with particles which follow the flow field and which are illuminated with a laser source. A camera captures the Mie scattering of these particles at a sampling frequency of 100 kHz. The velocity fields are obtained for each time step by estimating the displacement of the particles between two successive images. To do so, these images are separated into small windows, also named interrogation window. Then a cross-correlation algorithm is applied between the corresponding windows between two image acquisitions in order to obtain their most probable displacement. Knowing the duration between each image acquisition, one can calculate the instantaneous velocity for each interrogation window. The planar velocimetry technique applied in this thesis is described in detail in chapter 5, which focusses on this technique and the developments made on it. It is called PCMV (Planar Continuous laser-based Mie scattering Velocimetry) in the following (see chapter 5 for more information).

2.3 Experimental results

2.3.1 Flame visualizations

The mean and RMS intensities of the OH* chemiluminescence allow to obtain the flame shape and its position in the chamber. Besides, they allow to identify the regions where the flame front is moving at most. The three operating points generate similar flames.

The Abel transformed mean OH* chemiluminescence of **Op16-0-2**, **Op16-2-0** and **Op13.4-4.6-0** is shown in figure 2.1. The flame is not perfectly radial symmetric as the lower half of the flame is slightly longer than the upper half. Nevertheless the Abel transform is conducted in order to better visualize the flame position. This assumption is made due to the topology of the flame which features a strong rotational motion. It can thus be deduced from the images that the flame exits the injector in a conical shape and impacts the walls.

The mean OH* fields of the two points **Op16-0-2** and **Op16-2-0** also have similar intensities with the highest values at the chamber walls. They have a swirl cone angle (angle between the high OH* chemiluminescence cone and the chamber axis) of around 35°. **Op13.4-4.6-0** on the other hand has a swirl angle at the injector of about 25° and thus impacts the walls at a higher x position. It has lower mean intensities at the chamber walls, while the intensity in the swirling cone is similar to that of the two other points.

The mean images show that the positions and shapes of the flame are close for all operating points with small differences between **Op13.4-4.6-0** on the one hand and **Op16-0-2** and **Op16-2-0** on the other hand.

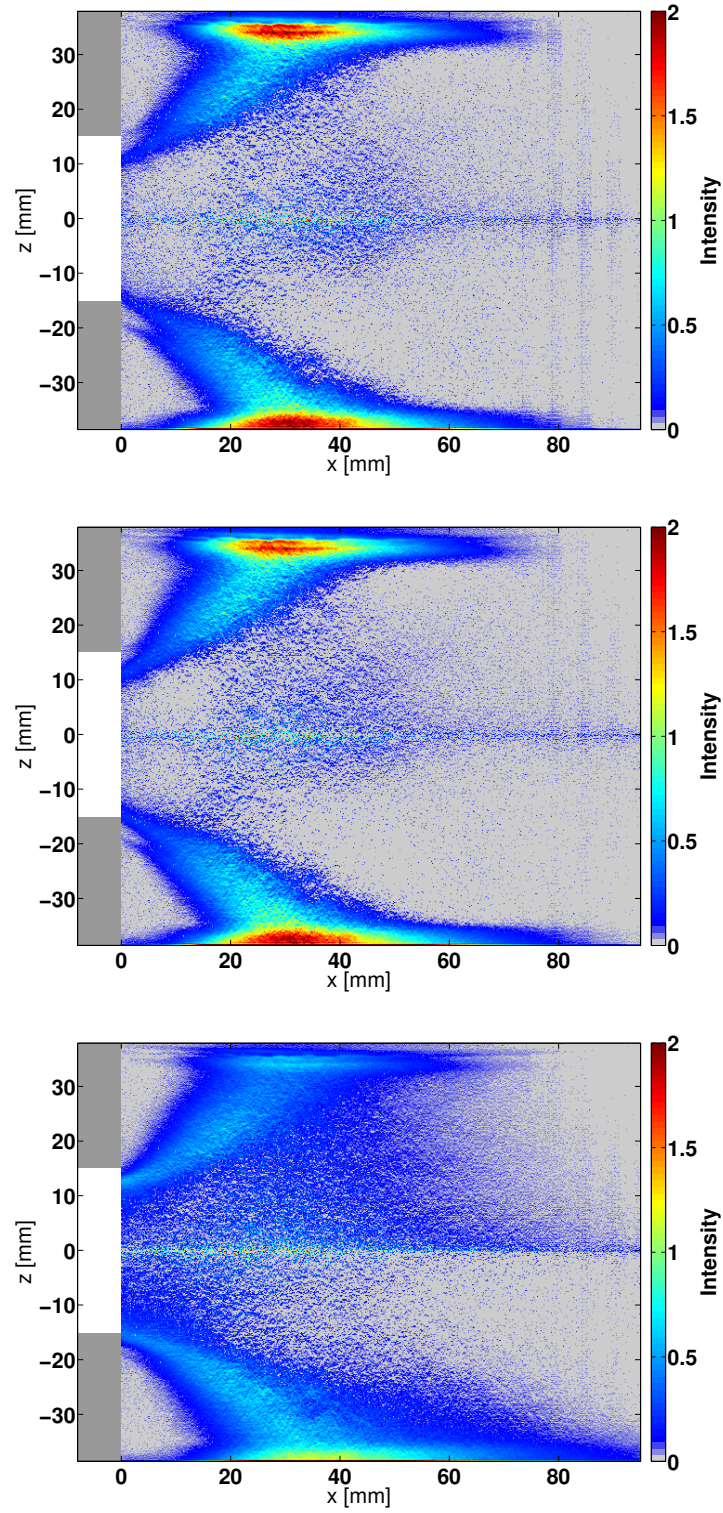


Figure 2.1: Abel transformed mean OH^* chemiluminescence fields of the three operating points. Top figure: *Op16-0-2*; Middle figure: *Op16-2-0*; Bottom figure: *Op13.4-4.6-0*

The RMS OH* chemiluminescence fields can be seen in figure 2.2. They show the local fluctuations of OH* chemiluminescence and hence give insight on the flame dynamics. The fluctuations are located in the regions of highest mean OH* chemiluminescence, especially close to the chamber walls. The swirl cone angles are thus the same as observed in the mean OH* fields. Again, the RMS OH* chemiluminescence fields of **Op16-0-2** and **Op16-2-0** are almost equal, while the field of **Op13.4-4.6-0** is different. It features a smaller swirl cone angle and the flame impingement area is longer than for the two other operating points. This means that at some moment the flame was located in these regions. This higher length is an indicator that **Op13.4-4.6-0** has larger flame motion in axial direction. This suggestion will be confirmed by the results in chapter 4.

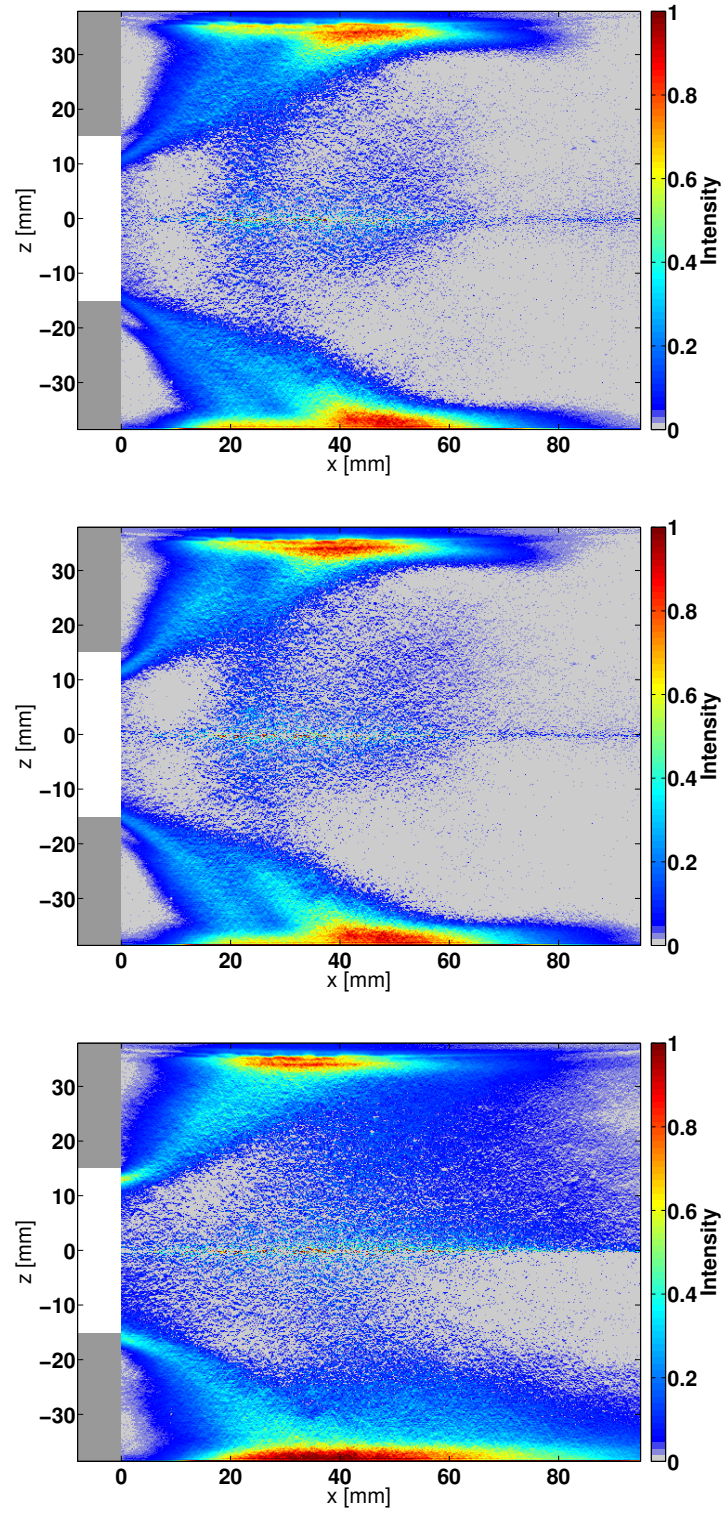


Figure 2.2: Abel transformed RMS OH^* chemiluminescence fields of the three operating points. Top figure: *Op16-0-2*; Middle figure: *Op16-2-0*; Bottom figure: *Op13.4-4.6-0*

The OH* chemiluminescence fields give first insight about the flame position and dynamics. They show that the three operating points feature a classic flame shape for a swirled premixed combustor. The flame has a conical shape and OH* has its highest intensities at the positions where the flame is impacting the chamber walls. **Op16-0-2** and **Op16-2-0** have almost equal OH* chemiluminescence fields, while the field of **Op13.4-4.6-0** is more stretched in the longitudinal direction. This difference is probably due to a higher axial flow rate for this operating point, as will be developed further with the help of the velocity fields.

2.3.2 Statistic analysis of the flow fields

In this section the velocity fields of the three operating points are presented. As mentioned before, the methodology is presented in detail in chapter 5, which also contains their validation. Still the mean and RMS velocity fields are presented here, since they are part of the analysis of the statistics. The velocity fields were only acquired on a limited region, at the entry of the burner with x up to 25 mm and for the upper half of the burner.

The vector view of the mean velocity fields for the three operating points is shown in figure 2.3. These figures show that the three operating points feature a high speed region with a width of a few millimetres and a certain angle compared to the chamber axis. The numerical value of the angle will be presented later on with the velocity profiles, since the numerical values obtained from them will allow to obtain a more precise calculation. If assuming radial symmetry this high velocity region can be considered to have a conical shape. It is adjacent to a low speed inner recirculation zone. Another recirculation zone can be observed in the wall proximity. This flow field shape is classic for a high swirling flame, where the inner recirculation zone has the aim to stabilize the flame (Candel et al. (2014)). However it can also be observed that the thickness of the high speed region **Op13.4-4.6-0** is almost twice as that of **Op16-0-2** and **Op16-2-0**. Furthermore, in the former operating point the longitudinal velocity in the inner recirculation zone is almost zero for $x < 10$ mm, while being clearly negative for the two other operating points. As explained in Candel et al. (2014) the negative velocity is associated with a sufficiently strong recirculation, which stabilizes the flame. Following this reasoning the stabilizing effect of this recirculation zone should thus be lower for **Op13.4-4.6-0**.

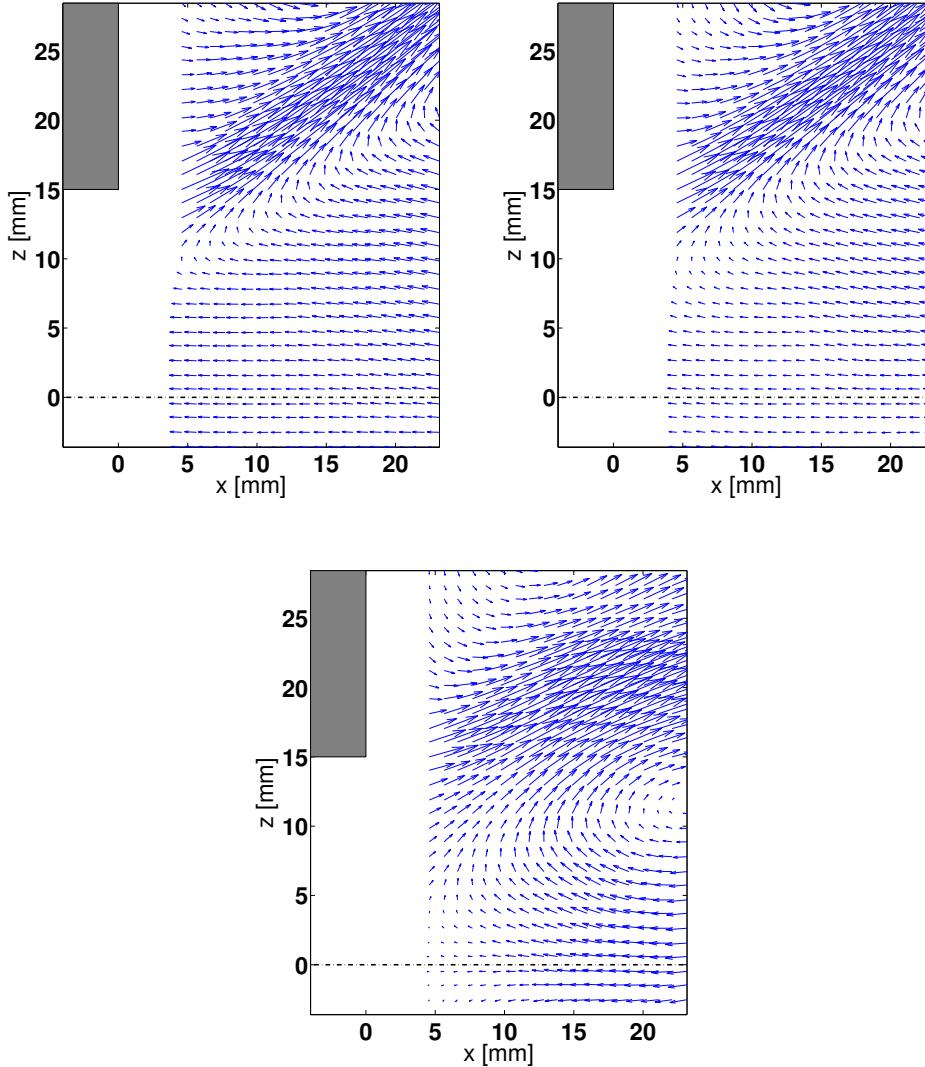


Figure 2.3: *Top left figure: Mean vector field of **Op16-0-2**; Top right figure: Mean vector field of **Op16-2-0**; Bottom figure: Mean vector field of **Op13.4-4.6-0***

The mean velocity fields are depicted in the figures 2.4 to 2.6 and the RMS fields in 2.7 to 2.9. They allow to quantify the observations made in the vector fields. The two operating points **Op16-0-2** and **Op16-2-0** are very close in terms of velocity levels (14 m/s maximal longitudinal and 10 m/s maximal transverse velocity).

Also in the inner recirculation zone the velocities are close, with a value of around -3 m/s. The cone angle of the high speed zone also seems to be similar for both operating points.

Different mean velocities are observed for **Op13.4-4.6-0**. Here, the maximum

mean velocities only reach 10 m/s in x- and 4 m/s in z-direction. The cone angle is about half of that of the two other operating points. The angles are calculated at a later point in this chapter, when the velocity profiles are considered.

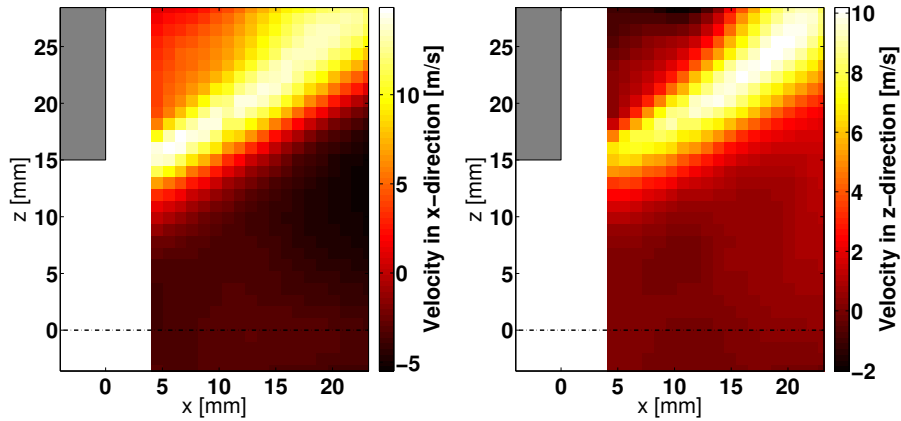


Figure 2.4: Mean velocity fields in x and z direction of *Op16-0-2*

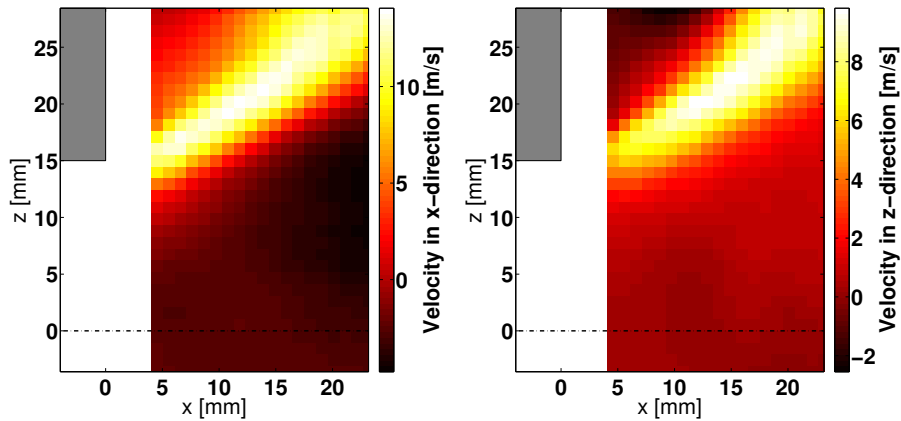


Figure 2.5: Mean velocity fields in x and z direction of *Op16-2-0*

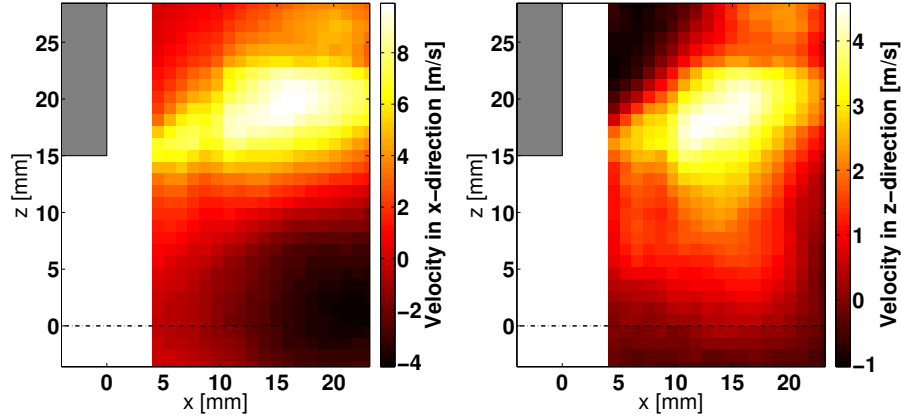


Figure 2.6: Mean velocity fields in x and z direction of *Op134-46-0*

The RMS velocity fields can be seen in Fig. (2.7) to (2.9). Again the fields are similar for both operating points *Op16-0-2* and *Op16-2-0*, with 13 m/s in the longitudinal and 10 m/s in the transverse direction. The highest RMS velocities can be found at the high speed regions, while they are below 50 % in the low speed regions. *Op13.4-4.6-0* has different RMS velocity fields. The operating point features two regions of high RMS velocities in x direction with values up to 10 m/s: the high velocity cone and the region along the burner axis. In z direction, high RMS velocities can only be observed in the high velocity cone, with values up to 5 m/s.

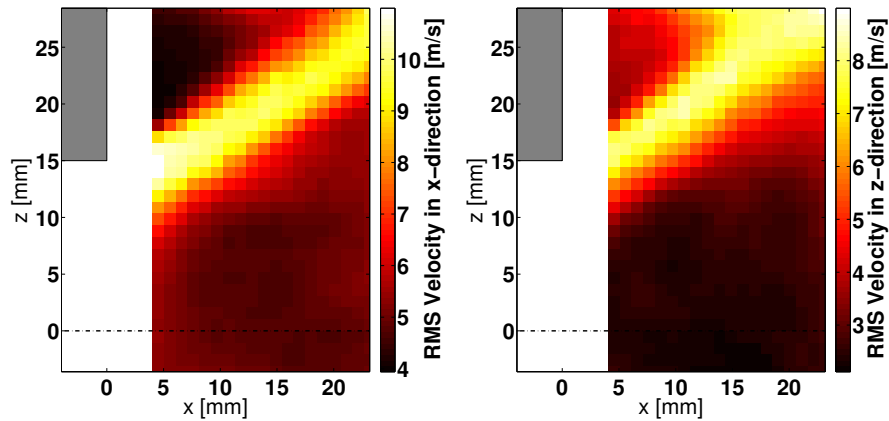


Figure 2.7: RMS velocity fields in x and z direction of *Op16-0-2*

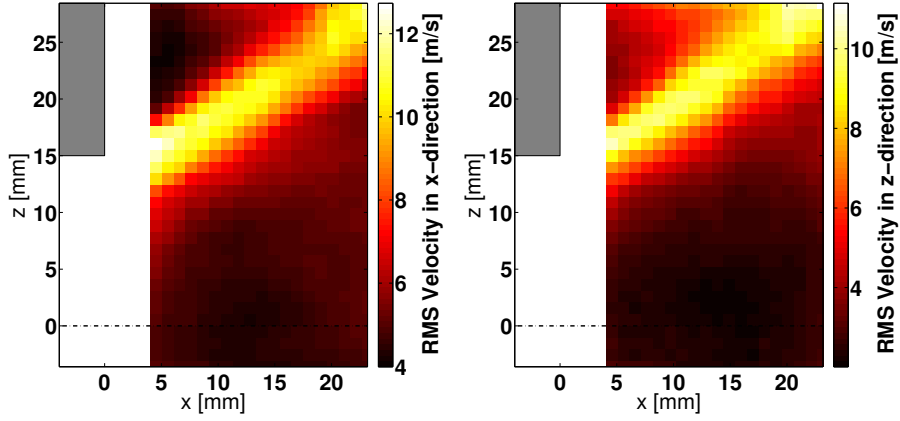


Figure 2.8: *RMS velocity fields in x and z direction of Op16-2-0*

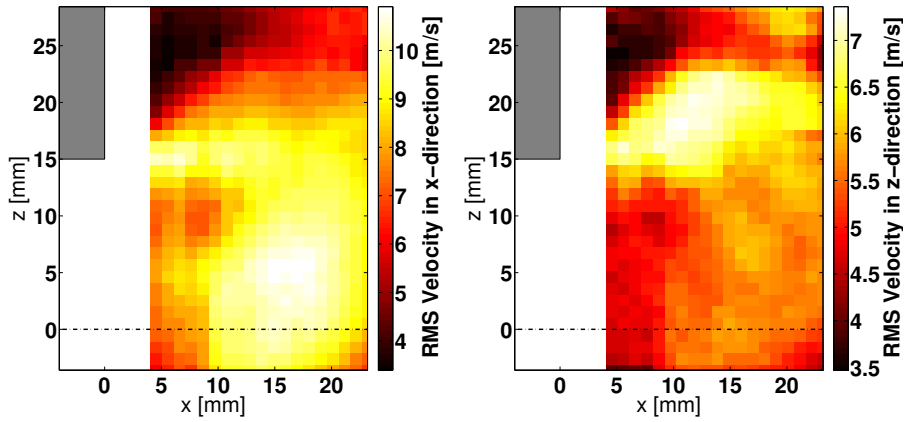


Figure 2.9: *RMS velocity fields in x and z direction of Op134-46-0*

The mean and RMS velocities are compared on different longitudinal positions ($x = 7$ mm, $x = 10$ mm and $x = 13$ mm) in figures 2.10 to 2.13. The x-values in the diagrams correspond to the PCMV discretisation and are thus not round figures.

The figures also allow to calculate the swirl cone angles for the three operating points. The swirl cone angle is defined as the angle between the line following the maximum velocity in the profile and the chamber axis. In a first

approximation it is calculated by the following equation:

$$\varphi = \arctan \frac{z_{u,max}(x = 12.85\text{mm}) - z_{u,max}(x = 6.61\text{mm})}{12.85\text{mm} - 6.61\text{mm}} \quad (2.1)$$

In this equation, the difference of the z coordinates of the highest u velocity at $x = 12.85$ mm and $x = 6.61$ mm is divided by the difference between the corresponding x values.

The mean x -velocities of the three operating points on the chosen axial positions are shown in figure 2.10. The mean velocities in x -direction of **Op16-0-2** and **Op16-2-0** are almost equal over the entire range and on the three longitudinal positions. The profiles also show, that the spatial velocity gradient between high speed region and low speed central zone is particularly high for these two operating points. The swirl cone angle has a value of 33.2° for both operating points.

The maximum mean velocity in x -direction is lower for **Op13.4-4.6-0** and the swirl cone angle has only a value of 18.1° . Besides, the spatial velocity gradient between high speed zone and low speed central zone is far lower. These observations lead to the suggestion that the swirling motion is stronger in the first two operating points. The high swirl cone angle, the negative velocity in the central zone and the high spatial gradients are indicators for this. Indeed, all these characteristics are weaker for **Op13.4-4.6-0**.

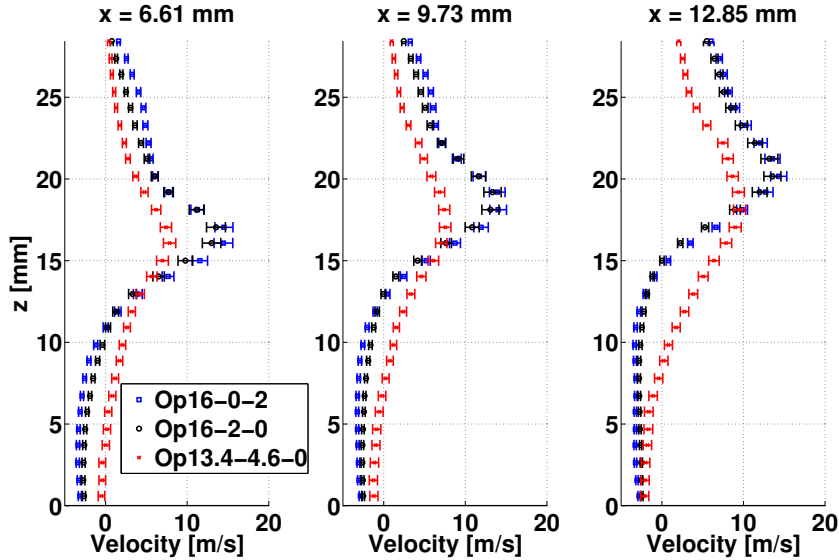


Figure 2.10: Mean velocity profiles in x -direction for different x -positions for the three operating points

The mean velocity profiles in z -direction are depicted in figure 2.11. As ob-

served for the x-direction, the velocity profiles are almost equal for **Op16-0-2** and **Op16-2-0**. They equally show the same swirl cone angle as calculated before and the same high spatial velocity gradient.

Op13.4-4.6-0 on the other hand has very low mean velocities in z-direction. It is also remarkable that the spatial velocity gradient between the velocity peak and the symmetry axis is almost constant. These observations are additional indicators that the swirling motion of **Op13.4-4.6-0** is weaker than for the two other operating points.

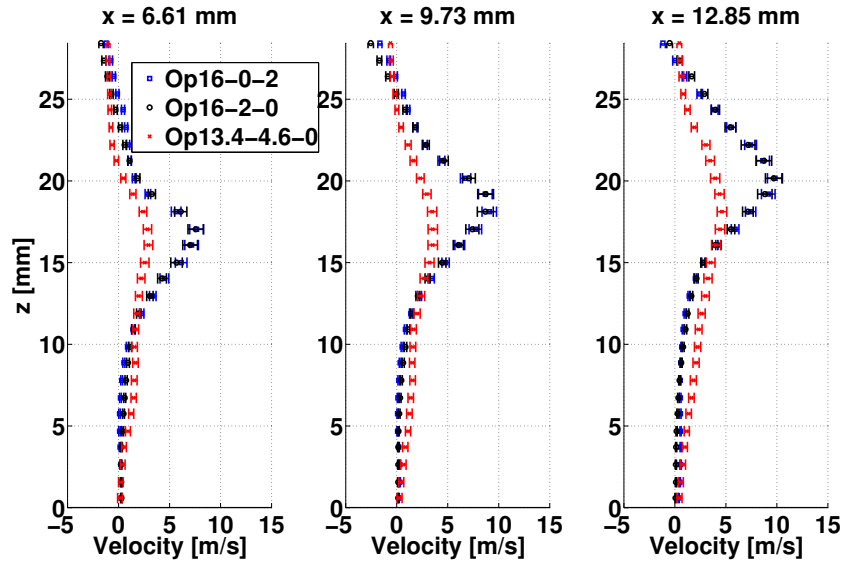


Figure 2.11: Mean velocity profiles in z-direction for different x-positions for the three operating points

The RMS velocities in x-direction are presented in figure 2.12. For **Op16-0-2** and **Op16-2-0** they are similar to the mean velocity fields, with the maximum velocity in a conical region and the low velocities in the inner and outer recirculation zones. The strongest axial velocity fluctuations can thus be found in the regions of the highest velocities.

For **Op13.4-4.6-0**, two regions with high RMS velocities are identified: the high speed conic region, but also on the axis of the burner. The RMS velocities are of the same order of magnitude in the x-direction. This indicates that the flow features strong axial fluctuations not only at the high speed cone, but also in the center.

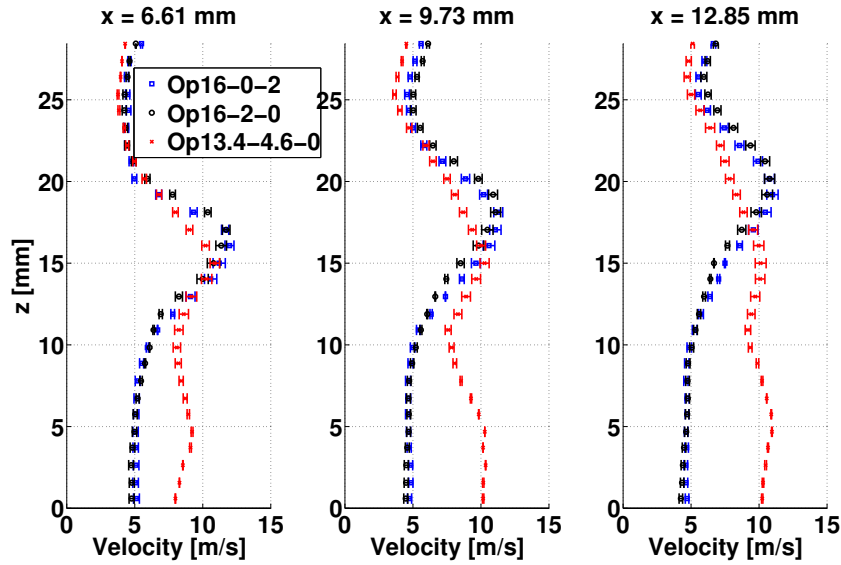


Figure 2.12: *RMS velocity profiles in x-direction for different x-positions for the three operating points*

The RMS velocities in the z-direction show that the strongest transverse fluctuations can be found in the high speed swirling cone for all the three operating points. For **Op13.4-4.6-0**, contrarily to the RMS in x-direction, the RMS velocity in z-direction has a low value. This shows, that the velocity fluctuations in the central regions take place in longitudinal direction. This might be related to an axial flapping motion and is investigated further in chapter 4.

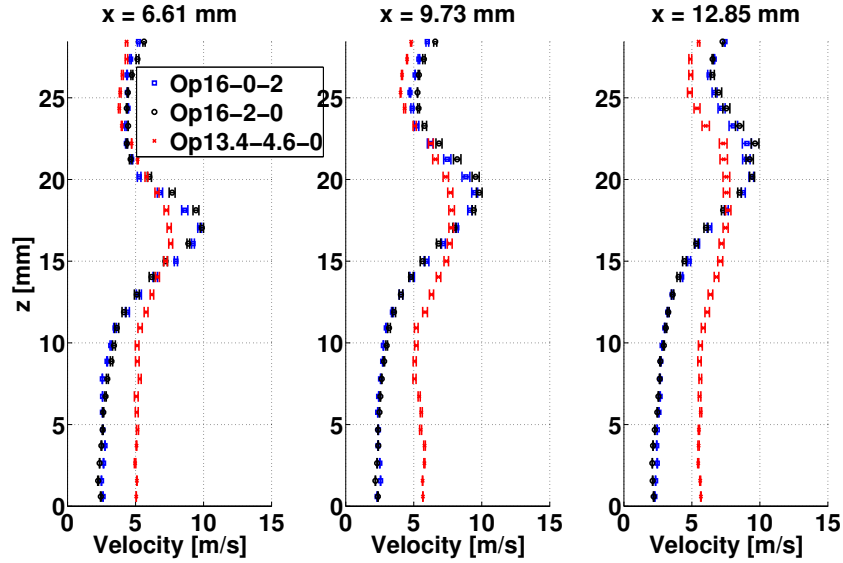


Figure 2.13: *RMS velocity profiles in z-direction for different x-positions for the three operating points*

To summarize, the observations made for the velocity fields confirm those made for the OH* chemiluminescence. The observed flow in the three operating points is typical for a configuration with high swirl values. They feature a high velocity cone and low speed recirculation zones around the chamber axis and near the chamber walls. While **Op16-0-2** and **Op16-2-0** have almost similar flow and OH* fields, **Op13.4-4.6-0** has a smaller swirl cone angle and stronger longitudinal dynamics on the chamber axis.

A possible interpretation can be made based on the different flow repartitions. Reminding the operating conditions presented in chapter 1, these are the only differences between the three points. **Op16-0-2** and **Op16-2-0** have the same axial mass flow rate. However the axial flow velocity is different as it is injected via the perforated plate for one flow and via the central jet for the other. On the other hand, **Op13.4-4.6-0** has a far higher axial air mass flow. The axial air is thus injected with a different longitudinal momentum $m \cdot v$ for the three operating points. This has possibly an effect on the swirl number of the total flow. This aspect is discussed by estimating the swirl number based on the injector geometries.

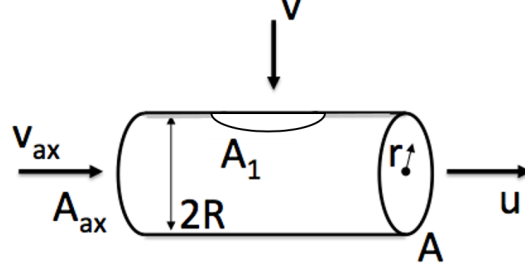


Figure 2.14: *RMS velocity profiles in z-direction for different x-positions for the three operating points*

In figure 2.14 and also in the following calculations, A is the axial surface at the combustion chamber entry, A_1 is the entry surface of the tangential stage (taking into account that there are two feeding pipes), A_{ax} the surface of the axial injection, v the entry velocity in the tangential stage, v_{ax} the velocity of the axial air flow and u the bulk velocity at the combustion chamber entry. The swirl is defined as the moment of the rotating flow divided by the moment of the axial flow. Using this definition, the swirl equation is the following in integral form (Gupta et al. (1984); Palies et al. (2011)):

$$S = \frac{\int_0^R \rho uv 2\pi r^2 dr}{R \int_0^R \rho u^2 2\pi r dr} \quad (2.2)$$

with ρ the density (which is assumed constant), r the radius taken from the symmetry axis, R the radius of the injection tube, u the longitudinal flow velocity and v the tangential velocity.

When the integral in the numerator of Eq. (2.2) is resolved, the following term is obtained:

$$\frac{2}{3} \rho uv \pi R^3 \quad (2.3)$$

The solution of the integral in the denominator of Eq. (2.2) is following:

$$\rho u^2 \pi R^3 \quad (2.4)$$

When these two terms are placed into Eq. (2.2), it becomes:

$$S = \frac{v}{1.5u} \quad (2.5)$$

In practical use, the mass flow rates are controlled. Therefore the mass flow equation is entered into the swirl equation for each velocity. In this case $\dot{m} = \rho u A$ for the bulk flow and $\dot{m}_1 = 2\rho v A_1$ for the tangential injection are used.

The factor 2 in the tangential injection term is due to the two feeding lines that are used to inject tangentially. With these two terms, Eq. (2.2) becomes (with $\dot{m} = \dot{m}_1 + \dot{m}_{ax}$):

$$S = \frac{1}{3} \frac{\dot{m}_1}{\dot{m}_1 + \dot{m}_{ax}} \frac{A}{A_1} \quad (2.6)$$

The surfaces are resolved with $A = \pi d^2/4$ and $A_1 = \pi d_1^2/4$ respectively, with d the diameter of the injection tube and d_1 the diameter of one of the tangential feeding lines. This finally leads to the following equation:

$$S = \frac{1}{3} \frac{\dot{m}_1}{\dot{m}_1 + \dot{m}_{ax}} \frac{d^2}{d_1^2} \quad (2.7)$$

The mass flows can include both, air and fuel mass flow. This equation consists of two divisions - the left one is a division of mass flow rates and the right one is a division of surfaces. It is directly visible, that the left term cannot be bigger than one. Therefore, the maximum swirl number is determined by the quotient of the surfaces. This swirl number is a geometric quantity since it assumes equal velocities over the sections, which is not the case in this combustor. Nevertheless this equation can be used to compare different operating conditions in terms of relative strength of rotational motion.

The equation also shows, that the influence of the axial air flow contribution only depends on the actual mass flow rate and not on its velocity. This can be an explanation for the similarity between the velocity fields and the flame visualisations for **Op16-0-2** and **Op16-2-0**. Both operating points have the same axial air flow, while the fact, that velocity of the axial flows is different, does not play a role.

Op13.4-4.6-0 has a substantially higher axial mass-flow rate as can be seen in table 2.1. At the operating conditions and geometries given in chapter 1, S has a value of 2.7 for **Op16-0-2** and **Op16-2-0** and only 2.3 for **Op13.4-4.6-0**. The swirl number is thus substantially lower for **Op13.4-4.6-0**, which is in agreement with the other observations in this chapter, such as thicker high velocity zones, lower negative velocities in the recirculation zone and a lower swirl cone angle. Even more, this high axial mass-flow rate seems to increase overall flame dynamics. The high RMS velocity in x-direction and the stretching effect of the OH* chemiluminescence images might be indicators of a strong flapping motion of the entire flame.

Table 2.1: Calculation of the geometric swirl number for the three operating points. The mass flow rates include air and fuel mass flows.

	Op16-0-2	Op16-2-0	Op13.4-4.6-0
\dot{m}_1	16.97 g/s	16.97 g/s	14.37 g/s
\dot{m}_{ax}	2 g/s	2 g/s	4.6 g/s
d_1	10 mm		
d	30 mm		
S	2.7	2.7	2.3

2.4 Conclusion

The global velocity fields give first insight about the flow and flame structures of the three operating points. The CESAM-HP combustor has velocity fields and OH* chemiluminescence fields that are classic for a swirling combustor. The flame is of conical shape. The velocity fields feature a high speed area of conical shape as well as low speed recirculation zones. These are located at the axis of the burner and at the combustion chamber walls.

The two operating points **Op16-0-2** and **Op16-2-0** have very similar dynamics, which are dominated by the strong swirling motion. Here, the swirl value is high, as the axial flow rate is small compared to the tangential flow rate. It could also be shown that the velocity of the axial flow does not influence the velocity and OH* fields, as long as the flow rate is the same.

For **Op13.4-4.6-0**, the axial flow part is more than twice as high as for the other operating points and plays an important role. The stabilization by inner recirculation zone seems to be disturbed by this strong axial flow. It leads to a swirl value that is 15% smaller and hence to positive mean axial velocities in the inner recirculation zone. Another suggested phenomenon is the strong axial flapping, which might be the consequence of this reduced stabilization.

The observations in this chapter put into evidence the high importance of the swirling motion in this combustor configuration. The RMS values of the velocity and OH* chemiluminescence show that the strongest dynamics can be found in the high velocity swirling cone. It can be expected that this will play an essential role in the further analysis, such as the time and spatially resolved analysis of pressure, velocity and heat release fluctuations (chapter 4) and the determination of direct and indirect combustion noise (chapter 7 and 8).

Chapter 3

Modal analysis of the test bench

In this chapter, the acoustic eigen modes of the CESAM-HP test bench are determined and their features are investigated. For this, a mixed approach of experimentation and analytical modelling is applied. One of the main conclusions is that the feeding lines have a strong influence on the acoustic behaviour and are associated with the main mode in the combustor. Most of the other modes are related to the combustion chamber and premixer geometries.

3.1 Introduction

The determination of the chamber eigen modes plays an important role in the study of direct and indirect combustion noise. These acoustic modes are expected to contribute to direct combustion noise, since they can be associated with a combustion instability that directly leads to high heat release rate fluctuations and thus high acoustic pressure oscillations. The present results were presented in ASME Turbo Expo 2015 (Mazur et al. (2015)).

The acoustic modes are detected and identified by a combined experimental and analytical approach. On the theoretical level, it is common to solve the Helmholtz equation or the linearised Euler equations instead of the compressible unsteady Navier-Stokes equations (Roux et al. (2005); Sisco et al. (2011)). Only longitudinal waves are taken into account and therefore the test bench is modelled as a collection of acoustic cavities with boundary and jump conditions. This approach is correct in low frequencies, which is the case for this study (Poinsot and Veynante (2005); Dowling and Stow (2003)).

On the experimental level, the analysis of the chamber modes was already performed in previous studies on the CESAM testbench (Tran et al. (2009b); Lamraoui (2011); Richecoeur et al. (2013)), which features a similar design but is operated at atmospheric pressure. In these works, the chamber properties and the acoustic boundary conditions of the ICS were modelled, while

the acoustic properties of the feeding lines were determined experimentally. The same approach is applied in the present work. However, the modelling of the ICS damping properties has been further elaborated until then (Scarpato (2014)) and the improved model is used here. Also, the choked exhaust nozzle is modelled analytically.

3.2 Procedure to identify the acoustic eigenmodes

3.2.1 Experimental procedure

The design and the geometry of the CESAM-HP test bench are detailed in chapter 1. A variety of diagnostics is applied on this combustor. Their positions are presented in figure 3.1.

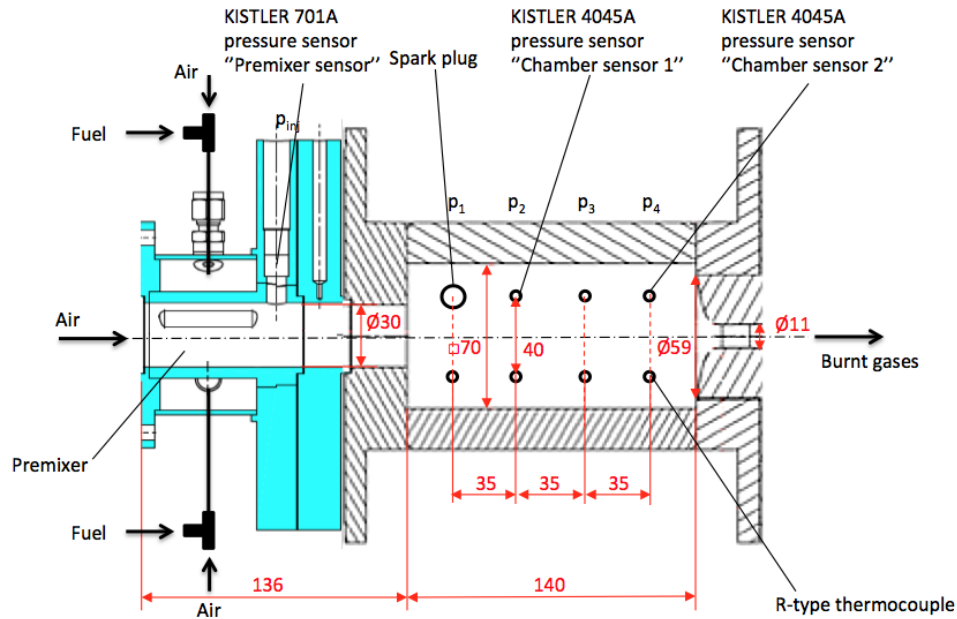


Figure 3.1: Positions of the installed sensors in the combustion chamber

Two types of pressure sensors are applied for the measurements. Their specifications are summarized in tables 1.1 and 1.2. Sensors of the type KISTLER 4045A are mounted in the combustor walls. They are of piezo-resistive type and measure static pressure as well as dynamic pressure fluctuations simultaneously. Their installation in the combustor walls requires a combined system of thermal protection and cooling, which is presented in chapter 1. Chapter 1 also presents the technical specifications of the pressure sensors. They are thus

not detailed here.

The acoustic impedance of the feeding lines is measured with a Pressurized Impedance Measurement System (PIMS). It was developed in EM2C Laboratory based on previous works (Lamraoui et al. (2010)). The schematic drawing of the system is shown in figure 3.2. The pressure sensors integrated in the PIMS are of type KISTLER 701A.

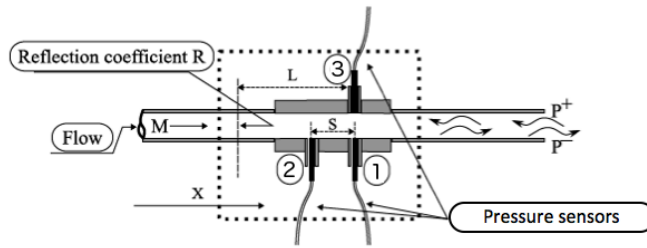


Figure 3.2: Schematic drawing of the Pressurized Impedance Measurement System (PIMS), adapted from Lamraoui et al. (2010)

The measurement technique needs to be calibrated in gain and phase in order to measure the acoustic impedance. While the gain calibration is straightforward using calibrated sources, the phase shift calibration is more complicated. The so-called three microphone method allows to perform the calibration easily and accurately (Chung and Blaser (1980)).

The phase shift is calibrated by switching sensors 1 and 2 under identical conditions during two measurement campaigns (see figure 3.2). The associated transfer function H_{12} between the pressures on sensor position 1 and sensor position 2 is obtained by calculating the geometric mean of the two transfer functions, which were determined during the two campaigns (where o stands for "original" and s for "switched"):

$$H_{12} = \sqrt{H_{12}^s H_{12}^o} \quad (3.1)$$

The signal-to-noise ratio of the measurement is increased by adding a third sensor in front of sensor 1. A coherence factor C_n can be determined between the three sensor signals in the original and switched configurations:

$$C_n = \frac{C_{23}^n}{C_{12}^n C_{31}^n} \quad (3.2)$$

with $n = o$ for the original and $n = s$ for the switched configuration. The two

coherence factors are introduced in the transfer function formula:

$$H_{12} = \sqrt{C^o H_{12}^o C^s H_{12}^s} \quad (3.3)$$

The specificity of the present acoustic impedance measurements is that it is the flame itself that acts as the acoustic source. The acoustic impedances can thus be determined on-the-fly using the PIMS. The range of frequencies that can be reached can be determined by calculating the coherence between the different pressure signals. The coherence of two signals describes to what extent they are linked in the frequency domain. It is defined by the following equation:

$$C_{12} = \frac{|G_{12}|^2}{G_{11}G_{22}} \quad (3.4)$$

with G_{12} the cross spectral density between the two signals and G_{11} and G_{22} the autospectral density of each of the signals.

The coherence between the pressure sensors is shown in figure 3.3. It can be seen that the coherence only reaches a value close to 1 between 50 and around 500 Hz. This means that the associated impedance (or reflection coefficient) is only valid in this range. The main reason for this behaviour is that the flame dynamics, which induce the pressure fluctuations, are too weak at higher frequencies to be properly measured. Better coherences could be achieved by acoustic forcing with loud speaker, however this is not trivial in a pressurized test bench.

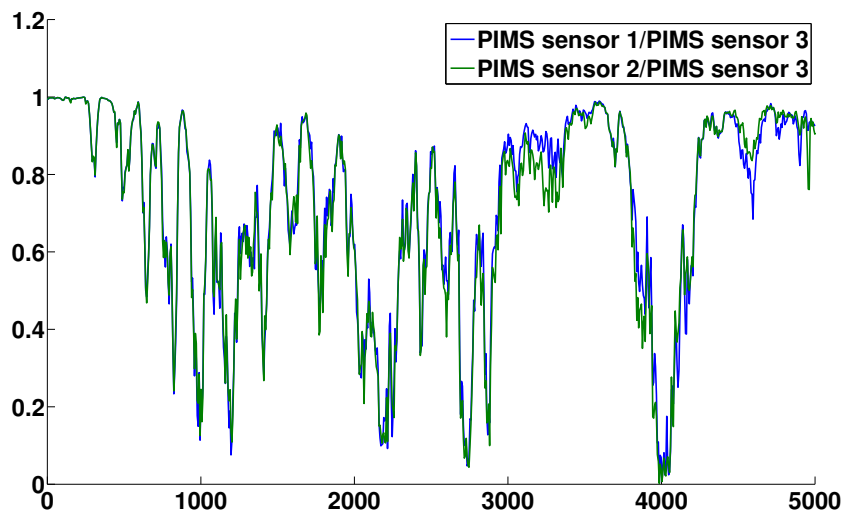


Figure 3.3: *Coherence of the PIMS pressure sensors. The diagram shows that the coherence drops for frequencies above 500 Hz.*

Figure 3.1 shows that a thermocouple is installed in the chamber walls. It is a 1.5 mm sheathed R-type thermocouple which allows to measure mean temperatures up to 1600 K. The thermocouple aims at measuring the mean temperature in the burnt gases. This information is needed for the analytical model, as will be explained in the following section.

The studied operating point is different from the three operating points proposed in chapter 1. While having the same fresh gas temperature and pressure, the total air mass flow is only 15 g/s. This operating point is hence intermediate between low power and high power regimes with a power of 37.5 kW. Indeed, this point features a chamber pressure of 1.83 bar, which is at the choking limit of the nozzle. The air repartition is as follows: tangential air flow of 13 g/s, axial air flow of 2 g/s through the ICS. The global equivalence ratio is 0.85. The point will be named **Op13-0-2** from here on.

When running at **Op13-0-2**, the measured mean burnt gas temperature is 1610 K and the mean temperature in the injector is 580 K due to a slight flashback. Pressure fluctuations are recorded at 25 kHz during 4 s. The Power Spectral Density (PSD) is determined using Hamming windows with 2048 samples and overlapping of around 50 %. The results are shown in figure 3.4. The most remarkable observation is that the spectra are very similar to the spectra of **Op16-0-2** (Fig. ??). They are characterized by a broadband component mixed with several distinct peaks. The sound pressure level of over 100 dB of the broadband part indicates the existence of combustion noise. However seven

distinct peaks can be observed in the low frequency region, which exceed the broadband component by almost 30 dB. The identified peaks are summarized in table 3.1 and the aim of this chapter is to reconstruct them with the help of analytical models in order to interpret their frequencies.

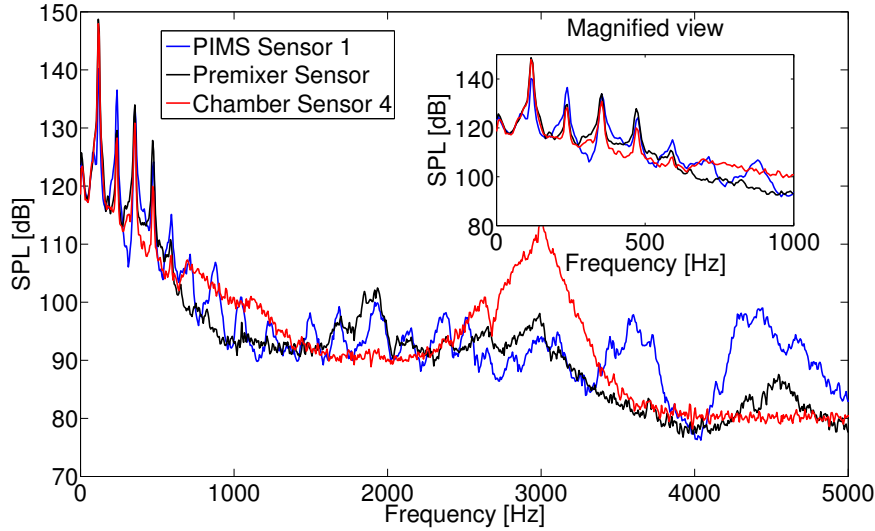


Figure 3.4: *PSD of the pressure sensors in the PIMS, the premixer and the combustion chamber*

3.2.2 Theoretical calculations

This section aims at describing the analytical approach developed to model the CESAM-HP test bench and to calculate the acoustic eigenmodes. The method has been elaborated in previous work (Richecoeur et al. (2013)) and is briefly presented here. The model uses the combustor geometries as well as the acoustic boundary conditions and the thermodynamic conditions (temperature), which are determined either experimentally or analytically. The modelling is conducted in two steps. First, the test bench is represented as two cavities (premixer + combustion chamber) with the ICS as upstream boundary and the choked nozzle as downstream boundary. In a second step, the model is extended with the feeding lines to a five-cavity model (feeding lines + premixer + combustion chamber). The boundary conditions of these feeding lines are determined experimentally with the PIMS. The two models are shown in figure 3.5.

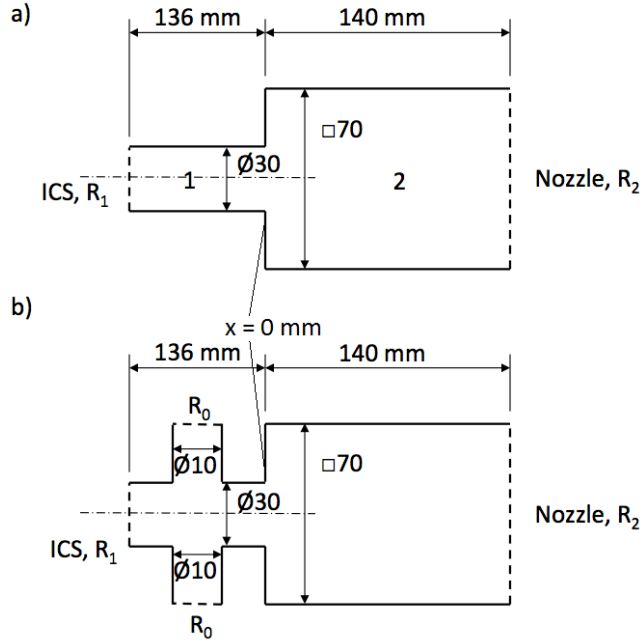


Figure 3.5: Modelling of the burner as a) two and b) five cavities. The main dimensions and boundary conditions are also indicated.

In the two-cavity model the combustor is reduced to two cavities which represent respectively the premixer and the combustion chamber. The cavity of the premixer has an inner diameter of 30 mm and a length of $L_p = 136$ mm. The cavity of the combustion chamber has a section of 70 mm x 70 mm and a length of $L_c = 140$ mm. In both cavities flow quantities such as pressure p , velocity u and density ρ are decomposed into their mean and fluctuating values (with the bar indicating the mean and the prime symbol the fluctuating value):

$$p = \bar{p} + p' \quad (3.5)$$

$$u = \bar{u} + u' \quad (3.6)$$

$$\rho = \bar{\rho} + \rho' \quad (3.7)$$

Since the flow Mach number in both cavities remains small ($M = 0.02$ as shown in section 3.3), the mean quantities are supposed to be constant. Thus only the fluctuation components are considered in the following.

The analysis used in this model is based on linear acoustics where waves can be decomposed into harmonics in the Fourier domain. Mean flow effects such

as acoustic dissipation are ignored in the cavities because of the small Mach number. However this is not the case for the flow in the perforates or the nozzle. To overcome this difficulty, the perforates and the nozzle are expressed as boundary conditions that are dependent on the inlet and outlet flow Mach numbers. The cut-off frequency of the first transverse mode is higher than 5 kHz in each of the cavities. Thus only longitudinal waves will be considered in the lower frequency range. As a result the acoustic perturbations (\hat{p} , \hat{u}) are described as the superposition of progressive and regressive plane waves in the frequency domain:

$$\hat{p}_i = P_i^+ e^{+i\omega x/c_i} + P_i^- e^{-i\omega x/c_i} \quad (3.8)$$

$$\hat{u}_i = \frac{1}{\rho_i c_i} \left(P_i^+ e^{+i\omega x/c_i} - P_i^- e^{-i\omega x/c_i} \right) \quad (3.9)$$

with i the cavity number, ρ_i and c_i the mean gas density and sound velocity in the numbered cavity and ω the pulsation. The abscissa of the following calculations is given by the x -coordinate and the origin $x = 0$ is set on the dump plane at the entry of the combustion chamber. P_i^+ and P_i^- represent respectively the pressure fluctuation amplitudes of the progressive and regressive plane waves. As explained before, mean flow effects such as acoustic dissipations are neglected because the Mach numbers in the premixing tube and the chamber are small.

The equations are complemented by the boundary conditions on the up- and downstream edge of the test bench and the jump condition between the premixer and the combustion chamber. On the upstream boundary, the reflection coefficient of the ICS is

$$R_1 = P_1^+ / P_1^-, \quad (3.10)$$

and can be calculated theoretically as a function of the Rayleigh conductivity K_R .

$$R_1 = \frac{ik_1 d^2 / K_R - i / \tan(k_1 L) + 1}{ik_1 d^2 / K_R - i / \tan(k_1 L) + 1} \quad (3.11)$$

with

$$k = \omega / c_1 \quad (3.12)$$

the wave number, d the spacing between the perforates (as shown in chapter 1) and L the length of the resonance back-cavity of the ICS. The complete solution of K_R is obtained by [Howe \(1979\)](#) and is a function of the Strouhal number.

$$St = \omega a / u_c, \quad (3.13)$$

It is based on the perforate radius a and the vortex convection velocity through the perforates u_c , as presented in Eq. (3.14).

$$K_R = 1 + \frac{1}{St} \cdot \frac{\frac{\pi}{2} I_1(St) e^{-St} - i K_1(St) \sinh(St)}{\frac{\pi}{2} I_1(St) e^{-St} + i K_1(St) \cosh(St)} \quad (3.14)$$

Here I_1 and K_1 are modified Bessel functions of first and second kind. The jump conditions between the two cavities are based on the acoustic compactness assumption (Poinsot and Veynante (2005)) and correspond to Eq. (3.15) and (3.16). In this model, the energy loss across the jump is ignored. It is supposed that the pressure and the acoustic flux are conserved, an assumption which is suitable for low Mach flows.

$$\hat{p}_1(x = 0^-) = \hat{p}_2(x = 0^+) \quad (3.15)$$

$$S_1 \hat{u}_1(x = 0^-) = S_2 \hat{u}_2(x = 0^+) \quad (3.16)$$

$S_{1,2}$ designate the cross section area of the two cavities.

The exhaust nozzle is assumed compact, because its length is very small compared to the wavelengths assumed in this study. Taking into account that the nozzle is choked, the reflection coefficient R_2 is determined by Eq. (3.17) (Marble and Candel (1977)).

$$R_2 = \frac{1 - \frac{1}{2}(\gamma - 1)M}{1 + \frac{1}{2}(\gamma - 1)M} \quad (3.17)$$

The characteristic waves P_1^+ , P_1^- , P_2^+ and P_2^- must satisfy the set of Eq. (3.11) to (3.17). The determinant of the linear system given by the boundary and jump conditions must be null to ensure non-trivial solutions, because the system has no source term. The obtained dispersion relation (Eq. (3.18)) which gives the eigenmodes of the two-cavity model is (with L_p and L_c respectively the length of the premixing tube and the combustion chamber):

$$(1 + \Xi) \cdot [e^{-i(k_1 L_p + k_2 L_c)} - R_1 R_2 e^{i(k_1 L_p + k_2 L_c)}] + (1 - \Xi) \cdot [R_1 e^{i(k_1 L_p - k_2 L_c)} - R_2 e^{-i(k_1 L_p - k_2 L_c)}] = 0 \quad (3.18)$$

where

$$\Xi = \frac{S_1 / \rho_1 c_1}{S_2 / \rho_2 c_2} \quad (3.19)$$

is an indicator for the acoustic coupling between the two cavities. Neglecting the mean pressure drop in the cavities, this expression can be simplified to

$$\Xi = \frac{S_1 \sqrt{T_1}}{S_2 \sqrt{T_2}} \quad (3.20)$$

with T_1 and T_2 the mean temperatures in the corresponding cavities.

In the five-cavity model (Figure 3.5b) the feeding lines are added to the existing model. Thus the premixing tube is split into two parts on the feeding line discharge plan. The two feeding line cavities have a diameter of 10 mm and are located 43.5 mm downstream of the perforated plate. The reflection coefficient R_0 is determined 60 mm from the mixing tube axis with the help of the PIMS according to the procedure described before. As already explained, the coherence between the pressure sensors of the PIMS can only be assured until around 500 Hz. Therefore the analysis of the five-cavity model is limited to this frequency range.

3.3 Results of the experimental and analytical study

Table 3.1: Summary of the acoustic modes obtained experimentally and analytically

n.	Exp	2-cavity model		5-cavity model	
	f_{peak} [Hz]	f^n [Hz]	ω_i^n [rad/s]	f^n [Hz]	ω_i^n [rad/s]
1	116	-	-	125	-231
2	238	-	-	185	-299.2
3	354	-	-	365	-190.5
4	470	-	-	442	-236.7
5	592	558	-391.7	566	-190.5
6	696	-	-	-	-
7	2935	2990	-5	-	-

In a first step the acoustic modes are calculated using the two-cavity approach. To do so the temperatures $T_1 = 660$ K and $T_2 = 1600$ K (as an approximation from the measured gas temperature) and $M = 0.02$ at the entrance plane of the nozzle are applied. For this case, the only frequencies that can be identified are $f^5 = 558$ Hz and $f^7 = 2990$ Hz. These eigenfrequency, as well as the others, are listed in Tab. 3.1 as follows:

$$\omega^n = 2\pi f^n + i \cdot \omega_i^n \quad (3.21)$$

The imaginary component of the frequencies corresponds to the growth rate of each mode. It has a negative value as there is no external acoustic excitation. Furthermore no flame response model is used here so the physical meaning of the growth rate can be criticized. The eigenfrequency f^7 seems to correspond to the fundamental half-wave mode of the combustion chamber, where the boundary conditions associated with the inlet and the outlet are wall-like.

With this simplified geometry one obtains $f_c^0 = 2757$ Hz for the first longitudinal eigenmode of the chamber only, which is about 200 Hz lower than the experimental peak frequency n.7 (Tab. 3.1). This difference is still acceptable since the chamber cavity is calculated using the mean chamber temperature T_2 . This temperature however was determined by thermocouple measurements in the burnt gases. The incertitude of this measurement is rather high and thus the error on the temperature value as well.

No analytical solution could be found for f^6 , but its frequency is close to the first harmonic of the quarter-wave mode of the premixer and combustion chamber as a total, which can be calculated by the following equation:

$$f = \frac{3c_p}{4(L_p + L_c)} \left(1 - \frac{\varphi(R_1)}{\pi} \right) \quad (3.22)$$

In this equation $\varphi(R_1)$ stands for the phase angle of the reflection coefficient of the perforated screen. A value around zero for $\varphi(R_1)$ means that there is no phase shift between the incident and reflected wave. The equation is based on the assumption of a reflection coefficient of $R = |R| e^{i\omega}$ for the perforated plate (Richecoeur et al. (2013)). It results in a theoretical frequency $f_{pc}^0 = 773$ Hz. However, the imaginary part of f^6 is small and the value changes a lot with the reflection coefficient R_1 used in the computations to model the ICS impedance. A higher precision could be obtained if the boundary conditions were determined experimentally. However the pressure measurement ports that would be necessary to conduct such tests are not available in the combustor.

As explained in the previous paragraph the two-cavity model permits to identify the high frequency modes analytically and to interpret their frequency. The results indicate that these mode are associated with the chamber and premixer geometries. However, the low frequencies (<500 Hz) in table 3.1 remain unknown. While these peaks are only visible in the reacting case by the chamber sensors, they are observed by the PIMS sensors also for non-reacting operation. This observation leads to the assumption that these modes are linked to the feeding lines. In order to verify this hypothesis, the five-cavity model is applied in a second step, in order to take into account the feeding lines.

The measured reflection coefficient of the feeding lines R_0 is presented in figure 3.6. The dispersion relation is obtained by applying a tenth-order polynomial fit, as shown in the figure. The found modes for the frequencies between 50 and 500 Hz are presented in table 3.1.

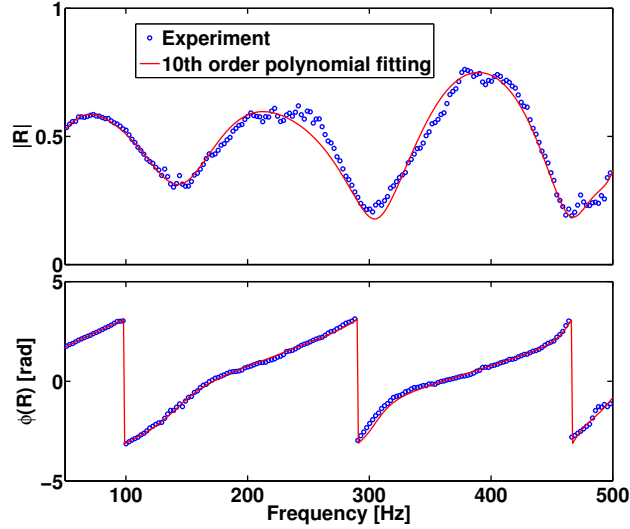


Figure 3.6: Reflection coefficient in the feeding line measured at a radial distance of 60 mm from the premixing tube axis. In red: 10th order polynomial fit

The frequencies found by the five-cavity model seem to correspond well to the measured low frequency peaks. However, the calculations showed that the reflection coefficient of the feeding lines R_0 influences the detected frequencies strongly. It would thus be interesting to apply a more powerful and broadband acoustic source to determine the feeding line impedance more precisely or to force the combustor externally with a loudspeaker. This however could not be done due to the pressurization of the test rig. Nevertheless, the present results indicate that these low frequency peaks are probably associated with the feeding lines.

As a further step, the analytically found modes are compared with the pressure sensor measurements on a structure point of view. For this the PSD values of the pressure measurements $f^1 = 116$ Hz, $f^5 = 592$ Hz and $f^7 = 2935$ Hz are non-dimensionalized, using the sensor in the premixer as the reference signal: $p(x)/p(x_2) = 1$ for $x = x_2$. The different mode structures can be seen in figure 3.7. While the structure of f^1 corresponds well to the findings of the five-cavity model, the other two modes seem much closer to the modes found with the two-cavity approach. The figure shows that the mode of the feeding line is almost constant over the entire combustor. The combustion chamber mode is of half-wave type, as has been shown before. One has however to take into account that the precision of these mode shapes is limited, since the functions were fitted with only three point.

The mode interpretations are summarized in table 3.2. The modes above 500 Hz

are detected with the 2-cavity model and correspond to the chamber and pre-mixer geometries. The low frequency modes can only be detected when the feeding lines are taken into account. This is done with the five-cavity approach which shows that indeed the low frequency modes are associated with the feeding lines. More precisely, these frequencies represent the 116 Hz mode and its harmonics. It is also interesting that very similar mode structures are obtained for the coupled mode associated with the frequency f^5 in the range [500-550] Hz with both models.

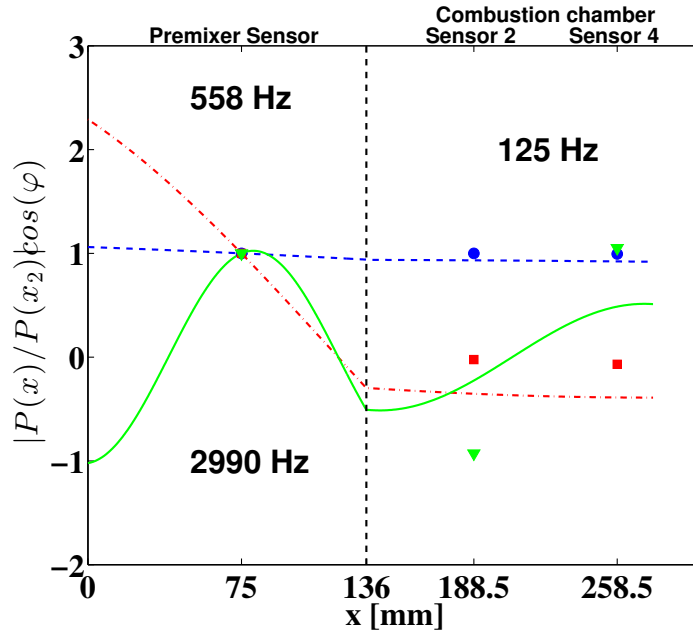


Figure 3.7: Structure of the modes $f^1 = 116$ Hz, $f^5 = 592$ Hz and $f^7 = 2935$ Hz. Lines: analytical modes. Symbols: experiments. Circle: 116 Hz; Triangle: 592 Hz; Square: 2935 Hz. ($x_2 = 75$ mm). The mode for $f^5 = 592$ Hz has a similar shape for both models.

Table 3.2: Summary of the mode interpretations for $n=1$ to 7. Frequencies found experimentally are also indicated.

n.	f [Hz]	Interpretation
1	116	Feeding line
2	238	Feeding line
3	354	Feeding line
4	470	Feeding line
5	592	Feeding line
6	696	Chamber and pre-mixer together
7	2935	Combustion chamber only

As described in the introduction, the studied operating point **Op13-0-2** does not correspond to the three operating points presented in chapter 1. However, it is close to **Op16-0-2** as it corresponds to the same axial air flow, the same global equivalence ratio and as the exhaust nozzle is choked. Moreover, this study shows that the modes of the CESAM-HP test bench are related to the geometry of the combustion chamber, the premixer and the feeding lines. These geometries do not change from one operating point to the other. One of the main modifications could be the field of sound speed that could be different from one point to the other, mainly because of different temperature stratification. In spite of that, one may expect that the eigenmodes remain similar from one operating point to the other. This statement corresponds to the observations for **Op16-2-0** as well as **Op16-2-0**. For all of these modes, the peaks associated with the feeding lines have the same value and also the higher frequency modes can be observed. In **Op13.4-4.6-0** the low frequency peaks do not exist, yet chapter 2 shows that due to the high axial air flow rate, the flow structure is completely changed, leading to the sound speed variations envisaged in the present paragraph.

3.4 Conclusion

In this chapter the acoustic modes of the CESAM-HP test bench are examined by a combined experimental and analytical approach. In this approach, the acoustic boundary conditions of the ICS and the nozzle are calculated analytically while the impedance of the feeding lines is determined experimentally with the PIMS.

The detected eigenfrequencies are analysed for the intermediary operating point **Op13-0-2**. The same frequencies are also observed for **Op16-0-2** and **Op16-2-0**, as shown in chapter 1 and detailed in chapter 4. The model shows that the frequencies above 500 Hz are related to the chamber and premixer geometry, while the lower frequencies are associated to the feeding lines. More generally, these results indicate the key role of the injector arrangement on the global combustor behaviour - an observation that will be repeated in various chapters during this study.

The results show that the acoustic behaviour is dominated by these eigenfrequencies. Their amplitude is several orders of magnitude above that of the broadband noise. This may be a first indicator that direct combustion noise is dominating in the CESAM-HP test bench, as will be shown in chapter 7 and 8. This is certainly due to the strong coupling between acoustics, aerodynamics and heat release at these specific frequencies. This aspect will be put into evidence in chapter 4.

Chapter 4

Time and spatially resolved analysis of the combustion instability

In this chapter the combustion instability in the CESAM-HP combustor is studied further. The aim is to put into evidence the mechanisms that are driving the pressure fluctuations as well as the effects of these pressure fluctuations on the flame dynamics. The analysis is done by conducting time and spatially resolved measurements of pressure, velocity and OH chemiluminescence on different locations of the combustion chamber. From these experimental data, the Power Spectral Density is calculated for chosen regions of the combustor. The experiments show that the studied operating points **Op16-0-2** and **Op16-2-0** are dominated by a 120 Hz instability, that can be detected in the studied regions by all the used diagnostics. **Op13.4-4.6-0** features a strong peak around 80 Hz, that is also detected by all diagnostics that are used. From these experiments, the interactions between the flame and the chamber walls and the interaction between the flame and the flow field are identified as mechanisms that drive the combustion instability. Even more, the acoustic perturbation of the flame by the pressure fluctuations is put forward. Based on these observations, first suggestions are made about combustion noise generation in the CESAM-HP burner.*

4.1 Introduction

In this chapter, the low frequency combustion instability suggested in chapter 3 is analysed further for the three operating points **Op16-0-2**, **Op16-2-0** and **Op13.4-4.6-0** by using high speed optical diagnostics. The regions where the corresponding frequency of 120 Hz (of 80 Hz for **Op13.4-4.6-0**) is dominating are chosen and the measurements are used to put into evidence the different

instability mechanisms that can be observed in the CESAM-HP combustor.

A large variety of interactions between the different elements of a combustor exists, which all lead to combustion instabilities (Candel (2002)), has been identified in literature. For the applications of gas turbine combustors that feature a lean premixed swirling flame, Ducruix et al. (2006) put forward six of them. They distinguished between two types of mechanisms: (1) Driving mechanisms are phenomena that lead to pressure fluctuations in the combustor. (2) Coupling mechanisms describe the effects of the pressure fluctuations on different phenomena in the combustor.

Three driving mechanisms are identified by Ducruix et al. (2006):

- One mechanism is the interaction between flame and vortex, more precisely the vortex roll up in the flame. During this process, the vortex entrains fresh gases which ignite abruptly, which then leads to fluctuations in heat release and finally in pressure. This process normally takes place periodically and is also described by Poinso et al. (1987) and Shadow et al. (1989).
- Another mechanism is the interaction between flame and wall, where the flame impact on the wall leads to periodic fluctuations of the flame surface and thus the heat release. This finally leads to pressure fluctuations. This process has been studied experimentally by Schuller et al. (2002).
- Finally, the interaction between neighbouring flame front leads to fluctuations of the flame surface. the consequence are fluctuations in heat release and thus also in pressure. Further precisions can be found in Durox et al. (2002).

Equally, three coupling mechanisms are described by Ducruix et al. (2006):

- The first mechanism is the acoustic perturbation of the flame. The associated pressure fluctuations lead to fluctuations of the velocities. This has an effect on the driving mechanisms, such as on the flame-wall interactions or the flame-vortex interactions. Further details can be found in Ducruix et al. (2000); Schuller et al. (2002).
- Another mechanism, proposed by Lieuwen and Zinn (1998), is the flame response to composition inhomogeneities of the fresh gases, where the pressure fluctuations interact with the fuel feeding lines. This leads to fluctuations of the equivalence ratio and thus to heat release fluctuations.

- The final mechanism described by [Ducruix et al. \(2006\)](#) is the flame response to unsteady strain rate. Here, the pressure fluctuations lead to fluctuations of the velocities, which influences the strain rate of the flame. This finally leads to fluctuations of the flame surface and the reaction rate. The process is described in detail by [Law \(1989\)](#) and [Peters \(2000\)](#).

The aim of this chapter is to use time and spatially resolved diagnostics in order to put into evidence the different driving and coupling mechanisms that can be observed in the CESAM-HP combustor.

4.2 Methodology for the spatially resolved observation of combustion instabilities

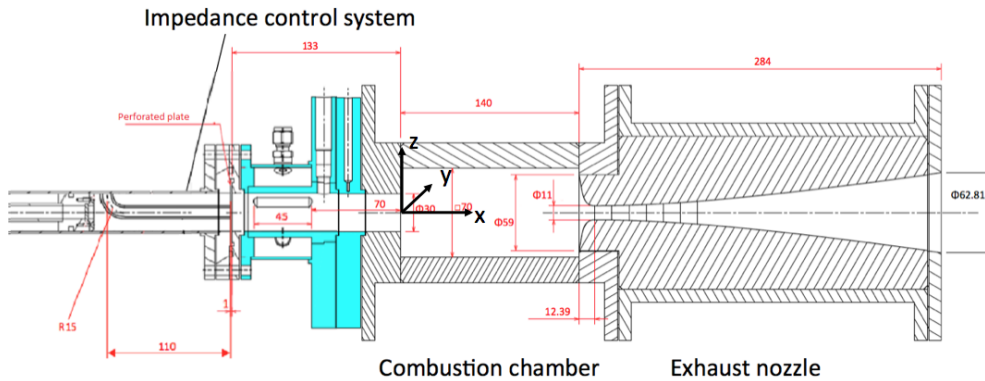


Figure 4.1: Applied coordinate system. Keep in mind that the coordinate system is right-handed. The y-coordinate is therefore showing away from the reader.

The pressure, the velocity and the heat release are observed using the following diagnostics: (1) The pressure fluctuations are obtained by using piezo-resistive sensors of type KISTLER 4045A. Their functioning and installation is explained in chapter 1. (2) The velocity fields are obtained experimentally with the help of high speed planar velocimetry. The applied PCMV system is explained and validated in chapter 5 and the mean velocity fields are presented in chapter 2. (3) The local heat release rate is obtained with a high speed camera and a filter which allows to select the bandwidth of OH* chemiluminescence. The technique is described in chapter 1 and the mean and RMS OH* chemiluminescence fields can be found in chapter 2. The experiments are conducted on the well-known operating points **Op16-0-2**, **Op16-2-0** and **Op13.4-4.6-0**

As the pressure measurement is a point measurement, the diagnostic is not spatially resolved in itself. However, the discussion of the spatial gradient of

the pressure fluctuations in chapter 7 shows that for frequencies up to 1000 Hz this gradient is low. This is justified by comparing the acoustic wave length with the combustion chamber length using the equation for the speed of sound:

$$c_0 = \lambda \cdot f \quad (4.1)$$

with λ the wave length and f the frequency of the acoustic wave. When assuming a speed of sound of 800 m/s in the burnt gases, an acoustic wave at 120 Hz would have a wave length of 6.7 m, thus far above the chamber length of 0.14 m. Even an acoustic wave of 1000 Hz would have a wave length of 0.8 m, thus five times more than the chamber length.

This calculation shows that the pressure fluctuations are almost equal over the entire combustion chamber length for frequencies up to 1000 Hz. It is thus assumed for this chapter that the pressure fluctuations are equal in all the regarded regions.

It needs also to be mentioned that the OH* chemiluminescence images used for this thesis are line-of-sight images. They are not Abel-inverted as this image treatment is only suitable for flows that are perfectly radially symmetric. This is not the case for instantaneous flows in this combustor. Due to this, the spectra of the OH* images can be directly compared to PM results but care must be taken when comparing with PCMV results as those are obtained on a single plane.

The frequency spectra of the three diagnostics are obtained by calculating the PSD of the different measurements. They are obtained using Welch's algorithm with Hamming windows (in order to reduce signal ripple) at around 50 % overlapping and a window size which allows for a frequency resolution of 5 to 10 Hz.

As described in section 4.1, this chapter has the aim to put into evidence different instability mechanisms in the CESAM-HP combustor. From the different mechanisms that are presented in section 4.1, the following are taken into account: Flame-Vortex interaction, Flame-Wall interaction, Acoustic perturbation of the flame and composition fluctuations. The two other mechanisms, the interaction between neighbouring flame fronts and the flame response to unsteady strain rate are not taken into account. To put them into evidence, simultaneous time resolved flame surface measurements (by OH-LIF) and 2D velocity measurements (PCMV or PIV) would be necessary. However these measurements are not available here.

The flame-vortex interaction is put into evidence by regarding the velocity fields as well as the spatially resolved OH* chemiluminescence. The idea is to show that vortexes can be observed in the regions with high OH* fluctuations. This can be done by drawing the instantaneous velocity fields on the rms fields of

OH* on the same 2D diagrams. In a second step the PSD of the OH* chemiluminescence and the velocity are compared in the shear layer between high velocity swirling cone and the recirculation zones. If the same frequencies can be observed, then this would be a first indicator for a possible interaction between the flame front and vortices.

The flame-wall interactions can be demonstrated by regarding the OH* chemiluminescence in the regions where the flame is impacting the walls. The regions can be identified from the RMS OH* fields that were obtained in chapter 2. In these regions, the PSD of the OH* chemiluminescence can be determined in order to verify whether the main eigen frequencies correspond to those of the combustion instability.

The coupling mechanism that corresponds to the acoustic perturbation of the flame can be demonstrated by regarding the PSD spectra of pressure, velocity and heat release in the flame front. In order to put into evidence this mechanism, all these three should have the same eigen frequency as the combustion instability.

The last mechanism that needs to be mentioned are the effects of the pressure fluctuations on the gas composition. As shown by [Lieuwen and Zinn \(1998\)](#) and described by [Ducruix et al. \(2006\)](#), the pressure fluctuations interact with the fuel flow controllers at the frequency of the combustion instability. More concretely an increase in pressure acts as counter-pressure on the flow controllers and thus decreases the fuel mass flow rate, and vice versa. This finally leads to fluctuations of the equivalence ratio of the combustor. The effects of the feeding lines were already analysed in chapter 3, which shows that they are linked to the low frequency instability with the combustor. This point is thus not treated further in this chapter.

Figure 4.2 indicates why the use of these different diagnostics is relevant in order to put into evidence the different mechanisms. The figure shows an instantaneous velocity field plotted together with the RMS OH* chemiluminescence for **Op16-0-2**. The velocity field is shown as streamlines which allows for an easier detection of vortices.

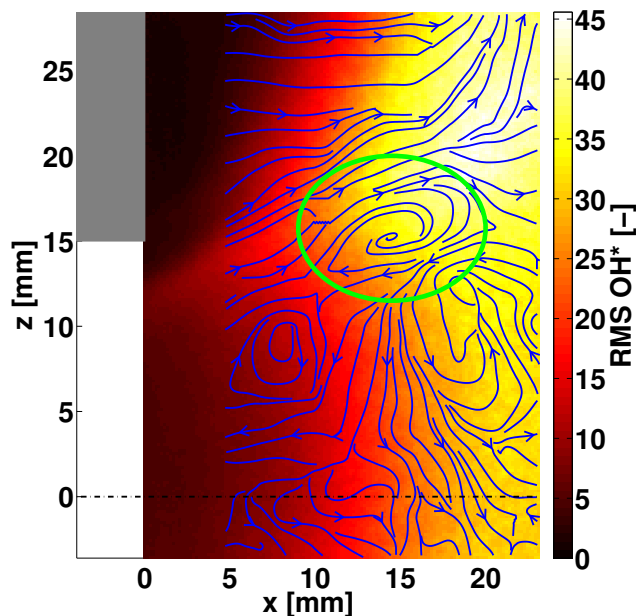


Figure 4.2: Time resolved plot of the streamlines together with the RMS OH* chemiluminescence for *Op16-0-2*

The instantaneous streamline field superposed with the RMS OH* chemiluminescence shows a topology that is typical for a lean premixed swirling flame. It features a conical region that is located in the region of highest OH* RMS and corresponds to the high velocity swirling cone that was already presented in chapter 2. Outside this high velocity zone, different flow directions can be detected. It also features the low velocity recirculation zones that can be in particular seen around the burner axis. Here, the flow direction is towards the injector with almost no transverse flow.

The most remarkable feature is the existence of a vortex that is located at the inner border of the high velocity swirling cone. The vortex has been marked with a green circle in figure 4.2. The streamlines located around this vortex are pointing downstream. This means that the vortex is probably propagating downstream along the high velocity cone. Since the vortex is located in the lower border of the region with high OH* chemiluminescence it can be assumed that both the flame front and the vortex are interacting. This could correspond to the mechanism of the flame-vortex interaction. However the figure is not sufficient to put into evidence this mechanism, because it is comparing the instantaneous velocity with a statistic value for OH* chemiluminescence. This does not allow to draw further conclusions. In order to do so, it would be interesting to conduct imaging of the flame front by OH-PLIF, while simultaneously obtaining the 2D velocity field. Since this was not available in this work,

no further statements can be made. Nevertheless these observations justify the interest for this particular region of the flame and the flow field.

The time and spatially resolved determination of the PSD of pressure, velocity and heat release rate will give better evidence on the different instability mechanisms. For this, different regions need to be chosen that are supposed to be affected by different mechanisms. Four points were chosen in this work. They are presented in table 4.1. The coordinates in this table correspond to the coordinate system shown in figure 4.1. The location of these regions is shown in figure 4.3. The figure shows an image of the RMS OH^* chemiluminescence of **Op16-0-2** that features in particular the high speed swirling cone and the zones where the flame is impacting the chamber walls. (More details about the diagram can be found in chapter 2). The chosen regions are marked as white squares on this figure. For regions 1 to 3, data for PCMV, OH^* and pressure exist, while the remaining region is only represented with OH^* visualizations and pressure measurements.

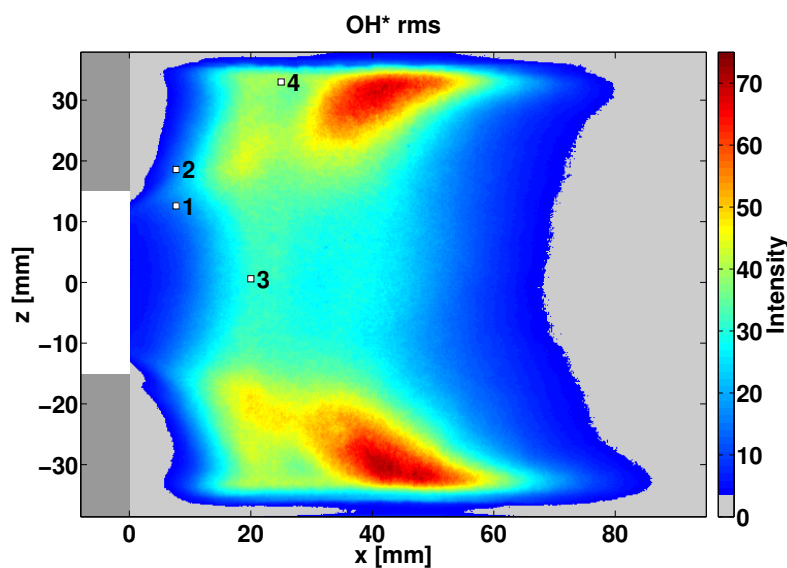


Figure 4.3: Image of the RMS OH^* chemiluminescence of **Op16-0-2** with the regions that are listed in table 4.1. The image is not Abel transformed and very low values are shown as gray. Further descriptions of the mean and RMS OH^* chemiluminescence fields can be found in chapter 2.

Two points are chosen around the high velocity swirling cone. This region is of interest for the flame/vortex interaction since the corresponding vortices can normally be located here. It is also interesting for the coupling mechanisms between the pressure fluctuations and the response of the flame because the effects can normally be observed here in the flame front. The chosen points are

the following:

- Area 1 corresponds to a part of the swirling cone, on the inner side. It is thus the interface between high speed swirling motion and the inner recirculation zone.
- Area 2 is a part of the swirling cone, on the outer side. Hence it is the interface between high speed swirling motion and the outer recirculation zone.

The second region is located on the burner axis. By determining the PSD of velocity and OH* in this region, it can be investigated whether the combustion instability leads to an axial motion of the flame. For this, the PCMV measurements in region around the axis are particularly interesting, as this region lies outside the high velocity swirling cone. The dynamics at the axis is thus not interfered by the strong dynamics associated with the swirling motion. This region is particularly of interest for **Op13.4-4.6-0**, since high longitudinal RMS velocities were observed in chapter 2 for this operating point in this region. The following point is regarded here:

- Area 3 located at the axis of the combustor.

The final chosen region is at the chamber walls, where the flame is impacting. The aim is to put into evidence the flame/wall interaction mechanism by comparing the main PSD of the OH* chemiluminescence with the acoustic eigen mode frequencies.

- Area 4 is located in the region where the flame is impacting the chamber walls.

The high velocity swirling cone and the recirculation zones are described in chapter 2.

The shown coordinates correspond to the center of the respective window, where the PSD is obtained over the spatial mean. For the PCMV measurements, it corresponds to the central point of a 0.97 mm × 0.97 mm square window. This value is exactly the chosen PCMV interrogation window size. For OH* chemiluminescence the PSD is conducted on the spatial mean intensity in windows of a size of 1.02 mm × 1.02 mm. This corresponds to windows of 7 px × 7 px and has been chosen to be close to the PCMV interrogation window size.

The OH* acquisitions with the high speed camera are validated by comparing their spectrum to that of the OH* chemiluminescence measured with a photomultiplier probe (PM). For this purpose the PSD is determined for the entire image field of the camera. The results of the PM are presented in detail in chapter 7 and are proven to correspond to the global heat release of the flame.

Table 4.1: *Chosen regions where the PSD is determined. The coordinates of the regions studied by OH* chemiluminescence indicate the central point of a 1.02 mm × 1.02 mm square. The coordinates of the regions studied by PCMV indicate the interrogation window in which the point is located. They indicate the center of a 0.97 mm × 0.97 mm square*

Area	x [mm]	z [mm]	PCMV	OH*	Comment
1	7.7	12.6	X	X	Swirl cone upstream, inner side
2	7.7	18.6	X	X	Swirl cone upstream, outer side
3	20.0	0.6	X	X	Center line
4	25.0	33.0		X	Wall impinging

The results are presented in figure 4.4 and show very good agreement between the two techniques in the entire frequency span. In the low frequency area, the peaks are well represented by both measurements in terms of frequencies and relative amplitudes. OH* high speed imaging thus correctly represents global heat release. Due to the findings of previous works (Schuller et al. (2002)) it can also be assumed that it correctly represents the heat release in the chosen regions.

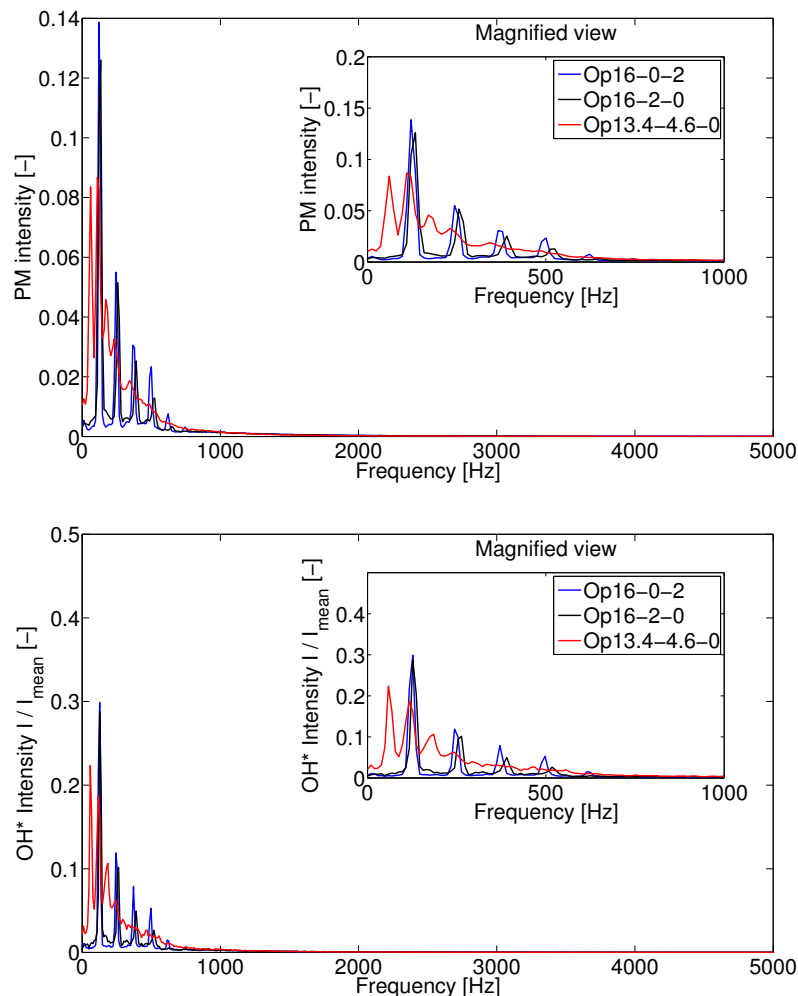


Figure 4.4: PM and total OH* chemiluminescence imaging spectra of the three chosen operating points for the entire combustion chamber. The figures show that the spectra for both diagnostics have the same peaks.

4.3 Experimental results

As a reminder, the spectrum of the in-chamber pressure measurements is shown in figure 4.5. The interpretation of each peak is explained in chapter 3 and 7. For this study, especially the low frequency peaks are of interest, as they show the strongest dynamics. As described before, the pressure fluctuations are considered equal over the entire length of the chamber for frequencies up to 1000 Hz.

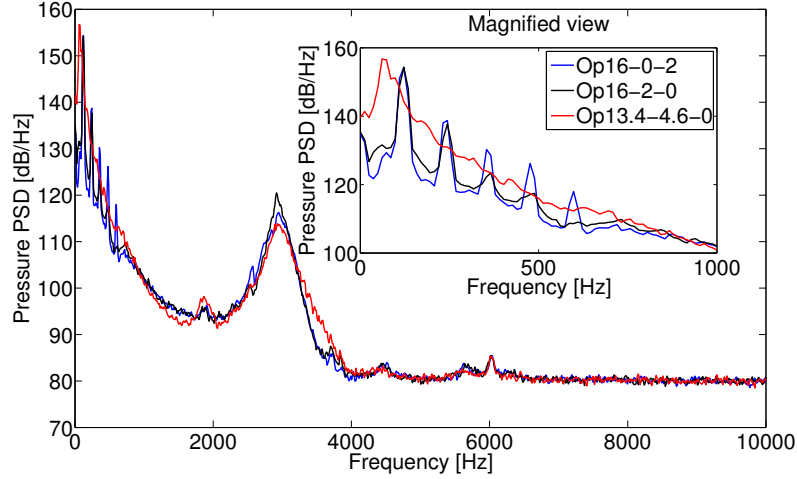


Figure 4.5: The pressure spectra of the three chosen operating points show strong pressure fluctuations in the low frequency region. **Op16-0-2** and **Op16-2-0** feature their strongest peak at 120 Hz and also the harmonics of that frequency. **Op13.4-4.6-0** is characterized by a more broadband peak with its maximum frequency at around 80 Hz.

Figures 4.6 and 4.7 show the PSD of the OH* chemiluminescence and of the velocity in x and z directions for the four chosen regions. Their content is described and discussed in the following sections.

The spectra for **Op16-0-2** and **Op16-2-0** are depicted together in figure 4.6 because of their similarity. The spectra of **Op13.4-4.6-0** are shown separately in figure 4.7.

In all diagrams, the regarded frequency is limited to 1000 Hz, since no spectral content can be found for higher frequencies neither for the velocities nor for the OH* chemiluminescence. Both figures are separated in lines and columns. Every column stands for one of the four regions, while each line stands for the measured physical quantity. There are no velocity measurements available for region 4 because it is outside the region where the PCMV measurements were conducted.

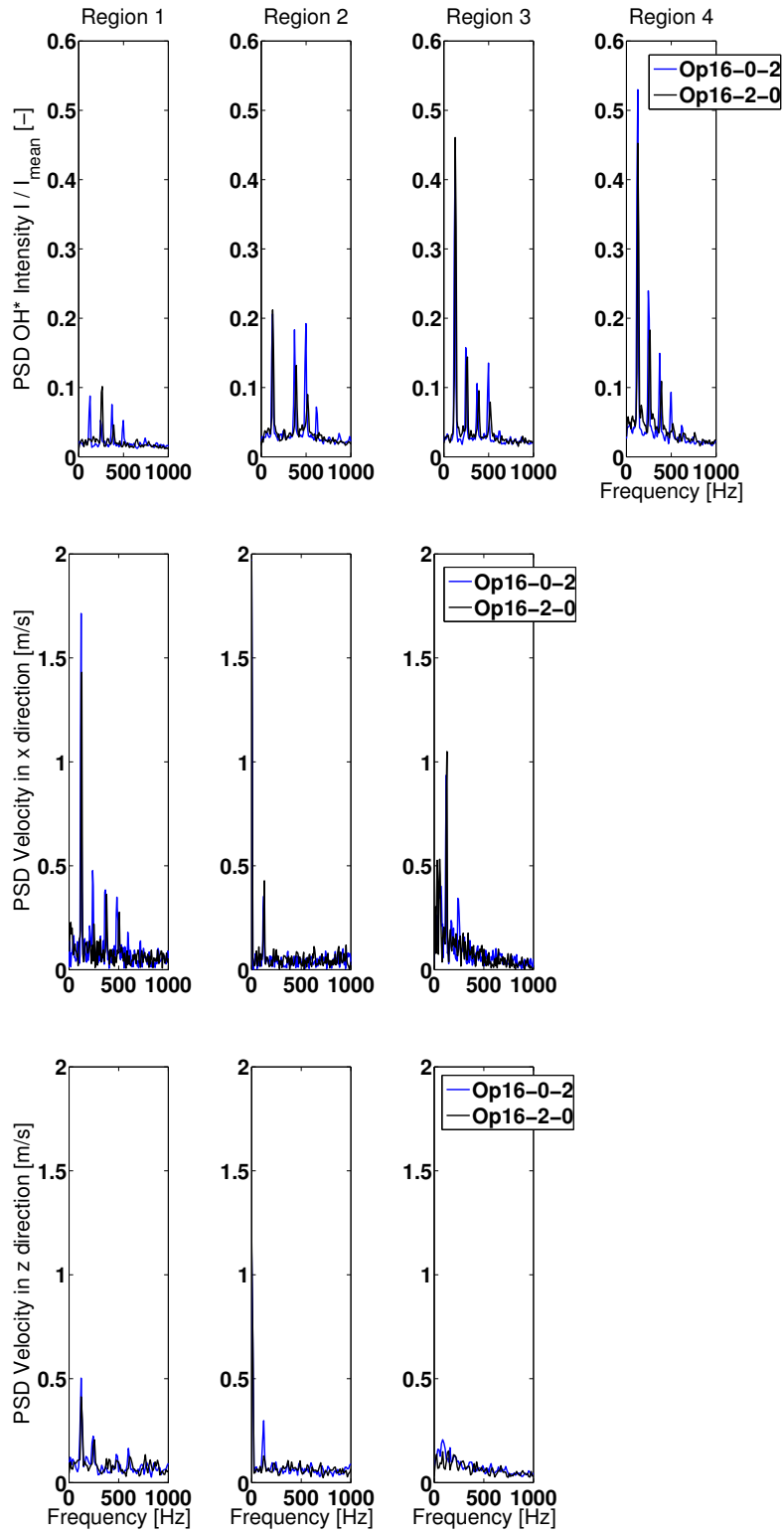


Figure 4.6: PSD of the OH^* and velocity fluctuations in regions 1 to 4 for *Op16-0-2* and *Op16-2-0*

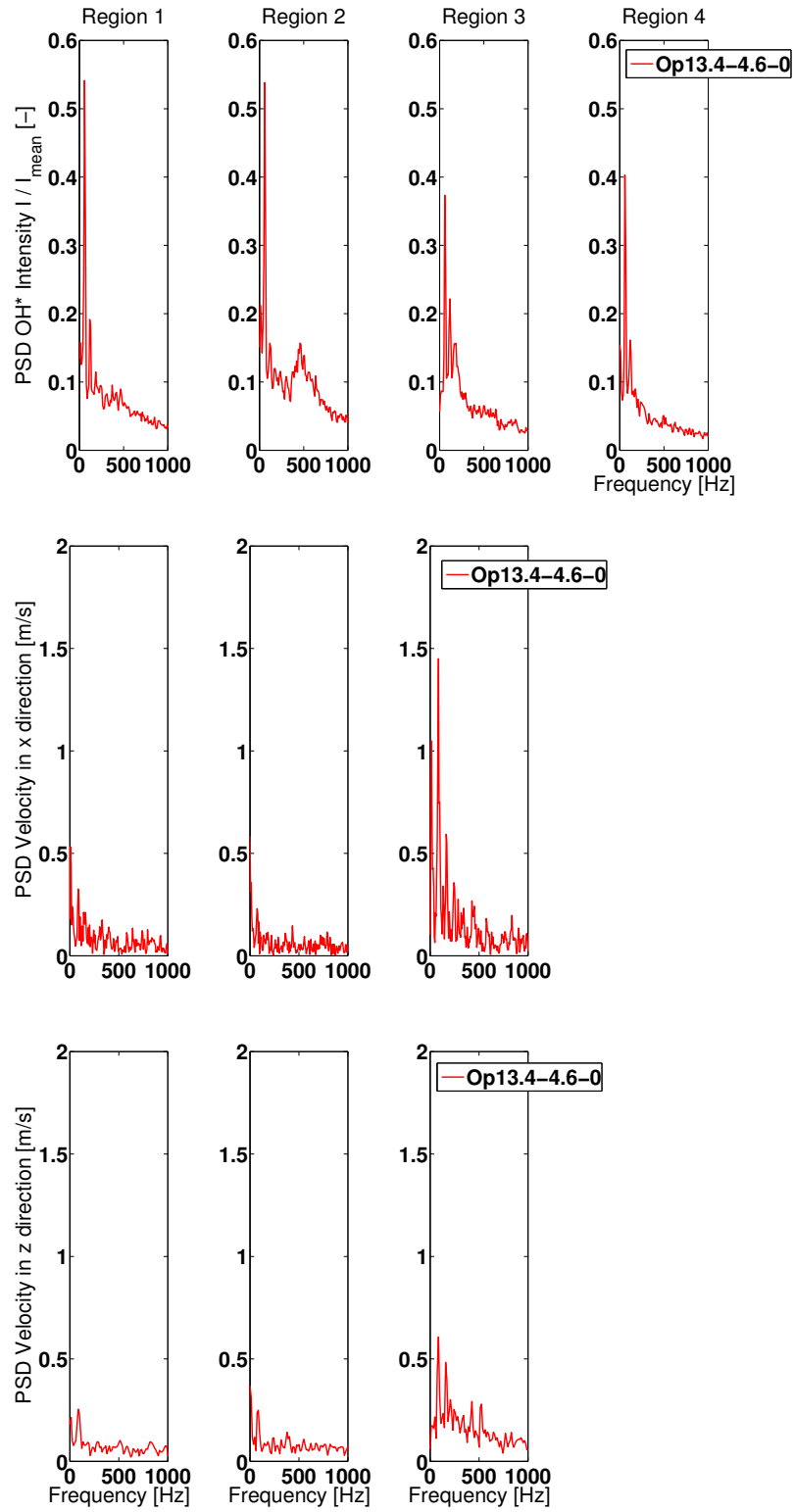


Figure 4.7: PSD of the OH^* and velocity fluctuations in regions 1 to 4 for *Op13.4-4.6-0*

4.3.1 Velocity and OH* fluctuations in the shear layer between high velocity zone and inner recirculation zone

Area 1 is located at the interface between the high speed swirling cone and the inner recirculation zone. The velocity and OH* spectra are shown in the first column in figures 4.6 and 4.7. The PSD amplitudes are very high for the velocity in x direction for **Op16-0-2** and **Op16-2-0**. The spectra of these operating points both feature the 120 Hz peak and its harmonics. The amplitude of these peaks are very close. These peaks are also visible for the OH* chemiluminescence, however their amplitude is limited. **Op13.4-4.6-0** has far weaker amplitudes in the velocity spectra, even in the x direction. However its amplitudes are higher in the OH* spectra, by a factor of 5 compared to the two other operating points. The PSD in z direction is weak for all operating points.

The PSD diagrams give insight about the aerodynamics and the flame dynamics in the combustor. As already suggested in chapter 2, **Op16-0-2** and **Op16-2-0** are dominated by its high velocity swirling cone. In this region the velocity spectra show their highest values. Even more, in the swirling cone, the PSD spectra of the pressure measurements, the velocity field and the OH* visualisation are dominated by the 120 Hz peak and its harmonics. The existence of the same peak for all three diagnostics in the same regions is an indicator of a coupling of acoustics, aerodynamics and heat release. This coupling has been described by [Candel \(2002\)](#) and [Ducruix et al. \(2003\)](#). Furthermore these findings suggest that the pressure fluctuations effectively perturb the flame via the mechanism described in section 4.8.

Similar results seem to be observable for **Op13.4-4.6-0**, however the dynamics in this region is far weaker for this operating point.

Another possible mechanism that can be possibly deduced from these results is the flame-vortex interaction. Already the comparison of the instantaneous streamlines with the RMS OH* field indicates that the vortices propagate downstream in the regions with highest heat release fluctuations, i.e. the flame front. The comparison of the PSD spectra seems to confirm this assumption, since both measurements have the same eigen frequency in the regarded region. However, more information would be needed to draw further conclusions. Examples are information about the phases of the two physical quantities or even instantaneous flame front imaging and velocity measurements. The phases between pressure and OH* were analysed in 7 and the results show that both are in phase, thus fulfilling the Rayleigh criterion for combustion instabilities (?). It would thus be possible that the phase between the different phenomena in the different regions is equally close.

4.3.2 Velocity and OH* fluctuations in the shear layer between high velocity zone and outer recirculation zone

The interface between the high speed swirling cone and the outer recirculation zones is represented by area 2 and the corresponding spectra are shown in the second column of figures 4.6 and 4.7. The velocity spectra show, that the velocity fluctuations are weaker than in in area 1, for all three operating points. The velocity amplitude of the 120 Hz frequency of **Op16-0-2** and **Op16-2-0** is the highest in these spectra. However it is only about a fourth of that in region 1. The peak amplitude of the operating point **Op13.4-4.6-0** is even lower and can be barely distinguished from the white noise. Similarly as in area 1, the transverse velocity fluctuations are negligible. The PSD spectra of the OH* chemiluminescence for region 2 are equally dominated by the low frequency phenomena, with the 120 Hz peaks having the highest amplitudes for **Op16-0-2** and **Op16-2-0**. The OH* spectra of both operating points also feature the harmonics of the 120 Hz peaks. The OH* chemiluminescence amplitude is even higher for a peak around 80 Hz for **Op13.4-4.6-0**. Besides, the spectrum for **Op13.4-4.6-0** possesses a broadband part in the frequencies below 1000 Hz.

In this region, the OH* chemiluminescence is high for the three operating points, however the velocity fluctuations are rather low. This means that the coupling between heat release rate and velocity is probably not that high as in region 1. Nevertheless due to the recirculation in this zone, some interaction between the flame and vortex will probably exist.

4.3.3 Velocity and OH* fluctuations along the combustor axis

The area 3 is located on the symmetry axis of the combustor. Its velocity and OH* spectra are shown in the third column in figure 4.6 and 4.7. The velocity spectra show strong dynamics for all three operating points in x direction, and almost no dynamics in z direction. As in region 1 and 2, the velocity fluctuations of **Op16-0-2** and **Op16-2-0** are dominated by the low frequency around 120 Hz. Its harmonics can also be observed; however they are weak. **Op13.4-4.6-0** has axial dynamics which are in the same order of magnitude and with even slightly higher amplitudes in region 3. Even more, these are the regions, where the amplitude of the velocity PSD is highest for **Op13.4-4.6-0**. This can be seen for the peak around 80 Hz that has an amplitude at least three times as high as for the other observed regions. The dynamics of the OH* spectra of area 3 correspond to those of area 1. **Op16-0-2** and **Op16-2-0** are dominated by the 120 Hz peak and its harmonics. **Op13.4-4.6-0** features equally strong peaks, with that around 80 Hz at its highest value of all the regarded regions.

These results are particularly interesting for the characterization of **Op13.4-4.6-0**. As described in chapter 2, this operating point features a strong central jet, which reduces the overall swirl value and disturbs the rotating motion. The consequence is a strong axial flapping, which can be observed in two aspects: (1) The velocity spectra have their highest value in x-direction on the chamber axis. They are far below in the swirl cones and non-existing in z-direction. (2) The cone angle of **Op13.4-4.6-0** is well below that of the other operating points. This can be possibly linked to the fact that the full swirling motion cannot be established due to the axial flapping and the low swirl value. As in the two other operating points the PSD spectra of pressure, velocity and OH* chemiluminescence feature the same dominating frequency - in particular the peak at about 80 Hz. This leads to the suggestion, that also in this operating point the flame is perturbed by the low frequency pressure fluctuations that are associated with the combustion instability. However the instability is in particular linked to the axial flapping motion.

4.3.4 Velocity and OH* fluctuations in the region where the flame is impacting the chamber walls

Area 4 is located in the regions where the flame collides with the chamber walls. As these regions are outside the field of view of the PCMV measurements, only OH* chemiluminescence is shown. The OH* spectra can be found in figures 4.6 and 4.7 in the first line.

As in the other regarded regions, the OH* chemiluminescence spectra of **Op16-0-2** and **Op16-2-0** have their highest amplitude at 120 Hz and the following ones at a multiple of the main peak. The amplitudes are very high and have similar values to those of region 3. For **Op13.4-4.6-0** the strongest dynamics are located at 80 Hz and have an amplitude below that of the other operating points. Still, the values are high compared to regions 1 to 2, and of the same order of magnitude as in region 3.

To sum up, the areas associated with the wall impinging of the flame feature strong heat release fluctuations at the same frequency as the combustion instability. This observation is made for the three operating points and allows to suggest, that the interaction between the flame and the chamber walls are a contributing driver of the combustion instability.

These results allow to identify the driving mechanism named flame-wall interaction. Here the wall impact of the flame leads to surface fluctuations and thus to fluctuations of the heat release and finally to pressure fluctuations. In this work, this mechanism is put into evidence by regarding the PSD spectra of the heat release rate and the pressure in the regions where the flame is impacting the walls. The results show that for all operating points the main eigen frequencies are equal for both measurements. Moreover, the RMS OH*

chemiluminescence is the highest at the chamber walls and the amplitude of the OH* chemiluminescence PSD is high compared to the other regions. All these observations are an indicator that the pressure fluctuations are partly driven by the flame heat release fluctuations at the chamber walls, which just corresponds to the mentioned mechanism.

4.4 Conclusion

The results allow to put forward the dominance of the low frequency phenomena on the dynamics of the velocity and the local heat release, as well as the pressure. The relevant mechanisms for the combustion instability in this combustor are summarized in figure 4.8. It is limited to the four combustion instability mechanisms that are treated in this chapter and that were described by Ducruix et al. (2006). In the figure the red texts mark the different instability mechanisms. The blue texts show the experimental results that indicate the existence of the corresponding mechanism in the CESAM-HP combustor.

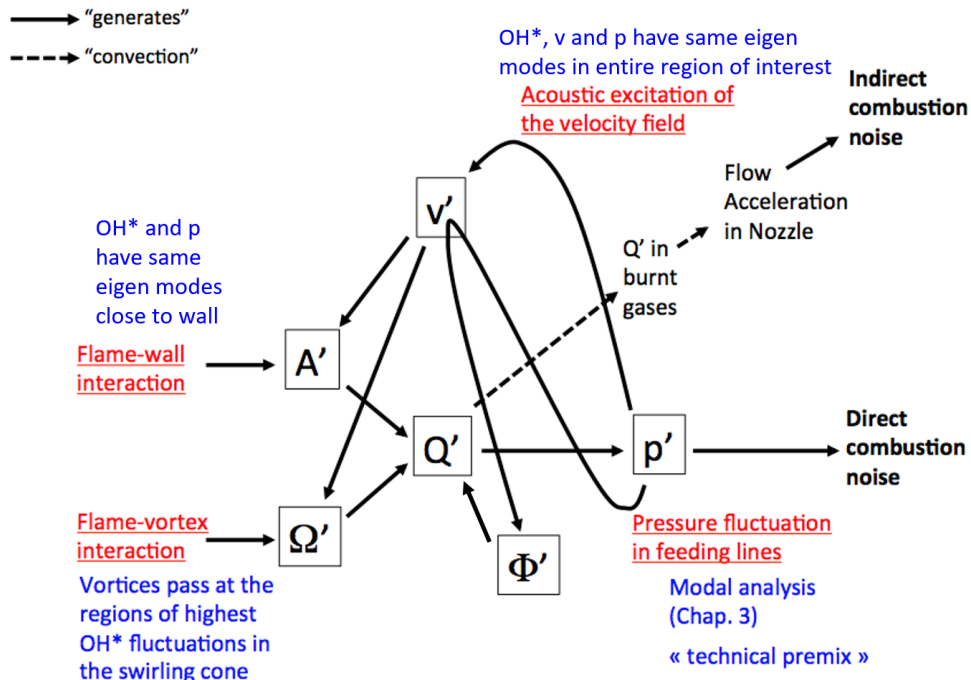


Figure 4.8: Summary of the identified combustion instability mechanisms. The blue text corresponds to the experimental indications that presented in this chapter. p : Pressure, Q : Heat release, v : Velocity, Ω : Vorticity, Φ : Equivalence ratio, A : Flame surface

Similar to what was described in section 4.1, the figure shows two mechanisms that are causing pressure fluctuations and two mechanisms in which these pressure fluctuations interact with other elements of the combustor. Due to the latter two, the schematic becomes a positive feedback circle - similar to what is mentioned in [Candel \(2002\)](#).

The first driving mechanism is the interaction between flame and the wall, which is described in section 4.3.4. The strongest fluctuations of OH* close the chamber walls have the same frequencies as the combustion instability, which is an evidence for his mechanism.

The second observed driving mechanism is the interaction between the flame and the vortices. It is put into evidence by the high fluctuations of OH* and velocity in the shear layer between the high velocity conical region and the central recirculation zone. These fluctuations have the same frequencies and since the regarded region corresponds to the flame front as well as the shear layer, an interaction between the flame and the vortices at instability frequency is probable.

The first coupling mechanism that is regarded is the acoustic excitation of the flame and the entire combustor. As explained by [Ducruix et al. \(2006\)](#), the acoustic fluctuations will act on the velocity fields in the region where the flame is impacting the walls, as well as on the vortices that interact with the flame front. As the strongest pressure fluctuations act at a certain frequency on the different parts of the combustor (the combustion instability frequency), it should be possible to detect this frequency when measuring in different positions of the flame. This is the case in the PSD spectra that are obtained for velocity and OH* in different positions of the flame, which is an indicator for the existence of this coupling mechanism.

The second coupling mechanism is the variations of composition due to the pressure fluctuations. These pressure fluctuations lead to fluctuations of fuel mass flow rate in the fuel mass flow controllers. This mechanism was examined in chapter 3, where a combined experimental and analytical approach could show that the low frequency fluctuations are associated with the feeding lines. It can thus be concluded that this corresponds to the mentioned mechanism.

The schematic drawing in figure 4.8 also suggests, how direct and indirect combustion noise is generated from this combination of different mechanisms. As described in the introduction, direct combustion noise corresponds to the pressure fluctuations that result from the heat release fluctuations of the flame. As the results of this chapter indicate, these pressure fluctuations are finally all related to the four presented instability mechanisms. It can thus be concluded that the combustion instability plays an important role for the combustion noise generation and that it will lead to a high contribution of direct combus-

tion noise.

Figure 4.8 also takes into account the indirect combustion noise generation. It can be seen that the heat release fluctuations are transmitted from the flame to the burnt gases. As the burnt gases are flowing towards the nozzle where they are accelerated, the density fluctuations generate pressure fluctuations. These are called indirect combustion noise. At this point it is not possible to quantify this contribution. Nevertheless, due to the strong combustion instability and the existence of the associated mechanisms, it is clear that direct combustion noise contribution will make up most of total combustion noise. However, since the frequencies are equal, it can also be one of the drivers of indirect combustion noise.

The estimation of combustion noise contributions based on the different instability mechanisms would however be a very crude one. More quantitative methods are presented in the two following chapters: in chapter 7, the direct combustion noise contribution is investigated based on the heat release fluctuations of the flame. Finally in chapter 8, the temperature fluctuations in the burnt gases are determined experimentally by Laser Interferometric Vibrometry (LIV). From these and from the in-chamber pressure fluctuations, the direct and indirect combustion noise contributions are calculated analytically.

Part II

Development of optical diagnostics

Summary

The second part of the thesis is focussing on the work that was done on the development and use of optical diagnostics. These have the potential for a future application in combustion noise studies, however further steps need to be done to carry them to this stage. Two diagnostics are presented here, high speed planar velocimetry at a sampling frequency of up to 100 kHz and focusing Schlieren for the visualization of entropy waves.

Chapter 5 deals with the development of a new planar velocimetry technique, called PCMV (Planar continuous laser based Mie scattering Velocimetry). The technique is based on the use of a continuous wave laser as a light source. In this case the sampling frequency is exclusively determined by the shutter opening and closing times of the applied high speed camera. In this chapter, the PCMV system is described and its validation is attempted experimentally on the CESAM-HP test bench. Latter is done by first observing the instantaneous Mie scattering and velocity fields and then by comparing the mean and rms velocity fields obtained by PCMV with those obtained by a classic low speed PIV system. Finally, different error sources are discussed and further means of validation are proposed.

Chapter 6 describes the application of a focusing Schlieren system on the CESAM-HP combustor. This system is based on the combination of a camera lens with two complementary grids and allows to visualize density fluctuations in a field depths of only a few millimetres. The Schlieren system is used to observe flame front and the density fluctuations in the burnt gases. While the detected frequencies are equal to those found by Laser Interferometric Vibrometry (see chapter 7), further work needs to be done in order to quantify the density fluctuations.

Chapter 5

Development of a high speed planar velocimetry technique

In this chapter the velocity measurements conducted in this thesis are presented. For this, a new high speed planar velocimetry technique was developed, which allows to capture velocity fluctuations at very high sampling frequencies. The technique is based on the use of a continuous wave laser, which illuminates the particles that are supposed to move along the flow they are seeded in. The Mie scattering images are acquired at very high frequencies with a high-speed camera. The velocity fields are obtained by applying classical PIV algorithms on successive images. The properties of the system are described and discussed and a validation is attempted in two steps. First, the instantaneous velocity fields obtained on the CESAM-HP combustor are studied. They capture the flame topology correctly, with the high speed regions of conical shape and the low speed recirculation zones. Afterwards, the new velocimetry technique is compared with a classical low speed PIV system. This is done by conducting experiments with both systems on the CESAM-HP test bench and by comparing the mean and RMS of the obtained velocity fields. The results show a non-negligible error between the two techniques. Finally, the reasons for this error are discussed and improvements are proposed. Nevertheless, since the flame topology is captured correctly, this technique is interesting to study the velocity fluctuations of the CESAM-HP combustor.

5.1 Introduction

Particle Image Velocimetry (PIV) is today one of the standard measurement techniques for measuring velocity fields in reacting and non-reacting flows ([Adrian \(1991\)](#); [Adrian \(2005\)](#)). It has the advantage of being non-intrusive and of measuring velocities in two or nowadays even three dimensions. In this thesis, PIV

is used with two aims. The first aim is to determine the mean and RMS velocity fields of the CESAM-HP test bench. These fields allow to obtain first insights about the flow field geometries, such as the swirl cone angle. The RMS velocity fields also allow to determine the areas with the highest aerodynamic activity in the burner. The analysis of the mean and RMS velocity fields have been presented and described in chapter 2. The second application of PIV was shown in chapter 4 and concerns the study of the main combustion instabilities in the CESAM-HP test bench. This was done by putting forward the coupling between velocity fluctuations, pressure fluctuations and the fluctuations in local heat release in various locations in the combustor. For this purpose the spectra of these measurements were compared especially in regions where all three phenomena were measured.

In PIV, particles are seeded into the flow and are supposed to move along with it. The particles are illuminated by a laser sheet and scatter the light. The illumination is of very short duration (a few nanoseconds) and is hence called laser pulse. In classical PIV two pulsed lasers are used to illuminate the seeded flow with a time span of a few microseconds in between. The Mie scattering is captured by a camera with a pair of images corresponding to two successive pulses. The studied region is separated into a grid of smaller windows and a cross correlation algorithm is used to determine the displacement of each window during the time span between two laser pulses.

The sampling frequency of a PIV system is determined by the time span between two pairs of images and has increased over the years, allowing researchers to extend the application fields of PIV. Three application fields can be identified for PIV. (1) For a determination of the mean and RMS velocity fields, a PIV system of a low sampling frequency is sufficient. The high laser power levels allow for a large region of interest and the low sampling frequency leads to a higher statistical quality due to the long duration of acquisition. (2) In experiments with turbulent flames in a confined space and with swirling motions, acoustic phenomena and instabilities can be observed at frequencies of typically up to 1 kHz (Candel (2002); Candel et al. (2014)). The consequent pressure fluctuations in the combustor lead to velocity fluctuations at the same frequencies. In order to capture these velocity oscillations, an even higher acquisition frequency is required. In order to fulfil the Nyquist-Shannon theorem, at least 2 kHz are needed, and for a characterisation of higher quality, even 10 kHz are preferable. Today's high speed PIV systems are able to achieve these frequencies. (3) The third application is the following of turbulent structures, such as wakes in the flow. These require higher sampling frequencies as will be demonstrated now. In the example of a turbulent flame with a high swirl value, such as in a gas turbine combustor, tangential velocities can reach the same orders of magnitude as longitudinal ones. (Candel et al. (2014)). When assuming a swirling combustion with 40 m/s longitudinal and transverse veloc-

ity and a laser sheet of 20 mm width and 0.4 mm thickness, a particle would need 500 μs to cross the laser sheet longitudinally. For Nyquist-Shannon's theorem one would need 4 kHz to capture this particle and 20 kHz for a high quality characterization. These frequencies already exist in actual high speed PIV systems. However, due to the high transverse velocity, it would take the particle only 10 μs to cross this laser sheet transversally. If now a wake of 5 mm diameter is considered to propagate in transverse direction at the same velocity of 40 m/s, it would need 125 μs to cross the laser sheet. Consequently it can only be captured at a sampling frequency of 16 kHz for Nyquist-Shannon and between 40 and 80 kHz for a high quality acquisition.

Current high speed PIV systems at sampling frequencies up to 20 kHz attain their limits when turbulent structures of high speed swirling flames need to be followed. Only recently, sampling frequencies of 100 kHz were reached by using PIV based on pulse-burst lasers, however this technique is very costly and requires special treatment (Miller et al. (2016)). This work has the aim to narrow this gap by presenting and validating a novel velocimetry technique which can reach frequencies up to 100 kHz in an economic and ergonomic way. To do so, a continuous wave laser is used as the light source and the image pairs are obtained with the opening and closing of the shutter of a high speed camera. The time resolved velocities are then determined with the same cross-correlation algorithms that are used for PIV. This approach has been used very recently for high-speed measurements in non-reacting environments (Willert (2015)) with a very small region of interest. However due to the relatively low power of the continuous wave laser, no attempt was made yet to use this kind of laser for velocity measurements on laboratory scale combustors. Such an attempt is made here. The results of this study were already presented during the Gordon Research Conference 2015 (Mazur et al. (2015)) and are detailed further in this chapter.

5.2 Presentation of the new velocimetry technique

The functioning of this new technique, named PCMV (Planar Continuous laser-based Mie scattering Velocimetry) in the following, is shown in figure 5.1. As described before, the PCMV system is characterized by the use of a continuous wave laser. The laser energy is hence constant over the time. Consequently, the PIV measurement is influenced by four timing parameters of the high speed camera, which are shown in the figure.

- The time δt is the time span between each image acquisition made by the high speed camera. It directly corresponds to the sampling frequency of the camera.

- The time t_0 corresponds to the shutter opening time per image acquisition. It influences the image quality. While a high t_0 leads to higher image intensities due to a longer time of illumination, the image becomes less sharp. This is due to the fact, that the particles are moving at a certain velocity. At high velocities and high t_0 the particles are captured as "traces" rather than "dots". This effect is also called smearing in literature (Tropea et al. (2007)). For example, at maximum velocities of 40 m/s, at a spatial resolution of 10 px/mm and at a δt of 10 μs (which corresponds to a sampling frequency of 100 kHz), this would lead to a trace length of around 4 pixels. Taking into account that at these configurations these traces would have a thickness of 1 to 2 pixels, the smearing effect is not negligible.
- dt is the time between the images chosen to perform the PIV algorithm. It is thus the time between two images that make up an "image pair". The time has an influence on the image displacement and is chosen according to the 25 % rule for PIV. This classical rule says that the highest particle displacements should not exceed 25 % of the chosen PIV window size. (Keane and Adrian (1990))
- The time Δt corresponds to the time between two image pairs. It determines the actual sampling frequency of the HSPIV system $F_s = 1/\Delta t$.

These four parameters can be chosen accordingly to the optical system and to the studied application.

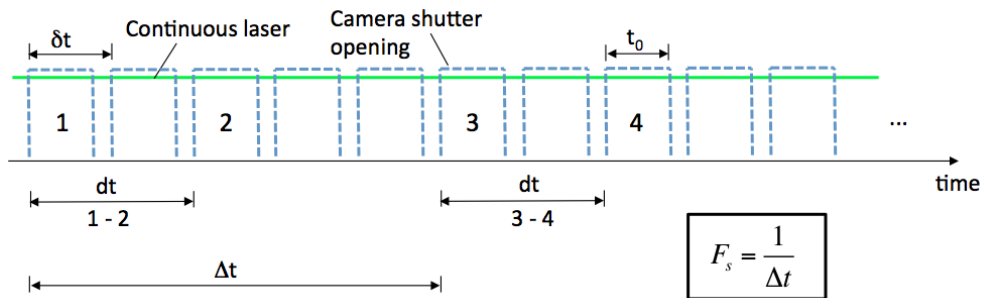


Figure 5.1: Description of PCMV with continuous laser source and the different timing parameters of the technique

It has been chosen to rename the technique due to its fundamental differences to PIV. Because of the long exposure duration, which is necessary due to the relatively low laser power, the particles are captured as "traces" rather than "dots", as shown in figure 5.2. This has important effects on the technique. While the cross-correlation algorithm does not differentiate between dot or trace and cal-

culates for both the most probable displacement, the particle images of PIV and PCMV are physically not the same. In PIV the exposure duration is very short and the Mie scattering images thus show the instantaneous position of the particles. In PCMV on the other hand, the exposure duration is longer and the Mie scattering images represent the path that the particle passed during this time. Therefore, when the cross-correlation algorithm calculates the displacement between a time span, it calculates the displacement of these two particle paths, or differently spoken, of the mean position of the particles in this path.

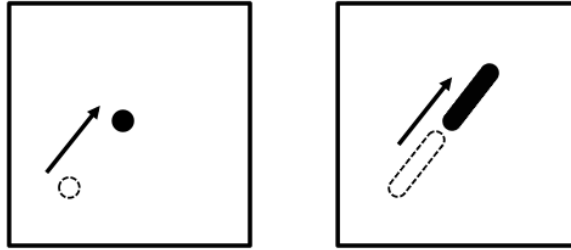


Figure 5.2: *Left: Displacement of a particle that is captured as a dot by classic PIV. Right: Displacement of a particle that is captured as a trace by PCMV*

The fundamental differences between PCMV and PIV can be also demonstrated mathematically. For this, it is compared, how the instantaneous velocity between two successive windows is calculated for both techniques when using classical cross-correlation algorithms on the acquired images. Figure 5.3 shows the different time steps that are important for this demonstration:

- $t_{1,1}$ is the starting time of the camera shutter opening of the first image for PCMV. It also corresponds to the timing of the first laser pulse for PIV. Since the pulse duration is only of a few ns, the pulse is assumed to be a Dirac.
- $t_{1,2}$ is the ending time of the camera shutter opening of the first image for PCMV.
- $t_{2,1}$ is the starting time of the camera shutter opening of the second image for PCMV and the timing of the second laser pulse for PIV.
- $t_{2,2}$ is the ending time of the camera shutter opening of the second image for PCMV.

In this demonstration, only the displacement U in x-direction is regarded, since the demonstration for the z direction is done analogously.

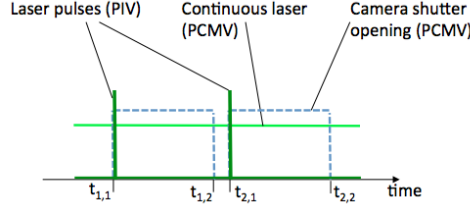


Figure 5.3: Different time steps that are relevant for PIV and PCMV

For PIV, the instantaneous velocity between two images corresponds to the displacement of the particle divided by the time between the two pulses:

$$U_{PIV} = \frac{x(t_{2,1}) - x(t_{1,1})}{t_{2,1} - t_{1,1}} \quad (5.1)$$

The velocity calculation for PCMV is more complicated since here, the displacement of two trajectories is calculated. The velocity corresponds to the difference of the x-positions of the mean point of the trajectories, divided by the time span of the moments where the camera shutter is opening:

$$U_{PCMV} = \frac{(x(t_{2,1}) + \frac{1}{2} \int_{t_{2,1}}^{t_{2,2}} u(t) dt) - (x(t_{1,1}) + \frac{1}{2} \int_{t_{1,1}}^{t_{1,2}} u(t) dt)}{t_{2,1} - t_{1,1}} \quad (5.2)$$

When subtracting Eq. (5.1) from Eq. (5.2), one obtains the difference between the instantaneous velocity that is obtained by the two techniques:

$$U_{PCMV} - U_{PIV} = \frac{\frac{1}{2} \int_{t_{2,1}}^{t_{2,2}} u(t) dt - \int_{t_{1,1}}^{t_{1,2}} u(t) dt}{t_{2,1} - t_{1,1}} \quad (5.3)$$

The difference between the velocity obtained by PIV and by PCMV thus in theory is due to the integrating effect of the long exposure duration. However, in classical velocimetry measurements in fluid mechanics, the time between two images is very short, of the order of 10 μs . If it is assumed, that the velocity $u(t) = u$ is constant in such a short time span, Eq. (5.2) is simplified to:

$$U_{PCMV} - U_{PIV} = \frac{1}{2} u \frac{(t_{2,2} - t_{2,1}) - (t_{1,2} - t_{1,1})}{t_{2,1} - t_{1,1}} \quad (5.4)$$

Since the shutter opening time stays equal during image acquisition, $t_{2,2} - t_{2,1}$ is equal to $t_{1,2} - t_{1,1}$ and the difference between U_{PCMV} and U_{PIV} becomes zero. The technique is thus used under the hypothesis that the velocity is constant between two time steps.

The hypothesis can be validated by calculating Eq. (5.4) for an example. For this a velocity oscillation between -40 m/s and +40 m/s at a frequency of 2.5 kHz is supposed. At this frequency the velocity needs 0.0002 s to change from its smallest to its highest value. If assuming that the velocity increases linearly, this corresponds to an acceleration of $a = 800000m/s^2$. This acceleration is used in $u = a \cdot t$ in Eq. (5.4). When calculating this equation, the resulting difference between the velocity measured by PIV and by PCMV would be resolved to $1.8 \cdot 10^{-5}$ m/s, which is a very small value. This difference is therefore negligible.

The application of this PCMV technique has been enabled due to advances in laser technology. These have increased the stability and intensity of the laser system. However, in order to reach image intensities close to those of pulsed systems, t_0 is chosen at the biggest value that is permitted by the camera system at the chosen sampling frequency. In this work, t_0 has a value of 9 μs at a δt of 10 μs (The resulting 1 μs closing time corresponds to the minimal shutter closing time of the used camera). This long exposure time does not fix the particle position, but classical PIV algorithms can still be applied on the images, since the cross correlation can be calculated independently from the shape of the captured particles.

The image intensity of the present PCMV system is compared with that with existing PIV systems from literature with different arrangements as shown in table 5.1. The aim is to show that at the chosen parameters, the PCMV technique can reach intensities that are close to existing PIV systems. These studied systems are two HSPIV (High speed PIV) techniques with a pulsed laser source (Providakis et al. (2013); Boxx et al. (2009)), one classic low speed PIV (PIV) technique (Letty et al. (2013)), and one HSPIV technique with continuous laser source but a non-reacting flow (Willert (2015)). The comparison is conducted by calculating a normalized laser intensity I_{norm} , since the laser sheets have different dimensions in the different works. I_{norm} is expressed by the following equation, which takes into account the laser energy and the laser sheet dimensions:

$$I_{norm} \propto \frac{E_{per-image}}{wt} \quad (5.5)$$

$E_{per-image}$ is the laser energy per image. In a pulsed laser it corresponds directly to the laser pulse energy. In a continuous wave laser it is the product of the constant laser power and the camera shutter opening duration. The variables w and t stand respectively for the laser sheet width and the laser sheet thickness. The comparison between the different PIV systems (table 5.1) shows that while the normalized intensity of the present PCMV is below that of a classic PIV, it attains the levels of other HSPIV techniques from literature,

where velocity measurements were conducted successfully. This is due to three factors: (1) As explained before, continuous laser sources have become more performing over the years. (2) The shutter opening time has been chosen as long as possible. (3) The laser sheet dimensions were chosen smaller than in the other arrangements. While this reduces the region of interest which can be studied, it remains sufficient for the compact structure of the flame in this work.

Work	Present	1	2	3	4
Type	c	p	p	c	p
F_s [kHz]	100	5	1.4	20	LS
$E_{per-image}$ [mJ]	0.18	5	0.4	0.05	120
w [mm]	20	80	32	7.2	80
t [mm]	0.4	1	0.5	0.2	0.5
I_{norm} [$\mu\text{J}/\text{mm}^2$]	22.5	62.5	25.0	34.7	3000

Table 5.1: Comparison of the present laser system with existing systems from literature. *c*: Continuous laser source, *p*: Pulsed laser source, *LS*: low speed, F_s : Sampling frequency, $E_{per-image}$: Energy per image, t_{laser} : Laser opening duration per image, *w*: Laser sheet width, *t*: Laser sheet thickness, I_{norm} : Normalized Intensity. 1: [Providakis et al. \(2013\)](#). 2: [Boxx et al. \(2009\)](#). 3: [Willert \(2015\)](#). 4: [Letty et al. \(2013\)](#).

Apart from the increased sampling frequency, the proposed PCMV technique has other advantages. The system is easier to handle than traditional two-shot systems as the laser intensity is kept constant over the time. Hence the problems of aligning two laser sources and of synchronizing them with each other and the camera do not exist. Equally the problem with intensity differences between the two sources is solved. Besides, the high sampling frequency allows to acquire large quantity of data in a very short time. While this can create issues in terms of statistic quality, it is advantageous in highly confined systems, where particle deposition on the windows degrades the image quality considerably already after a few seconds.

However, as explained in the previous sections, the PCMV system is obtaining the velocity from images where the particles are smeared. Differently spoken, PCMV is physically not the same as PIV. Therefore it needs to be verified, whether the velocities obtained with PCMV are correct. This verification is conducted in the following section.

5.3 Experimental procedure for validation

As explained in the previous sections, the PCMV system is characterized by smeared particles due to the long exposure time per shot. It must be therefore verified, whether the velocities obtained by PCMV are quantitatively correct .

The most evident way would be to conduct instantaneous and synchronous velocity measurements with a PCMV and a PIV system and to compare the obtained velocities. However these measurements are not available. Therefore the approach presented in the following has been chosen.

Two steps are conducted. In a first step, the instantaneous velocities are measured by the presented PCMV, and the topology of the velocity field is investigated. Secondly, the mean and RMS velocity fields determined by PCMV are compared to those obtained by a classic PIV system on the CESAM-HP test bench.

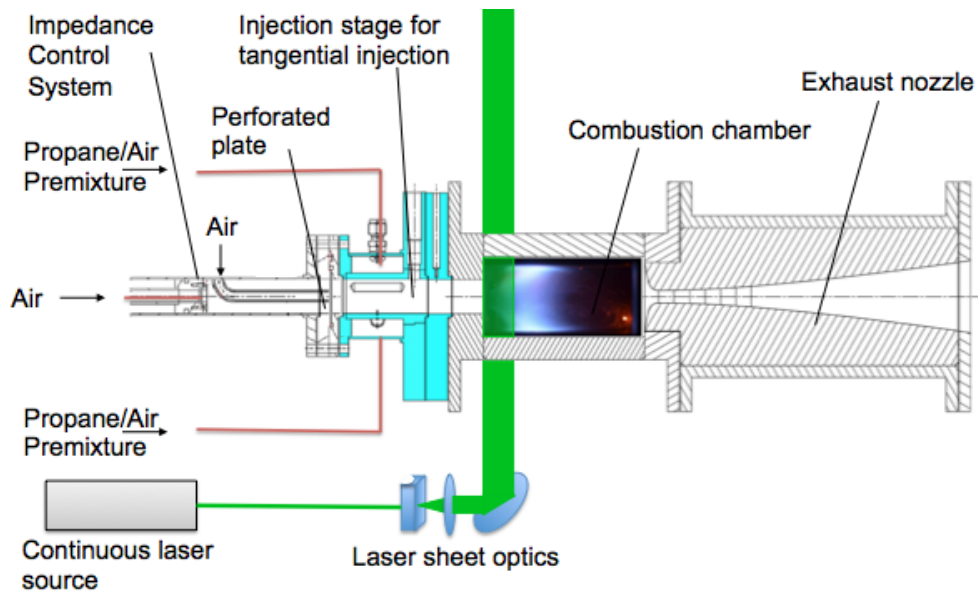


Figure 5.4: Schematic drawing of the CESAM-HP combustor also showing the position of the PIV laser sheet

The PCMV/PIV is installed at the entry of the combustion chamber of the CESAM-HP test bench, as displayed in figure 5.4. The properties of the test bench were described in the previous chapters. The validation is conducted on the operating point **Op16-0-2**.

The used laser system for PCMV is a COHERENT Verdi G20 continuous wave Nd:Yag laser with a maximal light power of 20 W and a wave length of 532 nm. The high speed camera is a Photron FASTCAM SA-X2 with a maximal resolution of 1024×1024 pixels. During acquisition at 100 kHz the camera resolution is reduced to 256×440 pixels. At the used arrangement this leads to a spatial resolution of 9.3 pixels/mm. The laser sheet width is 20 mm and its thickness

is 0.4 mm at its focal line, both measured with photographic paper. The flow is seeded with ZrO₂ particles of 1 μm size and a seeder of cyclone type (Melling (1997)). The properties of the PCMV system are summarized in table 5.1

In this arrangement no intensifier is mounted because it would increase image noise. This noise would be perceived as white dots on the images. It would thus be interpreted as particles by the cross correlation algorithm and increase the error of the determined displacements.

The following timing parameters were chosen for the PCMV system:

- $\delta t = 10\mu\text{s}$, hence a camera acquisition rate of 100 kHz,
- $t_0 = 9\mu\text{s}$, thus the maximal shutter opening time,
- $dt = 10\mu\text{s}$ in order to capture high flow velocities and
- $\Delta t = 10\mu\text{s}$, which results in a PIV sampling frequency of 100 kHz.

The acquisitions are taken during 200 ms, hence 20000 samples are obtained.

The PIV system consists of a CONTINUUM Surelite Nd:Yag laser, with a power of 100 mJ per shot, a pulse duration of 8 ns and a sampling frequency of 10 Hz. The timespan between two shots is 10 μs , thus equal to that of the PCMV system. The laser sheet dimensions are equal to those of the PCMV system, as the lens and mirror arrangement was kept for both experiments. The used camera is of type Dantec Flowsense with a resolution of 1600x1200 pixels. The system has a spatial resolution of 14.1 px/mm. The PIV tests were performed with 1600 image pairs, hence during 160 s.

The images of each image pair are split spatially with a chosen interrogation window size W_s . It has been chosen 16x16 pixels for PCMV and 32x32 pixels for PIV due to the spatial resolutions of the respective cameras. The windows are chosen with 40 % overlap in order to increase the spatial resolution of the velocity fields. Then a cross-correlation map is calculated for each interrogation window with the following equation, based on previous work (Taylor et al. (2010)):

$$\Phi = FFT^{-1}(FFT(I_a^*) * FFT(I_b^*)) \quad (5.6)$$

with $I_i^* = I_i - \bar{I}_i$ the intensities of the interrogation window I_i minus their spatial mean value \bar{I}_i . The index i is chosen as a for the image at a time t and b at a time $t + dt$. This equation is a simplified form of the classical cross correlation equation (presented in Theunissen (2013)), which allows for a simpler application and lower computation durations. Due to these advantages it

is commonly used in open-source (Taylor et al. (2010)) and commercial PIV (Dantec DynamicStudio) software. The resulting cross-correlation map indicates the probability of different displacements from $-W_s$ to $+W_s$ in x and z directions. Its highest peak thus shows the most probable displacement in both directions.

The displacement determined with this equation is in the precision of one pixel. As this is a very crude estimation, the peak position is determined by a subpixel interpolation. This is achieved by assuming the cross-correlation peak to be gaussian. It is then compared with its surrounding, which allows obtain a displacement below the pixel scale. The used equation is the following, in this case for the x displacement (Theunissen (2013); Taylor et al. (2010)):

$$\delta x = \frac{0.5(\log\Phi_{m_p-l,n_p} - \log\Phi_{m_p+l,n_p})}{\log\Phi_{m_p-l,n_p} - 2\log\Phi_{m_p,n_p} + \log\Phi_{m_p+l,n_p}} \quad (5.7)$$

with $\Phi_{m_p+i,n_p} = \Phi(m_p + i, n_p)$.

As a final step, false vectors are detected and removed. For this the peak ratio is calculated, i.e. the ratio of the main peak and the second peak in the cross-correlation map. It is typically chosen to be at least 1.2. Peaks with a lower peak ratio are systematically refused and the velocity is chosen to be zero in this field. Finally, excessively high velocities which differ extremely from their neighbours and have unrealistically high values are also removed.

The comparison of the two velocimetry techniques is accompanied with an error estimation. The aim is to determine error bars in order to visualize possible deviations from the found results. Previous works (Xue et al. (2013); Xue et al. (2014)) have shown that the displacement error has two sources: (1) The signal to noise ratio (SNR) and (2) the existence of false vectors. As false vectors were removed in the first place, the second term is estimated zero. For this simplified case the size of the error bar depends only on the signal to noise ratio of the correlation map. The exact value would be very difficult to obtain. Charonko and Vlachos (2013) also suggest to estimate the error using the simple function $1/SNR$. Even though this is a crude estimate, it is shown in Charonko and Vlachos (2013) that it gives fair trends. This choice makes it easy to compare the error associated with the different methods and test cases. The signal to noise ratio itself is determined for each interrogation window by dividing the value of the cross correlation peak by the mean of the remaining values of the cross-correlation map.

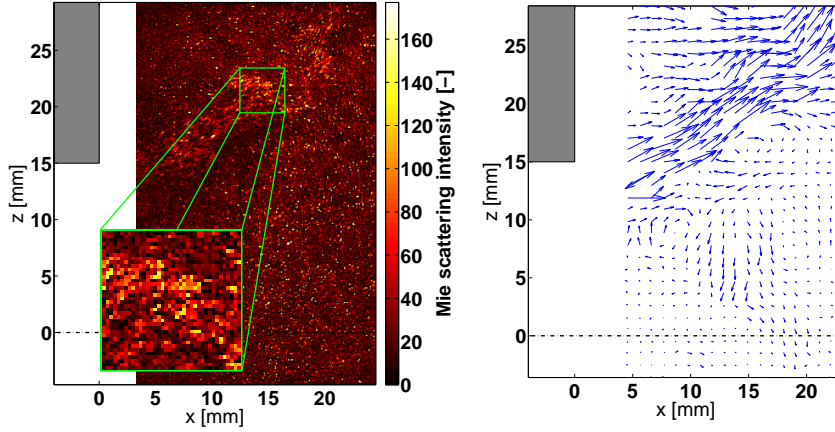


Figure 5.5: *Left: Example of the instantaneous Mie scattering at the studied operating point. The images are taken at 8 bits and the maximum intensity is thus 255. Right: Example of the instantaneous velocity vectors of the studied operating point at the same time step.*

5.4 Results

In a first step, the instantaneous velocity obtained by PCMV is examined. This is done by observing the Mie scattering images that are acquired with the high speed camera as well as the velocity fields that are calculated from these Mie scattering images.

Figure 5.5 shows an example of an instantaneous field of Mie scattering and the corresponding velocity vectors obtained by the correlation algorithm presented in section 5.3. In the Mie-scattering image, a high particle density can be observed along a line that corresponds to the high velocity region in the vector field of the same figure. As described in section 5.2, the particles are smeared and represented as traces in the image. These traces have a thickness up to 2 pixels and a length up to several pixels due to their high velocity and the long exposure time. In the other regions, this smearing cannot be observed. Here the particles are represented as dots of up to 2 pixels diameter. This is probably due to the difference in density between fresh and burnt gases and is explained in previous works (Picano et al. (2011)).

The particle density is considerably lower in this region. As described by Melling (1997), this is probably due to the increased centrifugal forces in the high velocity part. These draw the particles out of the central recirculation zone towards the high velocity regions.

Figure 5.5 also shows the instantaneous velocity field that is calculated from the presented Mie scattering image and that in the following time step. It can

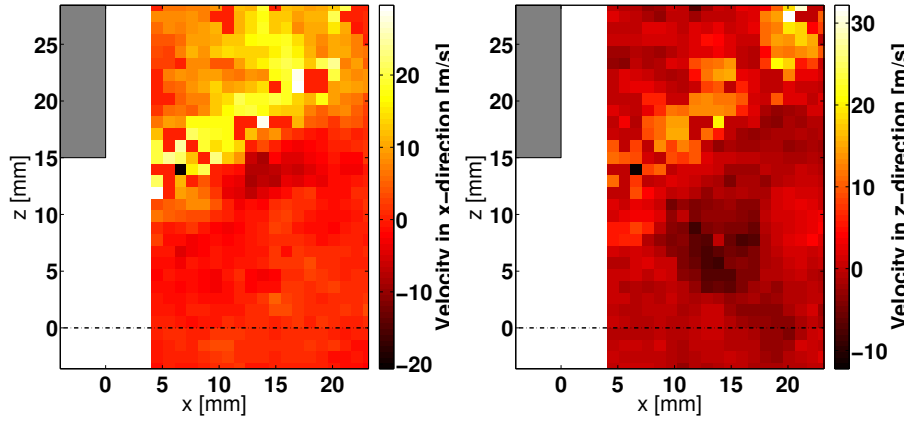


Figure 5.6: Example of the instantaneous velocity field in x -direction and z -direction for the studied operating point

be seen that the quantity of false vectors is low (as a reminder, the refused false vectors are set to zero), nevertheless a few outliers can still be observed, since vector corrections are limited to a minimum (no filtering etc.). However their quantity is sufficiently low so that their influence is supposed to be negligible. The velocity field has features, that are typical for a swirled premixed flame (Providakis et al. (2013); Candel et al. (2014)). It has a high velocity region of conical shape and recirculation zones at the chamber axis and outside the swirling cone. The regions between the high and low velocity zones feature vortices that are a transition between these zones.

Quantitative results of the same instantaneous velocity field are shown in figure 5.6. The figure contains the mean velocity in x and z direction. The velocities in the swirling cone reach values up to 30 m/s in x and up to 15 m/s in z direction. In the low velocity recirculation zones; the velocities stay well below 10 m/s in x and in z directions. Taking into account that for the studied operating point the bulk velocity (calculated by $\dot{m} = \rho Av$) is around 20 m/s, these values seem realistic and not excessively low or high.

In a second step the statistic quality of PCMV is verified by comparing its results with those obtained by PIV. The velocity fields of the two techniques are compared quantitatively by tracing velocity profiles at three axial positions.

The mean and RMS velocity profiles at different x -positions are shown in figures 5.7 to 5.10. These figures show reasonable agreement between the two techniques in terms of flow topology. As with the instantaneous velocity field,

the mean and RMS fields show features that are typical for a swirling flame. Furthermore, the z position of the region with the highest mean or RMS velocities is equal for all profiles. This means that the cone angle is represented correctly. Discrepancies are found in the values of the velocities. In low velocity regions this error accounts for up to 1 m/s. While in terms of percentage this is a high value (up to 50 %), in terms of pixel displacement error it is low with an error of below 0.2 px. The error in the high speed regions is slightly higher but results in lower error percentages up to 20 %.

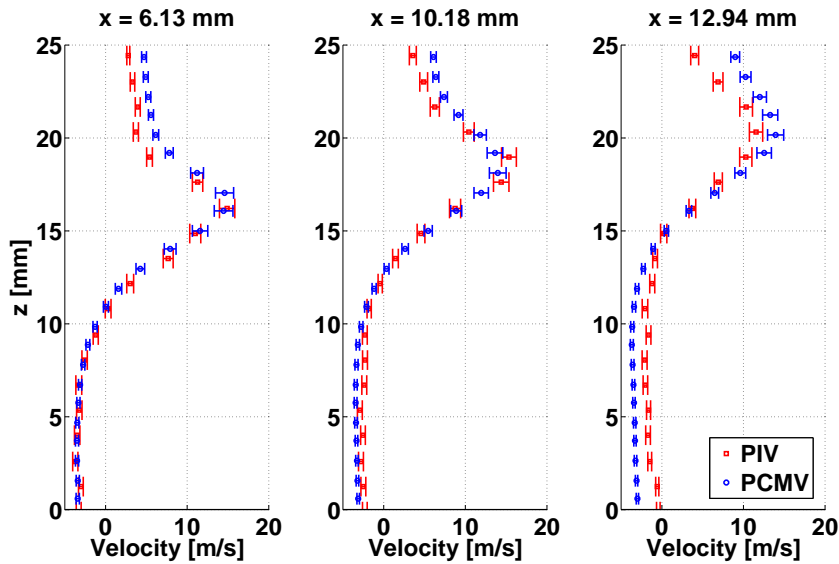


Figure 5.7: Mean velocity profiles in x direction for different axial positions for PCMV and PIV

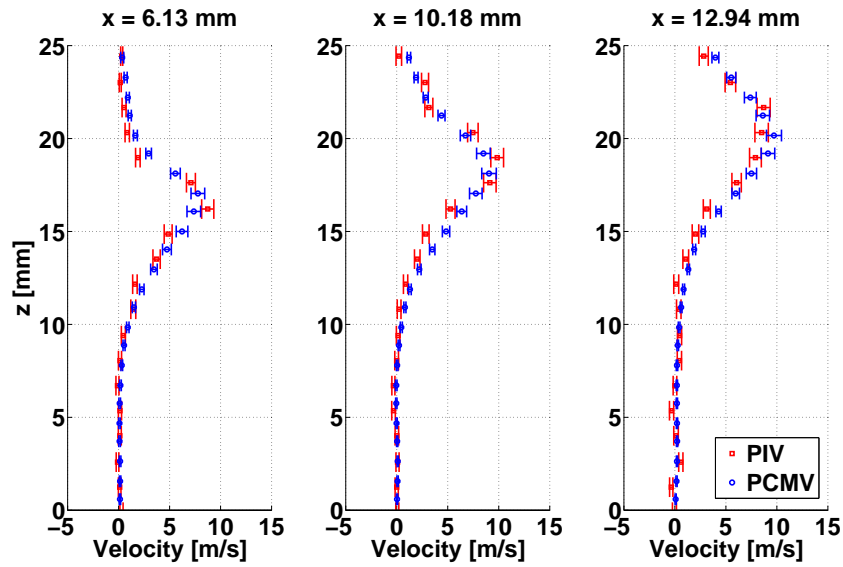


Figure 5.8: Mean velocity profiles in z direction for different axial positions for PCMV and PIV

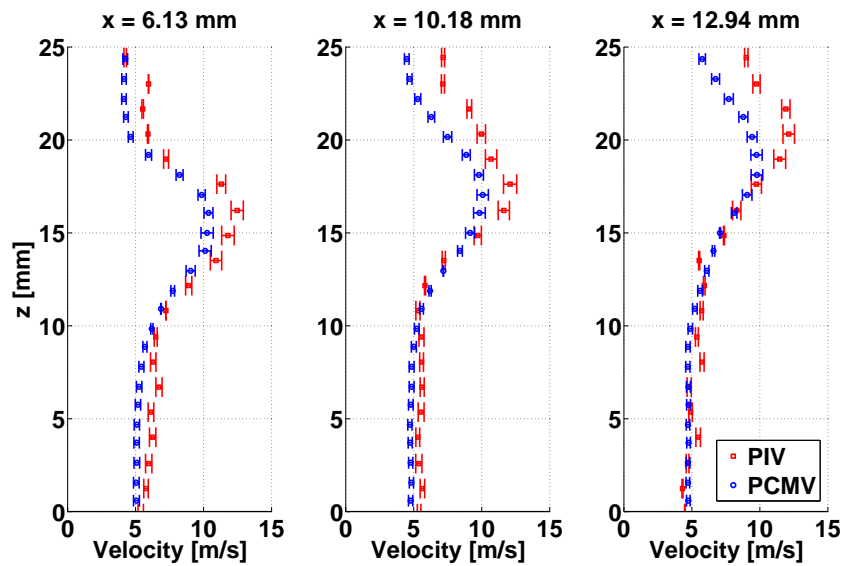


Figure 5.9: RMS velocity profiles in x direction for different axial positions for PCMV and PIV

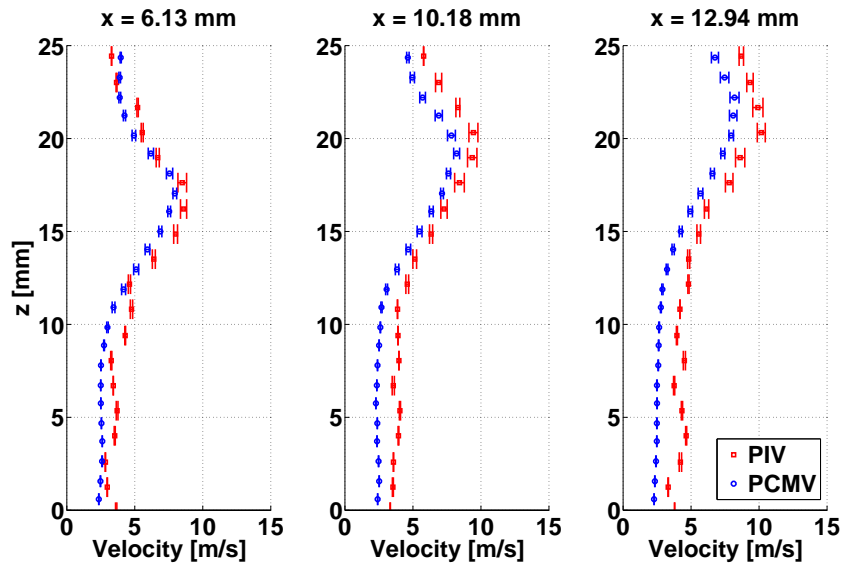


Figure 5.10: *RMS velocity profiles in z direction for different axial positions for PCMV and PIV*

The results show that the proposed PCMV technique globally characterizes the flow correctly in this test bench. Nevertheless, the error is non-negligible. The discrepancies can be due to a variety of reasons, that are discussed in the following paragraphs

A possible error source is the long exposition duration that is necessary for PCMV. As discussed in section 5.2, this means that PCMV and PIV are determining the velocities from images that represent physically not exactly the same phenomena. In PIV the exposure duration is very short and the Mie scattering images thus show the instantaneous position of the particles. In PCMV on the other hand, the exposure duration is longer and the Mie scattering images represent the path that the particle passed during this time. Therefore, when the cross-correlation algorithm calculates the displacement between a time span, it calculates the displacement of these two particle paths. The problem is the fact, that during this long exposure durations particles have the time to leave the image plane, or other ones have the time to enter it. This is especially an issue for swirling flows with a high tangential velocity component. A third point is the possibility that particle trajectories can be divided when the region of interest is separated into interrogation windows. In this case the mean position of the "shortened" trace is not estimated perfectly correctly. Mazur et al. (2017) have however found by numerical simulation that this contribution is rather weak.

Other possible errors could exist due to alignment: The laser systems of the two

techniques might not be aligned perfectly equally. Even more the two lasers of the PIV might have differences in alignment and laser shot intensity.

Due to the high sampling frequency of PCMV and the limited camera memory, the acquisition duration is very short, in this case only 200 ms, which can have an influence on statistics. In the velocity fields presented here the PCMV mean and rms velocities converge at less than 10000 time steps. The chosen 20000 time steps thus lead to well converged mean and RMS velocity fields. Another consequence is the fact that very slow phenomena are difficult to capture as they occur only a few times during this short acquisition duration.

Due to the low sampling frequency of PIV, the acquisition duration is much longer. However, as particles rapidly deposit on the chamber windows (after a few seconds), the image quality is strongly degraded. As mentioned before, this issue is due to the strong confinement of the chamber.

Another aspect is that the applied cross-correlation algorithm is very basic. No advanced algorithms were used, such as window refinement and deformation or adaptive window size. Equally, no filters were applied. This choice was made in order to keep the comparison close to the level of the raw images. Each additional algorithm would add other uncertainties. On the other hand however their use could possibly improve the quality of the calculated velocities.

Due to their scope these issues are not treated and the comparison is limited to this basic statistic study. However, the results are already close and sufficient for the applications in this thesis. PCMV is used here for two purposes:

As a first point, the planar velocity measurements are used to obtain the statistic aerodynamic behaviour, thus the mean and RMS velocity fields of the combustor (cf. chapter 2). These have the aim to identify the mean topology of the velocity field and to identify the regions with the strongest velocity fluctuations.

The second application is the local determination of the main velocity fluctuation frequencies. This application depends on a correct determination of the instantaneous velocity field, which is difficult to validate. However, chapter 4 shows that the main frequencies in the velocity fields determined by PCMV correspond to the frequencies obtained by pressure and OH* chemiluminescence measurements. This leads to the conclusion that the present PCMV technique is able to capture the same dynamics as the two other diagnostics.

While for both applications it is important that the diagnostic correctly captures the topology of the flow fields, some error in terms of absolute numbers is acceptable. Therefore the technique is adequate for a use in this work.

5.5 Conclusion

In this chapter, a novel planar velocimetry technique is proposed. It is named PCMV (Planar Continuous laser-based Mie scattering Velocimetry) and characterized by the use of a continuous laser source and a high speed camera. This arrangement can attain sampling frequencies up to 100 kHz.

Besides the high sampling frequency, the PCMV technique offers the advantage of a simpler and less costly arrangement. Also due to the short acquisition duration, image quality degradation due to particle deposition on windows is not an issue here.

The PCMV technique is validated in two steps. First, the topology of the instantaneous flow fields is regarded. They feature a high velocity region of conical shape and recirculation zones next to it. This topology corresponds to that found in literature for similar flames. This leads to the assumption that the main features are captured by the PCMV technique. Second, the results of the PCMV measurements are compared with those obtained from a classical PIV technique. To do so, mean and RMS velocity fields are determined on the CESAM-HP combustion chamber with both techniques. The comparison of the resulting velocity profiles on different axial positions shows good agreement between the two techniques. The swirl angle is represented correctly and the displacement error lies in the order of a few tenth of pixels, thus close to the limits of PIV measurements. Nevertheless this error is non-negligible, as it reaches percentages of up to 20 %, especially for the RMS. Different reasons for this error are presented and discussed afterwards. Nevertheless, the presented PCMV allows to obtain mean and RMS velocity fields that are of a quality sufficient for this thesis. Additionally the Fourier processing of the instantaneous velocity fields in chapter 4 shows that the observed frequencies correspond to those detected by the in-chamber pressure and OH* chemiluminescence measurement. This observation does not validate the diagnostic for all possible experimental configurations, but it shows that the presented PCMV technique allows to detect the phenomena that are looked for in this thesis.

In order to validate the correctness of the PCMV technique in general, the instantaneous fields need to be validated quantitatively. This could be achieved by two different approaches: The first approach would be to conduct simultaneous experiments to obtain the velocity fields, for example by using PCMV and PIV in parallel and synchronously. In terms of experimentation this approach is not trivial especially due to the rapid degradation of image quality due to particle deposition on the windows. Furthermore, other possible error sources, such as errors due to alignment cannot be excluded. The second approach would thus be the use of numerical simulation. LES simulations could be used to calculate the velocity fields and particle displacement of a particle

laden swirling flow. From the results, synthetic images could be created that represent the Mie scattering of particles that are illuminated by a laser sheet. Since LES calculations typically have time steps of a few nanoseconds, the exposure times of a classic PIV (10 ns) and that of the present PCMV ($9 \mu s$) could be simulated with the synthetic particle image. Finally, the cross-correlation algorithm presented in section 5.2 could be applied to calculate the velocity fields. By comparing these velocity fields, one can finally examine the effect of the exposition duration, which is theoretically the main difference between the proposed PCMV and classic pulsed PIV techniques. This approach is presented in Mazur et al. (2017) and suggests that the influence of the smearing is not excessively high.

Chapter 6

Visualization of the density fluctuations with focusing Schlieren

In this chapter, the density fluctuations in the flame and the burnt gases are visualized in the CESAM-HP test bench with the help of focusing Schlieren. The technique allows to acquire images of density fluctuations on a field of view of small thickness at high sampling frequencies. The imaging is conducted for the three known operating points and the results are analysed by calculating the PSD of the Schlieren image intensity. In a final step, the determined frequencies in the burnt gases are compared with line of sight integrated density measurements obtained by LIV in the same position in the burner.

6.1 Presentation of focusing Schlieren as a technique to visualize density fluctuations

In chapter 8, the density fluctuations in the burnt gases are determined quantitatively with the help of Laser Interferometric Vibrometry (LIV). The results show that the main frequencies of the density fluctuations in the burnt gases are dominated by the low frequency phenomena presented in the other chapters of this thesis. While these measurements allow to obtain the separation of direct and indirect combustion noise, they have certain limitations. Being a line of sight technique, LIV has the risk to neglect phenomena by averaging over the entire measuring path. Thus for example it also takes into account phenomena like temperature inhomogeneities of the chamber windows. The second issue is the fact, that the vibrometry measurement is taken on one point. Thus no conclusion can be made about what the density fluctuations and hence the entropy waves actually look like. In this chapter, a technique is applied that shows the density fluctuations on a 2D field with a field depth of only a few millimetres.

Density gradients in flows are classically obtained experimentally with the Schlieren technique. Schlieren is well explained by [Settles \(2001\)](#) and will be presented here. The technique is based on the deflection of light due to gradients of refractive index created by gradients in density of a flow. This relation is expressed by the Gladstone-Dale relation:

$$n = 1 + G\rho \tag{6.1}$$

with n the refractive index, G the Gladstone-Dale coefficient and ρ the fluid density. Changes in density will lead to a bending of the passing light. The associated deflection angle ϵ_x is expressed by the following equation:

$$\epsilon_x = \frac{L}{n_0} \frac{\partial n}{\partial x} = \frac{L}{n_0} G \frac{\partial \rho}{\partial x} \tag{6.2}$$

with n_0 the refractive index of the medium, x the direction perpendicular to the optical axis of the light beam and L the length of the regarded region. In classical Schlieren, a knife edge is used to cover a part of the deflected light. Due to this, the density gradients are displayed as the typical dark and light images.

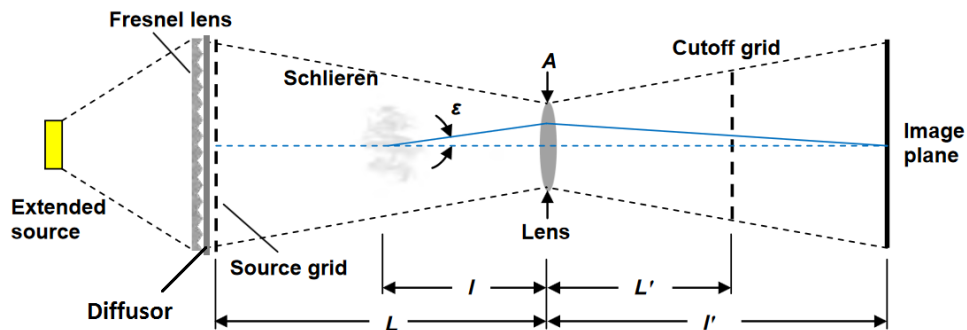


Figure 6.1: Schematic drawing of the focusing Schlieren technique (based on [Floryan et al. \(2012\)](#))

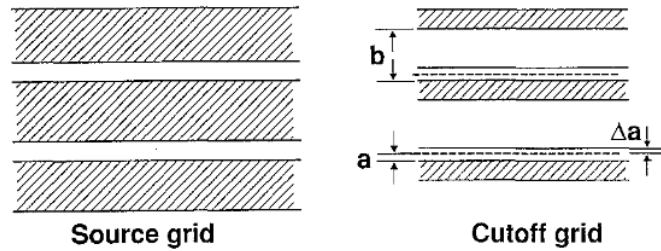


Figure 6.2: Layout of the source grid and the cut-off grid (Weinstein (1993)). The dimensions of the source grid are chosen freely and are oriented on the optical complement of the cut-off grid, thus taking into account the zoom of the camera lens.

A special variation of Schlieren is the focusing Schlieren technique, also called lens-and-grid Schlieren. It was developed by Weinstein (1993) and reviewed in a later work (Weinstein (2010)). A schematic drawing of the technique is presented in figure 6.1. The system is constituted of a light source, a Fresnel lens, two optically complementary grids (the source and the cut-off grid, cf. figure 6.2 for their layout) and a camera lens. The particularity of this system is that it only shows the density fluctuation of a chosen field of view of a few millimetres thickness. Weinstein (1993) explains that the focussing effect of the Schlieren system is due to the combination of grids with the camera lens. In the source grid, each slit corresponds to a separate light source. In the cut-off grid on the other hand, each bar represents a Schlieren knife edge for the corresponding light source. Thus due to these grids the system is a combination of multiple separate Schlieren systems. Due to the focussing properties of the camera lens, the resulting images of these separate Schlieren systems are combined on the image plane. While the density visualizations in the focal plane are added up, the visualizations outside this plane eliminate each other. The effect is that only the density fluctuations of a zone of only a few millimetres thickness is visible on the image plane.

The thickness of this visible zone as well as the sensitivity and the image quality depend on the grid dimensions, the camera lens and the chosen distances. These parameters have to be chosen with care in a trade-off between high image sensitivity, high image resolution and low focal plane thickness. For the dimensioning of the focusing Schlieren system, Weinstein (1993) developed a set of equations, that are presented in the following.

As shown in figure 6.1 and 6.2, the system has the following parameters: a and b correspond to the grid dimension shown in figure 6.2. L is the distance between source grid and camera lens, L' between camera lens and cut-off grid. l is the distance between observed flow and the camera lens, while l' is the distance between camera lens and image plane. Finally A is the aperture of the camera lens.

The lengths L , L' , l and l' are determined by the focusing of the camera lens. In the focusing Schlieren system L and L' are chosen in a way, that the image of the source grid is focussed on the cut-off grid. Only then, the cut-off grid will be able to act as a collection of Schlieren knife edges. The distances l and l' on the other hand are determined by the focusing of the observed flow on the image plane.

The sensitivity of the focusing Schlieren system is described by the following equation:

$$\epsilon_{min} = 20626a \frac{L}{L'(L-l)} \text{arcsec}, \quad (6.3)$$

which expresses the smallest deflection angle that can be detected as an intensity difference in the Schlieren image. As explained at the beginning of this section, the angle ϵ is the deflection angle of a light beam due to a density gradient on its path. As the deflected beams are partly blocked by the knife edge, this gradient results in changes of intensity. In Eq. (6.3), [Weinstein \(1993\)](#) assumes that the smallest detectable change in intensity is 10 %. Since ϵ_{min} corresponds to the minimal deflection that is detectable by the focusing Schlieren system, it is desirable that its value is low. The drive for a high intensity explains the necessity for very fine grids with a low value for a .

The resolution of the Schlieren system is expressed by the following equation:

$$w = 2 \frac{(l' - L')\lambda}{mb} \quad (6.4)$$

with w the smallest flow dimension that can be observed, λ the wave length of the used light, b the grid dimension according to figure 6.2 and $m = l'/l$ the image magnification due to zooming by the camera lens. In this equation, the value w needs to be small in order to obtain a high degree of detail in the Schlieren image and capture small flow features. The equation shows that this can be achieved by a wide grid spacing b . However, if the grid is too widely spaced, the final image is constituted of a low quantity of points. The out-of-focus grid lines then can be observed as unsharp images. The number of used lines is determined by the following equation:

$$\Phi = An \frac{l' - L'}{2l'} \quad (6.5)$$

with n the amount of grid lines per millimetre for the cut-off grid. Φ needs to have a high value (at least 5, according to [Weinstein \(1993\)](#)), which is achieved by a high n , thus a low b . The grid dimension b needs thus to be chosen as a trade-off between image resolution as of eq. 6.4 and image quality as of eq. 6.5.

Finally, the depth of focus of the Schlieren system is determined by two equations defined by [Weinstein \(1993\)](#). They express the sharp focus depth DS and the unsharp focus depth DU as following:

$$DS = 2Rw \quad (6.6)$$

$$DU = 4R \quad (6.7)$$

with $R = l/A$ the distance between flow field and camera lens divided by the camera aperture. This equation shows that the camera lens should have a low focal length (resulting in low distances of the Schlieren system) and a high aperture.

Table 6.1: *Summary of the Schlieren system parameters*

Variable	Value
L	250 mm
L'	180 mm
l	125 mm
l'	950 mm
f	105 mm
A	58.3 mm
a	80 μ m
b	320 μ m
n	2.5 1/mm
λ	532 nm
m	7.6
R	2.14
ϵ_{min}	18.3 arcsec
w	0.34 mm
Φ	59.0
DS	1.46 mm
DU	8.56 mm

The dimensions of the focusing Schlieren system used in this work are summarized in table 6.1. The focusing Schlieren system, shown in figure 6.1, is set up with grids with dimensions of $a = 80\mu\text{m}$ and $b = 320\mu\text{m}$, produced by KLOE. The grids were produced by lithography and are constituted of a carrier of glass, which is transparent for visible light, and on which the grids are produced as a non-reflecting metallic deposit. The advantage of this solution is the high

precision (of the order of μm) and the resistance against high temperatures. For the process of finding the most appropriate grid dimensions, test versions of the grids can be fabricated very rapidly by printing on transparent plastic sheets with a common laser printer. The camera lens is a Nikon lens with a focal length of 105 mm and an aperture of $f/1.8$, thus 58.3 mm. As a light source, a COHERENT Verdi G20 continuous wave laser is used, with a power of up to 20 W and a wave length of 532 nm. The laser source is followed by a diverging lens in order to simulate a point light source. This arrangement corresponds to that used by Kouchi et al. (2015) and has the advantage of a low heat release compared to the light intensity. Due to the coherent character of the laser light, a diffuser is installed between the Fresnel lens and the source grid. The Schlieren images are captured with a Photron SA-X2 high speed camera at a sampling frequency of 10 kHz.

With these chosen parameters, the main performance numbers can be calculated by the Eq. (6.3), (6.4), (6.5), (6.6) and (6.7). The values are summarized in table 6.1 and are close to those of the focusing Schlieren system applied by Kouchi et al. (2015). The smallest detectable density difference is linked to the beam deviation ϵ_0 , which has a value of 18.3 arcsec. While this value is rather high, it was similar in the work of Kouchi et al. (2015), which showed results of sufficient sensitivity. This value can also be used to crudely estimate the smallest detectable temperature fluctuations. This is done by using Eq. (6.2), where n_0 is calculated by Eq. (6.1). It assuming that Schlieren is performed in the burnt gases with a mean temperature of around 1900 K, a mean density of about 0.4 kg/m^3 (see chapter 8 for more details) and a Gladstone-Dale index of $2.5 \cdot 10^6 - 4 \text{ m}^3/\text{kg}$ (Giuliani et al. (2009)). dx corresponds to the spatial resolution w and L corresponds to the distance between focusing plane and Schlieren lens, as can be seen in figure 6.1. Eq. (6.2) thus becomes:

$$\epsilon_x = \frac{l}{1 + G\bar{\rho}} G \frac{\rho'}{w} \quad (6.8)$$

with the bar describing the mean value and the prime the fluctuation value. For the chosen parameters the smallest detectable density fluctuation is 0.00094 kg/m^3 , thus 0.235 % of the mean value. If the ideal gas law $p = \rho r T$ is used and the pressure, density and temperature are supposed to be the sum of the mean and fluctuating part, one obtains following:

$$\frac{p'}{\bar{p}} = \frac{T'}{\bar{T}} + \frac{\rho'}{\bar{\rho}} \quad (6.9)$$

If a constant pressure is assumed, the equation shows that a density change of 0.235 % leads to a temperature change of the same percentage. At a mean burnt gas temperature of 1900 K, this would correspond to a minimal detectable

temperature difference of less than 5 K.

The spatial resolution w shows that the smallest phenomena that can be detected are of 0.34 mm. This value is sufficient as the technique is especially interesting for the burnt gases. In these gases the density fluctuations are supposed to have a smaller spatial gradient than for example in a flame. The value Φ is 59 and thus well above the required 5. [Weinstein \(2010\)](#) also described that best image qualities are obtained when Φ is a multiple of 0.5. This is the case in the presented configuration. Finally, the sharp and unsharp focal depth, DS and DU respectively are rather small, with respectively 1.46 mm and 8.56 mm. Better sensitivities and focal depths could be easily achieved by decreasing the grid parameter a , however this would result in a lower light intensity due to the reduced slit size in the source grid. Another possibility would be to use a camera lens with higher apertures, however the value of 1.8 is already close to the lower limit of commercially available lenses at the chosen focal length.

As demonstrated by [Kouchi et al. \(2015\)](#), the obtained Schlieren images require image pre-processing in order to obtain a visualization of good quality. In this work, it is performed in two steps. First, the background is subtracted from the Schlieren images, which increases the visibility of the density fluctuations. In a second step the laser noise is removed by applying a spatial low-pass filter on the images. In this case, a circular averaging filter with a radius of 9 pixels is used. The effects of the two pre-processing stages are shown in figure 6.3. The shown Schlieren image was taken at the burner lip. More details can be found in section 6.2.1 and are not described here, since at this stage only the pre-processing is shown.

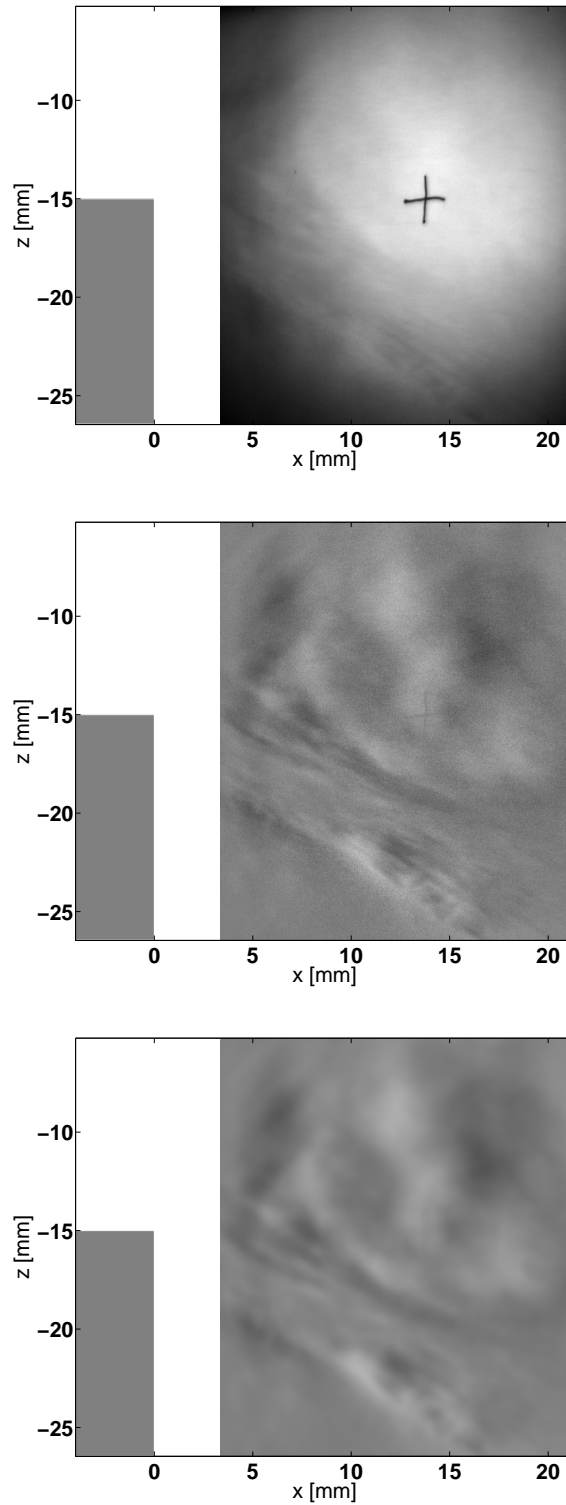


Figure 6.3: Different stages of pre-processing of the Focusing Schlieren visualization. The image is taken at the burner lip of the CESAM-HP combustor for **Op16-0-2**. Top: Raw image, Middle: Image after background subtraction, Bottom: Image after background subtraction and spatial filtering

Figure 6.3 shows two issues for the raw images, which were also observed by [Kouchi et al. \(2015\)](#): (1) inhomogeneous illumination due to the laser source and (2) high image noise. While the first issue is resolved with the background subtraction, the second one is resolved by the spatial filtering. The effect of the latter measured on the image seems limited, however the filtering is crucial in regions with less sharp density gradients. The background subtraction on the other hand has the consequence that the image intensity is not proportional to the density ρ , but to the density deviation ρ' . Therefore it is difficult to obtain information about the actual densities in the different regions.

Before conducting the Schlieren visualizations on the CESAM-HP test bench, the focal depth of the system is tested with a basic experimental setup, which is shown in figure 6.4. Two high speed jets from choked tubes of 2 mm diameter are crossed in the focal plane of the Schlieren system. As the air is at room temperature and the tubes are choked, the flow velocity is at the speed of sound of about 340 m/s. Therefore the air mass flow can be estimated with the equation $\dot{m} = \rho Av$ to 1,28 g/s. Since the tubes are choked, the flow features shocks in diamond shape, such as observed by [Kouchi et al. \(2015\)](#). While one of the two jets is kept in the focal plane, the other is displaced longitudinally on the Schlieren system axis. As shown in figure 6.5, the second jet is unfocused quickly when leaving the focal plane. Already 2 mm from the focal plane, the jet visualization loses its sharpness. At 5 mm distance, the shock diamonds cannot be recognized any more, with an even increased blurring at 10 mm. At 20 mm, the jet is not visible any more. This experiment shows that the Schlieren system indeed focuses over a plane of only a few millimetres and is not too far from the calculated focus depths DS and DU. While the flow disappears only just after 10 mm from the focal plane, this system is considered sufficient since the density gradients of these shocks are very high. It can be supposed that for example the density gradients in the burnt gases are lower and thus according to Eq. (6.2), the intensity difference of the captured Schlieren image is also lower. The intensity difference would disappear thus already closer from the focal plane.

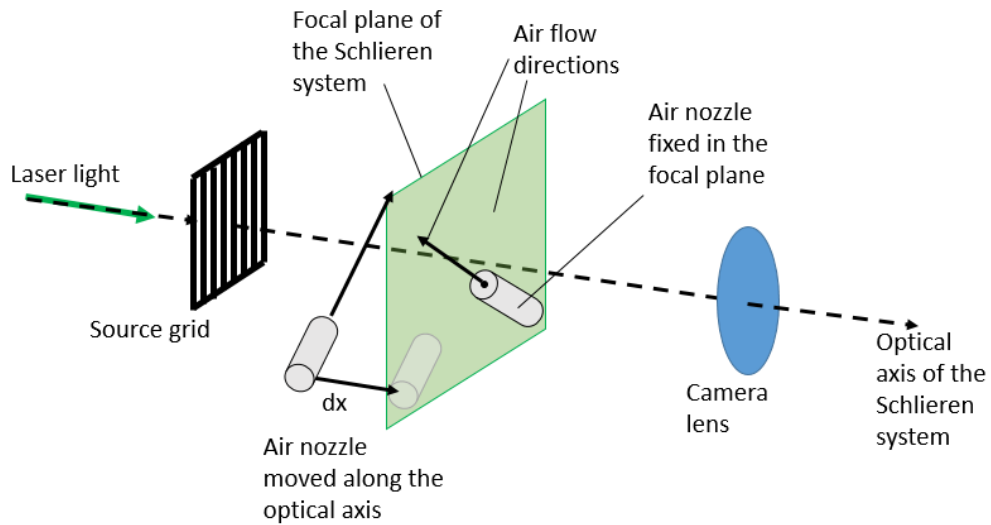


Figure 6.4: Validation experiment for the focusing Schlieren system. Both jets come from a choked tube of 2 mm diameter. While one jet is kept in the focal plane of the Schlieren system, the other is displaced on the Schlieren system axis. In this image dx corresponds to the distance from the focal plane.

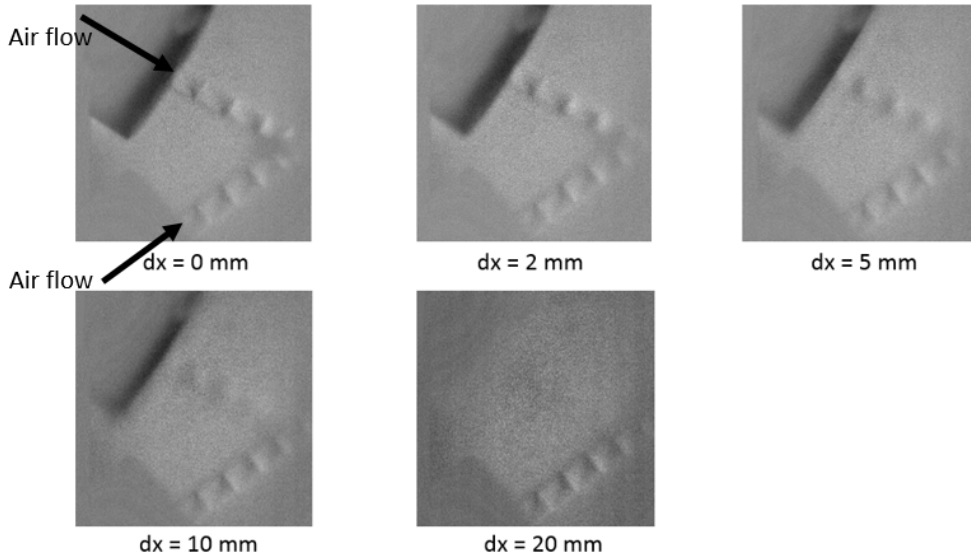


Figure 6.5: Results of the validation experiment for the focusing Schlieren system. The results are equal for a positive or negative displacement.

In general, the Schlieren images capture the flow of an area of around $20 \text{ mm} \times 20 \text{ mm}$. This limited region is chosen in order to preserve a sufficiently high laser intensity. Other limits for a larger field of view are the size of the grids ($45 \text{ mm} \times 45 \text{ mm}$) and the aperture of the camera lens. The region that

can be studied is rather limited, however Schlieren images taken at the injector and in the combustion chamber allow to observe the density fluctuations in these regions. The resulting Schlieren images are described in sections 6.2.1 and 6.2.2.

6.2 Experimental results

6.2.1 Density gradients at the burner lip

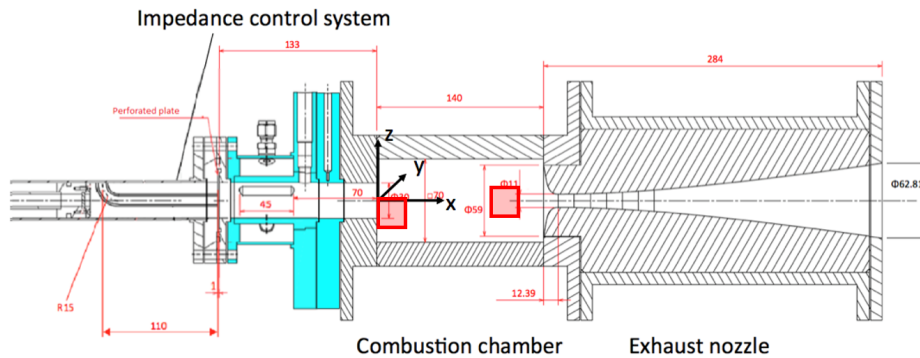


Figure 6.6: Schematic drawing of the CESAM-HP test bench with the applied coordinate system. The system is a right-hand coordinate system, thus the y coordinate is showing away from the reader. The figure also includes the two regions where the Schlieren imaging is applied.

In order to obtain the Schlieren images in the injector, the Schlieren system is aligned around the lower burner lip (which itself is located at $z = -15$ mm), with x being between 3 mm and 22 mm and z between -27 mm and -5 mm (see figure 6.6 for the coordinate system). The focal plane is chosen to go through the burner axis at $y = 0$ mm. As in the other chapters of this work, **Op16-0-2**, **Op16-2-0** and **Op13.4-4.6-0** are chosen as operating points

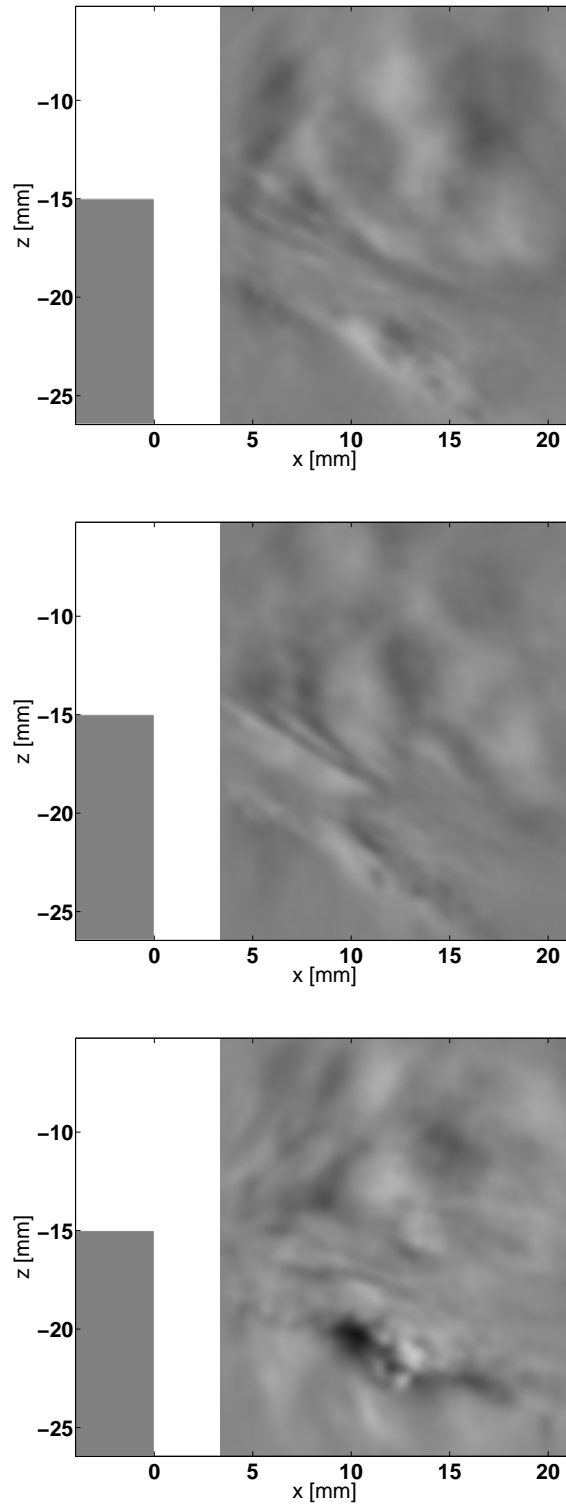


Figure 6.7: *Focusing Schlieren visualization taken at the burner lip of the CESAM-HP combustor for Op16-0-2 (top), Op16-2-0 (middle) and Op13.4-4.6-0 (bottom). The images were pre-processed for a better visibility of the density gradients.*

Examples for the focusing Schlieren visualization for the three operating points at the burner lip are shown in figure 6.7. The Schlieren images feature two zones. (1) The first zone is a high density gradient that is located diagonally at a straight line with an angle of around 30 degrees to the burner axis (around 20 degrees for **Op13.4-4.6-0**). This angle is close to the swirl cone angle identified in chapter 2. It can thus be assumed that this area is related to the high speed rotational region that is characteristic for a swirling flame. In this region the density gradient is particularly high. Together with the flame visualizations in chapter 2 these observations allow to suggest that this region is the flame front. It is interesting that vortices can be observed in this region, which is an indicator for a high resolution of the Schlieren system. (2) The second region is closer to the burner axis. It is constituted of a high-low intensity regions (at very weak gradients) that propagate longitudinally at a velocity of around 20 m/s (as is visible in videos of this acquisition). If assuming these to be harmonic waves, they would have a wave length of about 4.7 mm.

These observations lead to various conclusions. As a first conclusion, the image is a proof of concept of the focusing Schlieren technique for this experimental setup. If the Schlieren technique was not focused on a small thickness, then the wave-like phenomenon would not be visible. It would be covered by the high speed swirling cone due to the integration over the line of sight. The second conclusion is, that from the central region a characteristic frequency can be calculated, associated to the wave-like phenomenon. To do so, the following equation is applied:

$$c = \lambda \cdot f \tag{6.10}$$

with c the propagation velocity of the waves, λ the wave length and f the frequency.

With the mentioned velocity and wave length, a frequency of around 4.2 kHz is obtained. In order to find other frequencies and in order to compare the calculated frequency with other existing frequencies, Fourier analysis is conducted. For this the Schlieren images are acquired at a sampling frequency of 10 kHz during 4 s. The PSD of the Schlieren signal is calculated on regions of 2 mm \times 2 mm (around 40 px \times 40 px) using Welch's algorithm with Hamming windows with 2048 points and 50 % overlap.

The same equation can be applied for the 127 Hz mode. If assuming the same longitudinal velocity of 20 m/s, this frequency would correspond to a wave-length of 166 mm, thus longer than the combustion chamber itself.

Table 6.2: overview of the regions at the injector, where the Intensity PSD of the Schlieren images was calculated. $y = 0$ mm for all regions. The indicated x and z coordinate correspond to the central point of the $2 \text{ mm} \times 2 \text{ mm}$ region.

Number	x [mm]	z [mm]	Op16-0-2	Op16-2-0	Op13.4-4.6-0
1a	11	-23	X	X	
1b	12	-22	X		X
2	15	-12	X	X	X

Two regions were chosen, which are summarized in table 6.2. The first region is located in the zone associated with the high velocity swirling cone. It is divided into 1a for **Op16-0-2** and **Op16-2-0** and 1b for **Op13.4.6-0**. With this division, the different positions of the flame front are taken into account. The second region is located closer to the burner axis and has thus the aim to observe the wave-like phenomenon.

The PSD of the three operating points for region 1 is shown in figure 6.8. The spectrum also contains a fourth curve which correspond to a reference case at no combustion and thus exclusively related to the measurement system. The spectra show, that the measuring system accounts for the major part of the very low frequency fluctuations (below 30 Hz). Besides, peaks of 50 Hz and its harmonics are visible for the reference curve. These are probably related to the electric system. The main visible frequencies for the three operating points are the low frequencies that were already observed in chapter 4. This indicates that the flame is probably located in this region. It is thus consistent with chapter 4 that the found frequencies correspond to those already found before. At high frequencies, on the other hand, no frequency could be detected in this region.

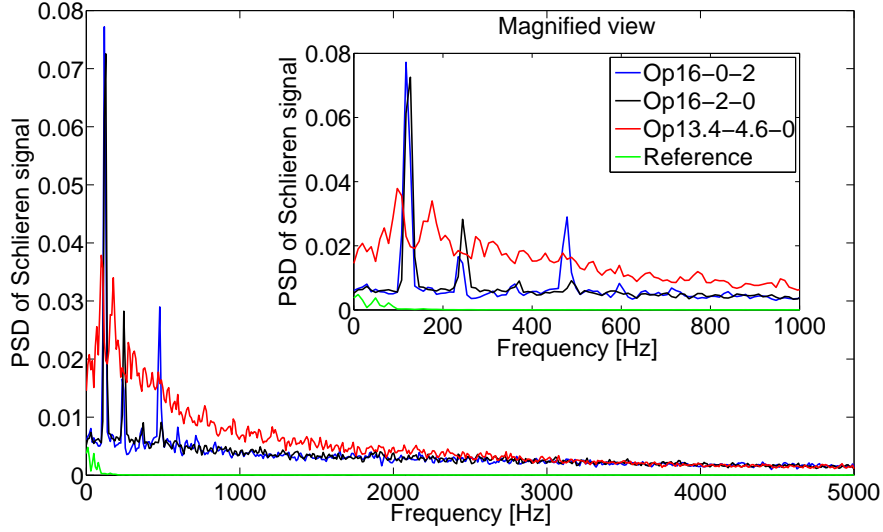


Figure 6.8: PSD of the Focusing Schlieren visualization taken at the burner lip of the CESAM-HP combustor for **Op16-0-2**, **Op16-2-0** and **Op13.4-4.6-0** in region 1. The fourth diagram corresponds to a reference point taken at no combustion. It can be seen that the low frequency fluctuations associated with the combustion instability are well represented. The 4.2 kHz frequency, which is detected in the 2D Schlieren images, seems to be masked by other phenomena.

The PSD spectrum of region 2 is shown in figure 6.9. Similarly to that of region 1, the spectrum features the low frequency peaks associated to the main combustion instability. On the other hand, no activity can be observed at higher frequencies.

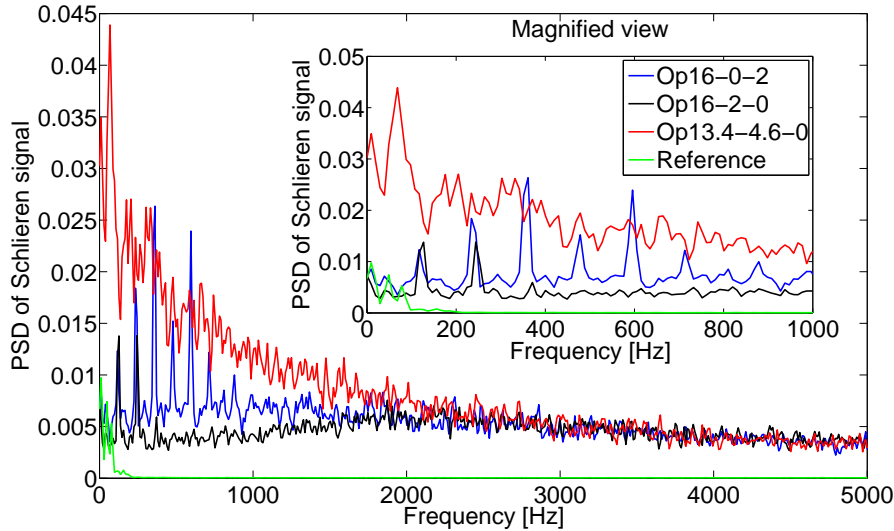


Figure 6.9: PSD spectra of the Focusing Schlieren visualization taken at the burner lip of the CESAM-HP combustor for **Op16-0-2**, **Op16-2-0** and **Op13.4-4.6-0** in region 2. The fourth diagram corresponds to a reference point taken at no combustion.

It can be summarized that two frequencies could be identified: (1) A low frequency peak around 127 Hz (or 100 Hz for **Op13.4-4.6-0**, which corresponds to the eigenfrequency of the combustion instability, and (2) A frequency around 4.2 kHz, which seems to be associated with the wave-like phenomenon inside the swirling cone. While this frequency can be observed in the Schlieren images, its amplitude is extremely weak. Furthermore this frequency cannot be seen in the PSD graphs. This means that this density fluctuation at 4.2 kHz is very weak compared to the density fluctuations directly on the flame front.

In a second step, 2D PSD spectra of these two frequencies are calculated. The PSD is calculated similar as before, except that it is calculated for each pixel of the Schlieren visualizations. The aim is to localize the regions where the respective mode is dominating.

The resulting 2D PSD images are shown in figure 6.10 to 6.12. Each of the three figures contains the 2D PSD amplitude for the low frequency associated to the combustion instability on the top of the figure. On the bottom of each figure, the 2D PSD amplitude for 4.2 kHz is shown. It can be seen that both modes have a fundamentally different structure. The low frequency mode has its highest amplitude inside the swirling cone. The bottom image shows a periodic change between low and high intensity with the same distance as determined before, thus at 4.2 kHz.

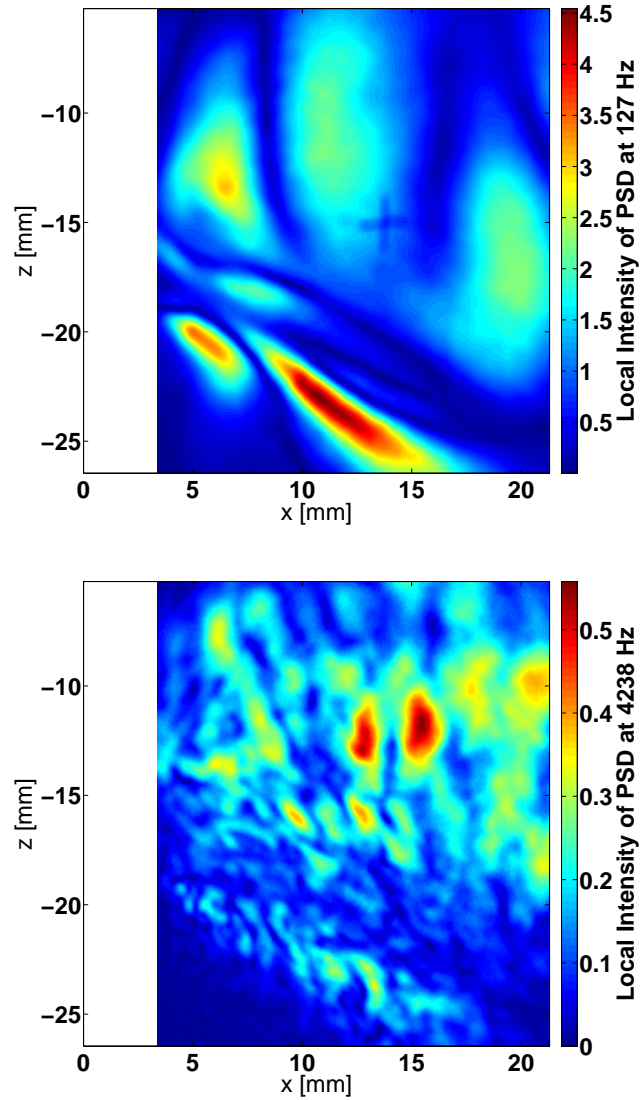


Figure 6.10: 2D PSD of the Focusing Schlieren visualization taken at the burner lip of the CESAM-HP combustor for *Op16-0-2*. The top image corresponds to the 127 Hz mode and the bottom image to the 4.2 kHz mode.

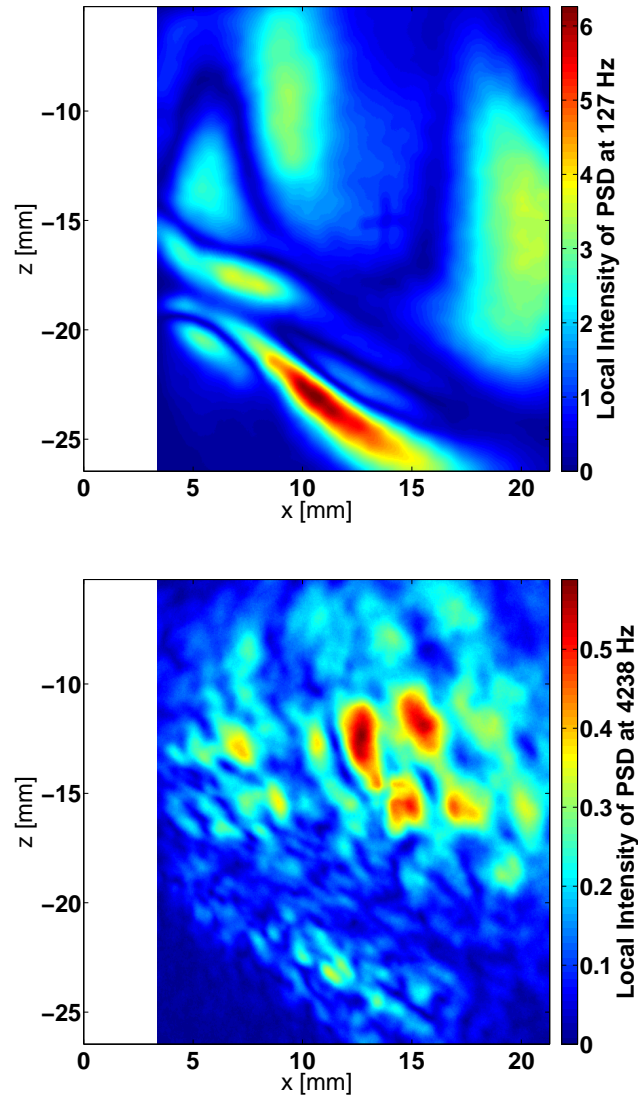


Figure 6.11: 2D PSD of the Focusing Schlieren visualization taken at the burner lip of the CESAM-HP combustor for Op16-2-0. The top image corresponds to the 127 Hz mode and the bottom image to the 4.2 kHz mode.

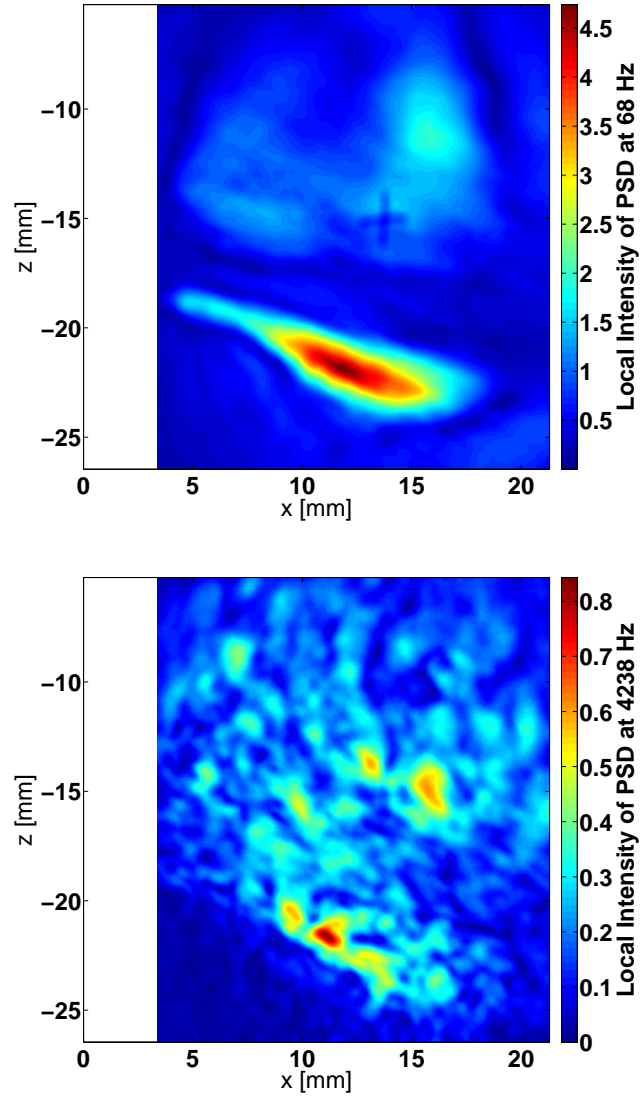


Figure 6.12: 2D PSD of the Focusing Schlieren visualization taken at the burner lip of the CESAM-HP combustor for *Op13.4-4.6-0*. The top image corresponds to the 98 Hz mode and the bottom image to the 4.2 kHz mode.

6.2.2 Density gradients in the burnt gases

In a second step, the Schlieren system is aligned at the exhaust region, with x being between 92 mm and 114 mm and z between -2 mm and 21 mm (see figure 6.6 for the coordinate system). The focal plane is equally chosen to go through the burner axis at $y = 0$ mm. The study is conducted for *Op16-0-2*, *Op16-2-0* and *Op13.4-4.6-0*.

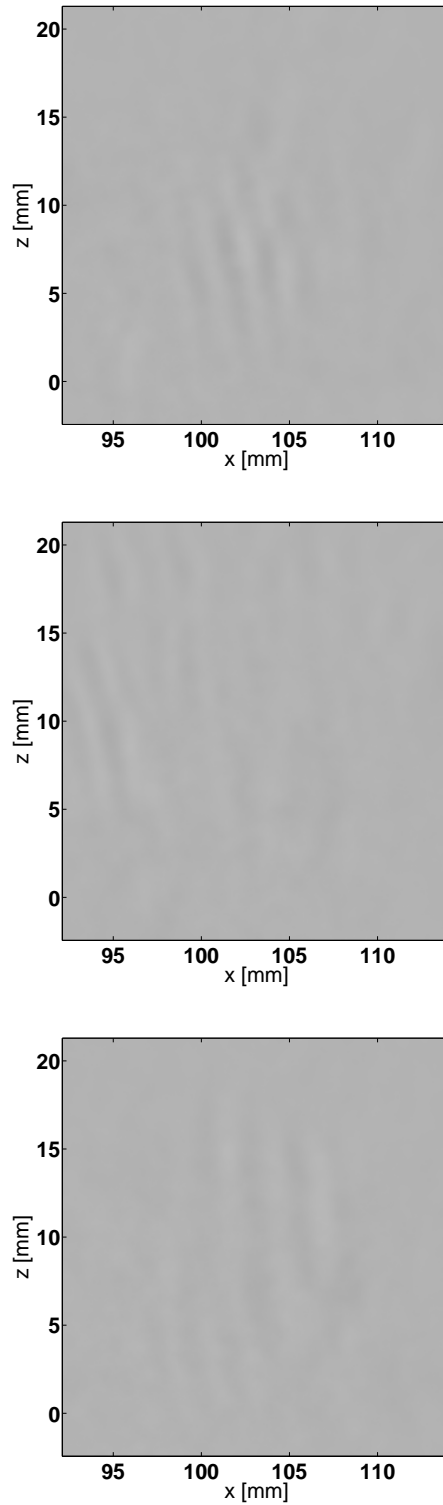


Figure 6.13: *Focusing Schlieren visualization taken at the exit of the CESAM-HP combustor for Op16-0-2 (top), Op16-2-0 (middle) and Op13.4-4.6-0 (bottom)*

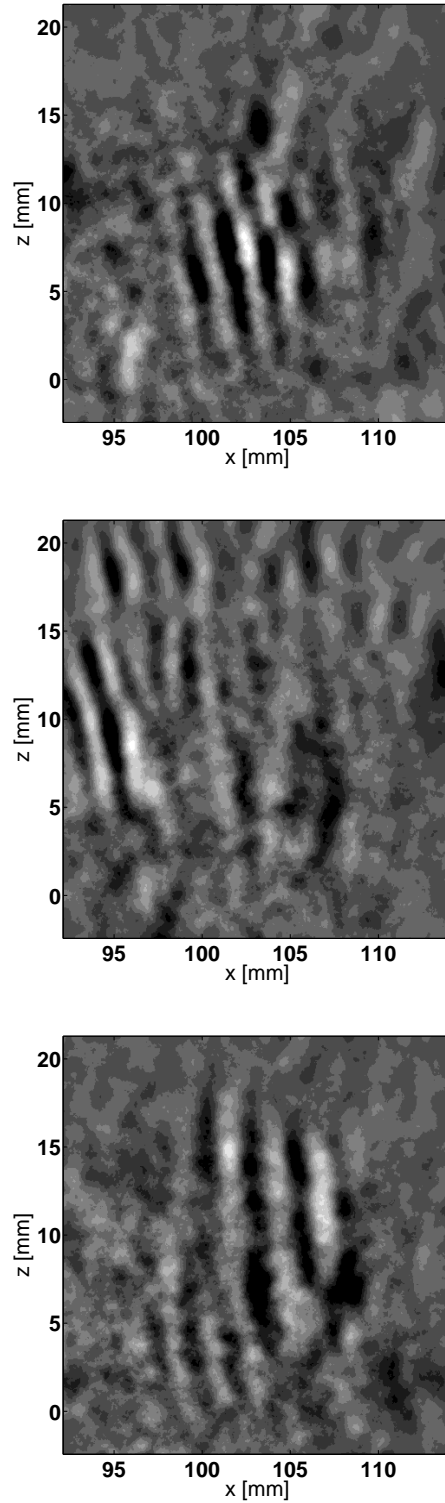


Figure 6.14: *Focusing Schlieren visualization taken at the exit of the CESAM-HP combustor for Op16-0-2 (top), Op16-2-0 (middle) and Op13.4-4.6-0 (bottom) with an increased contrast*

An example for the focusing Schlieren visualization at the exhaust region is shown in figure 6.13. Since the flow features are very difficult to distinguish due to the low density gradients (compared to that in the injector area), the same images with increased contrast are depicted in figure 6.14. Both figures show that, contrary to the region at the burner lips, the Schlieren image is constituted of wave-like phenomena that propagate longitudinally at a velocity of 6.5 m/s and have a wavelength of about 1.5 mm. If Eq. (6.10) is applied on these data, a frequency of 4.2 kHz is obtained. This frequency is equal to that found close to the injector.

Furthermore, the 6.5 m/s can be justified by a simple assumption for the flow velocity u of the burnt gases using the following equation:

$$u = \frac{\dot{m}}{\rho A} \quad (6.11)$$

with \dot{m} the total mass flow, A the combustion chamber section and ρ the density of the burnt gases. The density can be estimated with the ideal gas law:

$$p = \rho r T \quad (6.12)$$

with p the chamber pressure, r the ideal gas constant and T the burnt gas temperature.

When assuming a total mass flow of 19 g/s and a burnt gas temperature of 1900 K, the burnt gas velocity is calculated to around 8 m/s, thus in the order of magnitude of the velocity observed from the Schlieren images. This wave-like phenomenon might thus be the density fluctuations transported by the burnt gases, thus entropy waves accordingly to the description by [Marble and Candel \(1977\)](#). However further tests need to be conducted in order to verify this assumption.

Another interesting observation is made on the films which are made from these images: These harmonic wave-like phenomena appear and disappear periodically at a frequency of around 100 Hz. This might be associated with the main instability frequency, however this needs to be verified as well.

For this verification, a Fourier analysis is conducted. To do so the Schlieren images are taken at a sampling frequency of 10 kHz during 4 s. The PSD of the Schlieren signal is calculated on regions of 2 mm \times 2 mm (around 40 px \times 40 px) with Welch's algorithm with Hamming windows with 2048 points and 50 % overlap. In this test, one 2 mm \times 2 mm region is chosen. It has its central point at $x = 95$ mm and $y = z = 0$ mm. The same eigen frequencies are obtained in the other regions of the Schlieren images, thus only the results of

this chosen region are presented here.

The PSD spectrum of the three operating points for the chosen region is shown in figure 6.15. The spectrum also contains a fourth curve which correspond to a reference case. This reference spectrum is again obtained at no combustion and is thus exclusively related to the measurement system. The spectra show high activities below 30 Hz and peaks related to the 50 Hz electric system. The low frequency peak associated with the combustion instability is visible for the three operating points, however its amplitude is very weak. For **Op16-0-2** and **Op16-2-0** no harmonics are visible. Nevertheless, the low frequencies are equal to those observed in section 6.2.1 and to the results in chapter 4. This means that appearing and disappearing of the wave-like phenomena described before can be associated with these low frequencies. These phenomena therefore seem to appear in "packets" at the frequency of the main combustion instability.

The second visible frequency is a strong peak at 4.2 kHz for all three operating points. This frequency corresponds to that of the wave-like phenomena, which is observed in the Schlieren visualizations.

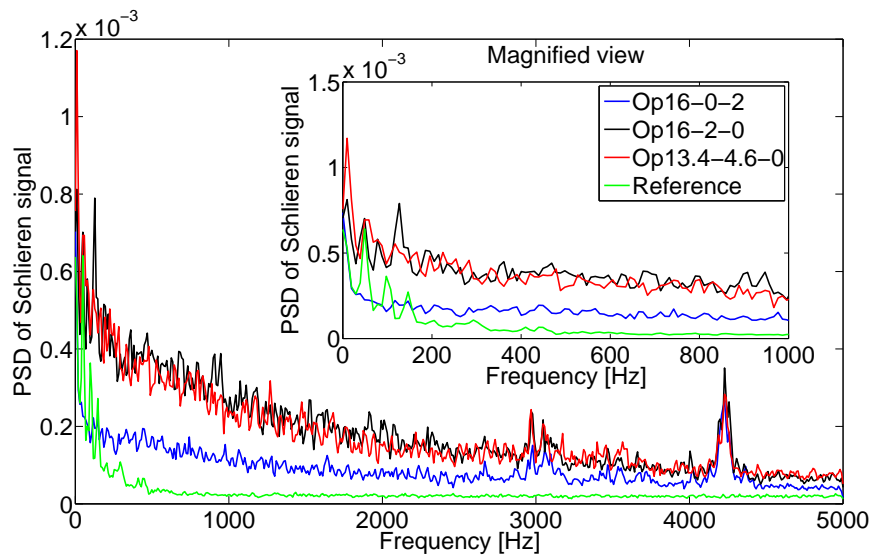


Figure 6.15: PSD spectra of the Focusing Schlieren visualization taken at the exit of the CESAM-HP combustor for **Op16-0-2**, **Op16-2-0** and **Op13.4-4.6-0**. The fourth diagram corresponds to a reference point taken at no combustion.

It can be summarized that two frequencies can be distinguished: (1) A low frequency peak around 127 Hz (or 100 Hz for **Op13.4-4.6-0**, which corresponds to the eigenfrequency of the combustion instability), and (2) A frequency around 4.2 kHz, which is associated with the wave-like phenomenon that propagates at the burnt gas velocity.

In the following step, 2D PSD spectra of these two frequencies are calculated. The PSD is calculated similar as for the diagrams, except that it is calculated for each pixel of the Schlieren visualizations. (taking into account that the images were pre-processed) The aim is to localize the regions where the respective mode is dominating.

The resulting 2D PSD images are displayed in figures 6.16 to 6.18. Each of the three figures contains the 2D PSD amplitude for the low frequency associated to the combustion instability on the top of the figure. At the bottom of each figure, the 2D PSD amplitude for 4.2 kHz is shown. It can be seen that both modes have a fundamentally different structure. For the low frequency mode, the regions of high amplitude are distributed arbitrarily. This would correspond to the observation that these wave-like phenomena appear and disappear at this frequency. Some kind of fringes seem to be visible at a higher wave length (around 5 mm), however this wavelength is not associated with the acoustic waves or any other waves. At a speed of sound of 800 m/s, the wave length would be of more than one meter.

The 2D PSD image for the 4.2 kHz mode seems to have a more distinct periodicity. Furthermore, the distance in x direction between the high amplitude regions is around 1.5 mm, thus equal to the identified wave length when assuming a velocity that corresponds to the mass flow rate of the burnt gases. However for a downstream propagating wave, these fringes would not be visible (only for a standing wave for example). The consequence is, that further proof needs to be found for the existence of the 4.2 kHz mode in the burnt gases.

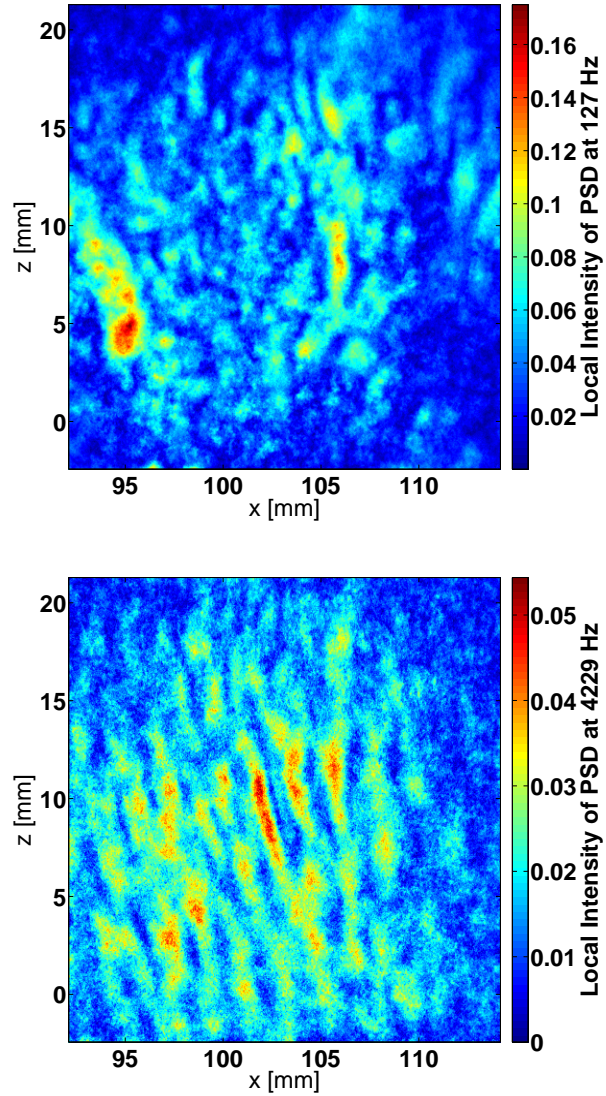


Figure 6.16: 2D PSD of the Focusing Schlieren visualization taken at exhaust of the CESAM-HP combustor for **Op16-0-2**. The top image corresponds to the 127 Hz mode and the bottom image to the 4.2 kHz mode.

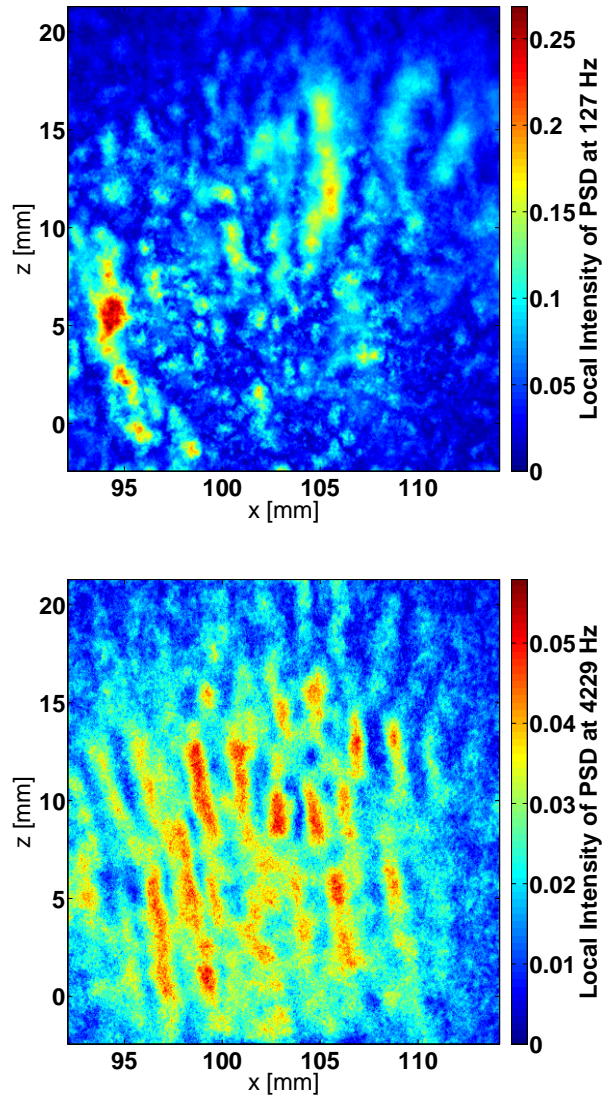


Figure 6.17: 2D PSD of the Focusing Schlieren visualization taken at the exhaust of the CESAM-HP combustor for *Op16-2-0*. The top image corresponds to the 127 Hz mode and the bottom image to the 4.2 kHz mode.

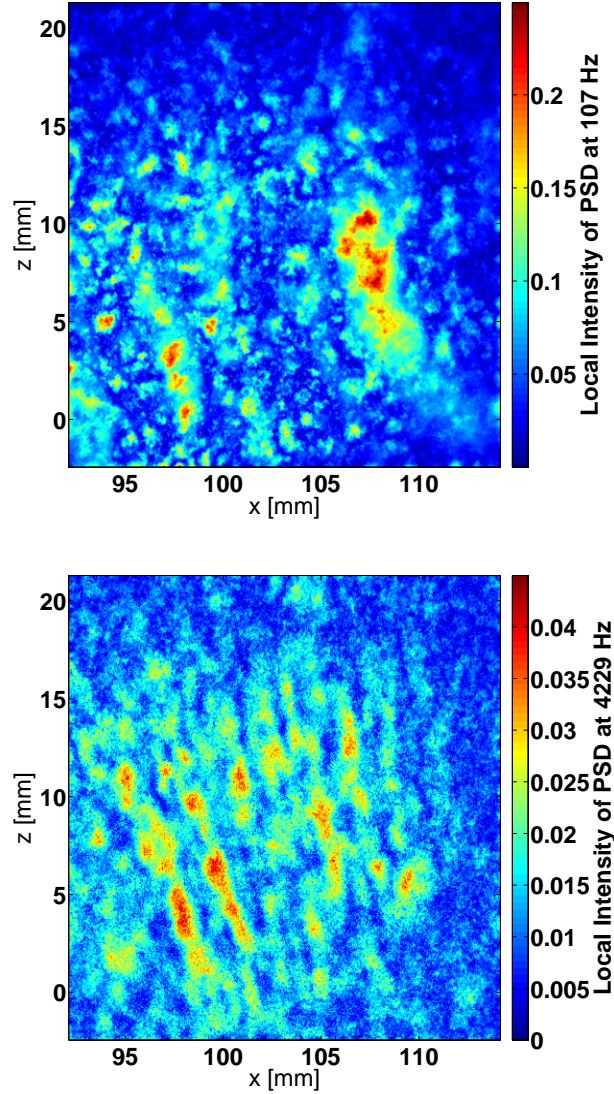


Figure 6.18: 2D PSD of the Focusing Schlieren visualization taken at exhaust of the CESAM-HP combustor for Op13.4-4.6-0. The top image corresponds to the 98 Hz mode and the bottom image to the 4.2 kHz mode.

To sum up, the Schlieren measurements allow to identify two major frequencies for the density fluctuations in the plane. The first frequency is a low frequency associated with the main combustion instability. It is clearly dominating in the injector region, which is consistent with the results in chapter 4. It is thus probably uniquely related to the pressure fluctuations in the combustor. Besides, a wave-like movement can be observed that is propagating downstream and has a frequency of around 4.2 kHz - however its amplitude is too low to be detected in the PSD spectra, where other phenomena are proba-

bly more dominating. These two frequencies are also observed in the burnt gas region. The low frequencies correspond to a periodic apparition and disappearance of wave packets. As demonstrated in chapter 8, the density oscillations at low frequencies has two contributors in the burnt gases - the density fluctuations associated with the pressure fluctuations, and those associated with the entropy waves. Furthermore, the 4.2 kHz frequency can be clearly associated to the downstream wave-like movement. It is also observed that these fringes propagate at around 6 m/s downstream (which corresponds to the debit velocity of the burnt gases) and have a wavelength of about 1.5 mm. The observed phenomenon might be the density fluctuations transported by the burnt gases, thus entropy waves accordingly to the description by Marble and Candel (1977). However further tests need to be conducted in order to verify this assumption. This is done in the next section, where the results of the Schlieren measurements in the burnt gases are compared to vibrometry measurements.

6.2.3 Comparison with LIV measurements

The focusing Schlieren technique allows to obtain 2D images of the density fluctuations of the burnt gases. Their analysis showed that two phenomena are dominating, the low frequency combustion instability as well as the propagation of a wave-like phenomenon with a frequency of around 4.2 kHz. As this high frequency phenomenon has not been visualized experimentally before, it is necessary to validate the found frequency with a known technique. In this work, Laser Interferometric Vibrometry (LIV) is used to measure density fluctuations in the burnt gases (chapter 8). While its results are integrated over the line of sight, the technique is extremely precise and reaches the same sampling frequencies as the here presented Schlieren acquisitions. LIV is thus used to indicate, whether the Schlieren measurements correctly retrieve the oscillation frequencies of the density in the burnt gases.

The vibrometry measurements are conducted only in the burnt gas region, thus $x = 95$ mm and $z = 0$ mm. It would be interesting to perform these measurements also in the flame region. However the flame is of conical shape and due to the integrating character of LIV, the strong dynamics of the flame would be dominating and no other phenomena could be observed.

A detailed description of LIV can be found in chapter 8 and is not repeated here. The vibrometer measurements are acquired at a sampling frequency of 25 kHz during 4 s. The PSD spectra are obtained using Welch's algorithm with Hamming windows of 8192 points per window and 50 % overlap. It is reminded that the measurements are conducted at the same position as the spectra shown in figure 6.15.

The resulting PSD spectra of the LIV and Schlieren measurements for the three

operating points are shown in figures 6.19 to 6.21. For all the three operating points the two frequencies described in section 6.2.2 are visible. The peak associated with the low frequency combustion instability is visible in the Schlieren as well as the Vibrometer spectra. However, the amplitude is far higher for the Vibrometer spectra. Even more, the Vibrometer spectra of **Op16-0-2** and **Op16-2-0** feature some of the harmonics of this low frequency. The second frequency visible with both diagnostics is the high frequency above 4 kHz. While this peak is sharp and of high amplitude for the Schlieren measurements, it is of more broadband nature in the LIV spectrum and has a very low amplitude.

Other peaks are visible in the Vibrometer measurements, that are not detected by Schlieren. On the one hand there is the broadband region around 1.5 kHz. On the other hand, there is a sharp peak around 800 Hz and two equi-distanced peaks around it. While no explanation can be found for the first peak, the second one can be explained when conducting a LIV measurements without combustion. In that case, the 800 Hz peak and the peaks around still exist and have a similar amplitude. These peaks are thus related to the measuring system. (See also chapter 8 for more details)

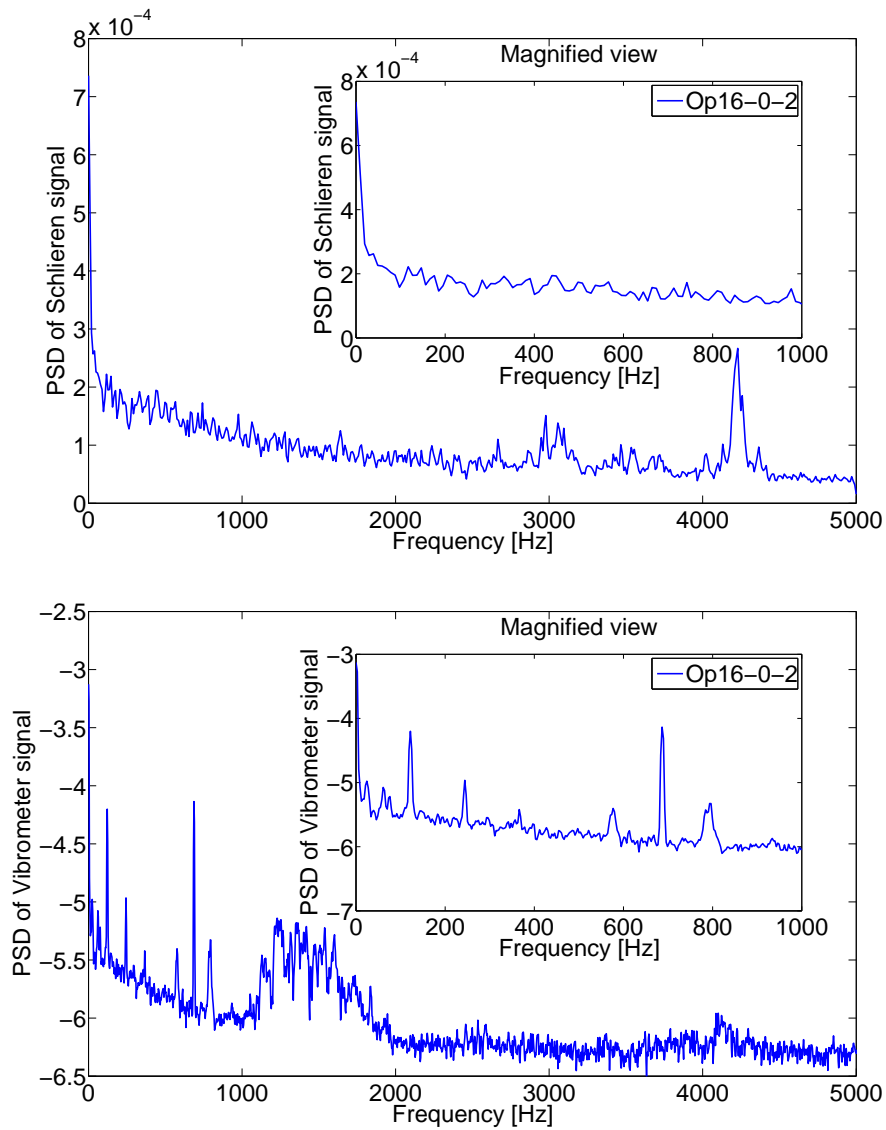


Figure 6.19: PSD spectra of the Schlieren and Vibrometry measurements for *Op16-0-2* at $x = 95$ mm and $z = 0$ mm. Top: Focusing Schlieren measurements; Bottom: LIV measurement

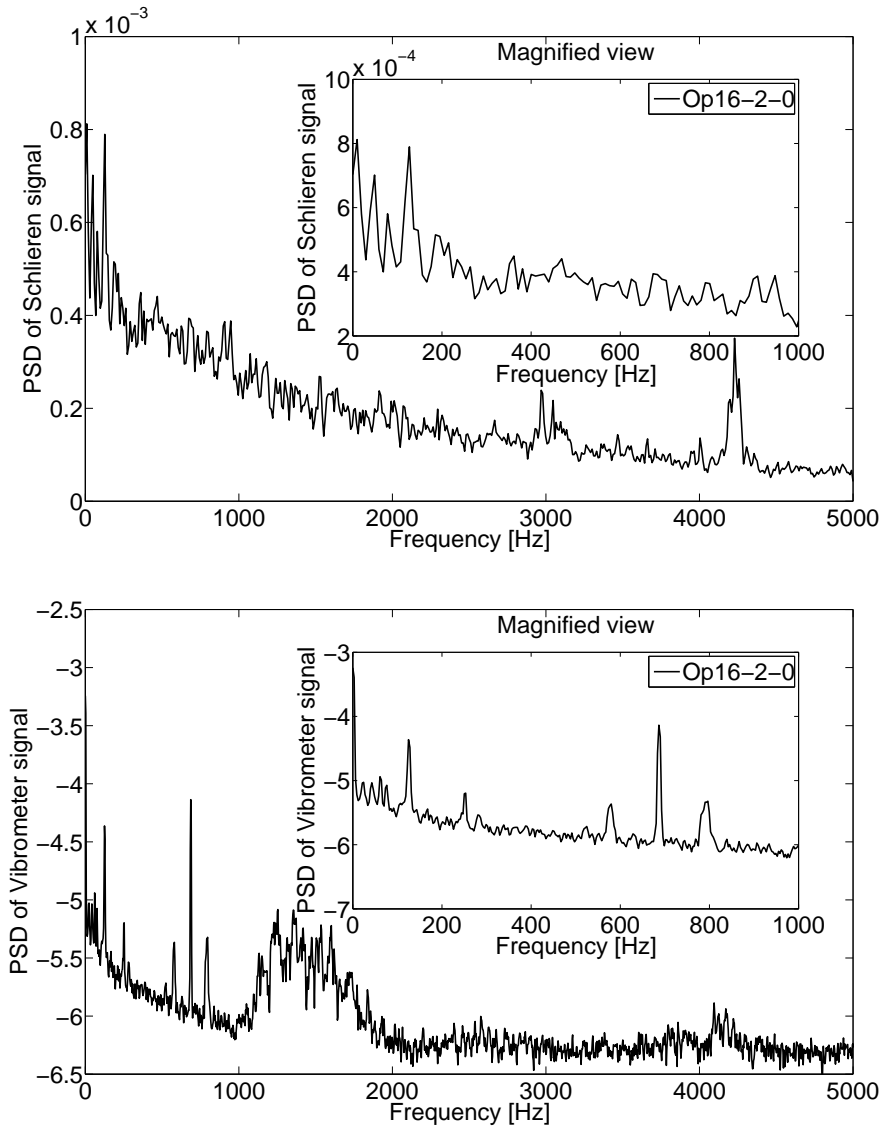


Figure 6.20: PSD spectra of the Schlieren and Vibrometry measurements for *Op16-2-0* at $x = 95$ mm and $z = 0$ mm. Top: Focusing Schlieren measurements; Bottom: LIV measurement

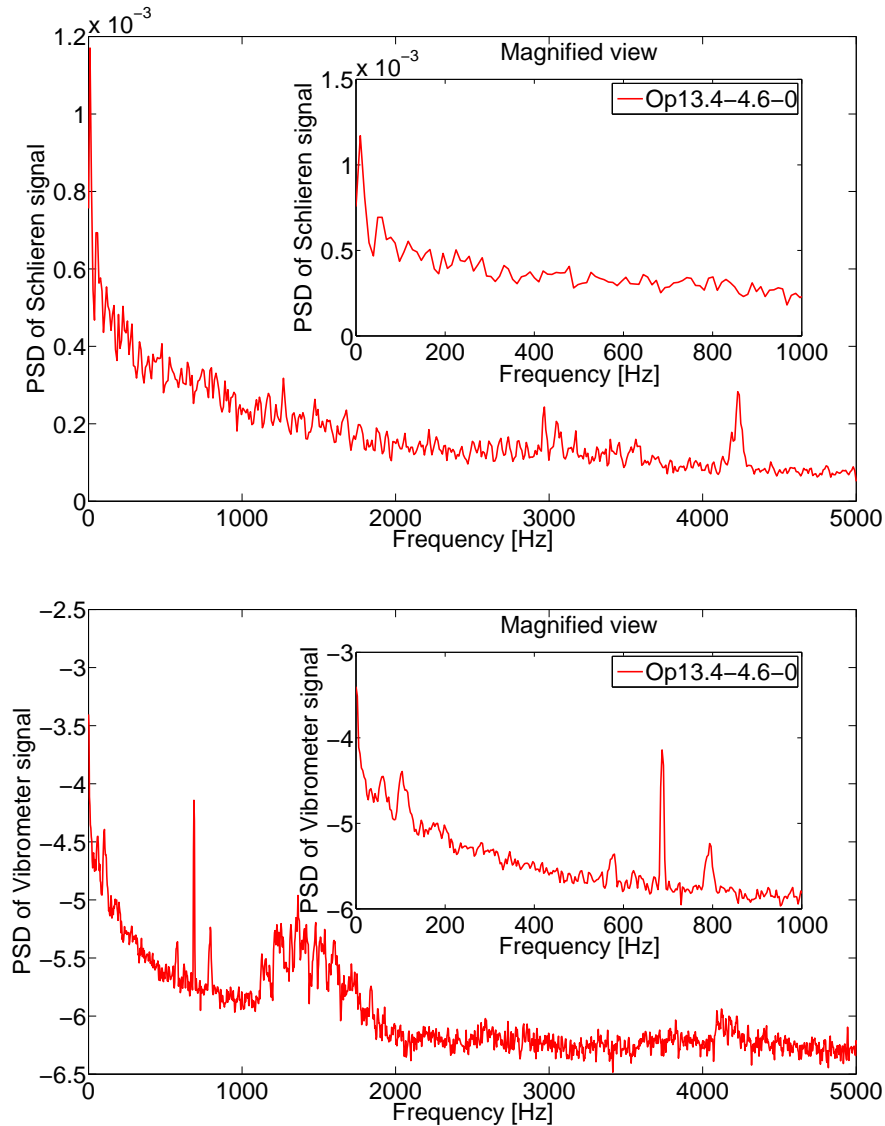


Figure 6.21: PSD spectra of the Schlieren and Vibrometry measurements for *Op13.4-4.6-0* at $x = 95$ mm and $z = 0$ mm. Top: Focusing Schlieren measurements; Bottom: LIV measurement

The fact that both techniques allow to retrieve the low frequency instability as well as the 4.2 kHz frequency peak allow to assume that the phenomena shown by the focussing Schlieren system are physically correct. However, big differences can be observed for both phenomena, especially in terms of peak amplitude. While the low frequency peak is shown clearer by Vibrometry, the focussing Schlieren technique gives a stronger peak for the 4.2 kHz phenomenon. The reason for this difference is probably the fact, that the LIV result is integrated over the line of sight, while Schlieren images are not. The

consequence is, that Vibrometry takes into account more phenomena: The temperature fluctuations outside the focal plane $y = 0$ mm, including glass window inhomogeneities and interactions between burnt gases and the glass walls (at $y = \pm 35$ mm). Furthermore, at some instances even the tip of the swirling flame can arrive to the chosen x value. Due to the line-of-sight character, the low frequency instability leads to stronger peaks for the LIV spectra because the combustion instability is a phenomenon that acts on the combustion chamber as a global. Chapter 4 shows that the low frequency heat release fluctuations happen in particular at instability frequency in most of the chamber regions. Logically, these low frequency fluctuations are passed to the burnt gases by the entire flame. It is thus probable that these fluctuations are detected in all of the burnt gases and are thus added up by the vibrometer measurements. The 4.2 kHz on the other hand seems to be a more local phenomenon. It does not appear in the glass window and is also weak close to the flame as shown in section 6.2.1. Thus this phenomenon is detected by both diagnostics, however it appears masked by other phenomena in the LIV measurements. This is due to the integrating nature of LIV and leads to these very low amplitudes.

6.3 Conclusion

In this chapter, the density fluctuations are visualized with the help of a focusing Schlieren technique. This technique is constituted of two optically complementary grids and a camera lens, which lead to a field of view of only a few millimetres thickness. It is thus complementary to LIV, which measures line of sight integrated density fluctuations (see chapter 8 for more details). The focusing Schlieren technique is presented in this chapter and its focusing ability is demonstrated by visualizing two crossed supersonic jets.

The focusing Schlieren technique is then applied on the CESAM-HP test bench on the three operating points **Op16-0-2**, **Op16-2-0** and **Op13.4-4.6-0**. The Schlieren imaging is conducted in two regions, near the combustion chamber entry and in the region of the burnt gases. In the chamber entry, the dynamics are dominated by the low frequency combustion instability that was already described in chapter 4. It is especially strong in the conical flame front that can be observed in the instantaneous images. In these images also a wave-like phenomenon at 4.2 kHz propagating downstream can be observed, however the phenomenon is too weak to be detected in the PSD spectra. These frequencies are also observed at the chamber exit. The wave-like phenomenon of 4.2 kHz is visible and can be detected in the PSD spectra, while the spectra of the combustion instability peaks is weaker. In the instantaneous images, these low frequencies can be observed in the appearing and disappearing of these wave-like phenomena.

In a final step, the Schlieren measurements of the burnt gases are compared with LIV measurements in the same region for the three operating points. The spectra obtained from the measurements with both diagnostics feature two peaks: One low frequency peak corresponding to the combustion instability and one high frequency peak around 4.2 kHz associated with the wave-like phenomenon. A high difference between both diagnostics can be observed in the amplitudes of the peaks. However this can be explained by the integrating character of the Vibrometry and the focusing of the applied Schlieren system.

A crude estimation shows, that the wave-like phenomenon propagates downstream at the velocity of the burnt gases. It can thus be assumed that the obtained density fluctuations correspond to the density inhomogeneities of the burnt gases. These density fluctuations can be associated with the downstream propagation of the entropy waves, however they can also be caused by the pressure fluctuation.

The results show that focusing Schlieren is useful to visualize already small density inhomogeneities. Also phenomena close to the swirling flame can be observed and are not covered by the flame itself, as it would be the case in classical Schlieren. The Schlieren images are however very noisy and especially the 4.2 kHz oscillations are very close to the noise of the measurement system. It would be important to optimize the arrangement in order to increase the signal to noise ratio.

Another perspective would be to quantify the observed density or temperature fluctuations. Indeed due to its high sampling frequencies and its focusing Schlieren can become a performing technique with the capability to obtain 2D temperature gradient fields. However, the intensities of Schlieren visualizations depend on the alignment of a system. This is a process which is difficult to be exactly repeatable due to the human factor. It would be thus interesting to develop a calibration process that allows to inject air flow with well defined temperature fluctuations and determine a calibration curve at the fixed optical setting. This optical setting would then be kept when conducting the Schlieren experiments during combustion.

Part III

Determination of direct and indirect combustion noise

Summary

The final part is dedicated to the determination of combustion noise on the CESAM-HP test bench with the help of experiments and analytical calculations. Two approaches are presented in chapter 7 and 8.

In chapter 7 the direct combustion noise is determined with the help of a photomultiplier probe. It is used to measure the heat release fluctuations of the flame. From these, the direct combustion noise contribution is estimated with an analytical calculation.

A different approach is used in chapter 8. Here, the indirect combustion noise is determined experimentally. For this, Laser Interferometric Vibrometry (LIV) is used to measure the line of sight averaged density fluctuations in the exhaust region of the combustion chamber. From these the temperature fluctuations are calculated. The temperature fluctuations, together with the simultaneously measured in-chamber pressure fluctuations, are then used to determine the direct and indirect combustion noise contributions analytically.

Chapter 7

Estimation of direct combustion noise

In this chapter the direct combustion noise contribution is analysed experimentally. This is done by comparing the chamber pressure fluctuations with the global heat release fluctuation, measured by a photomultiplier probe. The heat release fluctuations are used to determine the theoretical pressure fluctuations related to the flame motion. This is conducted using a simplified form of the wave equation. The comparison of this theoretical pressure fluctuations with the measured pressure fluctuation shows a strong coherence between these two signals. This leads to the assumption that the testbench is essentially dominated by direct combustion noise.

7.1 Introduction

The previous chapters show that the CESAM-HP combustor is dominated by a strong combustion instability. While in chapter 3 this instability is linked to the feeding lines of the burner, chapter 4 puts into evidence the other mechanisms that characterize this instability by the coupling between the fluctuations of pressure, velocity and heat release. The time and spatial analyses show that the strongest fluctuations are at low frequency and that the eigen frequencies are equal for the three measured quantities. These observations lead to the assumption that direct combustion noise must be dominating in the combustor.

In this chapter, the focus is put on the experimental determination of direct combustion noise. The approach is based on the link between direct combustion noise generation and the heat release fluctuations of the flame (Candel et al. (2009); Schuller et al. (2002)). With this approach, a theoretical pressure is estimated from the measured heat release rate of the flame. Finally a criterion is defined in order to compare the direct combustion noise generation with the total pressure fluctuations measured in the combustion chamber.

7.2 Theoretical approach to determine direct combustion noise

This section presents the method to calculate the direct combustion noise contribution from the measured pressure and heat release rate fluctuations. Direct combustion noise is generated by the fluctuations of the flame surface and hence the heat release rate. This heat release rate is proportional to the signal measured with a photomultiplier probe (PM). The idea is thus to use this signal to calculate a theoretical pressure p_{cal} which is exclusively associated to the flame dynamics. For this approach, the strong hypothesis is made, that all direct combustion noise is directly proportional to the heat release rate of the flame. The comparison of p_{cal} with the measured pressure p_{meas} can help to draw conclusions about the direct combustion noise contribution. Other hypotheses are that the combustion instabilities, which lead to the heat release fluctuations, are entirely related to direct combustion noise, and that the acoustic fluctuations all correspond to aerodynamic fluctuations.

The relation between heat release rate and pressure fluctuations can be taken from the simplified wave equation (Hassan (1974)):

$$\nabla \cdot (c_0^2 \nabla p') - \frac{\partial^2 p'}{\partial t^2} = -(\gamma - 1) \frac{\partial \dot{q}'}{\partial t} \quad (7.1)$$

c_0 represents the speed of sound, p' the pressure fluctuation and \dot{q}' the heat release rate fluctuation.

In the case of the present configuration it is assumed that the spatial gradients of the pressure fluctuations are small in the combustion chamber. This approach is justified when regarding the following equation for the acoustic waves:

$$c_0 = \lambda f \quad (7.2)$$

with λ the wave length and f the frequency of the acoustic wave. When assuming a speed of sound of 800 m/s in the burnt gases, an acoustic wave at 120 Hz would have a wave length of 6.7 m, thus far above the chamber length of 0.14 m. Even an acoustic wave of 1000 Hz would have a wave length of 0.8 m, thus five times more than the chamber length. These calculations are backed by the observations made in chapter 3. There, the acoustic modes are calculated analytically and presented in figure 3.7. The acoustic modes are also confirmed by the in-chamber pressure measurements on two different positions. Figure 3.7 shows that for frequencies up to 1000 Hz the pressure fluctuations are on the same level all along the chamber. These observations confirm that the spatial gradients of the pressure fluctuations are small. However, this approach would be only valid for low frequencies up to 1000 Hz.

The two terms of the left hand side of Eq. (7.1) can be compared directly when using the pressures which were measured on two positions in the combustion

chamber (position 2 and 4, see chapter 1). In this case the left term can be assumed by calculating the RMS of the difference between the two measured pressures, divided by the square of the distance of the two pressure sensors and multiplied by the square of the speed of sound. It thus becomes:

$$c_0^2 \cdot RMS\left(\frac{p'_{x=122.5mm} - p'_{x=52.5mm}}{122.5mm - 52.5mm}\right)^2 \quad (7.3)$$

The second term can be estimated by calculating RMS of the second derivative of one of the pressure sensors times the square of a chosen frequency. It therefore becomes:

$$f^2 \cdot RMS\left(\frac{\partial^2 p'}{\partial t^2}\right) \quad (7.4)$$

If the speed of sound is assumed as 800 m/s, then the second term is bigger than the first one for all frequencies. The consequence of this reasoning is that the first term of Eq. (7.1) is set to zero. Eq. (7.1) is thus simplified to:

$$\frac{\partial^2 p'}{\partial t^2} = (\gamma - 1) \frac{\partial \dot{q}'}{\partial t} \quad (7.5)$$

It was demonstrated in previous work that the heat release rate is proportional to the PM intensity, under the hypothesis of small fluctuation amplitudes (Schuller et al. (2002)):

$$\dot{q}' = kI' \quad (7.6)$$

with I' the fluctuations of the PM signal intensity and k a constant which depends from the experimental system. Applying this into the wave equation and summarizing all constants as K one obtains

$$\frac{\partial^2 p'}{\partial t^2} = K \frac{\partial I'}{\partial t} \quad (7.7)$$

with $K = (\gamma - 1)k$. The theoretical pressure can be obtained from this equation by integrating twice:

$$p'_{cal} \equiv K \int \int I' dt \quad (7.8)$$

The pressure fluctuations associated to direct combustion noise can thus be obtained by integrating the intensity. This operation is conducted numerically, however a value for the proportionality constant K is needed in order to have the link between PM intensity and the pressure fluctuations. In Schuller et al. (2002), the constant K is obtained by determining the heat release fluctuations from the flame surface (based on the approach of Clavin and Siggia (1991)). In

that work, the flame surface was determined with OH-PLIF on a laminar and radially symmetric flame. This approach cannot be applied in this work, since OH-PLIF measurements are not available. But even if they were, the flame surface could not have been determined correctly since the flame is highly turbulent and non-symmetric.

Thus K is chosen to have the value 1, and p_{cal} and p_{meas} are compared in terms of shape of the measured time series and PSD as well as the coherence between these two pressures. While this does not allow to quantify p_{cal} , it allows to put into evidence the coupling between those two pressures.

The measured and calculated signals are filtered with a 5th degree Butterworth low pass filter with a cut-off frequency of 1000 Hz in order to stay in the limits of the theoretical approach. The Pressure PSD are calculated using Welch's algorithm with Hanning windows with a window size of 2048 and an overlap of about 50 %.

Finally, the coherence is calculated between the two signals. It describes, to what extent they are linked in the frequency domain and is determined by the equation:

$$C_{12} = \frac{|G_{12}|^2}{G_{11}G_{22}} \quad (7.9)$$

with G_{12} the cross spectral density between two signals and G_{11} and G_{22} the autospectral density of each of the signals. The advantage of this approach is that it does not depend on the amplitudes of the signals. It can be thus calculated correctly without having a value for K .

7.3 Applied diagnostics

The direct combustion noise contribution is determined using a pressure sensor and a photomultiplier probe. Their functioning and installation is presented in chapter 1 and is not repeated here. Their positions are summarized in table 7.1, taking into account the coordinate system shown in figure 7.1.

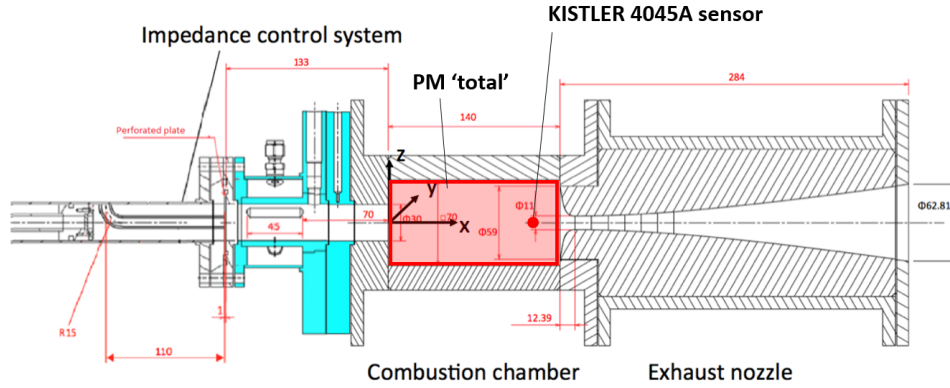


Figure 7.1: Applied coordinate system including the regions described in table 7.1. The coordinate system is right-handed. The y -coordinate is therefore showing away from the reader.

Table 7.1: Positions of the applied pressure sensor and PMs

Sensor	x [mm]	y [mm]	z [mm]
Kistler 4045A sensor	122.5	0	-35
OH* photomultiplier - total	0 to 110	line-of-sight	-35 to 35

The in-chamber static and dynamic pressures are determined by a sensor of type KISTLER 4045A, as described in chapter 1. The sensor is located 122.5 mm downstream of the dump plane, close to the exhaust nozzle. The pressure data is acquired at a 25 kHz sampling frequency during 4 s. The PSD is determined using Welch's algorithm, with windows of 2048 samples each and 50 % window overlapping. This corresponds to a frequency resolution of around 12 Hz

The global heat release rate is obtained by using a photomultiplier probe (PM) with a 313 nm filter, as described in chapter 1. This sensor has the aim to observe the entire combustion chamber. As done with the pressure signal, the OH* spectra are determined by applying Welch's algorithm, with windows of 2048 samples each and 50 % window overlapping.

7.4 Experimental results

7.4.1 Description of the acoustic and OH* emission spectra

The pressure signal and the PM signal are shown in figures 7.2 to 7.4 for the three operating points **Op16-0-2**, **op16-2-0** and **Op13.4-4.6-0**. The figures also contain their PSD. Both signals are drawn on the same diagram with two

separate axes in order to allow for an easier comparison. The scales of the PSD spectra were adapted in order to have a same amplitude at 1000 Hz and for the strongest PSD peak around 120 Hz.

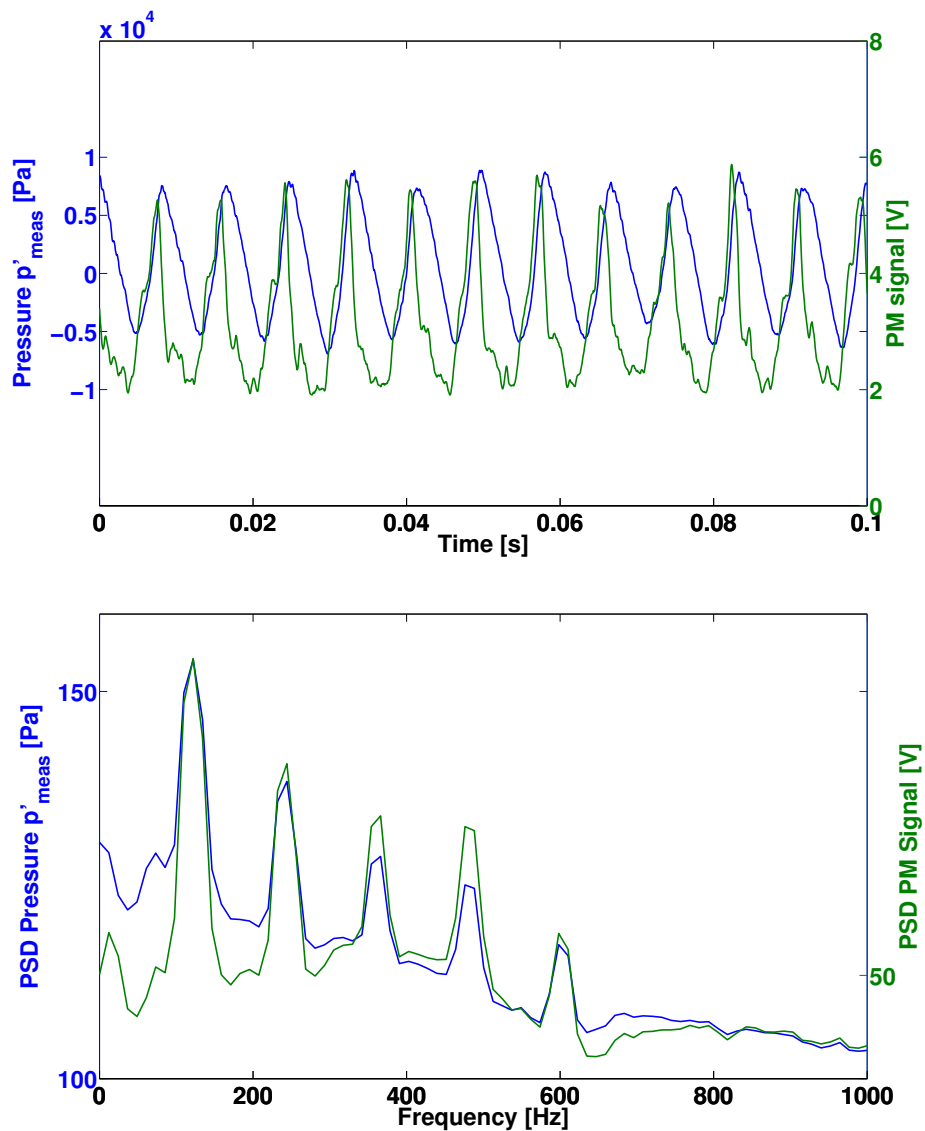


Figure 7.2: Top: Measured pressure and PM signal for *Op16-0-2*. Bottom: PSD pressure and PSD PM signal for the same operating point.

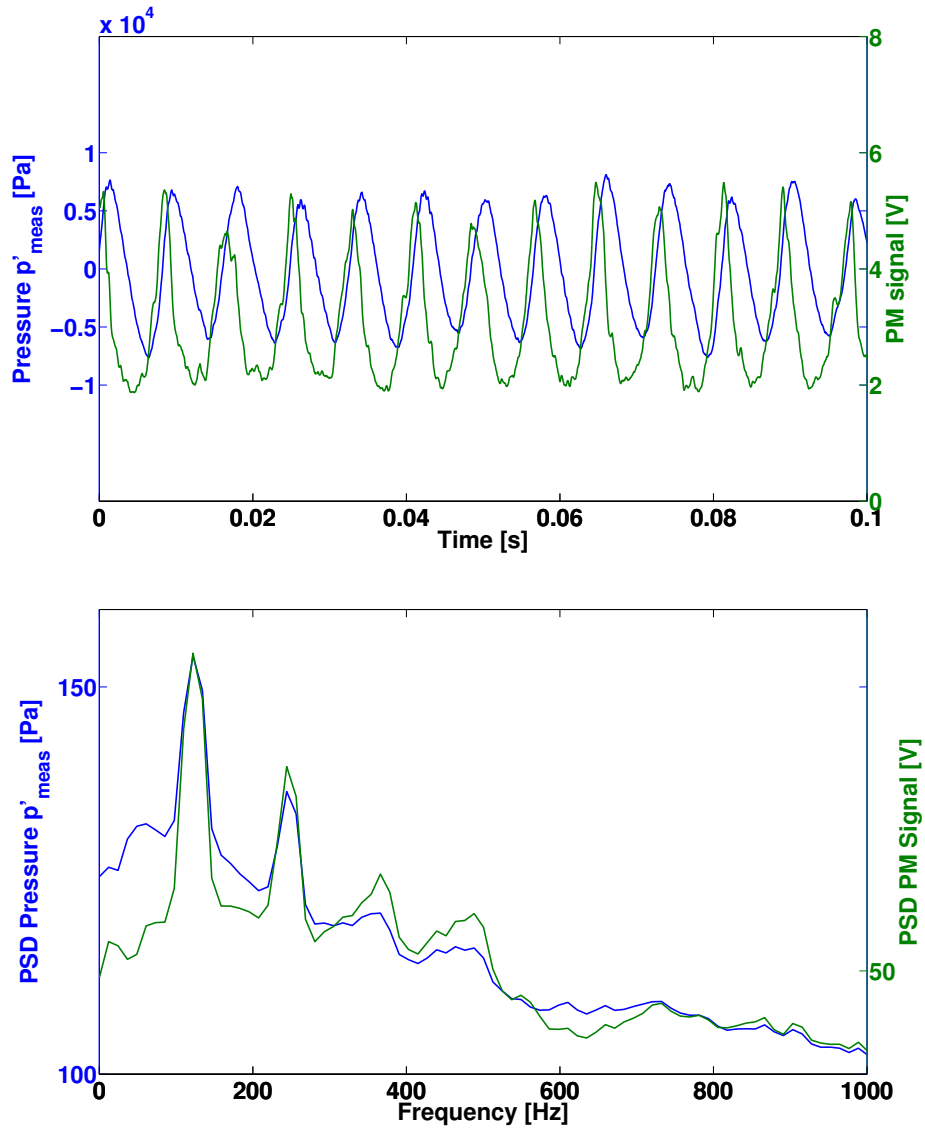


Figure 7.3: Top: Measured pressure and PM signal for *Op16-2-0*. Bottom: PSD pressure and PSD PM signal for the same operating point.

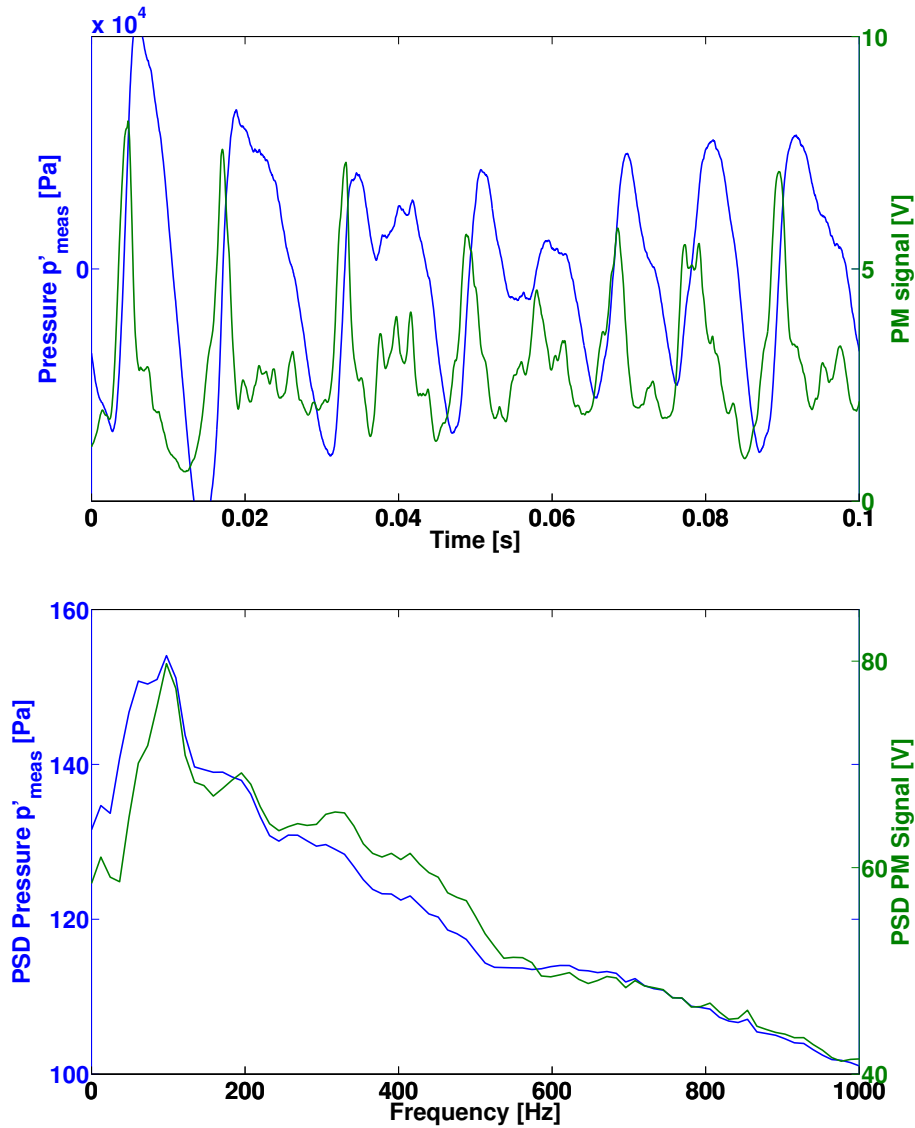


Figure 7.4: Top: Measured pressure and PM signal for **Op13.4-4.6-0**. Bottom: PSD pressure and PSD PM signal for the same operating point.

The figures show that the pressure and PM signal fluctuations for **Op16-0-2** and **Op16-2-0** are dominated by a low frequency fluctuation at a frequency of around 120 Hz. These can also be identified in the PSD spectra shown in the same figures. In the spectra, the same low frequency instability peak and its harmonics can be detected, however the relative amplitudes are not the same for the harmonics. It can also be observed that the low frequency broadband part has higher relative amplitudes in the pressure spectrum.

The amplitudes for **Op13.4-4.6-0** for both measurements are twice as high. Both signals are periodic and have a similar main frequency. However, the

similarity between pressure and PM signal are not as close as for the two other operating points. The PSD image shows for both measured quantities a broadband low frequency peak. In the low frequency region, the relative amplitudes of the pressure fluctuations are higher than those of the PM signal fluctuations. Moreover, a slight difference in amplitude can be identified between 300 and 500 Hz.

As presented and discussed in chapter 4, the distinct peaks in the pressure and PM signal spectra correspond to a low frequency combustion instability. For **Op16-0-2** and **Op16-2-0**, the peak around the 120 Hz is the main peak and the following are its harmonics. These peaks cannot be observed for **Op13.4-4.6-0**, where only one broad low frequency peak can be seen. As suggested in the previous chapters, this peak can be associated to a strong axial flapping motion of the flame.

The OH* results are an indicator for the global heat release dynamics in the test bench. The link between both was demonstrated in previous works (Higgins et al. (2001); Schulz and Sick (2005)). These works show that the PM intensity is proportional to the global heat release rate in the case of a lean premixed flame. This explains the similarity between the pressure and OH* measurements, which can be seen in figures 7.2 to 7.4.

Especially for **Op16-0-2** and **Op16-2-0**, the time profiles and spectra of the pressure and heat release rate are very similar. This allows to suggest that most of the pressure fluctuations in the combustor are associated with the sound generated directly by the flame, which means that direct combustion noise should be dominating. Furthermore, one can see that the pressure and OH* signal are almost in phase. According to the Rayleigh criterion (?), this would mean that the oscillations are associated with a combustion instability (as demonstrated in chapter 4. This would thus lead to a high direct combustion noise contribution.

In **Op13.4-4.6-0**, the similarity between pressure and heat release profile are not that close. Using the same reasoning as for the two other operating points, this would be an indicator for a higher indirect combustion noise contribution. Also here, the phase shift between the two signals seems to be zero, however it is not that clear. According to ?, direct noise should thus be dominant here as well, but not as strong.

7.4.2 Theoretical determination of the direct combustion noise contribution

Based on the obtained data, the direct combustion noise estimation is determined with the approach presented in section 7.2, taking into account that the factor K cannot be obtained for this configuration. The theoretical pressure

p_{cal} is calculated, by applying the integral Eq. (7.8) on the entirely acquired data (4 s at 25 kHz). The resulting p_{cal} for the three operating points as well as their PSL are shown in figure 7.5 to 7.7. The figures also show the measured pressures p_{meas} and their PSD spectra. p_{cal} is plotted in arbitrary unit, since the factor K is not known.

Op16-0-2 and **Op16-2-0** have very similar pressure profiles. The temporal pressure diagrams show that p_{cal} and p_{meas} have a very close shape for both operating points. The PSD are equally very similar for these points. For **Op13.4-4.6-0** the difference between the time profiles of the measured and calculated pressure are globally similar. The PSD results stay very close even for this point.

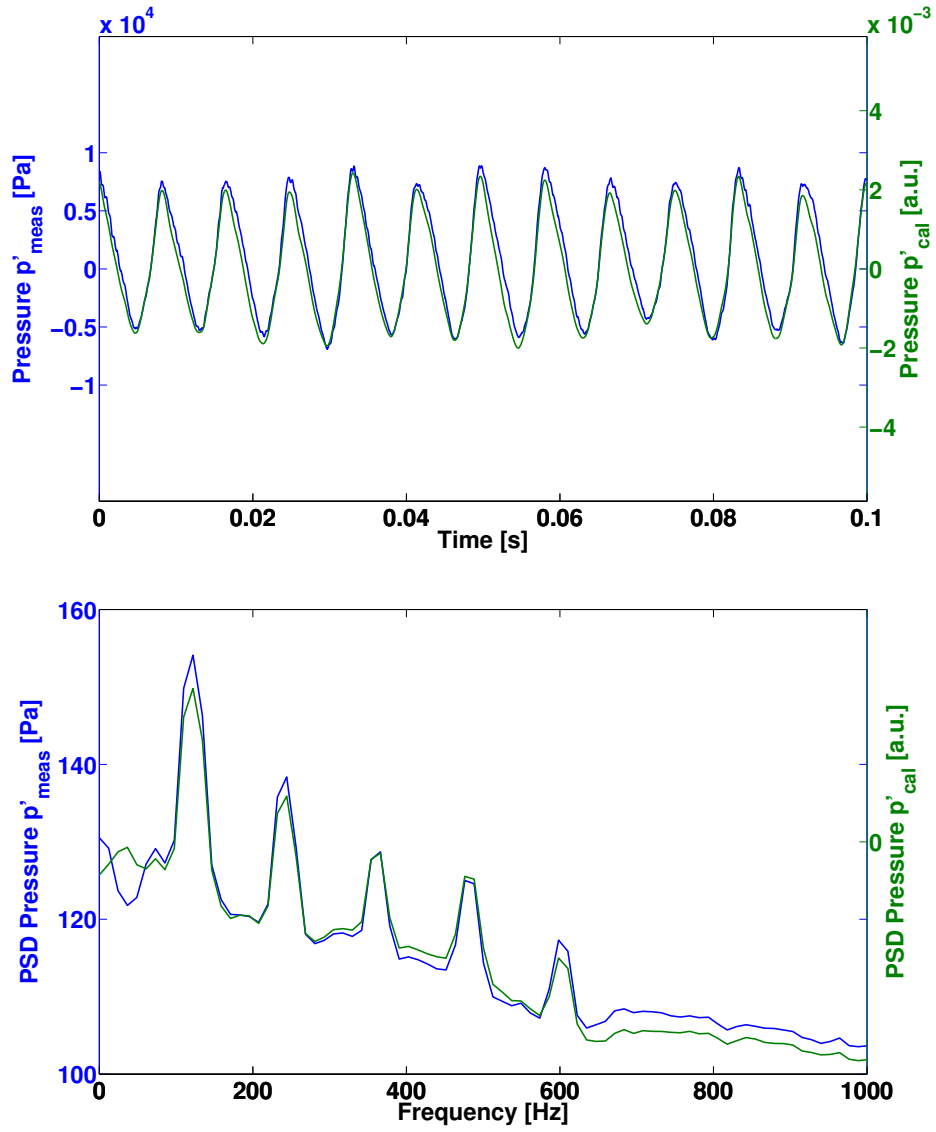


Figure 7.5: Comparison of calculated and measured pressure for *Op16-0-2* and the deduced PSD pressure

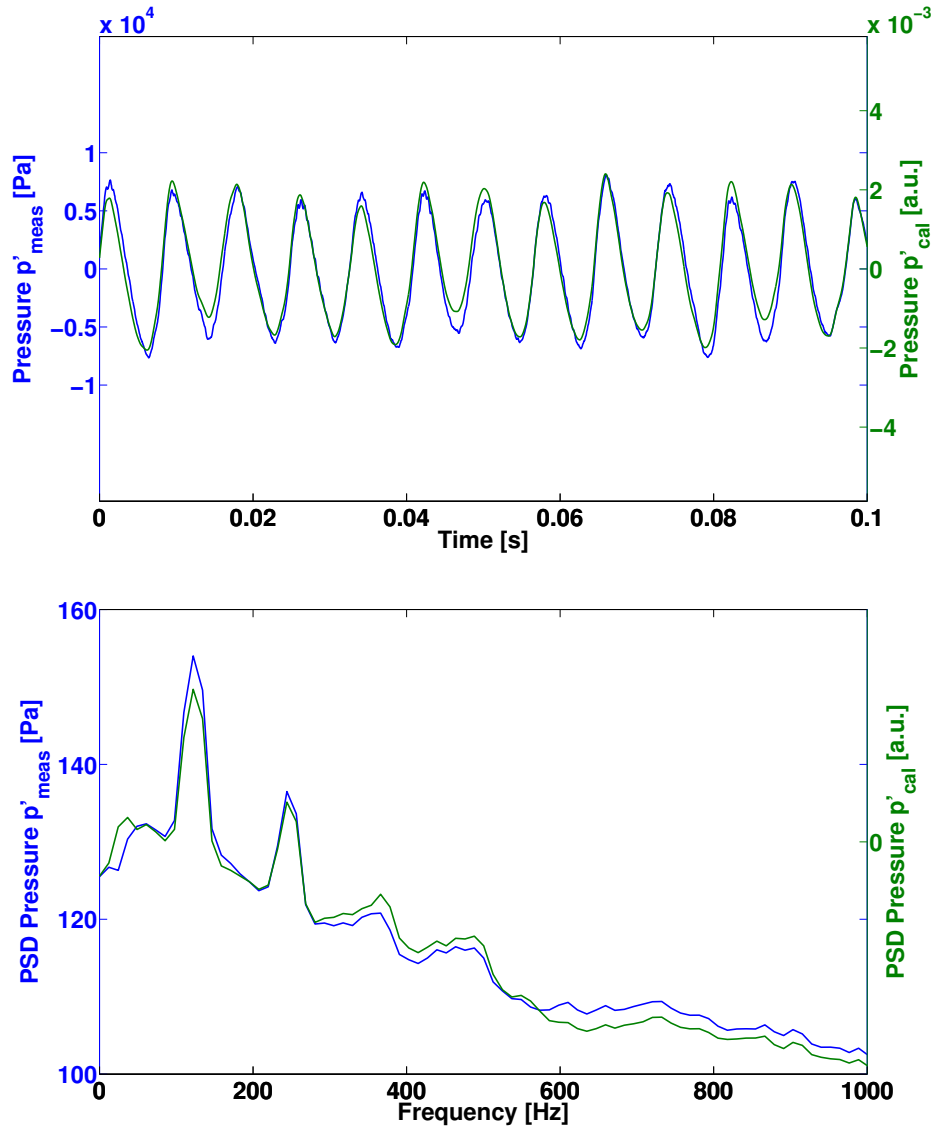


Figure 7.6: Comparison of calculated and measured pressure for *Op16-2-0* and the deduced PSD pressure

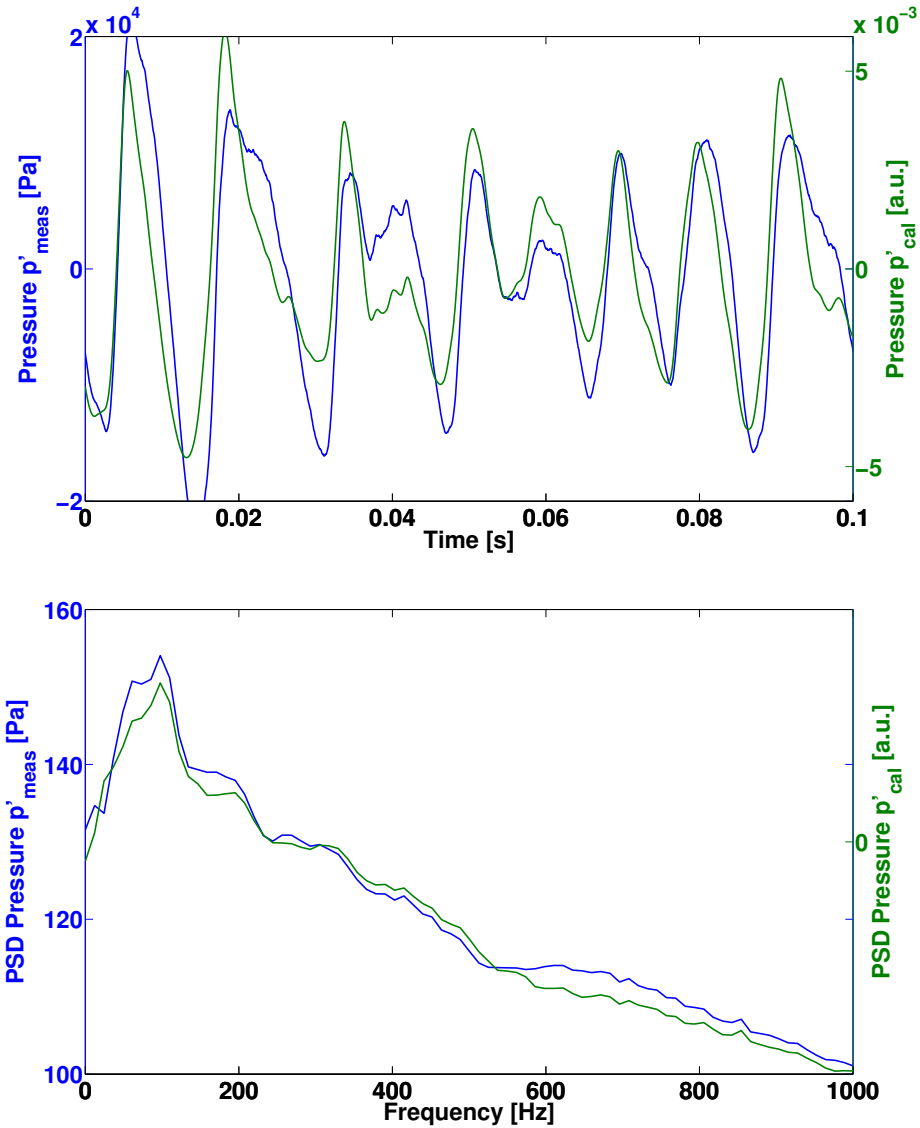


Figure 7.7: Comparison of calculated and measured pressure for *Op13.4-4.6-0* and the deduced PSD pressure

In order to quantify the coupling between p_{cal} and p_{meas} , the coherence between these two signals is regarded. It is shown in figure 7.8 and has a value very close to 1 for all the three operating points. For the main instability frequencies of 120 Hz and its first harmonic 240 Hz the coherence even reaches a value of exactly 1. On the other hand it is low for frequencies below 100 Hz and are also reduced around 600 Hz.

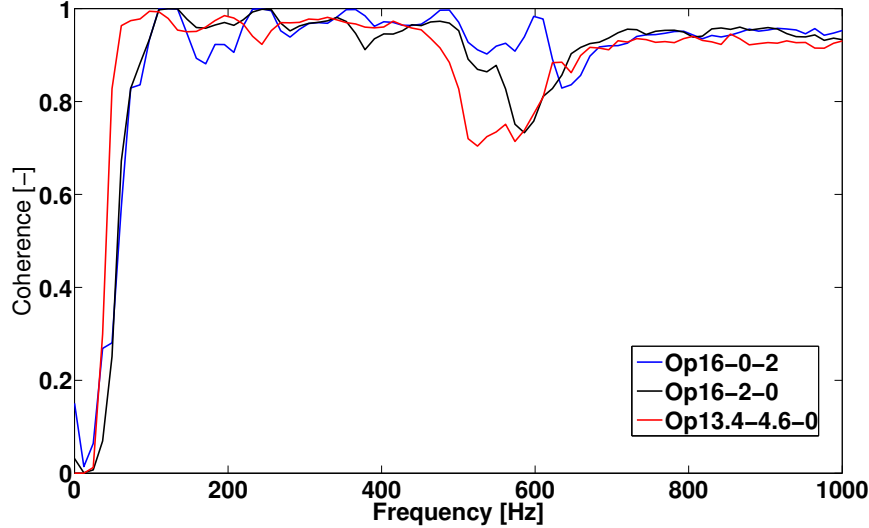


Figure 7.8: Coherence of p_{calc} and p_{meas} for **Op16-0-2**, **Op16-2-0** and **Op13.4-4.6-0**

The coherence corresponds to the observations that were made when comparing the measured pressure signal p_{meas} with the PM signal. It was shown that the relative pressure fluctuations below 100 Hz are higher than the relative PM fluctuations. This might be linked to low frequency pressure fluctuations in the combustor that are not directly linked to the heat release fluctuations of the flame (such as low frequency chamber vibrations).

The reduced coherence around 600 Hz seems to coincide with the fourth harmonic of the main instability peak, especially for **Op16-0-2** and **Op16-2-0**. The more this peak is attenuated, the lower the coherence becomes in this region. Therefore it is lowest for **Op13.4-4.6-0**. The spectra of p_{meas} and the PM signal have slight differences in this frequency range. This might be related to different phenomena, however there is no mean available to study this difference further.

However, even in these regions the coherence is still above 0.8, thus even here the pressure and heat release fluctuations are strongly related.

In spite of these two regions with reduced coherence, the results suggest that the pressure fluctuations are strongly coupled with the heat release fluctuation. This observation was also made in chapter 4 and leads to the suggestion that the three operating points are mostly dominated by direct combustion noise.

7.5 Conclusion

This chapter presents an approach that allows to calculate the direct combustion noise contribution. This is done by calculating a theoretical pressure p_{cal} that is based on the OH* chemiluminescence measurements. p_{cal} is based exclusively on the fluctuations of the flame surface and is hence associated with direct combustion noise. The OH* chemiluminescence is measured with a photomultiplier probe, while the pressure is measured with in-chamber pressure sensors at the same time.

The presented analysis is conducted on the three operating points **Op16-0-2**, **Op16-2-0** and **Op13.4-4.6-0**. The pressure spectra of the three studied operating points are dominated by the low frequency peak and its harmonics. Besides, higher eigen frequencies could be observed. The PM spectra on the other hand only show the low frequency phenomena.

The theoretical pressure fluctuations p'_{cal} are obtained by the presented approach and compared with the measured ones. The comparison shows large similarities in the low-frequency regions for **Op16-0-2** and **Op16-2-0** and **Op13.4-4.6-0**. The spectra between the measured and calculated pressure fluctuations are also very similar. These results suggest that all the three operating points are dominated by the low frequency fluctuations explained in chapter 3.

Finally, the coherence between the two signals is calculated between the theoretical and the measured pressure signals. The results show that for all operating points, both signals have correlations of almost 1. The results confirm the observations made before and also suggest a high direct noise contribution. However, this is a very crude estimation due to the strong hypotheses and simplifications made for this study. It equally does not allow to give a correct quantification since the linear factor between OH* intensity and heat release rate cannot be determined here. Thus for a correct quantification of the indirect combustion noise contribution, the temperature fluctuations of the burnt gases need to be known. This quantification is carried out in chapter 8 with the help of Laser Interferometric Vibrometry (LIV).

Chapter 8

Quantitative determination of direct and indirect combustion noise contributions

This chapter describes the experimental determination of direct and indirect combustion noise. It is based on synchronous measurements of in-chamber pressure and the temperature fluctuations in the burnt gases. The latter are measured by laser interferometric vibrometry, a technique which allows to capture temperature fluctuations at very high frequencies. The direct and indirect combustion noise contributions are obtained by the application of an analytical model of the choked nozzle. The results show that the frequencies of the temperature fluctuations correspond to the main combustion instability frequencies. Finally, the analytical calculation shows that direct combustion noise is the main contributor in the CESAM-HP test bench.

8.1 Introduction

In this chapter, the quantitative determination of direct and indirect combustion noise contributions is described. This is done in two steps: (1) The temperature fluctuations of the burnt gases are measured with the help of Laser Interferometric Vibrometry (LIV). (2) The direct and indirect combustion noise contributions are determined by performing a plane wave separation and using the work of [Marble and Candel \(1977\)](#). This part of the project was conducted under the leadership of Nancy Kings and was presented on various occasions. ([Kings et al. \(2015\)](#); [Kings et al. \(2016\)](#)).

8.2 Experimental procedure

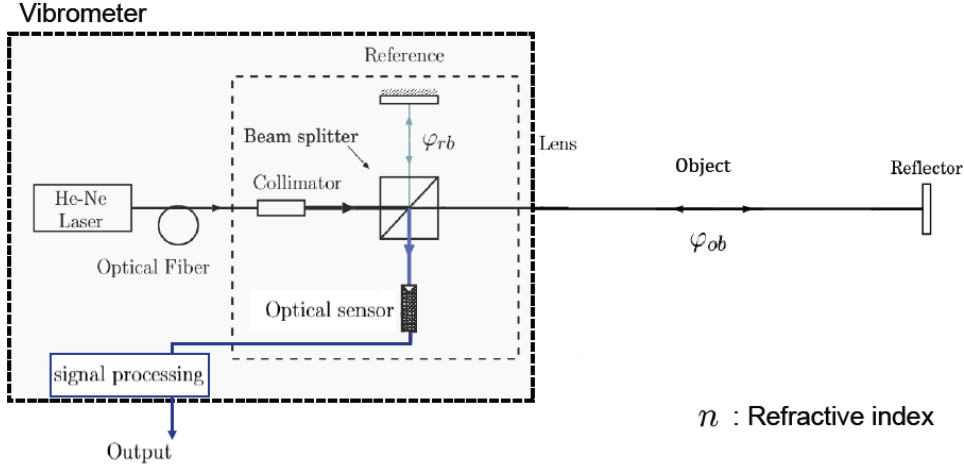


Figure 8.1: *Functioning of LIV (Li (2012); Kings et al. (2015))*

In this work, the temperature fluctuations in the burnt gases are measured by Laser Interferometric Vibrometry (LIV). The functioning of the diagnostic is shown in figure 8.1. A detailed description of the technique was made by Li (2012) and is summarized here.

LIV is traditionally a measurement technique applied to measure vibrations of solid surfaces. In this technique, a continuous laser beam is separated into two beams by a beam splitter. The first beam is reflected by a reference surface that is moving periodically ("reference beam" in the figure). The second beam is reflected by the solid surface, that is being measured ("object beam"), towards the vibrometer. The optical sensor in the vibrometer measures the light intensity which itself depends on the phase shift between the two laser beams and gives out this intensity as an electric voltage. The phase shift can be determined from the refractive indices that are integrated along the laser path:

$$\phi(x, y, t) = \frac{2\pi}{\lambda_0} \int_{object} n(x, y, z, t) dz - \frac{2\pi}{\lambda_0} \int_{reference} n(x, y, z, t) dz \quad (8.1)$$

with z the direction of the laser beam, λ_0 its wavelength and n the refractive index. x and y are constant in this arrangement. If the refractive index is constant one can easily deduce from this equation that the phase shift is proportional to Δz , thus the displacement of the solid object surface.

For the measurements of density fluctuations, the reflecting surface ("Reflector" in figure 8.1) is a fixed mirror. The phase shift hence depends exclusively on

the properties of the medium, in particular the refractive index over the entire beam path, as shown in Eq. (8.1). Thus now the output voltage signal of the vibrometer corresponds to the line-of-sight integrated changes in the refractive index. This is useful for the measurement of densities (and finally temperatures) in gases due to the link between refractive index and fluid density, which is expressed by the Gladstone-Dale relation (Leitgeb et al. (2013); Mayrhofer and Woisetschlager (2001)):

$$n - 1 = G\rho \quad (8.2)$$

with n the refractive index of the gas integrated along the beam line, ρ the gas density and G the Gladstone-Dale coefficient. The presented technique can be thus applied to measure line-of-sight integrated density fluctuations on the CESAM-HP test bench.

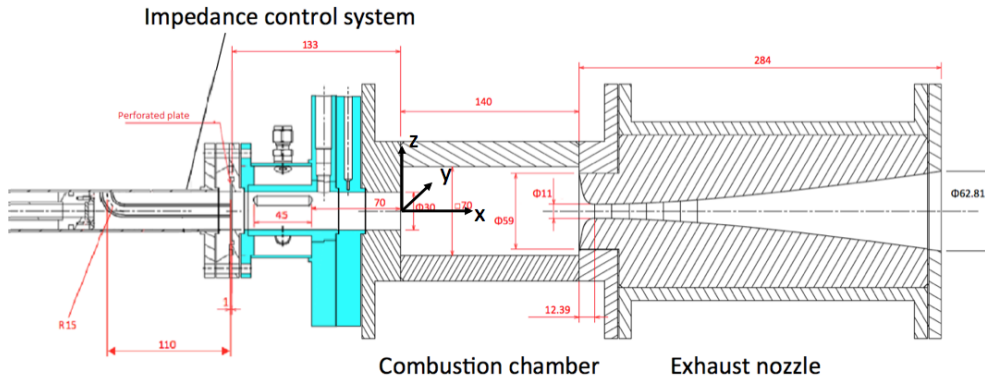


Figure 8.2: Schematic Drawing of the CESAM-HP test bench with the applied coordinate system

The LIV measurement is conducted close to the exhaust nozzle, at $x = 122.5$ mm (Figure 8.2). The vibrometer is of type LSV 2500 from SION Messtechnik GmbH. It can theoretically capture maximal frequencies of up to 500 kHz (GmbH (2006)), thus well above the here studied frequencies and faster than thermocouples (Childs (2003)).

Data acquisition is conducted during 10 s at a sampling frequency of 16384 Hz. The PSD are calculated by conducting Welch's algorithms with Hamming windows, a window size of 16384 elements and a window overlap of around 50 %.

Since the measured density is line-of-sight integrated, it can be expressed as follows (where $\langle \dots \rangle$ is used to write the line-of-sight integrated value in the following):

$$\langle \rho' \rangle = \frac{1}{L} \int_0^L \rho' dy \quad (8.3)$$

Giuliani et al. (2009) has shown, that the voltage signal of the vibrometer is proportional to the line-of-sight integrated density. Taking into account the integration in Eq. (8.3), they obtained the following:

$$U(t) = Gk_g \langle \rho' \rangle L \quad (8.4)$$

with $U(t)$ the vibrometer voltage signal, $k_g = 1000 \text{ V}/\mu\text{m}$ the adjusted vibrometer gain and $G = 2.5 \cdot 10^{-4} \text{ m}^3/\text{kg}$ the constant Gladstone-Dale coefficient (Giuliani et al. (2009)), which depends only on the wavelength of the used laser. The term $\langle \rho' \rangle L$ thus expresses the integral of the local density fluctuations over the line of sight. Typically, Abel transform is applied in order to obtain the density fluctuation at one point. (Giuliani et al. (2009); Köberl et al. (2010); Peterleithner et al. (2015)). In this work however, this approach is not justified due to the radial non-symmetry of the flame and flow. Indeed, the temperature profile calculated for this test bench by Tao (2015) and shown in figure 8.3 leads to the conclusion that radial symmetry cannot be assumed.

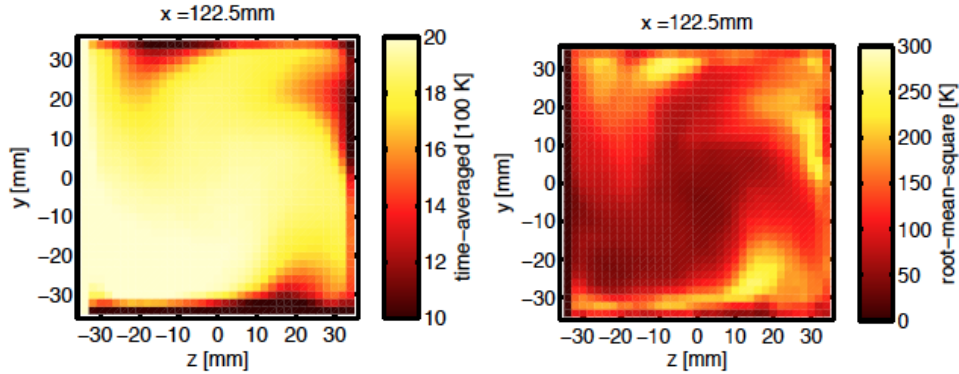


Figure 8.3: Temperature distribution on the y - z -plane at $x = 122.5\text{mm}$, calculated by LES (Tao (2015))

In the here presented calculations, the pressure, temperature and density are respectively decomposed into mean and fluctuating parts:

$$\rho = \bar{\rho} + \rho' \quad (8.5)$$

$$p = \bar{p} + p' \quad (8.6)$$

$$T = \bar{T} + T' \quad (8.7)$$

with the bar indicating the mean part and the prime indicating the fluctuating part.

The measured, line-of-sight averaged density fluctuations ρ'_{tot} have three contributors: (1) The density fluctuations which are caused by acoustic perturbations ρ'_a ; (2) The density fluctuations related to temperature inhomogeneities in the burnt gases ρ'_T ; and (3) A reference value of the measuring system ρ'_{ref} , which corresponds to the measurement noise of the vibrometer. The vibrations of the test bench are neglected in this work. The contributions of the totally measured density fluctuations ρ'_{tot} are additive in the temporal as well as in the frequency domain due to their linearity and are thus:

$$\rho'_{tot} = \rho'_{ref} + \rho'_a + \rho'_T \quad (8.8)$$

The density fluctuations due to composition heterogeneities are not taken into account, since sufficient premixing is assumed. When calculating the line-of-sight average of this equation, one obtains the following:

$$\frac{1}{L} \int_0^L \rho'_{tot} dy = \frac{1}{L} \int_0^L \rho'_{ref} dy + \frac{1}{L} \int_0^L \rho'_a dy + \frac{1}{L} \int_0^L \rho'_T dy \quad (8.9)$$

It has to be taken into account that the measured density fluctuations ρ'_{tot} and ρ'_{ref} are integrated due to the nature of the measurement technique. It is also assumed, that the acoustic and entropy waves are plane waves and that therefore the temperature, density and pressure fluctuations are constant in transverse direction. This hypothesis is typical in entropy noise analysed and has also been used by [Kings et al. \(2016\)](#). With these points, one obtains following:

$$\langle \rho'_{tot} \rangle = \langle \rho'_{ref} \rangle + \rho'_a + \rho'_T \quad (8.10)$$

The equation shows that in order to obtain the spectra of the temperature fluctuations, the reference signal and the acoustic contributors need to be subtracted from the measured signal.

The reference signal ρ'_{ref} is obtained by conducting measurements without flow using the vibrometer ([Kings et al. \(2016\)](#)). The acoustic contribution is calculated from the measured pressure signal (by the Kistler 4045A sensor on position 4) by the equation:

$$\rho'_a = p'_a / \bar{c}^2 \quad (8.11)$$

with p'_a the measured pressure fluctuations, taken by a KISTLER 4045A sensor on the same axial position as the vibrometer measuring location. The speed of

sound c is calculated based on the mean burnt gas temperature, determined by an R-type thermocouple at the same axial position. The mean temperatures are 1920 K for **Op16-0-2** and **Op16-2-0** as well as 1930 K for **Op13.4-4.6-0**. Due to the use of the thermocouple, the uncertainty is not negligible, however it is assumed here for the sake of simplicity.

The measured line-of-sight averaged density fluctuations are used to determine the temperature fluctuations based on the calculations presented in the following.

In a first step, the definition of entropy is used:

$$s' = c_v \ln \frac{p}{\rho^\gamma} \quad (8.12)$$

This equation can be transformed into the following by using basic logarithm rules:

$$s' = c_v (\ln(p) - \gamma \ln(\rho)) \quad (8.13)$$

The entropy fluctuations can be determined with the derivation of entropy, which results in the following equation:

$$s' = \left. \frac{ds}{dp} \right|_\rho p' + \left. \frac{ds}{d\rho} \right|_p \rho' \quad (8.14)$$

When this derivation is applied on Eq. (8.13), the following equation is obtained:

$$s' = c_v \frac{p'}{\bar{p}} - c_p \frac{\rho'}{\bar{\rho}} \quad (8.15)$$

when applying $\gamma = c_p/c_v$, the ideal gas law $\bar{p} = \bar{\rho}r\bar{T}$ and the equation for the speed of sound $c = \sqrt{\gamma r\bar{T}}$, one obtains the following equation, which can also be found in [Leitgeb et al. \(2013\)](#) and [Crighton et al. \(1992\)](#):

$$\rho' = \frac{p'}{\bar{c}^2} - \frac{\bar{p}}{c_p} s' \quad (8.16)$$

with ρ the density, c the speed of sound, p the pressure and s' the entropy fluctuations.

In a second step, Gibb's equation is used:

$$\bar{T} s' = c_v T' - \frac{\bar{p}}{\bar{\rho}^2} \rho' \quad (8.17)$$

Taking into account $\gamma = c_p/c_v$ and $c_p = \gamma r/(\gamma - 1)$, this equation becomes

$$s' = \frac{c_p T'}{\gamma \bar{T}} - \frac{\bar{p} \rho'}{\bar{\rho}^2 \bar{T}} \quad (8.18)$$

The density fluctuations can be obtained when combining the decompositions into mean and fluctuation part of density, pressure and temperature (Eq. (8.5) to (8.7)) with the ideal gas law $\bar{p} = \bar{\rho} r \bar{T}$. This combination leads to following equation:

$$\frac{p'}{\bar{p}} = \frac{\rho'}{\bar{\rho}} + \frac{T'}{\bar{T}} \quad (8.19)$$

When Eq. (8.19) is applied into Eq. (8.18), one obtains following:

$$s' = \frac{c_p T'}{\gamma \bar{T}} - \frac{\bar{p}}{\bar{\rho} \bar{T}} \left(\frac{p'}{\bar{p}} - \frac{T'}{\bar{T}} \right) \quad (8.20)$$

When simplifying this equation arithmetically and applying $c_p = \gamma r/(\gamma - 1)$, one finally obtains the following expression for the entropy fluctuations:

$$s' = c_p \frac{T'}{\bar{T}} - c_p \frac{\gamma - 1}{\gamma} \frac{p'}{\bar{p}} \quad (8.21)$$

When combining Eq. (8.16) and (8.21), one obtains the following equation:

$$\rho' = \frac{p'}{c^2} - \bar{\rho} \frac{T'}{\bar{T}} + \frac{\gamma - 1}{\gamma} \frac{p'}{\bar{p}} \bar{\rho} \quad (8.22)$$

Taking into account the ideal gas law $\bar{p} = \bar{\rho} r \bar{T}$, the equation for the speed of sound $c = \sqrt{\gamma r \bar{T}}$ and Eq. (8.11), one obtains the following:

$$-\frac{T'}{\bar{T}} = \frac{\rho'}{\bar{\rho}} - \gamma \frac{\rho'_a}{\bar{\rho}} \quad (8.23)$$

The line of sight averaged expression of this equation becomes:

$$-\frac{1}{L} \int_0^L \frac{T'}{\bar{T}} dy = \frac{1}{L} \int_0^L \frac{\rho'}{\bar{\rho}} dy - \frac{1}{L} \int_0^L \gamma \frac{\rho'_a}{\bar{\rho}} dy \quad (8.24)$$

Taking into account that the pressure is measured for the entire chamber, the equation becomes following (following the same reasoning as for Eq. (8.10)):

$$-\frac{\langle T' \rangle}{\bar{T}} = \frac{\langle \rho' \rangle}{\bar{\rho}} - \gamma \frac{\rho'_a}{\bar{\rho}} \quad (8.25)$$

In this case, $\langle \rho' \rangle$ corresponds to the measured line integrated density fluctuations minus the reference signal, thus $\langle \rho' \rangle = \langle \rho'_{tot} \rangle - \langle \rho'_{ref} \rangle$. In the present study, the Fourier transforms of the temperature fluctuations are searched for. Using the definition of the Fourier transform this leads to:

$$FT(-\langle T' \rangle) = \frac{1}{\sqrt{2\pi}} \int_{-\infty}^{\infty} \frac{\bar{T}}{\bar{\rho}} (\langle \rho' \rangle - \gamma \rho'_a) e^{-i\omega t} \quad (8.26)$$

Since the mean temperature and density are constant, they can be taken out of the integral. Equally, the linearity of the Fourier transform can be used to separate the sum. If this is done, one obtains finally following:

$$FT(-\langle T' \rangle) = -FT(\langle T' \rangle) = \frac{\bar{T}}{\bar{\rho}} (FT(\langle \rho' \rangle) - \gamma \cdot FT(\langle \rho'_a \rangle)) \quad (8.27)$$

Finally, the entropy related temperature fluctuations T'_e can be calculated. If assuming that the pressure oscillations do not generate any entropy oscillations, T'_e can be obtained by the following equation:

$$-\frac{T'_e}{\bar{T}} = -\frac{\rho'_e}{\bar{\rho}} \quad (8.28)$$

Using Eq. (8.8) and $p'_a/(\gamma\bar{p}) = \rho'_a/(\bar{\rho})$ (isentropy), one obtains the following equation:

$$-\frac{T'_e}{\bar{T}} = -\frac{\rho'_{tot} - \rho'_{ref}}{\bar{\rho}} + \frac{p'_a}{\gamma\bar{p}} \quad (8.29)$$

On this equation, the same line-of-sight averaging and Fourier calculation are applied as on Eq. (8.27).

Data acquisition is conducted during 10 s at a sampling frequency of 16384 Hz. The Fourier transforms are calculated with the classic FFT algorithm. While this has the disadvantage of a high noise level (higher than that of the Welch algorithm for example), it keeps the information about the phase.

8.3 Temperature fluctuations of the burnt gases

The measured raw density profiles $\langle \rho'_{tot} \rangle$ of **Op16-0-2**, **Op16-2-0** and **Op13.4-4.6-0** are respectively shown in figures 8.4 to 8.6. They also include the calculated density fluctuations due to pressure and temperature fluctuations ρ'_a and ρ'_T . Besides, they include the measured reference signal $\langle \rho'_{ref} \rangle$. The diagrams are shown in linear scale in order to compare the amplitudes of the different contributors. The figures show the norm of the signals in order to compare the intensities of the fluctuations.

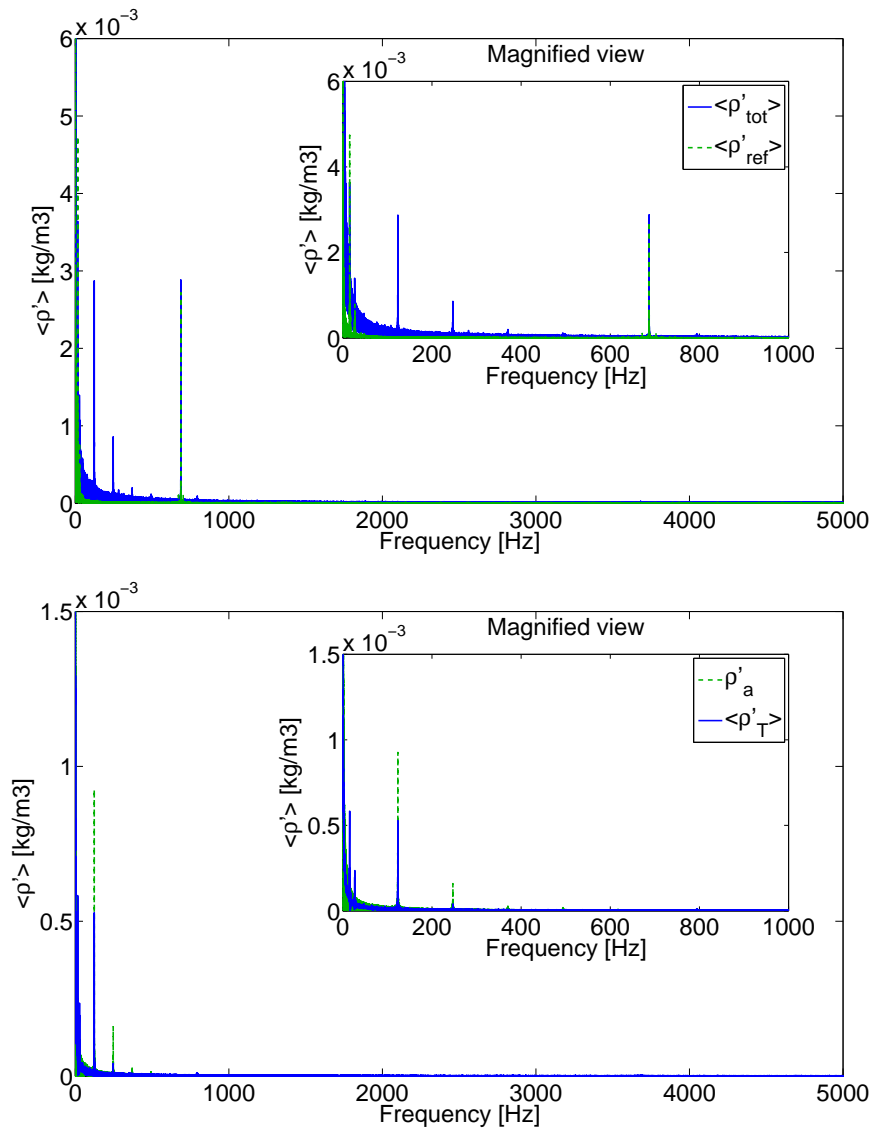


Figure 8.4: Top: Raw density spectrum of *Op16-0-2* measured by LIV, including the contribution of the measurements system vibrations. Bottom: Density fluctuations calculated from in-chamber pressure fluctuations and the temperature fluctuations

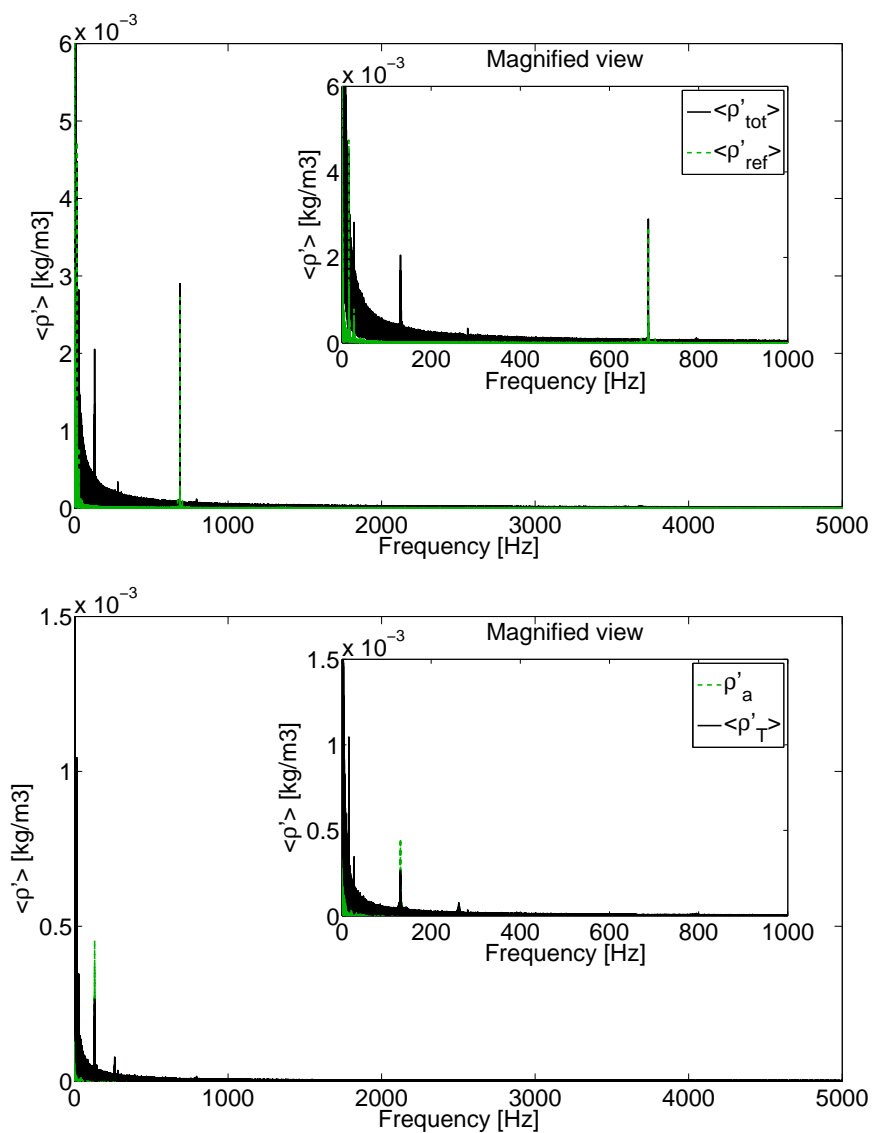


Figure 8.5: Top: Raw density spectrum of *Op16-2-0* measured by LIV, including the contribution of the measurements system vibrations. Bottom: Density fluctuations calculated from in-chamber pressure fluctuations and the temperature fluctuations

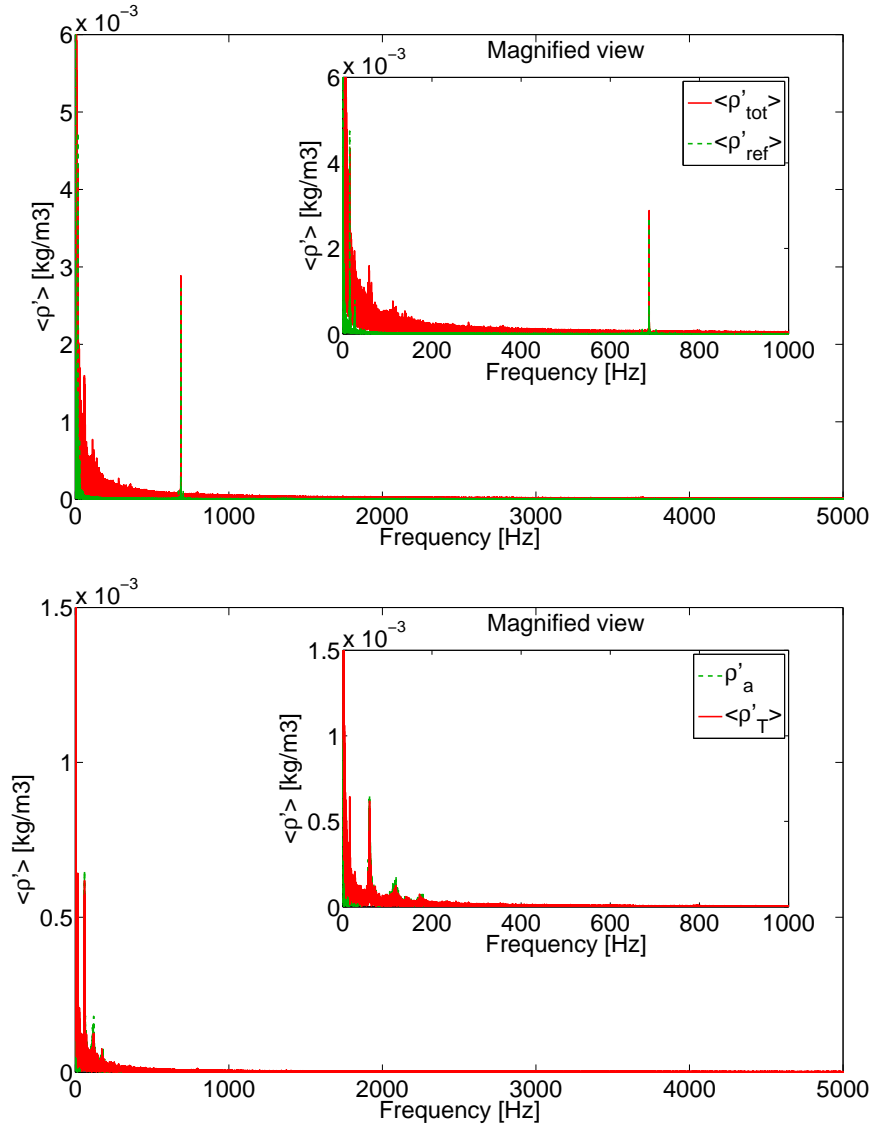


Figure 8.6: *Top: Raw density spectrum of Op13.4-4.6-0 measured by LIV, including the contribution of the measurements system vibrations. Bottom: Density fluctuations calculated from in-chamber pressure fluctuations and the temperature fluctuations*

For the three operating points, most of the oscillations are observed for frequencies below 1 kHz. The sharp low frequency peaks observed in **Op16-0-2** and **Op16-2-0** are at around 120 Hz and their harmonics were already observed in chapter 3 and 4. **Op13.4-4.6-0** equally features its main activity in the low frequency region around 100 Hz. The FFT spectrum has a broad band contribution, which was also seen in chapter 4 for this point. An important peak can be observed at 700 Hz, however it has the same intensity for ρ_{tot} and ρ_{ref} and therefore is probably associated to the measurement system. Besides

these peaks, the measurements show activity in the very low frequency region below 25Hz for all three operating points, however no explanation was found for it. As shown in the modal analysis in chapter 3, this frequency does not belong to the detected ones and thus cannot be linked to combustor acoustics. The figures also show, that the pressure-related density fluctuations are well above those that are associated with the temperature fluctuations.

The line-of-sight averaged temperature spectra are obtained from these density spectra by the procedure described at the end of section 8.2. Therefore the test bench vibrations and the density fluctuations due to acoustics are subtracted from the raw vibrometer signal.

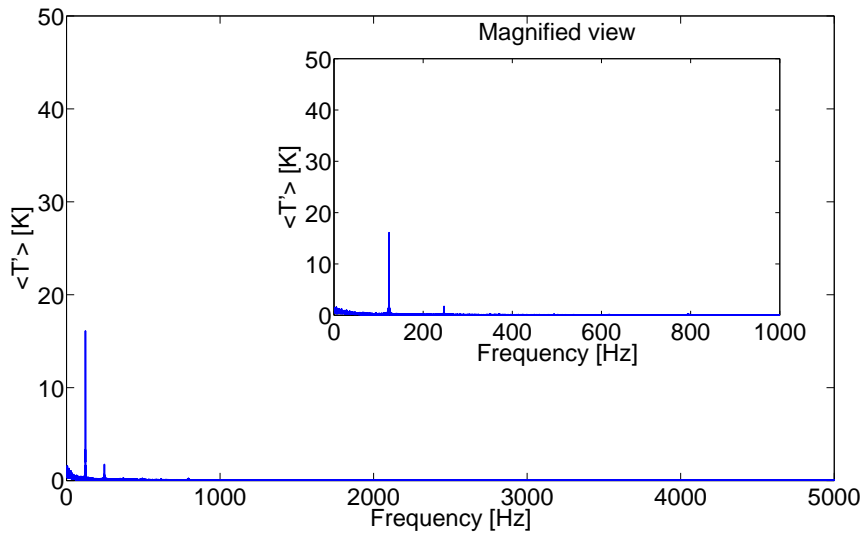


Figure 8.7: *Temperature spectrum of Op16-0-2 measured by LIV*

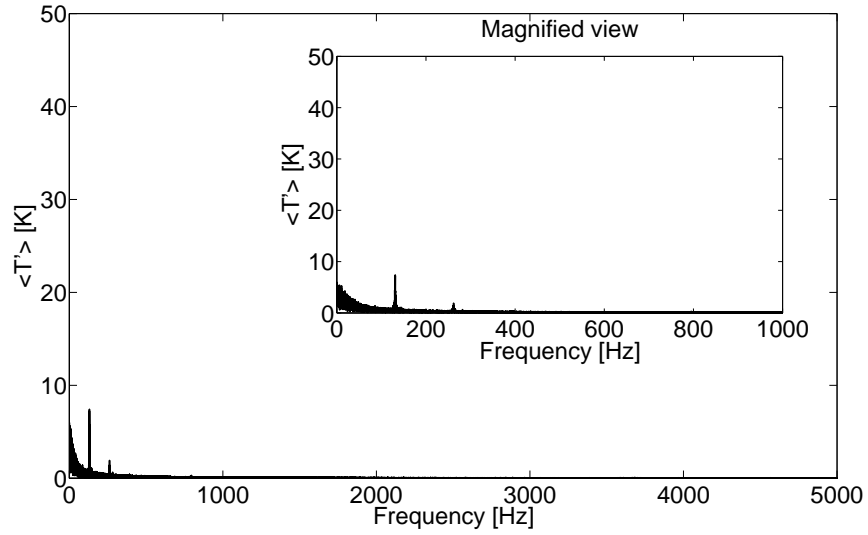


Figure 8.8: Temperature spectrum of *Op16-2-0* measured by LIV

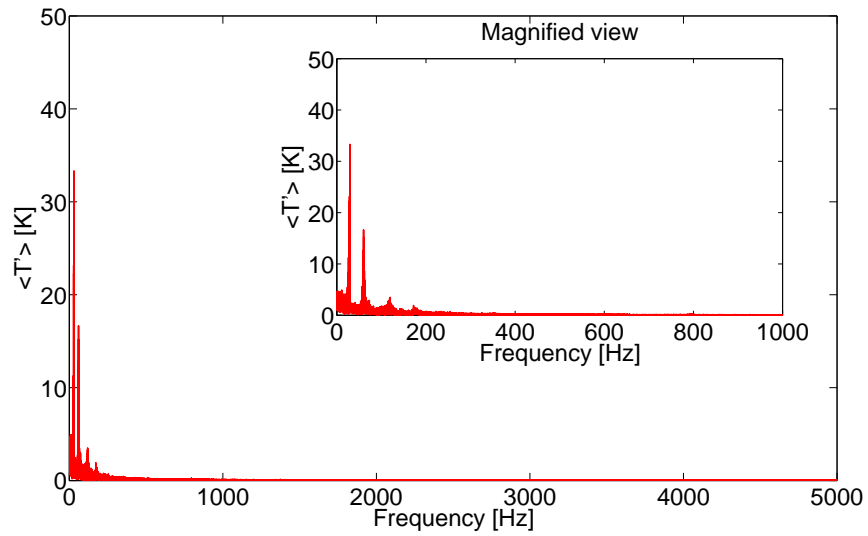


Figure 8.9: Temperature spectrum of *Op13.4-4.6-0* measured by LIV

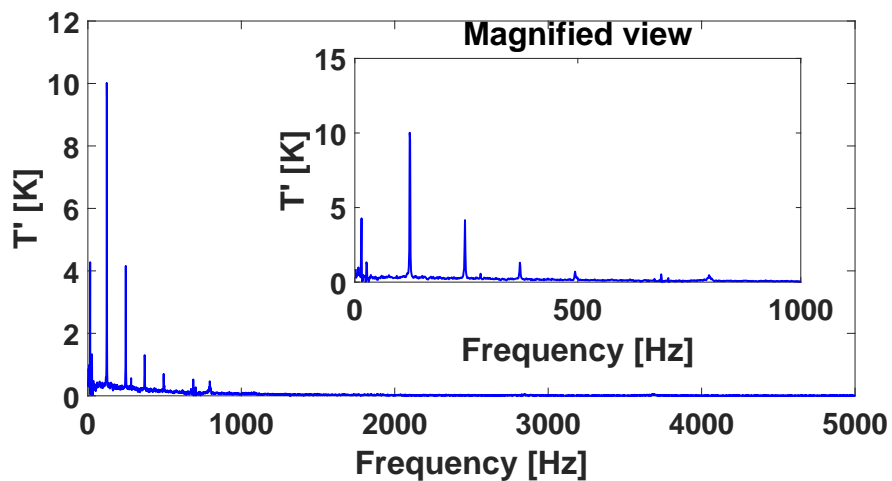


Figure 8.10: Entropy related temperature spectrum of *Op16-0-2* measured by *LIV*

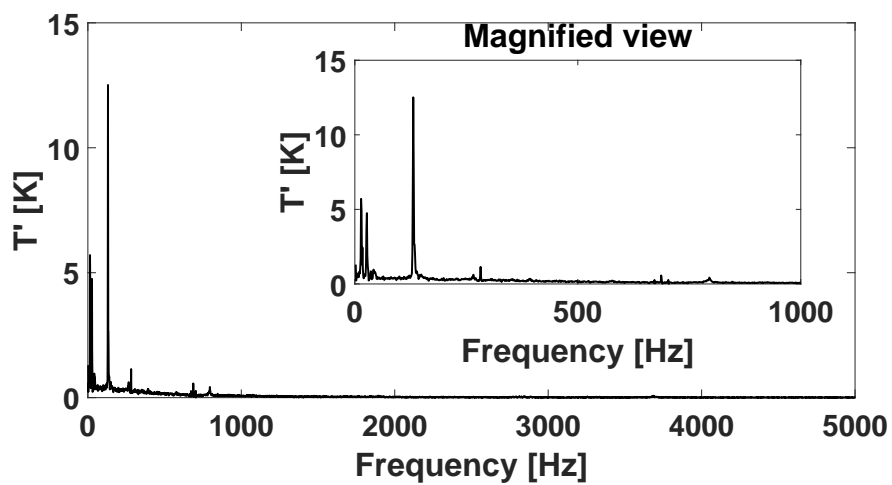


Figure 8.11: Entropy related temperature spectrum of *Op16-2-0* measured by *LIV*

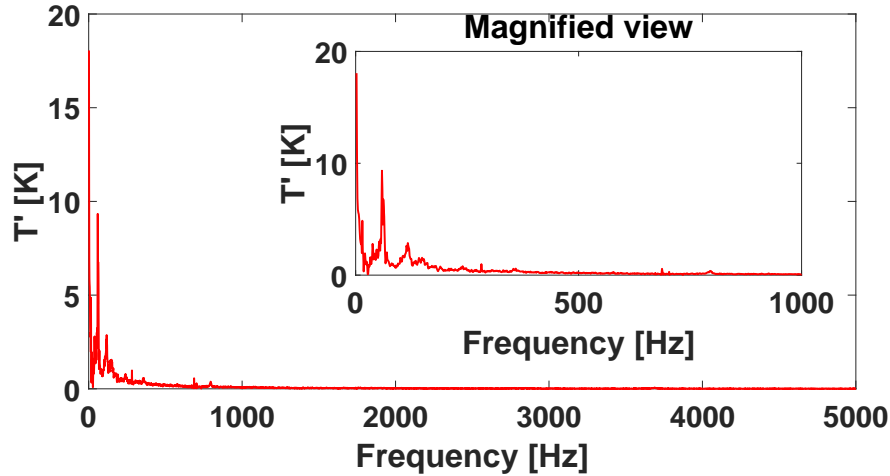


Figure 8.12: Entropy related temperature spectrum of **Op13.4-4.6-0** measured by LIV

The Fourier transforms of the integrated temperature fluctuations are shown in figures 8.7 to 8.9 for the three operating points. The spectra are dominated by the low frequency oscillations. The comparison between the density and temperature spectra of **Op16-0-2** and **Op16-2-0** shows that in particular the harmonics of the main low frequency peaks are attenuated. Equally, for all three operating points the very low frequency dynamics are reduced. The first observation allows for the estimation, that this is due to the subtraction of the acoustic part, where these harmonics are strong. The second observation confirms the assumption that the very low frequency phenomena below 25 Hz are partly associated with the measuring system vibrations.

The Fourier transform of the entropy related line-of-sight integrated temperature fluctuations are shown in figures 8.10 to 8.12. They feature the same frequency peaks as the other temperature spectra however their amplitude is lower, at around 10 K for all operating points. Furthermore, the harmonics are stronger for this case.

The spectra also show that the temperature fluctuations are low for all three operating points. They have values below 40 K for **Op13.4-4.6-0** and even below 20 K for the two other operating points. Furthermore, these temperature spectra have the same peak structure as observed in the study of the combustion instability in chapter 4. The same low frequency dynamics are dominating the velocity fields, the flame chemiluminescence visualisations and the pressure measurements. These dynamics are associated with a low frequency combustion instability, which causes direct combustion noise. Indeed, the acoustic and aerodynamic fluctuations of the flame might not only cause the strong tempera-

ture fluctuations of the flame itself but generate the heat release fluctuations in the burnt gases. Finally these results lead to the assumption that the generated indirect combustion noise is rather low.

Finally the time signals of the temperature fluctuations are obtained by directly calculating Eq. (8.27). Figures 8.13 to 8.15 show this temperature signal for the three operating points, as well as the pressure signal. Both are measured at the same axial position $x=122.5$ mm.

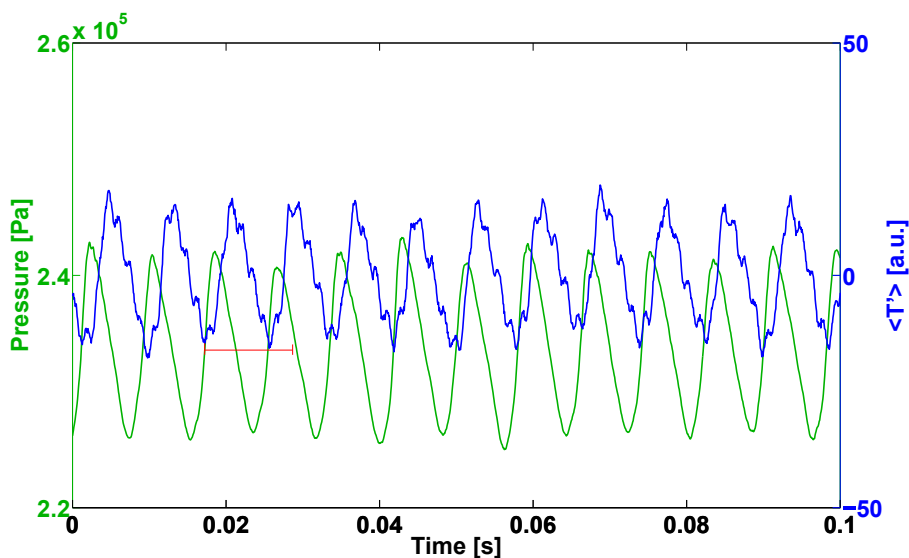


Figure 8.13: Time signal of the pressure and the temperature for *Op16-0-2*. The red horizontal line shows the phase shift between the two signals.

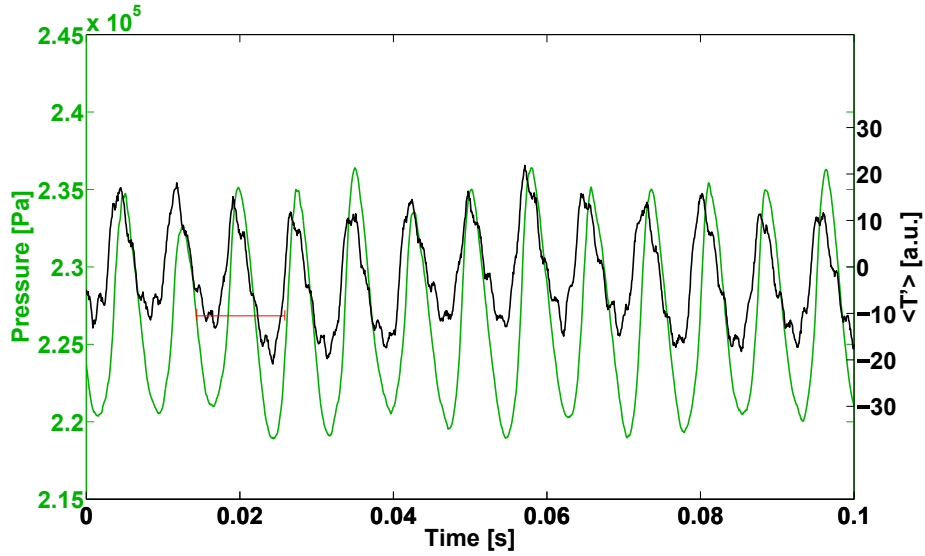


Figure 8.14: Time signal of the pressure and the temperature for *Op16-2-0*. The red horizontal line shows the phase shift between the two signals.

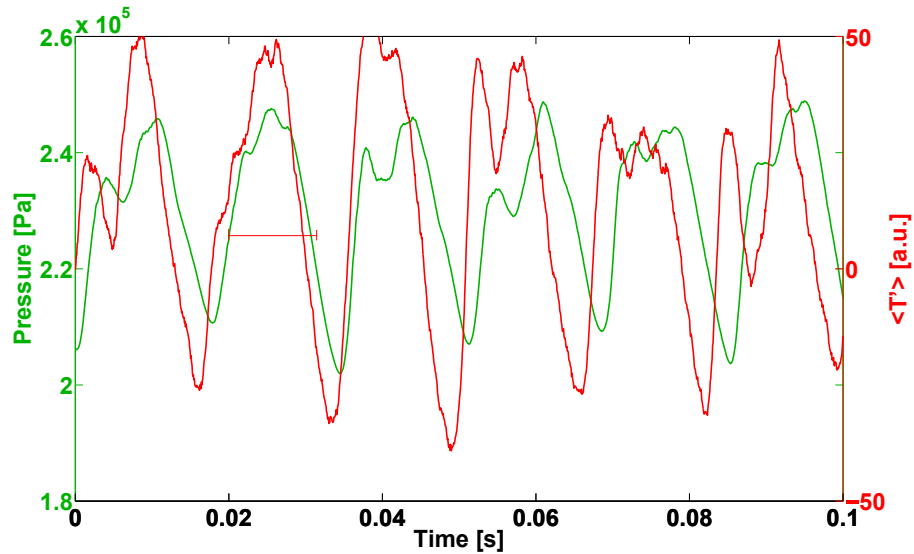


Figure 8.15: Time signal of the pressure and the temperature for *Op13.4-4.6-0*. The red horizontal line shows the phase shift between the two signals.

The figures show that the main oscillation frequency of the temperature signal is equal to that of the pressure signal. This is obvious, since already the FFT spectra have shown that the pressure and temperature fluctuations have the same eigen frequency. But the temperature signal has also oscillations of higher frequencies. These seem to be related to measurement noise, as distinct peak

can be observed above 1 kHz in the temperature spectra. It can also be seen that the temperature and pressure signals do not have the same phase, which is due to the different velocities of the acoustic and entropy waves. When assuming that both are generated in the injector dump plane $x=0$ mm, they cross a distance of 122.5 mm until they arrive to the location where the pressure and temperature fluctuations are measured. At a speed of sound of around 670 m/s (see table 8.1), this leads to a propagation duration of 0.18 ms. The entropy waves propagate at the flow velocity of the burnt gases. When assuming a total mass flow rate of 19 g/s and a burnt gas temperature of 1900 K and a square chamber section of 70 mm \times 70 mm, the burnt gas velocity is calculated to around 8 m/s. Therefore, the temperature fluctuations need around 15.31 ms to propagate until the position where the temperature fluctuations are measured. The phase difference in the figures is thus 15.13 ms. This corresponds to more than one and a half periods of the 120 Hz eigenfrequency, which corresponds to around 11.4 rad.

8.4 Determination of direct and indirect combustion noise contribution

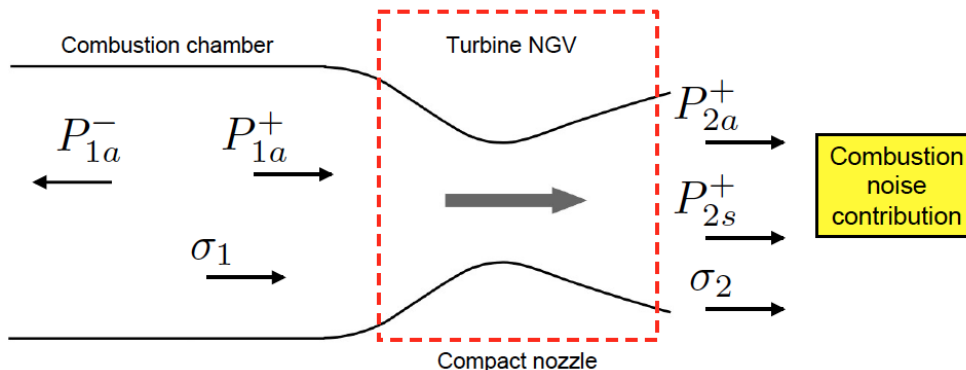


Figure 8.16: Representation of the approach to determine direct and indirect combustion noise contributions (Kings et al. (2015)). The reflections at both ends are neglected.

As indicated in the beginning of this chapter, the measured temperature fluctuations can be used to determine the indirect combustion noise contribution. The approach is presented in figure 8.16 and consists of three steps: (1) The in-chamber acoustics are separated into upstream and downstream characteristic waves. (2) The entropy fluctuations are calculated from the determined temperature fluctuations. (3) The combustion noise resulting from the acoustic and the entropy wave propagating through the exhaust nozzle are calculated using the results of Marble and Candel (1977).

The plane wave separation is based on the work of [Chung and Blaser \(1980\)](#) and the pressures measured by the in-chamber pressure sensors. The pressure measured by each sensor is normalized to $P = p/(\gamma\bar{p})$ ([Marble and Candel \(1977\)](#)) and expressed as follows in the frequency domain for the sensor positions 2 and 4:

$$\hat{p}'_2 = P^+ e^{-ik_+(x_2-x_0)} + P^- e^{ik_-(x_2-x_0)} \quad (8.30)$$

$$\hat{p}'_4 = P^+ e^{-ik_+(x_4-x_0)} + P^- e^{ik_-(x_4-x_0)} \quad (8.31)$$

with \hat{p}'_2 and \hat{p}'_4 the measured pressure fluctuations in the frequency domain, P^+ and P^- the amplitudes of the up- and downstream propagating pressure wave, (x_2-x_0) and (x_4-x_0) the axial distance of the respective pressure sensor from the origin and k_+ and k_- the wave numbers of the up- and downstream propagating pressure wave. These wave numbers are expressed as follows:

$$k_+ = \frac{k}{1 + M_1} \quad (8.32)$$

$$k_- = \frac{k}{1 - M_1} \quad (8.33)$$

with k the wave number and M_1 the Mach number of the burnt gases just before entering the exhaust nozzle.

Based on [Marble and Candel \(1977\)](#) the normalized downstream entropy wave can be calculated by

$$\sigma = \frac{s'_1}{c_p} = \frac{T'}{\bar{T}} - \frac{\gamma - 1}{\gamma} \frac{p'}{\bar{p}} \quad (8.34)$$

where all values are either measured in the testbench or nature constants.

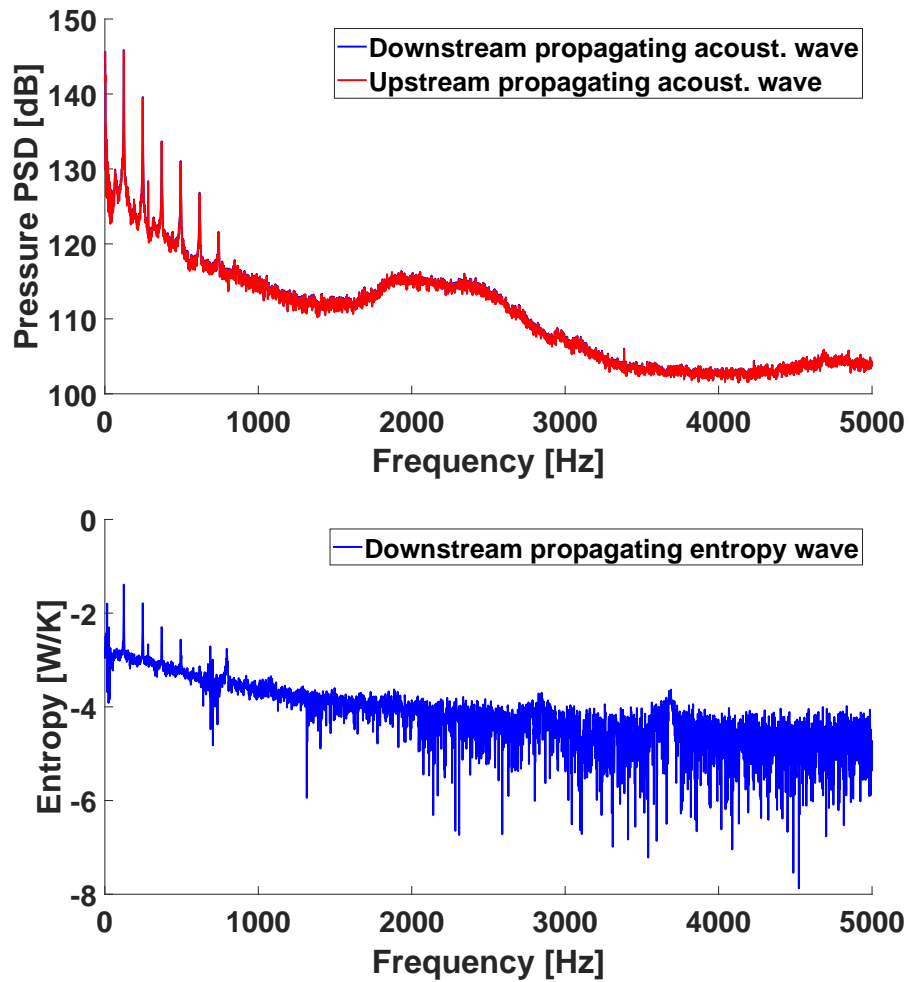


Figure 8.17: Spectra of the pressure oscillations of the up- and downstream propagating acoustic wave as well as of the downstream propagating entropy wave in the combustion chamber for *Op16-0-2*

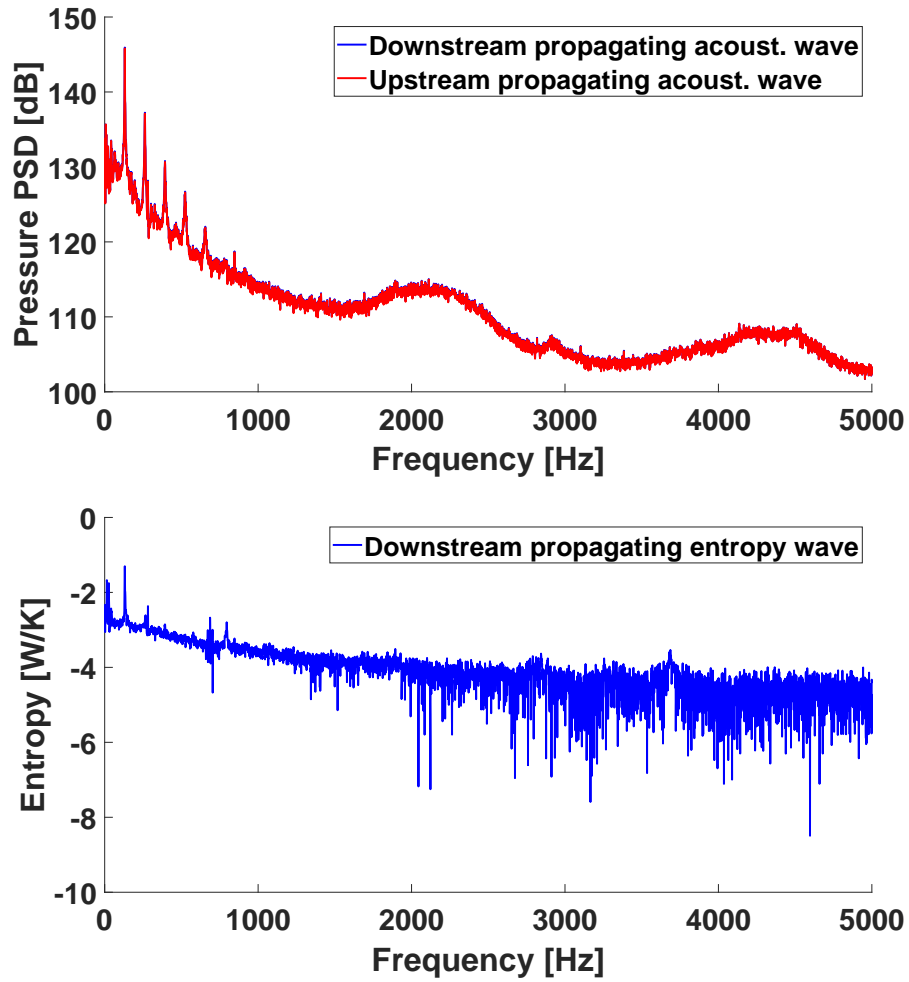


Figure 8.18: Spectra of the pressure oscillations of the up- and downstream propagating acoustic wave as well as of the downstream propagating entropy wave in the combustion chamber for *Op16-2-0*

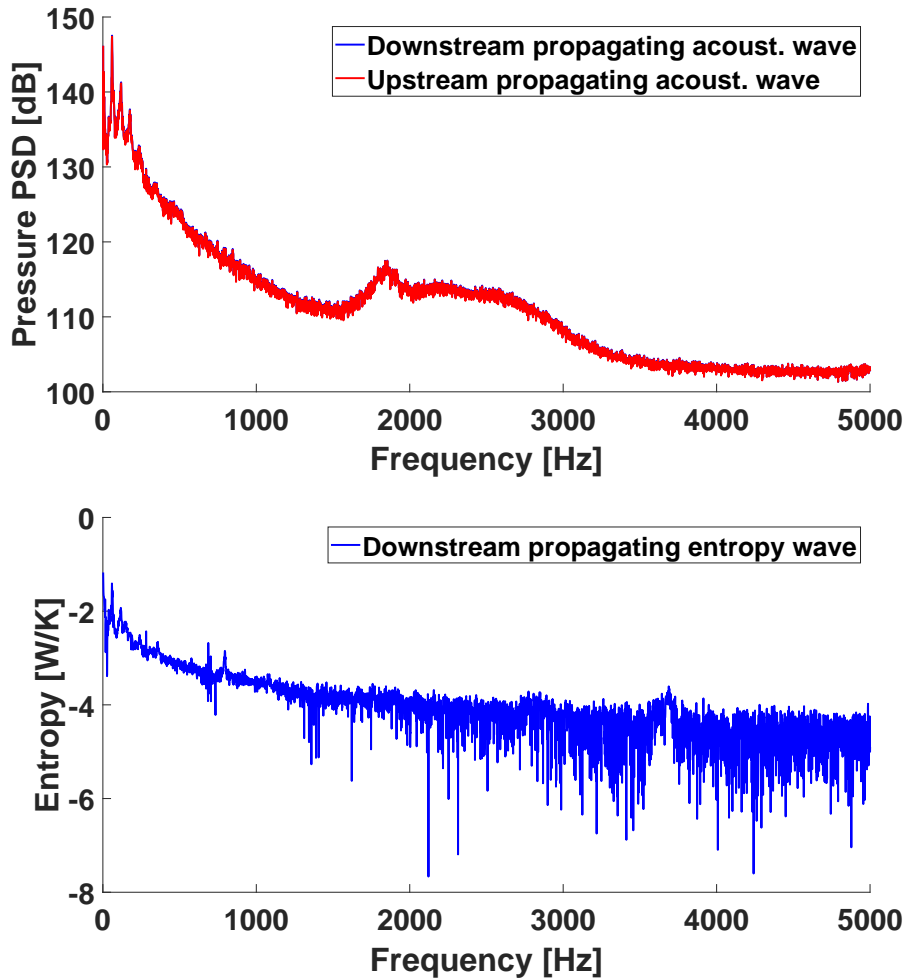


Figure 8.19: Spectra of the pressure oscillations of the up- and downstream propagating acoustic wave as well as of the downstream propagating entropy wave in the combustor for *Op13.4-4.6-0*

The pressure fluctuations of up- and downstream propagating pressure wave in the combustor and of the generated entropy wave in the combustor are shown in figures 8.17 to 8.19. The pressure waves feature the low frequency oscillations that could also be identified in the other parts of this work. Furthermore, their amplitude is rather high, almost as high as the measured in-chamber pressure. The upstream propagating pressure wave indicates the strong combustion instability, while the high amplitudes of the downstream propagating pressure waves indicate a high direct combustion noise contribution. The entropy oscillations in the combustor on the other hand are rather low and have their strongest amplitudes at the combustion instability frequency.

Finally the downstream acoustic wave P_{1a}^+ and the downstream entropy wave σ_1 are used to calculate the direct and indirect combustion noise contribution

Table 8.1: Calculation of the Mach values for the three operating points

	Op16-0-2	Op16-2-0	Op13.4-4.6-0
$\gamma[-]$	1.27		
$r[J/kgK]$	187		
$T_m[k]$	1920	1920	1930
$c[m/s]$	675	675	677
$\rho[kg/m^3]$	0.66	0.66	0.65
$v_1[m/s]$	10.49	10.49	10.67
$M_1[-]$	0.0155	0.0155	0.0158
$M_2[-]$	1.57	1.57	1.57

P_{2a}^+ and P_{2s}^+ (Marble and Candel (1977)):

$$P_{2a}^+ = \frac{1 + \frac{1}{2}(\gamma - 1)M_2}{1 + \frac{1}{2}(\gamma - 1)M_1} \cdot P_1^+ \quad (8.35)$$

$$P_{2s}^+ = \frac{M_2 - M_1}{2} \cdot \frac{\frac{1}{2}\sigma}{1 + \frac{1}{2}(\gamma - 1)M_1} \quad (8.36)$$

In these equations, the Mach number before entering the nozzle M_1 is estimated with the help of the total gas mass-flow rate and the speed of sound calculated with the help of the measured gas temperature. The Mach number downstream of the exhaust nozzle M_2 is calculated assuming an isentropic nozzle with a choked throat:

$$\frac{A}{A_*} = \frac{1}{M} \left[\frac{2}{\gamma + 1} \left(1 + \frac{\gamma - 1}{2} M^2 \right) \right]^{\frac{\gamma + 1}{2(\gamma - 1)}} \quad (8.37)$$

with A the surface of the regarded nozzle section and A_* the surface of the nozzle throat. The equation has two solutions, a subsonic and a supersonic solution. Since the nozzle throat is supposed to be choked, the flow leaving the nozzle is supersonic, thus $M_2 > 1$. The resulting Mach numbers are summarized in table 8.1.

The Fourier transforms of the resulting combustion noise contributions are shown in figure 8.20 to 8.22. They contain the total combustion noise ($P_{2a}^+ + P_{2s}^+$) as well as the direct (P_{2a}^+) and indirect combustion noise (P_{2s}^+) contributions for the three operating points.

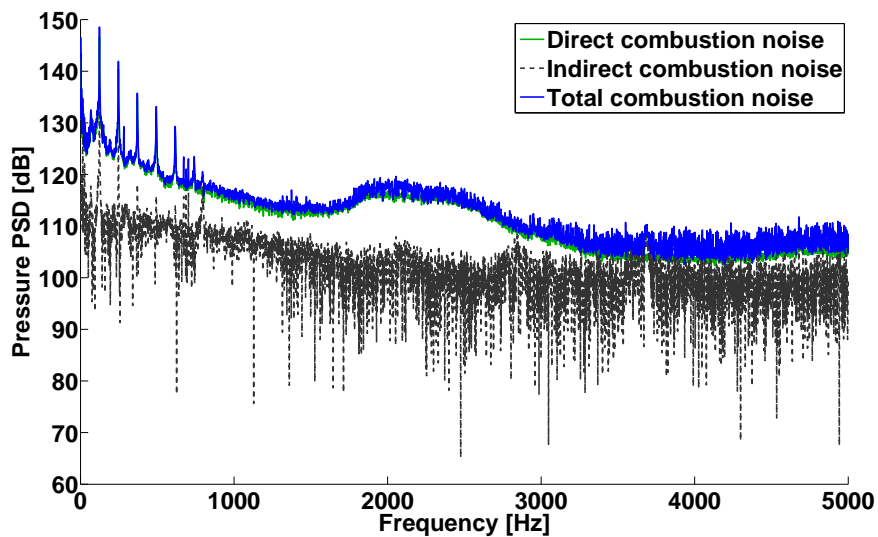


Figure 8.20: Direct, indirect and total combustion noise spectra of *Op16-0-2*

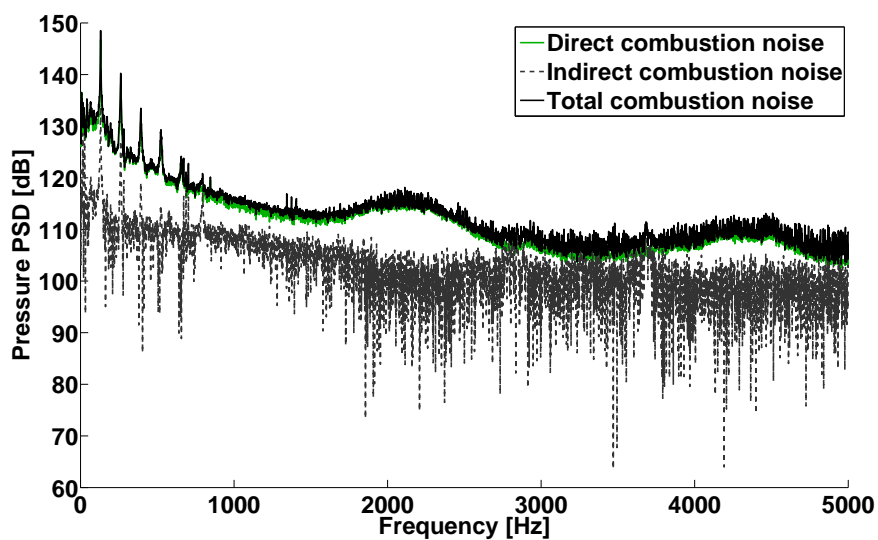


Figure 8.21: Direct, indirect and total combustion noise spectra of *Op16-2-0*

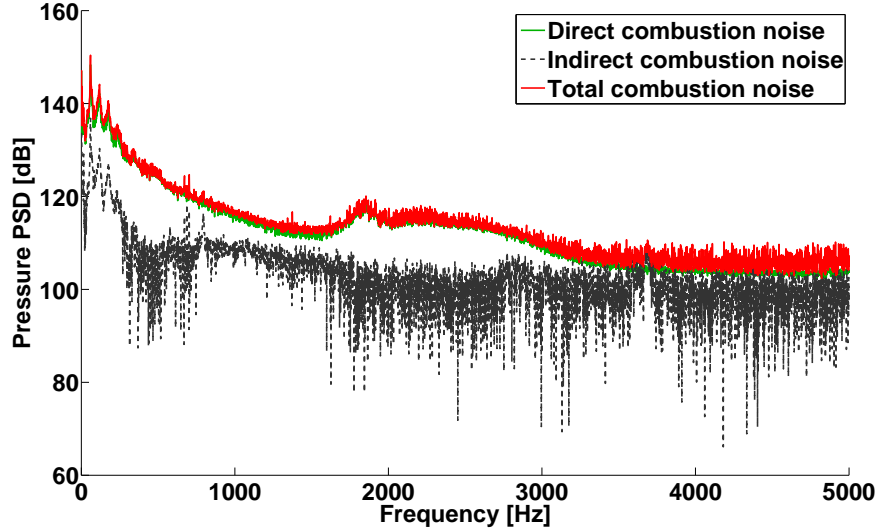


Figure 8.22: Direct, indirect and total combustion noise spectra of *Op13.4-4.6-0*

In these diagrams, the coloured line corresponds to the total combustion noise, while the gray dashed line corresponds to the indirect combustion noise contribution. The full green line corresponds to the direct combustion noise contribution. The diagrams show, that the direct combustion noise is well above the indirect combustion noise contribution for almost the entire frequency span and has its highest amplitudes at frequencies below 1 kHz. The highest peaks for direct and thus also total combustion noise are at 120 Hz for **Op16-0-2** and **Op16-2-0** and around 100 Hz for **Op13.4-4.6-0**. Indirect combustion noise can also be perceived especially at these frequencies. Besides, a small indirect combustion noise dominated peak can be detected around 800 Hz. However its amplitude is far below those of the principal low frequency peaks. Indeed, figures 8.10 to 8.12 show that the temperature fluctuations at these frequencies are only up to around 1 K. They are hence negligible compared to the other combustion noise contributors.

8.5 Conclusion

In this chapter a technique is proposed to determine direct and indirect combustion noise contributions. It is based on the measurements of temperature fluctuations with the help of laser interferometric vibrometry (LIV). The advantage of this technique is that it allows to measure temperature fluctuations at very high frequencies while being non-intrusive.

The obtained temperature spectra show that the temperature fluctuations of the burnt gases are strongly linked with the main combustion instability. In-

deed, the main peaks correspond to the peaks observed and explained in the previous chapters. The separation of direct and indirect combustion noise contributions confirms this observation. Its results show that direct combustion noise is clearly dominating over almost the entire frequency range. This is probably related to the strong combustion instability that is put into evidence in chapter 3 and 4.

However the technique has several drawbacks. One disadvantage is the fact that it measures a line-of-sight averaged temperature. Yet, the calculated temperature distribution shown in figure 8.3 suggests a temperature distribution which is far from being homogeneous. Furthermore, other effects are taken into account, such as inhomogeneities in the glass windows. Another disadvantage is the fact, that the measurement is done only on one point. A possibility to visualize planar density fluctuations without integrating on the line of sight is shown in chapter 6. The measurements there are based on a focusing Schlieren technique which allows to observe 2D density fluctuations on a field depth of a few millimetres.

Conclusion

The present thesis had the aim to study direct and indirect combustion noise experimentally in a combustor that is close to actual gas turbine combustors. For this, an appropriate test bench was designed, its flame and flow characterized experimentally and an experimental separation of direct and indirect combustion noise was conducted. Finally, work was done on different diagnostics that have a potential to be suitable for future studies of combustion noise and flame dynamics.

Specifically for this project, the so-called CESAM-HP test bench was designed. The design was chosen taking into account a variety of objectives: (1) The combustor architecture needs to be close to that of an actual gas turbine combustor. (2) The generation of indirect combustion noise must be high compared to that of direct combustion noise. (3) The acoustic boundary conditions need to be well defined (4) The combustion chamber needs to allow the use of different in-chamber and laser-based diagnostics in order to observe the flame and flow as well as acoustics; (5) The combustor needs to be operated in a safe and reproducible way.

The objectives are met by the different choices that were made during the design process. The test bench features lean premixed swirling combustion, which is close to an actual gas turbine combustor. The premixture is of propane and air and injected tangentially. While this is a simplification compared to actual aeronautic combustors, it allows to simplify the configuration and to concentrate on acoustics. The combustor has a pressure of up to 2.5 bar at the targeted operating points. This is well below that of actual combustors, but it is sufficient for this application. The pressure increase is achieved by an exhaust nozzle, which is choked at the targeted operating points. The exhaust nozzle geometry has been optimized in order to achieve maximal entropy noise generation. The acoustic boundary conditions are fixed upstream of the combustion chamber by an impedance control system and downstream by the choked exhaust nozzle. The impedance control system consists of a perforated plate with a bias flow backed by a cavity of adjustable length. It also features a direct axial injection. The combustion chamber has large optical access that allows for observation with optical diagnostics and different ports for in-chamber pres-

sure and temperature measurements. Finally, the combustor is water cooled in order to enable safe and reproducible operation.

Different tests on the CESAM-HP combustor show a wide operation range, with different flame types depending on the flow repartition and the global equivalence ratio. In this work three operating points were chosen with different air flow splits between tangential injection, direct axial injection and axial injection via the perforated plate of the ICS. In the operating point **Op16-0-2**, most of the air is injected tangentially, while a small part is injected through the perforated plate. In **Op16-2-0** the same air quantity is injected tangentially, while the axial air is completely injected through the direct axial air injection. Finally in **Op13.4-4.6-0**, a bigger part of air is injected by the direct air injection. In these three operating points, all fuel is injected tangentially at an equal global equivalence ratio. The differences in flow split lead to different PSD pressure spectra of the in-chamber pressure, with **Op16-0-2** featuring a low frequency peak at 120 Hz, **Op13.4-4.6-0** a more broadband peak around 100 Hz, and **Op16-2-0** a peak structure in between.

In the following part, the statistical behaviour of flow and flame is examined experimentally. The aim was to gain insight about the flame shape and position and to identify the regions with the strongest heat release and velocity fluctuations.

For these purposes, planar velocity measurements and OH* chemiluminescence imaging on the three operating points are conducted and the mean and RMS fields are examined. The experiments show that the flow and flame dynamics are essentially dominated by the strong swirling motion that results from the tangential injection. This leads to a conical shape of the flame that is typical for combustors of the chosen arrangement. The velocity fields have a topology which is typical for the present configuration. They feature a high velocity region of conical shape and the low velocity inner and outer recirculation zones. The OH* and velocity fields were determined for the three operating points. Both fields are similar for **Op16-0-2** and **Op16-2-0**. For **Op13.4.6-0** however, the swirling motion is not that distinct and strong axial velocity fluctuations can be observed.

In the following chapter, the acoustic modes of the CESAM-HP test bench are determined. For this, a mixed approach of experimentation and analytical modelling was applied. The combustor was modelled analytically by different cavities and acoustic boundary conditions were either determined experimentally or also calculated analytically. The results of this approach show that the feeding lines have a strong influence on the acoustic behaviour and are one of the sources of the main instability in the combustor. Other modes are related to the combustion chamber and premixer geometries.

The low frequency combustion instability in the CESAM-HP combustor is analysed by finding experimental evidence for the different driving and coupling mechanisms. For this purpose, time and spatially resolved measurements of pressure, velocity and OH* chemiluminescence are conducted. From these experimental data, the PSD is calculated for chosen regions of the combustor. The results show that the studied operating points **Op16-0-2** and **Op16-2-0** are dominated by a 120 Hz instability, that can be detected in the studied regions by all the used diagnostics. **Op13.4-4.6-0** features a strong peak around 80 Hz, that is detected by all applied diagnostics as well.

Two mechanisms that are driving the combustion instability in the combustor are proposed, the interaction between the flame and the chamber walls and the interaction between flame and vortices. Besides, two coupling mechanisms are proposed, the effect of pressure fluctuations on the feeding lines and the effects of the pressure fluctuations on the entire combustor and the flame. These coupling mechanisms lead to a positive feedback circuit, which leads to the strong amplitudes of the present combustion instability.

Another part of the thesis is dedicated to the work on different laser-based diagnostics. While they have the potential to be a useful mean to investigate the sources of combustion noise, further work needs to be done. In particular they need to be validated for more general cases. Two techniques are treated here, high speed planar velocimetry at 100 kHz and focusing Schlieren.

The new high speed velocimetry is named PCMV and is based on the use of a continuous wave laser as a light source. The Mie scattering images are acquired with a high-speed camera at 100 kHz with a constant time between each frame. The velocity fields are then obtained by applying classical PIV algorithms on successive particle scattering images. PCMV retrieves the flow topology in the combustor correctly, however a more quantitative validation is needed. For this, the PCMV technique was compared with classical low speed PIV system. This was done by conducting experiments with both systems on the CESAM-HP test bench and by comparing the mean and RMS of the obtained velocity fields. The results show reasonable agreement between the two techniques with errors in the order of magnitude up to 0.2 pixels, however this error is non-negligible. Nevertheless, together with a correct capturing of the main dynamics of the combustor, this technique is suitable for the qualitative studies and the spatially resolved determination of the eigen frequencies of velocity fields.

The second diagnostic worked on in this thesis is focusing Schlieren, which is used to visualize the density fluctuations in the flame and the burnt gases. The technique is rather recent (from the 1990s) and has until then mostly been used to visualize shocks in supersonic wind tunnels.

The technique allows to acquire images of density fluctuations on a field of view

of small thickness at high sampling frequencies (contrary to classical Schlieren, where the images are integrated over the line of sight). The imaging was conducted for the three known operating points at the flame front and at the combustion chamber exit. The results were analysed by calculating the PSD of the Schlieren image intensity. The density fluctuations in the flame area are dominated by the low frequency combustion instability that was also observed with the other diagnostics. In the burnt gases two main frequencies are detected, that belong to the low frequency instability and another one at around 4 kHz. According to the imaging, the instability frequency corresponds to the frequency of apparition of wave packets. These wave packets propagate at flow velocity and have a wavelength corresponding to the 4 kHz peak and probably are entropy waves. In a final step, the determined frequencies in the burnt gases were validated by conducting Vibrometry measurements in the same position in the burner.

The final part of this thesis deals with the actual determination of direct and indirect combustion noise. They are determined with two approaches that are presented in the following.

In the first approach, the direct combustion noise contribution is analysed experimentally. This is done by comparing the chamber pressure fluctuations with the global heat release fluctuation, measured by a photomultiplier probe. The heat release fluctuations are used to determine the theoretical pressure fluctuations related to the flame motion. This is conducted using a simplified form of the wave equation. This theoretical pressure is compared with the measured ones by regarding the PSD as well as the coherence between the two signals. It was shown that the test bench is essentially dominated by direct combustion noise, since the coherence is very high between the two signals, especially at the instability frequencies. However this method is only a crude estimation, since the wave equations are strongly simplified in this approach. Furthermore, the amplitudes of direct combustion noise could not be determined, because the factor between the photomultiplier voltage signal and the pressure was not available.

A more precise possibility for an experimental determination of direct and indirect combustion noise is proposed with the second approach. It is based on synchronous measurements of in-chamber pressure fluctuation and the temperature fluctuation of the burnt gases. The latter are measured by laser interferometric vibrometry, a technique which allows to capture temperature fluctuations at very high frequencies. The direct and indirect combustion noise contributions are obtained by the application of an analytical model of the choked nozzle. The results show that the frequencies of the temperature fluctuations correspond to the main combustion instability frequencies. However, indirect combustion noise accounts for a very small part of total combustion

noise. Indeed, the combustion noise generation is dominated by the pressure oscillations associated with the low frequency instability, thus direct combustion noise.

With the present results, the main research goals of this work were fulfilled to a large extent. A combustor test bench could be designed, which is close to the stated design objectives. Furthermore, different diagnostics were used and developed further to characterize the flame and flow dynamics of the combustor and to finally quantify direct and indirect combustion noise contribution.

However the results have also shown that the indirect combustion noise contribution is far lower than it was aimed for. This is due to the strong direct combustion noise contribution, which is associated with the low frequency combustion instability.

Different measures can be taken in order to increase indirect combustion noise. (Two possible ones, partially premixed operation and secondary air injection through the chamber walls, are analysed in annex A and not presented further here.)

In general, in order to increase indirect combustion noise, the pressure fluctuations associated with the movement of the flame must be kept low, while the density fluctuations that are transmitted to the burnt gases need to stay high. Furthermore, the pressure fluctuations generated from these density oscillations need to be the highest possible.

The latter point is already ensured, due to the optimized shape of the exhaust nozzle.

In order to decrease the pressure fluctuations generated by the flame, the combustion instability and its effects need to be damped. One possible measure could be to increase the chamber width and height or to increase the chamber pressure in order to obtain a more compact flame. Ideally, this would reduce the interaction between the flame and the chamber walls. Another measure would be to change the design of the injection system, however there are numerous possibilities to do so.

In order to increase the generation of sound from the entropy waves, the density fluctuations, which arrive to the exhaust nozzle need to be the highest possible. A possible measure to increase their amplitude (or rather to reduce their decreasing) would be to decrease the chamber length. By this, the entropy waves would be dissipated less until arriving at the nozzle. This could be especially done in combination with a pressure increase as well as a stabilisation of the flame, which both would lead to a more compact flame.

A further measure to increase indirect combustion noise would be to increase the chamber pressure. When keeping the same air and fuel mass flow rates, this could only be realized by reducing the nozzle throat diameter. This would then increase the nozzle exit Mach number, which according to [Marble and Candel \(1977\)](#) lead to an increase of noise generated from the acceleration of

the entropy waves.

Another point which requires further work is the identification of the different combustion instability mechanisms in the combustor. While the applied diagnostics give evidence about the existence of those, they are not sufficient to clearly identify them. A possibility to do so would be to conduct OH-PLIF measurements, synchronously with planar velocimetry measurements. These would allow observe the interaction between flame and vortices in the flame and also to observe the flame surface fluctuations, especially in the chamber walls.

Other possible points of further works can be found in the diagnostics that were worked on and used.

The here presented PCMV method still requires quantitative validation, due to its different nature from classic PIV. The most recent advancements can be found in [Mazur et al. \(2017\)](#), however an experimental comparison of instantaneous velocity fields taken by PIV and PCMV simultaneously and synchronously is still to be done.

The focusing Schlieren technique shows interesting perspectives as a diagnostic for planar time-resolved temperature measurements. To do so, a method must be found which allows to find the link between the Schlieren image intensity and the temperature gradient. Using those gradients, together with an instantaneous temperature measured somewhere in the combustor, one would obtain 2D temperature fields.

Appendix A

Potential improvements of the test bench

In this chapter, three modifications of the CESAM-HP testbench are proposed. The purpose is to increase the indirect combustion noise contribution. The modifications are the following: (1) The stabilisation of the flame via a rod that acts as a flame holder, (2) a separate fuel injection in order to test the effects of a partially premixed operation, and (3) secondary air injected through the chamber walls in order to increase the inhomogeneities of the burnt gases. The three modifications are presented and tested in order to evaluate their effectiveness. During the tests, different variations of air flow splits are compared in terms of RMS pressure, direct combustion noise contribution and static and dynamic flashback. The tests show that the flame holder rod only has very limited effects on flame dynamics and on indirect combustion noise. The partially premixed operation leads to a strong increase of instabilities however direct combustion noise contribution seems to decrease. Secondary air injection leads systematically to a little decrease of direct noise contribution and is thus equally interesting.

A.1 Proposed modifications of the test bench

This chapter is motivated by previous results of this thesis. Chapter 3 and 5 show that the flow and flame dynamics of the three operating points **Op16-0-2**, **Op16-2-0** and **Op13.4-4.6-0** are dominated by a low frequency combustion instability. The time and spatially resolved measurements of pressure, velocity and heat release in chapter 5 show in particular that the PSD of all these measurements have their strongest peaks at the same frequencies. For the two former points this frequency corresponds to the 120 Hz combustion instability and the harmonics of this peak. For the latter point the main instability frequency around 80 Hz is also associated with a axial flapping motion. Due to these strong dynamics in the injector region, most of the combustor noise

is generated by the flame surface fluctuations. Indeed, chapter 4 and 8 show quantitatively, that the indirect combustion noise contribution accounts for only around 5 % of total combustion noise.

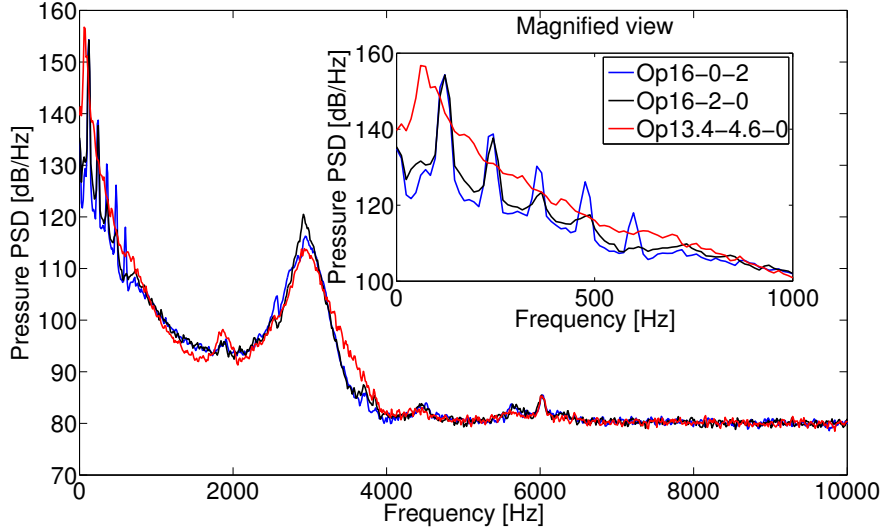


Figure A.1: PSD of the pressure signal recorded in the CESAM-HP test bench with the three operating points **Op16-0-2**, **Op16-2-0** and **Op13.4-4.6-0**. The highest activity can be observed in the low frequency region below 1000 Hz with distinct peaks that are associated with a combustion instability and a high direct combustion noise contribution.

Two reasons can be identified for the low indirect combustion noise contribution: (1) As described in the previous paragraph the strongest velocity and heat release fluctuations in the combustor can be observed in the injector region. The resulting combustion instability generates pressure oscillations with amplitudes of several orders of magnitude larger than combustion noise (cf. the SPL diagram in figure A.1). Thus the direct combustion noise contribution is far above the indirect combustion noise one. (2) Classic aeronautic combustion chambers feature a secondary air injection which helps to cool the chamber walls and the burnt gases. As a second effect, temperature inhomogeneities are added to the burnt gases. These are accelerated in the first turbine stages and lead to indirect combustion noise generation. The present combustion chamber does not feature such a secondary injection through the chamber walls for the sake of simplicity.

Based on these observations, three combustor modifications are proposed: (1) The installation of a flame holder at the chamber entry. The idea is that the flame would stabilize on the flame holder and thus have a more constant posi-

tion in the chamber. This would decrease the heat release fluctuations of the flame and thus direct combustion noise. (2) A separate fuel injection in order to change the combustion to partially premixed. While previous work has shown that this leads to an increase of the noise emission of the flame (Singh et al. (2005); Duchaine et al. (2009)), no attempts were made to estimate the contributions of direct and indirect combustion noise. For example fluctuations in equivalence ratio would lead an oscillation of the reaction rate in the flame. This would ultimately lead to fluctuations of density in the flame and thus also of density in the burnt gases. Since these are accelerated by the exhaust nozzle, these density fluctuations would finally lead to increased fluctuations of indirect combustion noise. However, this contribution cannot be quantified beforehand. Hence this type of flame is tested here. The associated modification of the combustor and its verification are presented in section A.5. (3) Introduction of a secondary airflow via the chamber walls. The aim is to increase the temperature fluctuations of the burnt gases by injecting cold air downstream of the flame. This modification is presented in section A.6.

A.2 Experimental procedure to verify the effectiveness of the modifications

In order to evaluate the effectiveness of the proposed modifications, several indicators are chosen. These need to be able to easily compare different modifications and operating points. To do so, the following aspects need to be taken into account:

- The RMS of the pressure fluctuations
- The contribution of direct and indirect combustion noise
- The tendency of the flame to flashback into the injector

The level of pressure fluctuations is determined by the RMS of the measured pressure signal p_{meas} . This indicator has the aim to give insight about the intensity of the combustion instability. The results in chapter 4 and 7 show that in general it is stronger than all other acoustic phenomena. In the present experiments, the sensor is installed on the closest position to the exhaust nozzle, on position 4. The functioning and installation of the in-chamber KISTLER sensors is presented in chapter 1 and is not repeated here.

The contribution of direct and indirect combustion noise is based on the theoretical chamber pressure p_{cal} calculated from the signal of the photomultiplier observing the entire combustion chamber. Its functioning, as well as the method to calculate the theoretical pressure, is presented in chapter 7. The direct com-

bustion noise contribution is estimated by calculating the mean coherence between these two pressure signals. As a reminder, the coherence describes, to what extent they are linked in the frequency domain and is determined by the equation:

$$C_{12} = \frac{|G_{12}|^2}{G_{11}G_{22}} \quad (\text{A.1})$$

with G_{12} the cross spectral density between two signals and G_{11} and G_{22} the autospectral density of each of the signals. The advantage of this approach is that it does not depend on the amplitudes of the signals. In his case the two signals are p_{meas} and p_{cal} , taking into account that p_{cal} does not have the correct magnitude (as described in chapter 7). Therefore, the coherence between those two signals is regarded, since it does not depend on the magnitude.

Flashback is a phenomenon which can lead to excessive heating of the injector and possibly to its damaging. The strong tendencies for flashback of this test-bench was demonstrated in a joint numerical and experimental study (Lapeyre et al. (2016)). Thus this criterion is relevant for the analysis in this chapter. The existence of the flame in the injector is verified experimentally. This is done with an optical fiber with direct optical access in the injector which is linked with a PM probe. As described in chapter 1, the presence of the flame leads to an increase of the PM signal. In this chapter, two values are regarded, the mean PM intensity and the RMS PM intensity. The mean PM intensity accounts for the mean position of the flame and allows to draw conclusions about static flashback of the flame. The RMS PM intensity is related to fluctuations of the flame base and thus to dynamic flashback. The obtained PM signal is kept in Volts, as it only observes a small part of the flame. It is thus not possible to create an equation which links the PM signal intensity and another physical variable quantitatively.

Three measurements are taken simultaneously during the experiments: (1) The in-chamber pressure via a Kistler 4045A piezo-sensor, (2) the OH* chemiluminescence in the combustion chamber via the PM "total" (as described in chapter 1) and (3) the OH* chemiluminescence in the injector via the PM connected to the optical fiber. In these tests, the only parameters that are varied are the direct air injection \dot{m}_{jet} and the bias air injection through the perforated plate of the ICS \dot{m}_{ICS} . A description of these two injections can be found in chapter 1. These two airflows are varied in 0.5 g/s steps and the experiments are conducted for all their combinations. In these experiments, \dot{m}_{jet} is varied from 0 g/s to 4 g/s and \dot{m}_{ICS} from 0 g/s to 2 g/s. Other parameters are kept constant in these experiments. For all the tested variations, the global equivalence ratio is 0.85 and the total air mass flow is 18 g/s, which corresponds to a power level of 45 kW.

A.3 Measurements in the fully premixed case without secondary air

A.3.1 Presentation of the test case

The fully premixed case without secondary air corresponds to the default configuration of the CESAM-HP test bench. The aim is to generate a set of data that can be used as a reference in order to test the effectiveness of the proposed modifications.

A.3.2 Experimental results

Figure A.2 shows the RMS pressure depending on the two mass flow rates \dot{m}_{jet} and \dot{m}_{ICS} . The figure shows that the pressure RMS increases equally when \dot{m}_{jet} or \dot{m}_{ICS} are increased and reaches values of over 10 kPa.

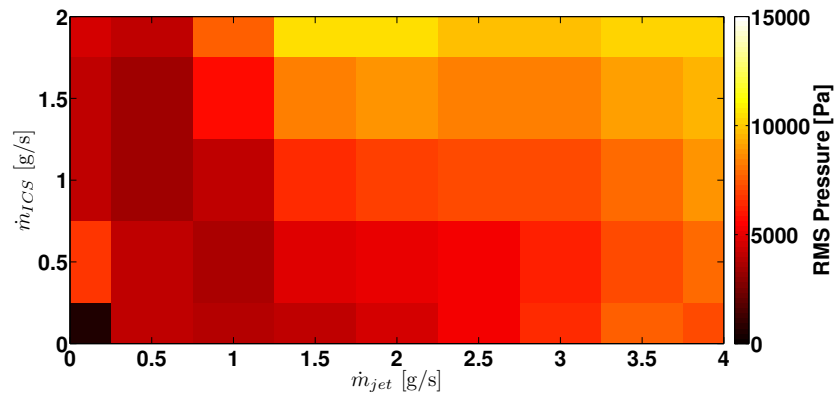


Figure A.2: RMS pressure map of the fully premixed case

The PSD of p_{meas} and p_{cal} are shown for four chosen operating points in figure A.3, as well as the coherence of the two signals. The chosen points are the followings:

- Fully premixed, 0 g/s air through the central jet and 0 g/s air through the ICS
- Fully premixed, 0 g/s air through the central jet and 2 g/s air through the ICS
- Fully premixed, 2 g/s air through the central jet and 0 g/s air through

the ICS

- Fully premixed, 2 g/s air through the central jet and 2 g/s air through the ICS

The PSD show that the four operating points are dominated by the low frequency instability that was already described in this thesis. It can also be seen that the spectra of p_{meas} and p_{cal} are very similar. This can also be seen in the coherence diagram, where very high values are reached for most of the frequency range. Especially for the instability frequency and its harmonics, the coherence between the two signals is almost 1, while it is slightly lower in the broadband part.

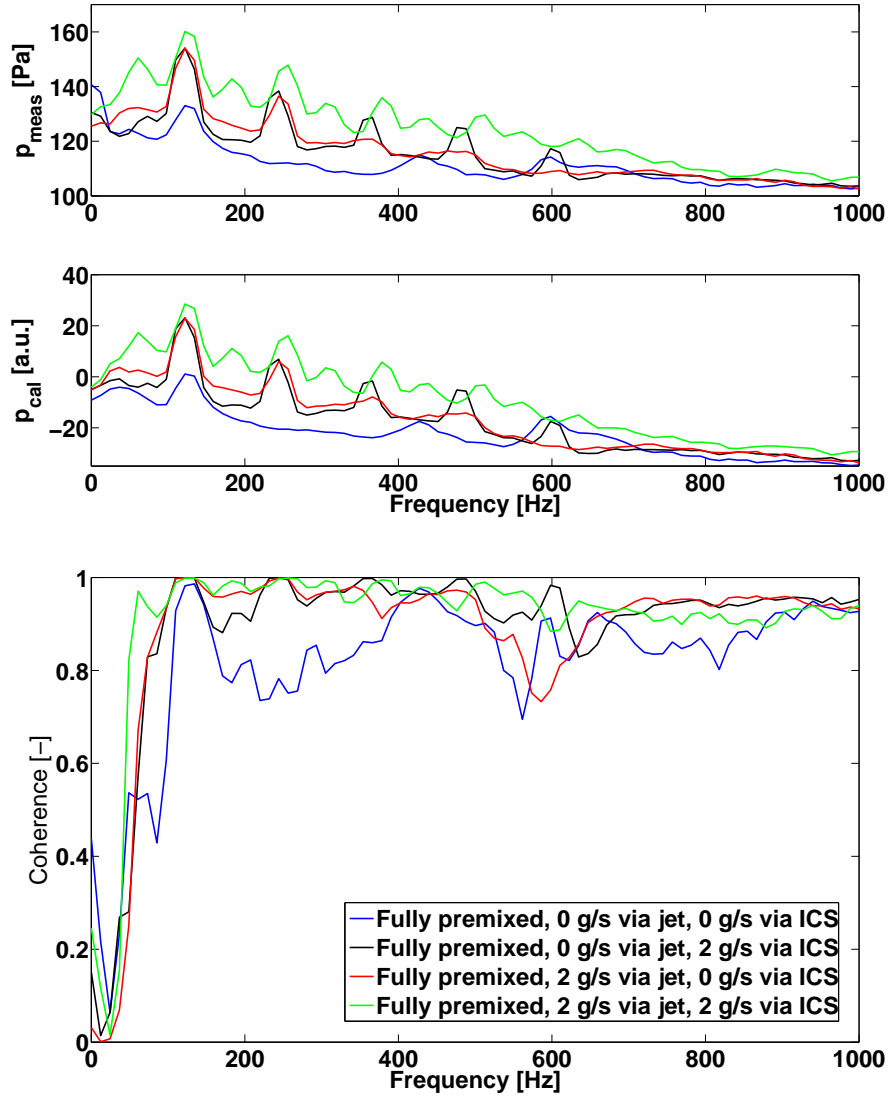


Figure A.3: PSD at 0 g/s axial air flow through the perforated plate of the measured pressure (top image) and the theoretically calculated pressure (middle image) for the different configurations. The bottom image shows the coherence of these two pressures.

Figures A.4 and A.5 present respectively the mean and RMS intensity of the PM that is installed in the injector. Both have a small value when the sum of axial flows is around 2 g/s and increases for all other values. Especially the RMS increases with an increasing jet mass flow rate.

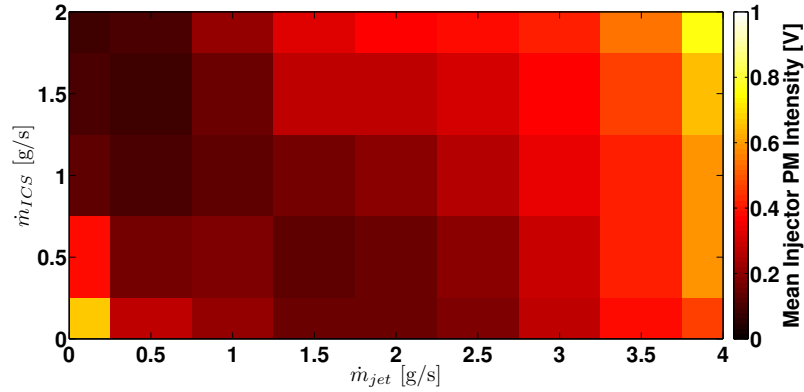


Figure A.4: Mean injector PM intensity map of the fully premixed case

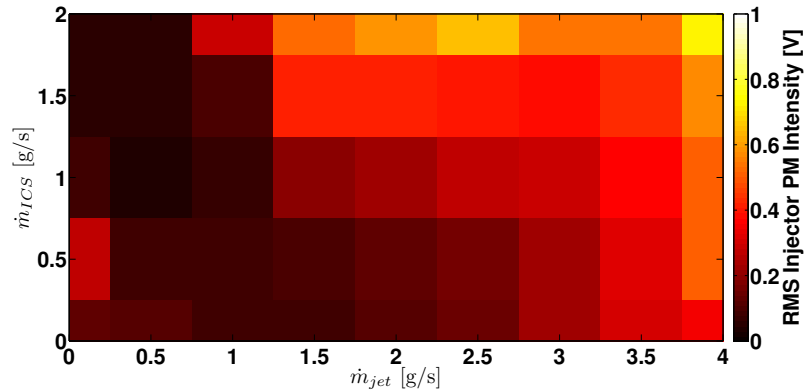


Figure A.5: RMS injector PM intensity map of the fully premixed case

The increasing RMS pressure shows that the axial air flow, whether it is \dot{m}_{jet} or \dot{m}_{ICS} , leads to an increase in the chamber pressure fluctuations. As demonstrated in chapter 7 these fluctuations are mostly caused by the dynamics of the flame itself. The increase of axial air flow seems to increase fluctuations in the flame surface, especially in the injector, as can be seen by the increasing RMS PM intensity there. These increasing dynamics mean, that the generated pressure oscillations are probably related to direct combustion noise. The results of p_{meas} and p_{cal} confirm this assumption as their coherence is almost everywhere above 0.7 and increases (even when very slightly) with increasing axial mass flow rates. Also, the intensity of the PM measurements in the in-

jector indicates the position of the flame in the injector. Both values increase when \dot{m}_{jet} or \dot{m}_{ICS} are increased. This means that the flame flashes back into the injector in two ways. On one hand the increase of the mean PM intensity shows that the mean flame position is more upstream in the injector. On the other hand the increase of the RMS PM intensity shows that the flame fluctuations in the injector are stronger. Especially the former observation is striking, since the axial injection has the aim to counterbalance flashback. The results in this section however show, that too high axial air flows have the contrary effect.

A.4 Effects of flame stabilisation by a flame holder rod in the injector

A.4.1 Presentation of the modification

One of the proposed modifications is the use of a rod as a flame holder. The aim is to achieve a stabilization of the flame on the rod. This assumption is based on previous works that have shown that the use of a bluff body (such as the rod) leads to the creation of a recirculation zone around the body (Kovitz and Fu (1961)). This zone stabilizes the flame and thus not only leads to lower flame surface fluctuations, but also prevents the flame from flashing upstream into the injector. The former effect leads finally to lower heat release fluctuations of the flame and thus possibly to less direct combustion noise. The latter effect is important for operational safety, since flashback can lead to damages of the injector.

A schematic drawing of the injection system with the installed flame holder rod can be seen in figure A.6. The central rod is fixed in the central jet arrangement and its tip is located 10 mm upstream of the combustion chamber entry. The consequence of this installation is that \dot{m}_{jet} cannot be varied for the partially premixed cases. Thus the only varied air mass flow rate is \dot{m}_{ICS}

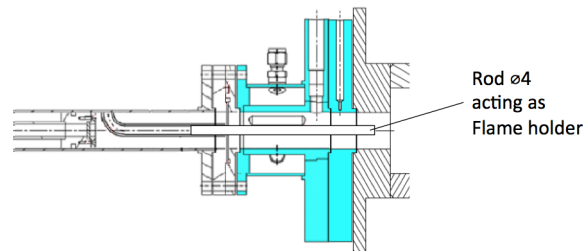


Figure A.6: Modified injector with the flame holder rod

A.4.2 Experimental results

The RMS pressure depending on the axial air mass flow rate through the ICS is shown in figure A.7. The figure shows that, apart from 0g/s axial flow, the installation of the rod leads to a reduction of the RMS pressure of around 20 to 30 %.

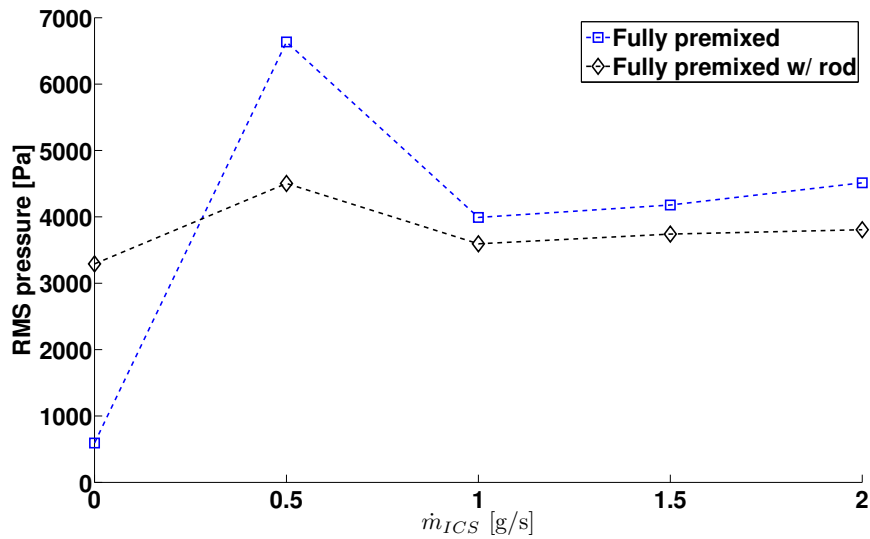


Figure A.7: RMS pressure in dependence from the ICS bias air flow rate for fully premixed combustion with and without flame holder rod

The PSD of p_{meas} and p_{cal} are shown for three chosen operating points in figure A.8, as well as the coherence of the two signals. For each operating point, the results with and without flame holder rod are shown. The chosen points are following:

- Fully premixed, 0 g/s air through the central jet and 0 g/s air through the ICS
- Fully premixed, 0 g/s air through the central jet and 1 g/s air through the ICS
- Fully premixed, 0 g/s air through the central jet and 2 g/s air through the ICS

The PSD show that all operating points are dominated by the low frequency instability that was already described in this thesis, independently on the existence of the rod. The spectra do not seem to depend from the existence of the rod, except for the first operating point, where the peak amplitude slightly

increases. It can also be seen that the spectra of p_{meas} and p_{cal} are very similar. The same observation is made in the coherence diagram, where very high values are reached for most of the frequency range and are not changed by the rod.

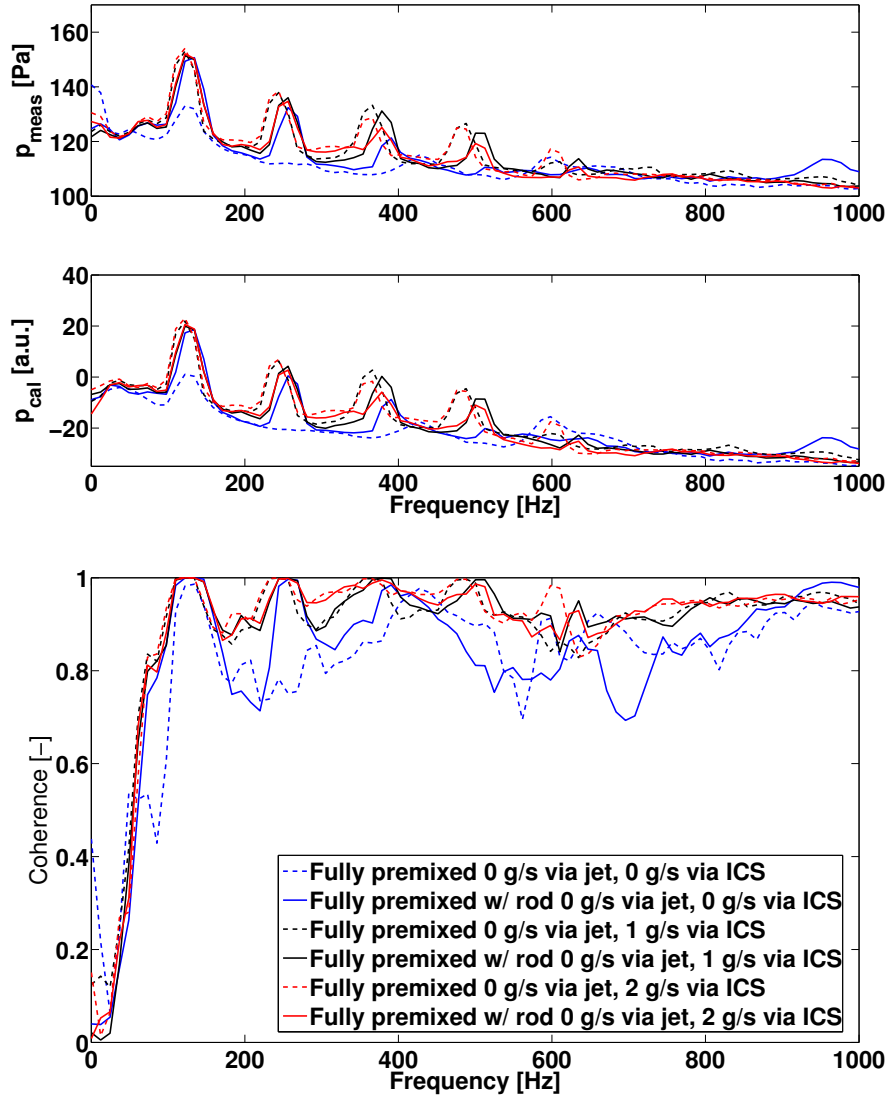


Figure A.8: PSD at 0 g/s axial air flow through the perforated plate of the measured pressure (top image) and the theoretically calculated pressure (middle image) for the different configurations. The bottom image shows the coherence of these two pressures.

The effect of the flame holder rod on static and dynamic flashback is shown in figure A.9 and A.10. These show respectively the mean and the RMS intensity of the PM signal measured in the injector. The measurements show that the

rod leads to a systematic reduction of both, mean and RMS signals.

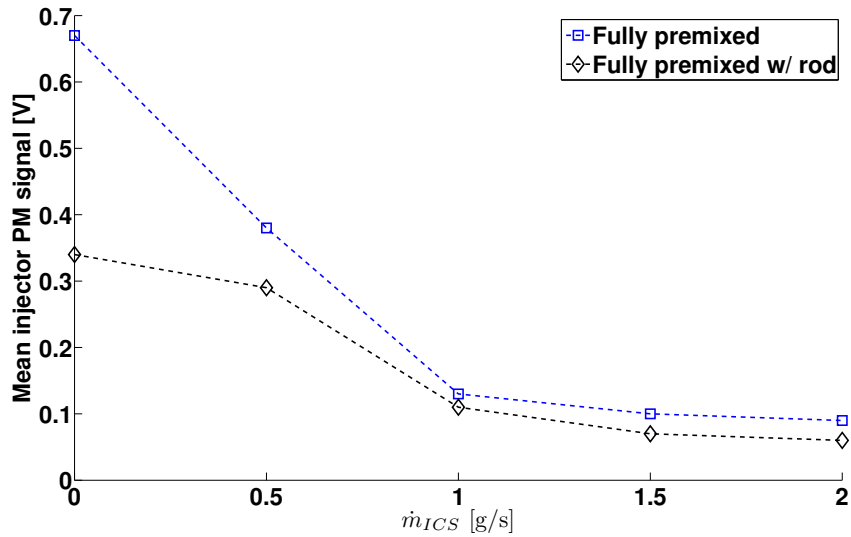


Figure A.9: Mean injector PM signal in dependence from the ICS bias air flow rate for fully premixed combustion with and without flame holder rod

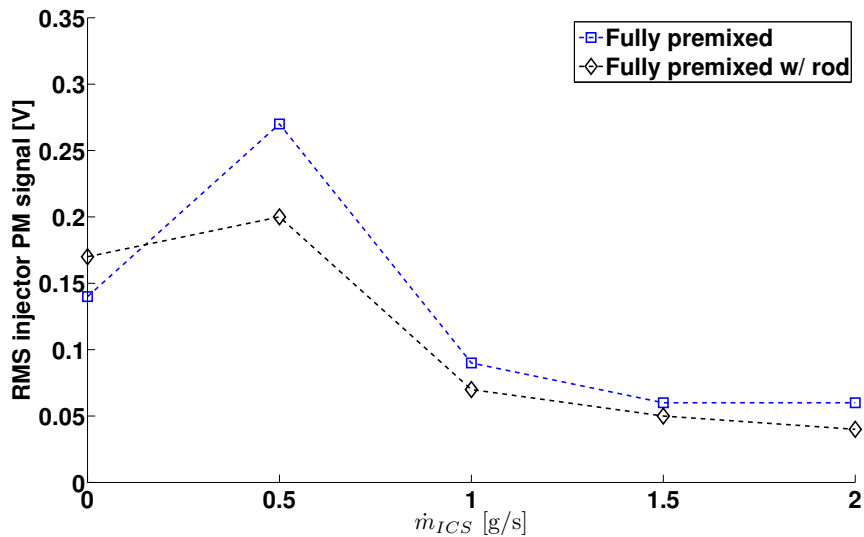


Figure A.10: RMS injector PM signal in dependence from the ICS bias air flow rate for fully premixed combustion with and without flame holder rod

The results suggest that the flame holder rod indeed leads to a stabilization of the flame. The decrease in RMS pressure indicates that the flame generates

lower pressure fluctuations. Since these are also related to a periodic movement of the flame (as shown and discussed in chapter 4) these results would mean that the flame is more stabilized. These assumptions are supported by the findings with the PM installed in the injector. As the RMS intensity of the signal measured by the PM is reduced, it can be deduced that the movement of the oscillations of the flame position in the injector are probably reduced as well. This means that the flame base is probably attached to the flame holder rod. The mean signal measured with the PM supports this, as it shows that the flame holder rod leads to a reduction of the mean signal. The flame base is thus positioned more downstream than it would be without the rod.

However this stabilisation seems not to have an impact on the direct combustion noise contribution. The comparison of p_{meas} and p_{cal} shows that it barely depends on the existence of the rod or not. This means that it does not have an influence on the coherence of the measured pressure signal and the theoretically calculated one. This possibly means that the flame rod does not influence the repartition of the generated direct and indirect combustion noise. As the heat release fluctuations of the flame are reduced by this measure, the heat release fluctuations in the burnt gases are probably reduced in the same extent. The effect is thus that the repartition of total combustion noise into its direct and indirect parts remains unchanged.

A.5 Effects of flame stabilisation by a flame holder rod in the injector and partially premixed operation due to separate fuel injection

A.5.1 Presentation of the modification

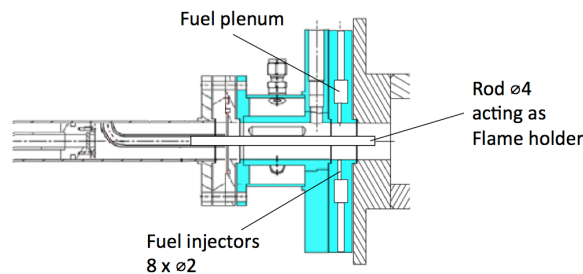


Figure A.11: Modified injector including the separate fuel injection. The fuel injection is installed in the last element before the combustor. The drawing also includes the flame holder that stabilizes the flame.

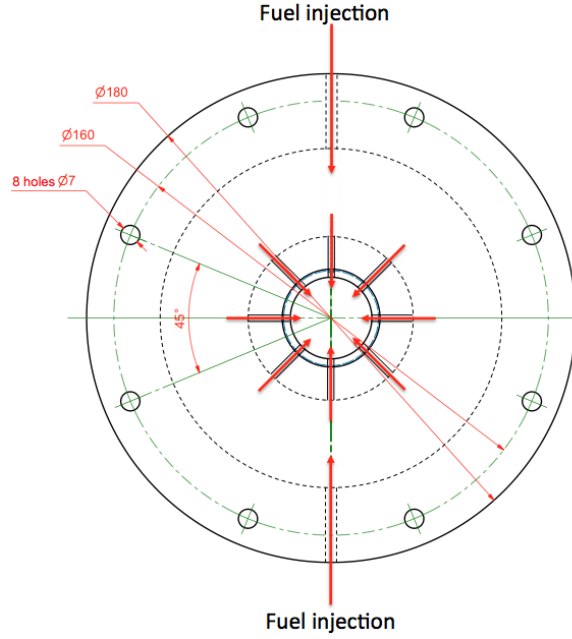


Figure A.12: Schematic drawing of the fuel injector element including the flow directions of the fuel.

As described before, the separate injection of fuel and air has the aim to obtain a partially premixed operation. A schematic drawing of the injector with the modified fuel injection system is shown in figure A.11. It is inspired from an arrangement previously used by Peterleithner et al. (2016). The drawing shows that the tangential stage only injects air, while all fuel is injected by an injector right before the combustion chamber. This fuel injector stage consists of a plenum which allows for an equal distribution of the fuel over the diameter (see figure A.12). The fuel is injected from this plenum over eight equally distributed orifices with a diameter of 2mm each. The dimensions have been chosen in a way that the fuel entry velocity has a value of around 20 m/s and hence corresponds to the bulk air velocity. As presented by Gruber et al. (1995) the quality of premixing depends on the ratio of the momentums of the bulk air flow and the injected fuel:

$$J = \frac{\rho_{fuel} \cdot u_{fuel}^2}{\rho_{air} \cdot u_{air}^2} \quad (A.2)$$

with ρ_{fuel} and ρ_{air} respectively the density of fuel and air and u_{fuel} and u_{air} respectively the velocity of the injected fuel and the velocity of the bulk air flow. When assuming an equal velocity for both flows, a density of 2 g/s for the fuel and 1.2 g/s for air, the equation results to 1.67. The momentums of both flows are thus close to each other. This condition enhances the mixing as shown by Schetz and Billig (1966).

The presented fuel injector replaces the most downstream piece of the original injector right before the combustion chamber. As a consequence all lengths and dimensions of the combustor remain the same.

First tests however show that the flame cannot be maintained under this configuration. This issue is solved by the central flame holder rod that is presented in section A.4 and stabilizes the flame. The central rod is fixed in the central jet arrangement and its tip is located 10 mm upstream of the combustion chamber entry. As in section A.4, the consequence of this installation is that \dot{m}_{jet} cannot be varied for the partially premixed cases. Thus the only varied air mass flow rate is \dot{m}_{ICS}

A.5.2 Experimental results

In literature it is described that the partially premixed case is less stable than the fully premixed one. This explains the necessity of the central body which acts as a flame holder. Without this modification, no flame can be sustained. The consequence is that only the air flow coming through the ICS \dot{m}_{ICS} can be varied.

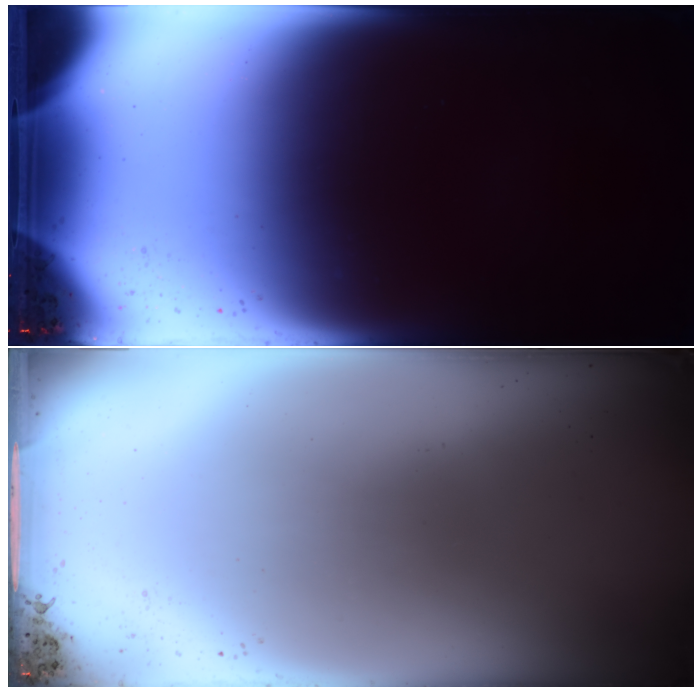


Figure A.13: *Flame shape of Op16-0-2 at fully premixed and partially premixed functioning*

Figure A.13 shows photographs of the fully premixed and partially premixed

flame for **Op16-0-2**. It can be seen on the figures that both flames have a conical shape. However a variety of differences can be observed compared to the partially premixed flame. Its colour is different and less blue, which is due to the fact that it is not fully premixed. Besides, the flame length is higher than in the fully premixed case. Indeed, the flame plume fills the entire combustion chamber for partially premixed operation. Furthermore, a red glowing can be observed in the injector. This glowing belongs to the flame holder rod that is heated up by the flame.

The effects of partial premixing are shown in figures A.14 to A.17. In these experiments, only \dot{m}_{ICS} is varied due to the installation of the flame holder.

The RMS pressures are compared in figure A.14. It can be seen, that the partially premixed flames have a far higher RMS pressure than the fully premixed ones. It attains values which are twice to three times as high.

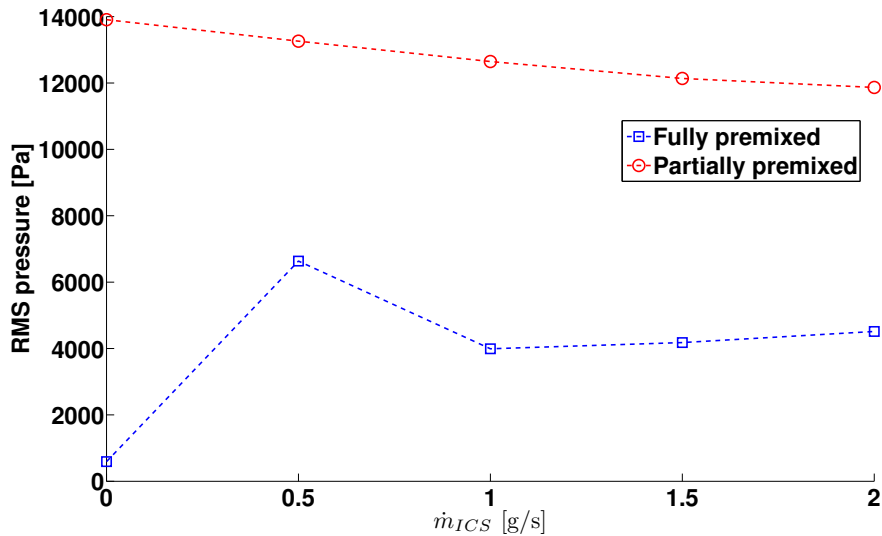


Figure A.14: RMS pressure in dependence from the ICS bias air flow rate for fully premixed and the partially premixed case

The PSD of p_{meas} and p_{cal} are shown for six chosen operating points in figure A.15, as well as the coherence of the two signals. Two parameters are varied, the axial air flow rate through the ICS and whether the flame is fully or partially premixed. The chosen points are thus the following:

- Fully premixed, 0 g/s air through the central jet and 0 g/s air through the ICS

- Partially premixed, 0 g/s air through the central jet and 0 g/s air through the ICS
- Fully premixed, 0 g/s air through the central jet and 1 g/s air through the ICS
- Partially premixed, 0 g/s air through the central jet and 1 g/s air through the ICS
- Fully premixed, 0 g/s air through the central jet and 2 g/s air through the ICS
- Partially premixed, 0 g/s air through the central jet and 2 g/s air through the ICS

The PSD show that all operating points are dominated by the low frequency instability that was already described in this thesis, whether the flame is fully or partially premixed. However the partially premixed case has far higher amplitudes. It can also be seen that the spectra of p_{meas} and p_{cal} are very similar. However a big difference can be seen above 600 Hz, where p_{cal} has higher amplitudes in the peaks than p_{meas} . The consequence is that the coherence is low in these frequencies for the fully premixed case. Apart from this, the coherence in general attains the value of almost 1 at the instability frequency and its harmonics.

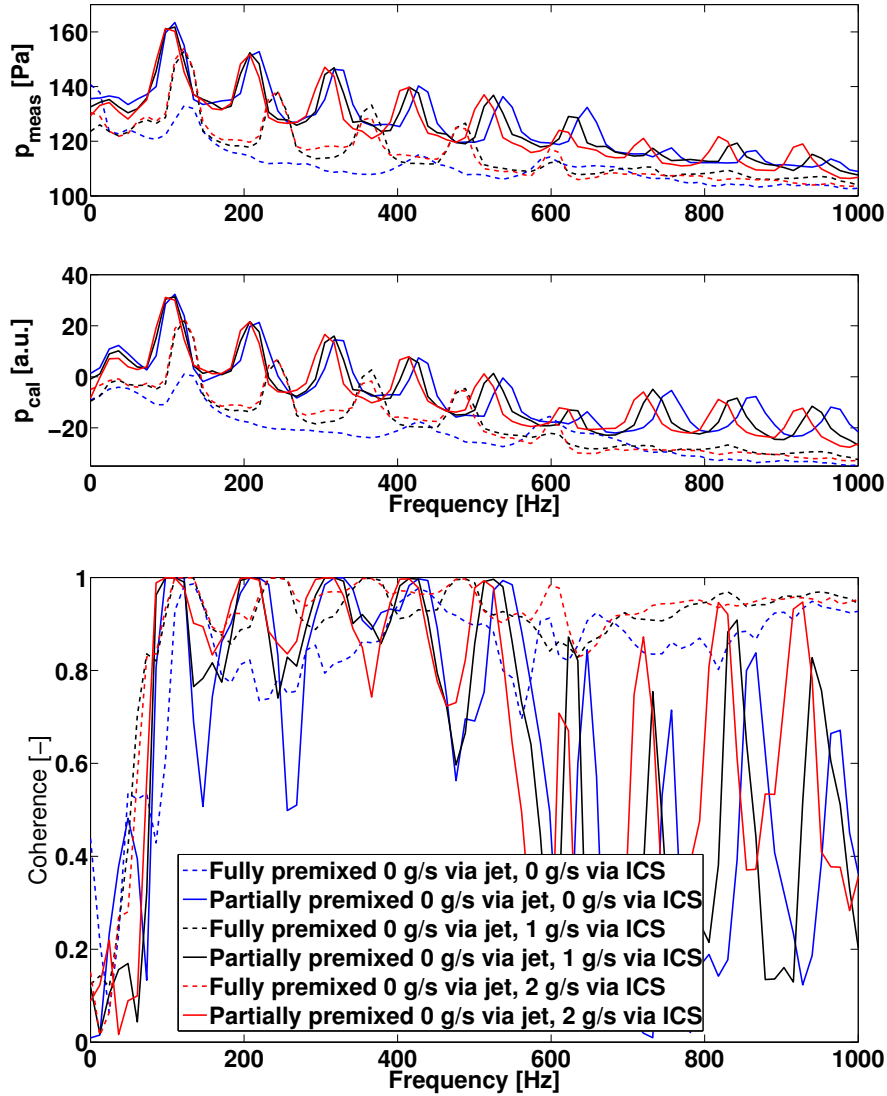


Figure A.15: PSD at 0 g/s axial air flow through the perforated plate of the measured pressure (top image) and the theoretically calculated pressure (middle image) for the different configurations. The bottom image shows the coherence of these two pressures.

The mean and RMS of the measurements of the injector PM are shown in figure A.16 and A.17. The values are above the values of the fully premixed case, independently of \dot{m}_{ICS} . Another interesting observation is that for the partially premixed flame, an increase of \dot{m}_{ICS} leads to a decrease of the mean and RMS injector PM signal.

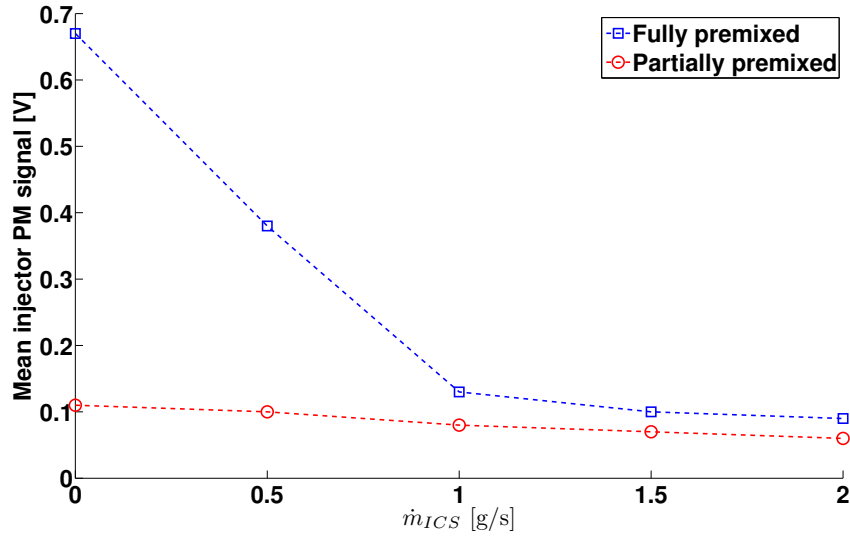


Figure A.16: Mean injector PM signal in dependence from the ICS bias air flow rate for fully premixed and the partially premixed case

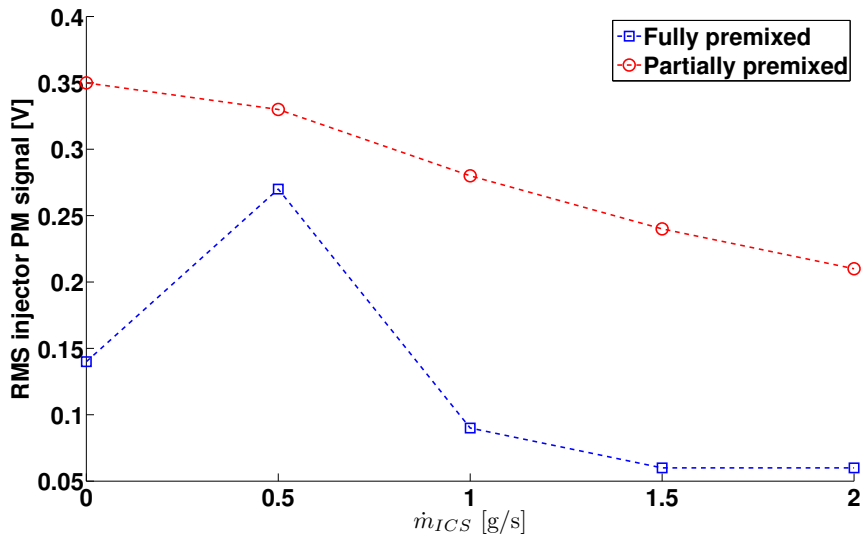


Figure A.17: RMS injector PM signal in dependence from the ICS bias air flow rate for fully premixed and the partially premixed case

The high pressure RMS corresponds to the first observation that the separate fuel injection leads to a more unstable flame. The pressures p_{meas} and p_{cal} and their coherence give insight about the influences of the modification on direct combustion noise. The modification of the injection system clearly leads to a decrease of the coherence between these two signals. This means that

for partially premixed combustion, a smaller part of the measured pressure fluctuations can be associated with the heat release fluctuations of the flame. These results could be an indicator for an increase in indirect combustion noise, however the measurements taken here are not sufficient to draw this conclusion.

The flashback behaviour can be deduced from the injector PM measurements. The mean and RMS values are below the values of the fully premixed case. The explanation for the low static flashback is straightforward: As fuel and air get in contact just before the entry of the combustion chamber, it is not possible that the flame flashes back into the injector. Another interesting observation is the fact, that an increase of the axial air flow decreases flashback. This means that while the axial flow pushes the partially premixed flame downstream, it seems to destabilize the fully premixed flame.

A.6 Effects of secondary air injection through the chamber walls

A.6.1 Presentation of the modification

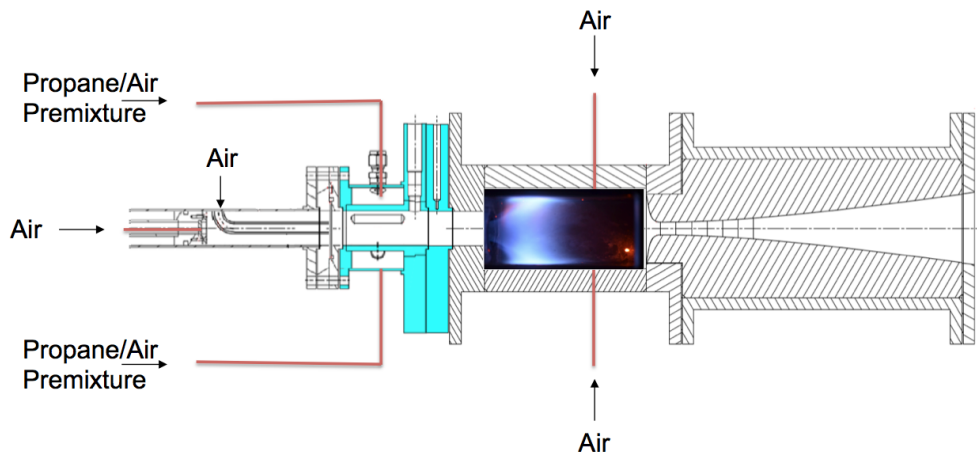


Figure A.18: Schematic drawing of the CESAM-HP testbench updated by the secondary air injection through the chamber walls.

The secondary air injection through the combustion chamber walls has the aim to increase the temperature inhomogeneities in the burnt gases. A schematic drawing of the CESAM-HP test bench with the secondary air injection is shown in figure A.18. The injection is integrated in the pressure sensor ports of the chamber walls. Their geometry is presented in chapter 1. The secondary air is injected in sensor position 3 (at $x = 87.5$ mm) on the upper and lower chamber walls. This position has been chosen in order to inject more downstream

than the flame in order to increase the temperature fluctuations in the burnt gases. Besides, the choice of the position takes into account that a pressure sensor is already installed at position 4. The total secondary airflow is limited by the diameter of the orifices in the chamber walls and has been chosen equal to 0.25 g/s per entry, thus 0.5 g/s in total. This accounts for less than 3 % of the total air mass flow of 18 g/s. With a diameter of 2 mm of the injection orifices, the mass flow rate of the secondary air injection corresponds to a velocity of about 66 m/s at ambient conditions.

Knowing the flow velocities, the ratio of momentums can be estimated with the following equation (Gruber et al. (1995)):

$$J = \frac{\rho_{secair} \cdot u_{secair}^2}{\rho_{burnt} \cdot u_{burnt}^2} \quad (\text{A.3})$$

with ρ_{secair} and ρ_{burnt} respectively the density of air and the burnt gases and u_{secair} and u_{burnt} respectively the velocity of the secondary air jets and the velocity of the burnt gases. When assuming a velocity 8 m/s for the burnt gases, a density of 0.3 g/s for the burnt gases and 1.2 g/s for air, the equation results to 272. The momentums of secondary jets is thus far above that of the bulk flow.

Three cases are tested with the secondary air injection, the configuration with fully premixed combustion without flame holder rod, the configuration with fully premixed combustion with flame holder rod and the configuration with partly premixed combustion with flame holder rod.

A.6.2 Experimental results of the fully premixed case with secondary air injection

The figures A.19 to A.22 show the different measurements with \dot{m}_{ICS} going from 0 g/s to 2 g/s and \dot{m}_{jet} from 0 g/s to 3.5 g/s. For \dot{m}_{jet} values above 3.5 g/s, no stable flame can be achieved due to blowing out.

The RMS pressures for this case are presented in figure A.19. They have the same tendency as without the secondary air injection (see section A.3), but with a higher level for all cases. Indeed, the pressures reach values above 12000 Pa, which is an increase of 20 % compared to the case without secondary injection.

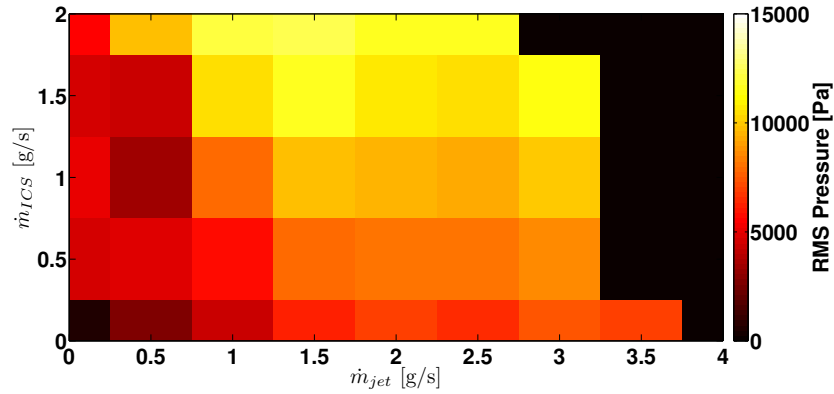


Figure A.19: *RMS pressure map of the fully premixed case with secondary air injection*

The PSD of p_{meas} and p_{cal} are shown for eight chosen operating points in figure A.20, as well as the coherence of the two signals. Two parameters are varied, the axial air flow rate through the ICS and whether flame is fully or partially premixed. The chosen points are thus the following:

- Fully premixed, 0 g/s air through the central jet and 0 g/s air through the ICS
- Fully premixed with secondary air injection through the chamber walls, 0 g/s air through the central jet and 0 g/s air through the ICS
- Fully premixed, 0 g/s air through the central jet and 2 g/s air through the ICS
- Fully premixed with secondary air injection through the chamber walls, 0 g/s air through the central jet and 2 g/s air through the ICS
- Fully premixed, 2 g/s air through the central jet and 0 g/s air through the ICS
- Fully premixed with secondary air injection through the chamber walls, 2 g/s air through the central jet and 0 g/s air through the ICS
- Fully premixed, 2 g/s air through the central jet and 2 g/s air through the ICS
- Fully premixed with secondary air injection through the chamber walls, 2 g/s air through the central jet and 2 g/s air through the ICS

The PSD show that all operating points are dominated by the low frequency instability that was already described in this thesis. It can also be seen that the spectra of p_{meas} and p_{cal} are very similar. However the secondary air injection seems to damp the instability peaks slightly. The consequence is that the coherence is slightly reduced in these frequencies. Apart from this, the coherence in general attains the value of almost 1 at the instability frequency and its harmonics.

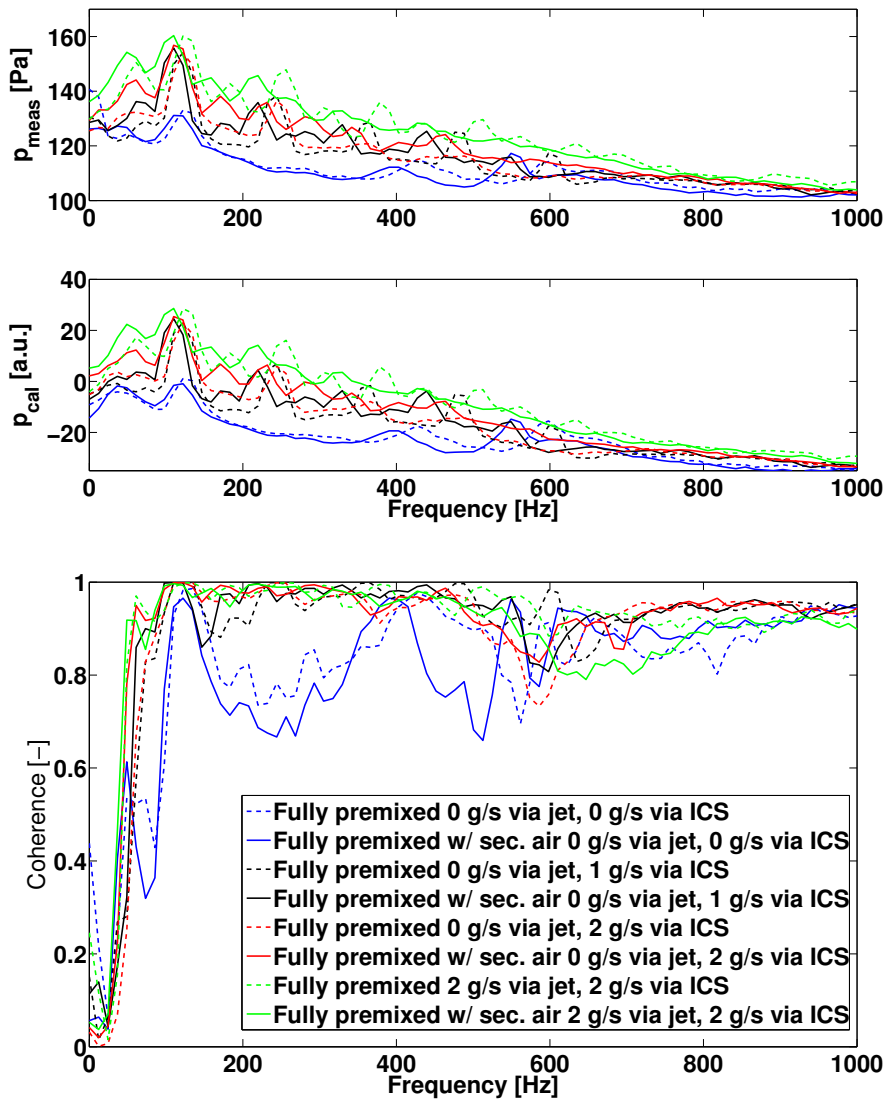


Figure A.20: PSD at 0 g/s axial air flow through the perforated plate of the measured pressure (top image) and the theoretically calculated pressure (middle image) for the different configurations. The bottom image shows the coherence of these two pressures.

The mean and RMS intensity of the PM in the injector is shown in figures A.21 and A.22 and features similar values for low axial air flows. At higher \dot{m}_{jet} , particularly the RMS intensity is increasing.

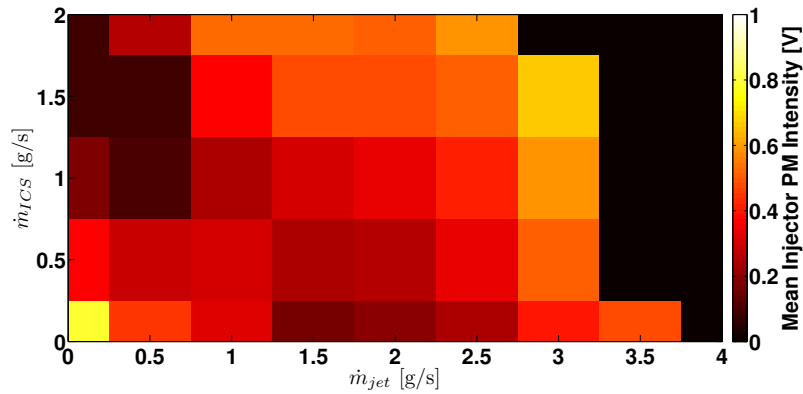


Figure A.21: Mean injector PM intensity map of the fully premixed case with secondary air injection

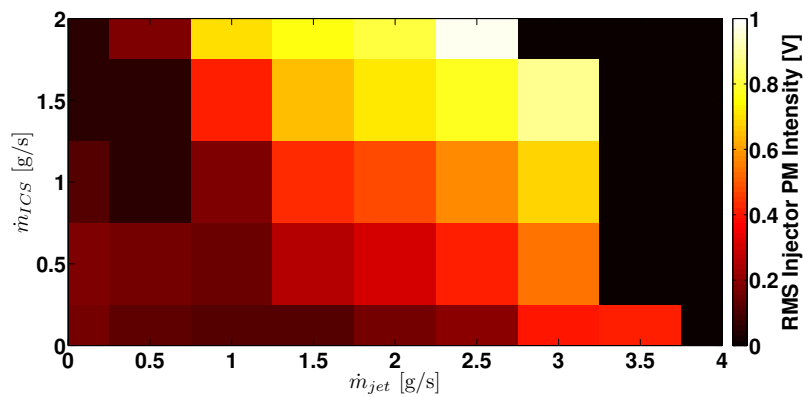


Figure A.22: RMS injector PM intensity map of the fully premixed case with secondary air injection

These observations show that the axial injection has a non-negligible influence on the overall acoustic level, as the RMS is increasing independently from the flow split between \dot{m}_{jet} and \dot{m}_{ICS} . The coherences between p_{meas} and p_{cal} on

the other hand stay the same, which means that this measure seems to have almost no impact on direct combustion noise contribution. This might be related to the fact, that the combustion instability, that was put into evidence in chapter 4 is acting on the entire flow and flame. Thus even if the wall injected air enters at very high velocities, it probably experiences the same combustion instability related velocity fluctuations as the rest of the combustion chamber.

As elaborated in section A.2, the mean and RMS intensity of the injector PM are associated with static and dynamic flashback respectively. The measurements show that especially at higher jet flows, dynamic flashback is increasing. A possible reason might be the direct interaction between the secondary flows and the flame. Indeed, the flame visualizations in chapter 2 show that a high jet flow rate leads to a lower swirl angle and a longer flame with stronger axial fluctuations. Hence, contrary to the cases with lower axial air flow rates, the flame might reach the axial position of the secondary injections. This might also be an explication for the decreased functioning range, however this hypothesis is not regarded further here.

A.6.3 Experimental results of the test with secondary air injection when using a flame holder rod and/or a separate fuel and air injection

As described before, the partially premixed flame can only be operated with a rod as a flame holder. Thus the only mass flow rate that is varied is \dot{m}_{ICS} . The experimental data obtained for this variation are presented in figure A.23 to A.25. These diagrams include the six possible combinations:

- Fully premixed combustion without flame holder rod or secondary air injection
- Fully premixed combustion without flame holder rod and with secondary air injection
- Fully premixed combustion with flame holder rod and without secondary injection
- Fully premixed combustion with flame holder rod and with secondary injection
- Partially premixed combustion with flame holder rod and without secondary injection
- Partially premixed combustion with flame holder rod and with secondary injection

The RMS pressures are presented in figure A.23. It can be seen, that the secondary air flow leads to a slight increase of the pressure RMS when \dot{m}_{ICS} is increased. However, the difference is far below the difference due to the change of the fuel injection system. It can also be seen that the fully premixed test cases have similar RMS pressures, independently from the existence of the flame holder rod.

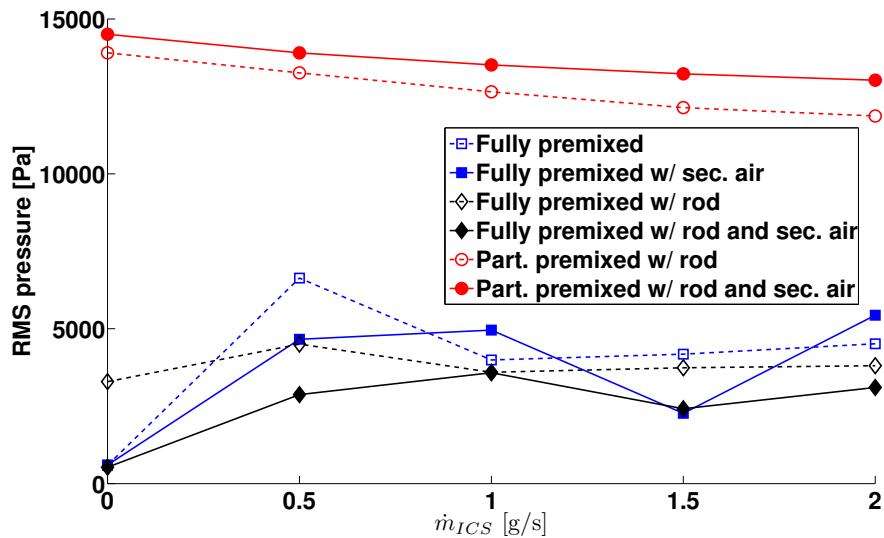


Figure A.23: RMS pressure in dependence from the ICS air flow rate for the different configurations

The injector PM measurements are shown in figure A.24 and A.25. For fully premixed operation mean and RMS PM intensities are a weakly affected by the existence of the secondary air injection. The only exception is at an \dot{m}_{ICS} of 0.5 g/s, where the secondary air injection leads to a decrease of the PM signal RMS by almost 50 %. This observation is made during several repetitions of the experiment, however no explanation can be given. For fully premixed combustion the flame holder rod leads to a decrease in the mean PM signal. For partially premixed operation the secondary air injection through the chamber walls decreases the mean injector PM signal, but even more the RMS.

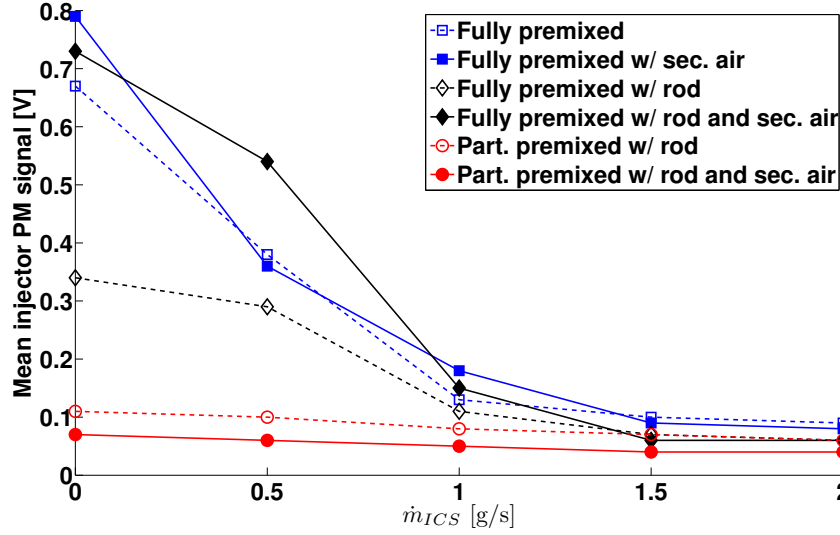


Figure A.24: Mean injector PM signal in dependence from the ICS air flow rate for the different configurations

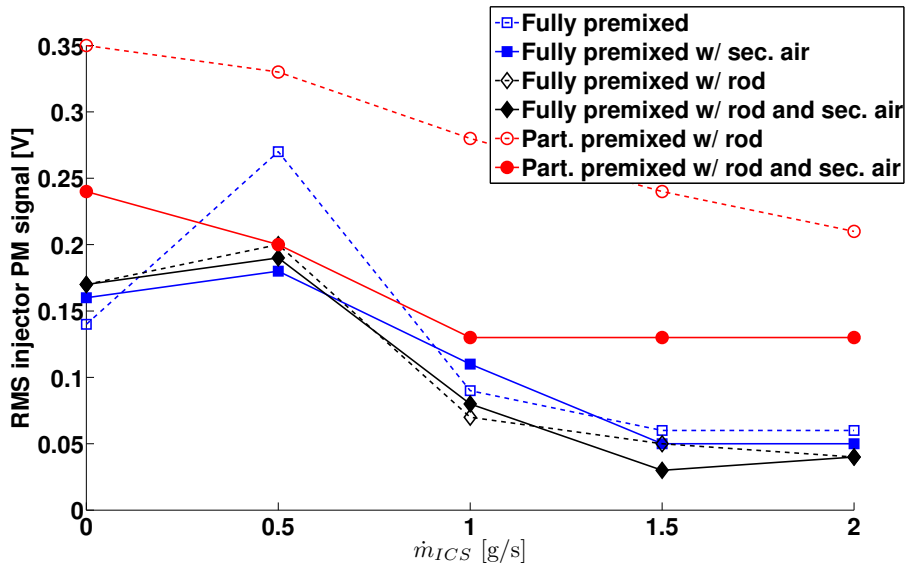


Figure A.25: RMS injector PM signal in dependence from the ICS air flow rate for the different configurations

The flashback behaviour can be deduced from the injector PM measurements, since the magnitude of the signal indicates the presence of the flame in the injector. It is shown that for fully premixed flames the secondary air injection has no influence, neither on static nor on dynamic flashback. The reason can be the fact that the flame is rather compact (as shown in figure A.13) and thus

not in direct contact with the secondary air injection. Therefore, its existence should not have any influence on the behaviour in the injector. An exception can be observed for an \dot{m}_{ICS} of 0.5 g/s. However no explanation can be given here. The installation of the flame holder rod in general decreases the mean intensity that is measured by the PM. This is probably related to the fact that the premixed flame is fixed on the rod and has thus a lower tendency to flash back further upstream. In partially premixed flames the secondary air injection decreases both the mean and RMS intensity of the PM signal. This means that the flame base is more downstream and fluctuates less. A reason for this influence might be the higher length of the partially premixed flame, as can be seen in figure A.13. However this does not explain why the secondary air leads to a decrease of both. This question is not answered here as it is out of the scope of this thesis.

A.7 Analysis of the PSD of measured and theoretical pressure for all tested configurations

In this section the PSD of the measured and the theoretically calculated pressure as well as their coherence are analysed for all tested cases in order to obtain insight about direct and indirect combustion noise contribution. The chosen variations are the following:

- Fully premixed combustion without flame holder rod or secondary air injection
- Fully premixed combustion without flame holder rod and with secondary air injection
- Fully premixed combustion with flame holder rod and without secondary injection
- Fully premixed combustion with flame holder rod and with secondary injection
- Partially premixed combustion with flame holder rod and without secondary injection
- Partially premixed combustion with flame holder rod and with secondary injection

For this test, the axial air mass flow rate through the ICS \dot{m}_{ICS} is varied from 0 to 2 g/s by steps of 1 g/s. The figures thus show the PSD for the test cases described in section A.6.3.

The PSD and the coherence for the operating point with 0 g/s ICS air are shown in figure A.26. All spectra show similarities, especially the fact that they feature the low frequency peak associated to the combustion instability and its harmonics. The PSD for the theoretical and the measured pressure are in particular similar for all fully premixed cases. The secondary air injection through the chamber walls on the other hand seems to damp the low frequency peaks for the case with flame holder rod. The PSD amplitudes are far higher for the partially premixed cases. Two other interesting observations can be made for these two cases: (1) The existence of the secondary air injection leads to a slight decrease of the main eigen frequency and thus also its harmonics. (2) While the distinct peaks are well represented in the spectra for both the measured and the theoretical pressures below 600 Hz, this is not the case for higher frequencies. At higher frequency the peaks have a higher relative amplitude for the theoretically calculated pressure while for the measured pressure they are almost completely damped.

These observations made on the PSD have an effect on the coherence of the two pressures. The coherence is in general high at the frequencies of the distinct peaks, where its value reaches 1. Outside these peaks, the coherence is lower, in particular for the partially premixed cases at frequencies above 600 Hz. This is probably due to the fact that these peaks are of lower amplitude for the measured pressure. The fully premixed cases, on the other hand have a high coherence over the biggest part of the regarded frequency span.

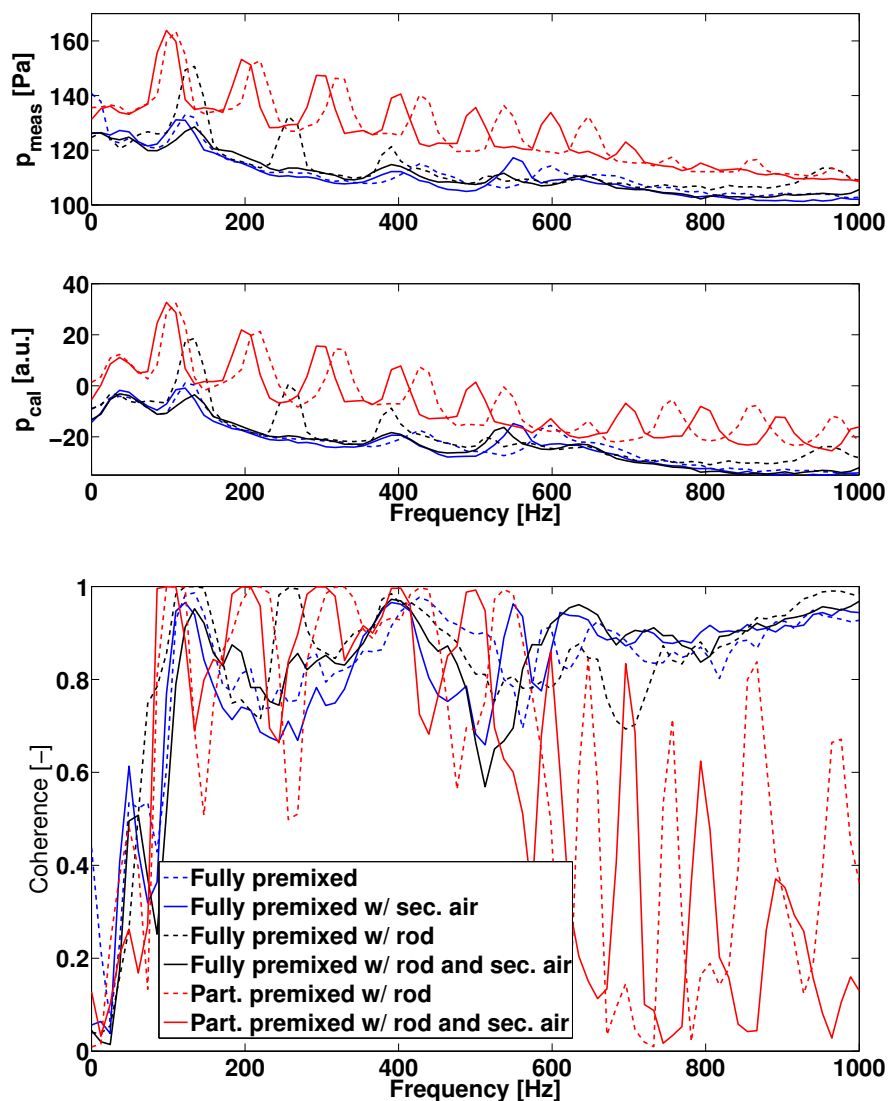


Figure A.26: PSD at 0 g/s axial air flow through the perforated plate of the measured pressure (top image) and the theoretically calculated pressure (middle image) for the different configurations. The bottom image shows the coherence of these two pressures.

The PSD and the coherence for the operating point with 1 g/s ICS air are shown in figure A.27. The observations are very similar to that of the operating point 0g/s axial air mass flow rate. The difference is that the low frequency peaks have a higher amplitude for the premixed cases. Besides, the secondary air injection through the chamber walls still seems to damp these peaks, however to a lower extent. Also it can be observed that the existence of the flame holder rod as well as of the secondary air injection lead to a small shift of the main low frequency peak and its harmonics. The observations made for the coherence

are similar to that for figure A.26.

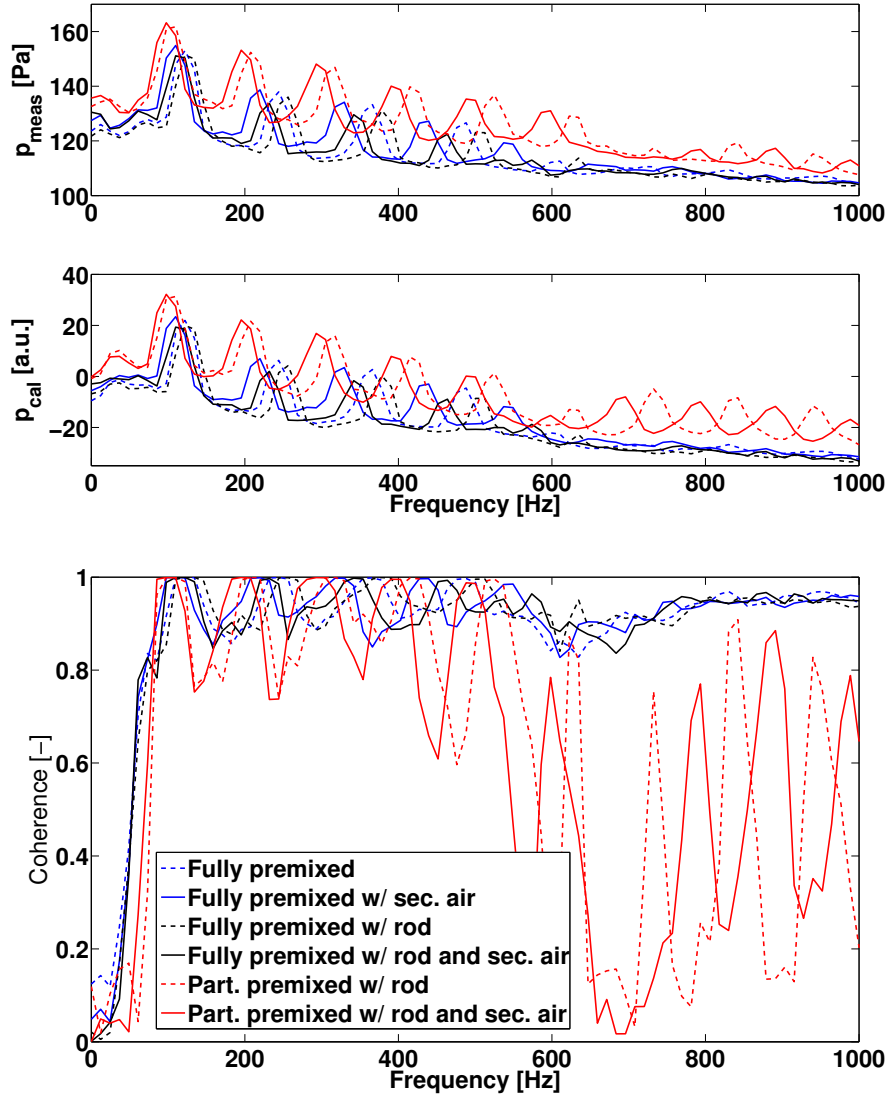


Figure A.27: PSD at 1 g/s axial air flow through the perforated plate of the measured pressure (top image) and the theoretically calculated pressure (middle image) for the different configurations. The bottom image shows the coherence of these two pressures.

The other operating point shown in figure A.28 shows a similar tendency as described for the two previous ones. With increasing axial mass flow rate, the amplitudes of the fully premixed cases without secondary mass flow rate are slightly increasing while the frequency shift is decreasing. The increase of the axial mass flow rate also leads to a higher PSD amplitude which is closer to that of partially premixed case. The coherences displayed in these figures sys-

tematically increase with an increasing axial mass flow rate, especially for the fully premixed cases.

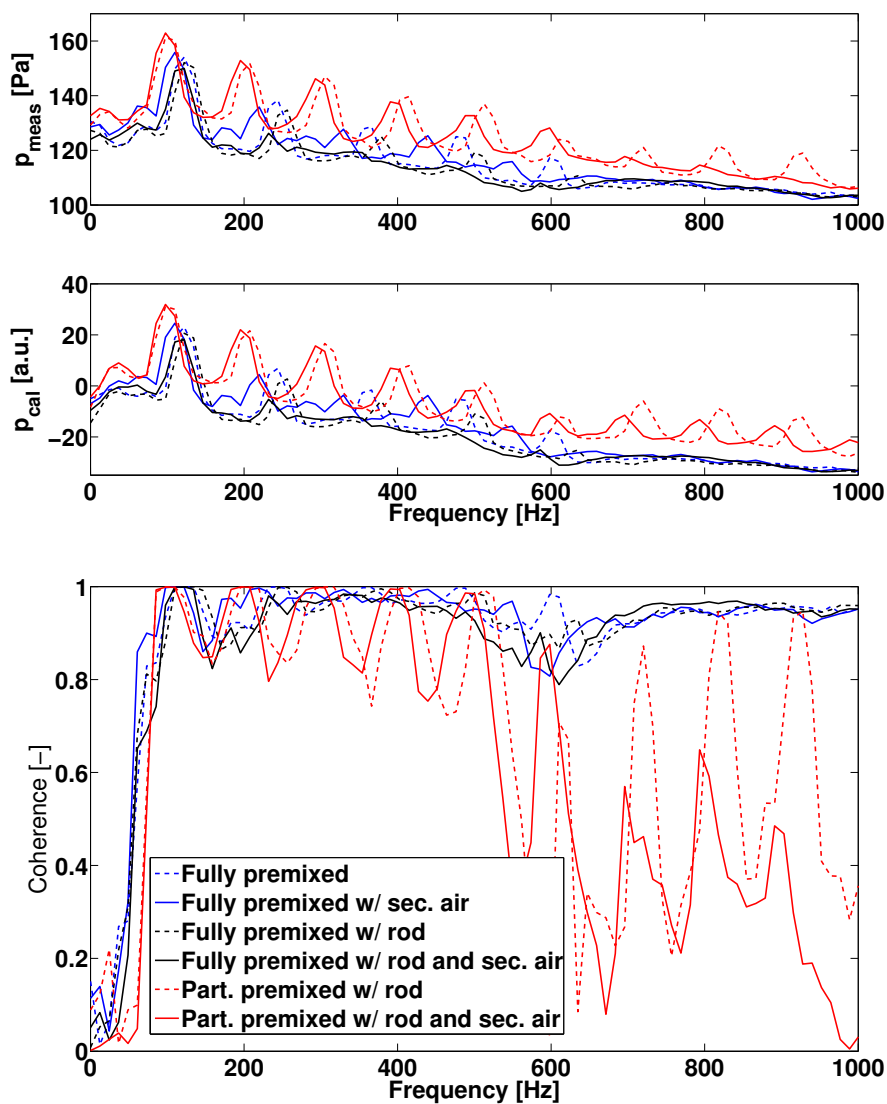


Figure A.28: PSD at 2 g/s axial air flow through the perforated plate of the measured pressure (top image) and the theoretically calculated pressure (middle image) for the different configurations. The bottom image shows the coherence of these two pressures.

The observations made for the spectra and the coherences can be related to the results in section A.6.3. The results show for the fully premixed cases, that the flame holder rod does not have a big influence on the PSD and the coherence. The only difference is a small reduction of the PSD amplitude when using the

flame holder rod. This corresponds to the stabilisation of the flame on the rod, which leads to a reduction of the flame movement and thus to lower oscillations of heat release and finally pressure. However the coherence stays almost the same for this modification for the entire frequency range, which probably means that the influence on the distribution of combustion noise on its direct and indirect parts is limited.

The secondary air injection also has very limited influence on the PSD. It leads to a reduction of the PSD amplitudes for the fully premixed cases and even more it leads to a small frequency shift of the distinct peaks. A possible explanation can be a decrease of temperature for the partially premixed case, which decreases the speed of sound and thus the frequency.

The partially premixed cases on the other hand have a very low coherence, especially for frequencies above 600 Hz. This is related to the fact that at these frequencies, the peaks have different amplitudes for the theoretical and the measured pressure.

A.8 Conclusion

In this chapter, three major modifications of the CESAM-HP test bench are presented and their effectiveness is tested. They have the aim to increase overall indirect combustion noise contribution. The motivation is the fact, that indirect combustion noise makes up only around 5 % of total combustion noise (cf. chapter 4). The first modification is the installation of central flame holder rod for flame stabilization. The second one is a separate fuel injection. This changes the combustor functioning to a partially premixed operation. The third modification is the introduction of a secondary air injection through the chamber walls. The goal is to add inhomogeneities to the burnt gases, which would directly increase indirect combustion noise.

The modifications are verified by testing different combinations of direct air flow \dot{m}_{jet} and ICS bias air flow \dot{m}_{ICS} . The results show that the installation of a separate fuel injection in general increases the pressure fluctuations, however the peak amplitudes between the theoretically calculated pressure (related to direct combustion noise) and the measured pressure PSD are different at frequencies above 600 Hz. This might be an indicator for a different source than direct combustion noise, however the conducted test do not allow to make further conclusions. The secondary air flow and the flame holder rod, on the other hand decrease direct noise contribution by only very little.

These results allow for the conclusion that non premixed operation can be an

interesting perspective in order to increase the indirect combustion noise generation in the combustor. However, further experiments need to be conducted in order to verify whether the added sound contribution is indeed indirect combustion noise. Different geometries and flow rates would be needed to be tested, also with laser-based diagnostics in order to identify the differences in flow field and flame. Also the other two modifications need to be tested more in-depth (with different bluff body geometries and different air mass flow rates through the chamber walls); since the chosen configurations only cover one of many possible variations and configurations. Therefore the here performed tests do not allow yet for a final conclusion concerning the effectiveness of these modifications.

References

- Abugov, D. I. and O. I. Obrezkov (1978). Acoustic noise in turbulent flames. *Combust. Explosions Shock Waves*, 14:606–612. (p. 11)
- Adrian, R. J. (1991). Particle-imaging techniques for experimental fluid mechanics. *Annual Review of Fluid Mechanics* 23(1), 261–304. (p. 50, 105)
- Adrian, R. J. (2005). Twenty years of particle image velocimetry. *Experiments in Fluids* 39(2), 159–169. (p. 50, 105)
- Bailly, C., C. Bogey, and S. Candel (2010). Modelling of sound generation by turbulent reacting flows. *International Journal of Aeroacoustics* 9(4-5), 461–489. (p. 11)
- Bake, F., A. Fischer, N. Kings, and I. Roehle (2009). Investigation of the correlation of entropy waves and acoustic emission in combustion chambers. *Combustion Noise, Springer-Verlag Berlin Heidelberg*. (p. 9)
- Bake, F., N. Kings, and I. Roehle (2008, 01). Fundamental mechanism of entropy noise in aero-engines: Experimental investigation. *Journal of Engineering for Gas Turbines and Power* 130(1), 011202–011202. (p. 9)
- Bake, F., C. Richter, B. Mühlbauer, N. Kings, I. Röhle, F. Thiele, and B. Noll (2009). The entropy wave generator (ewg): A reference case on entropy noise. *Journal of Sound and Vibration* 326(3-5), 574 – 598. (p. 9)
- Bell, W., B. Daniel, and B. Zinn (1973). Experimental and theoretical determination of the admittances of a family of nozzles subjected to axial instabilities. *Journal of Sound and Vibration* 30(2), 179 – 190. (p. 14)
- Bender, C., F. Zhang, H. Habisreuther, H. Buchner, and H. Bockhorn (2009). Measurement and simulation of combustion noise emitted from siwrl burners. *Combustion Noise, Springer-Verlag Berlin Heidelberg*. (p. 9)
- Bogey, C., X. Gloerfelt, and C. Bailly (2003, 2016/11/11). Illustration of the inclusion of sound-flow interactions in lighthill’s equation. *AIAA Journal* 41(8), 1604–1606. (p. 11)
- Boxx, I., C. Heeger, R. Gordon, B. Böhm, M. Aigner, A. Dreizler, and W. Meier (2009). Simultaneous three-component piv/oh-plif measurements of a turbulent lifted, c3h8-argon jet diffusion flame at 1.5 khz repetition rate. *Proceedings of the Combustion Institute* 32(1), 905 – 912. (p. xiii, 111, 112)
- Bräunling, W. J. G. (2015). Flugzeugtriebwerke. *Springer Dordrecht Heidelberg London New York, 4th edition, 2015*. (p. xv, 3, 4)

- Brouckaert, J.-F., M. Mersinligil, and M. Pau (2008, 12). A conceptual design study for a new high temperature fast response cooled total pressure probe. *Journal of Engineering for Gas Turbines and Power* 131(2), 021602–021602. (p. 36)
- Candel, S. (2002). Combustion dynamics and control: Progress and challenges. *Proceedings of the Combustion Institute* 29(1), 1 – 28. (p. 3, 4, 16, 82, 94, 98, 106)
- Candel, S., D. Durox, S. Ducruix, A.-L. Birbaud, N. Noiray, and T. Schuller (2009). Flame dynamics and combustion noise: Progress and challenges. *International Journal of Aeroacoustics* 8(1), 1–56. (p. 6, 7, 11, 163)
- Candel, S., D. Durox, T. Schuller, J.-F. Bourgoignie, and J. P. Moeck (2014). Dynamics of swirling flames. *Annual Review of Fluid Mechanics* 46(1), 147–173. (p. 3, 55, 106, 117)
- Charonko, J. and P. Vlachos (2013). Estimation of uncertainty bounds for individual particle image velocimetry measurements from cross-correlation peak ratio. *Measurement Science and Technology* 24(6), 065301. (p. 115)
- Childs, P. (2003). Advances in temperature measurement. 36, 111 – 181. (p. 8, 18, 181)
- Chu, B.-T. and L. S. G. Kovaszny (1958, 02). Non-linear interactions in a viscous heat-conducting compressible gas. *Journal of Fluid Mechanics* 3(5), 494–514. (p. 14)
- Chung, J. Y. and D. A. Blaser (1980). Transfer function method of measuring in-duct acoustic properties. i. theory. *The Journal of the Acoustical Society of America* 68(3), 907–913. (p. 69, 197)
- Clavin, P. and E. D. Siggia (1991, 07). Turbulent premixed flames and sound generation. *Combustion Science and Technology* 78(1-3), 147–155. (p. 11, 165)
- Correa, S. M. (1998). Power generation and aeropropulsion gas turbines: From combustion science to combustion technology. *Symposium (International) on Combustion* 27(2), 1793 – 1807. (p. 3)
- Crighton, D. G., A. P. Dowling, J. E. F. Williams, M. Heckl, and F. G. Leppington (1992). Thermoacoustic sources and instabilities. *Modern Methods in Analytical Acoustics Lecture Notes*, pp. 378–405. London: Springer London. (p. 7, 11, 184)
- Crocco, L. (1951). Aspects of combustion stability in liquid propellant rocket motors .1. fundamentals - low frequency instability with monopropellants. *Journal of the American Rocket Society* 21(6), 163–178. (p. 14)
- Cumpsty, N. (1979). Jet engine combustion noise: Pressure, entropy and vorticity perturbations produced by unsteady combustion or heat addition. *Journal of Sound and Vibration* 66(4), 527 – 544. (p. 14)
- Dioc, N. (2005). Etude expérimentale des mécanismes d'instabilité dans un brûleur à injection étagée. application aux turbines à gaz. *PhD Thesis, Ecole Centrale Paris*. (p. 17, 29, 32)
- Dowling, A. P., N. Hooper, P. J. Langhorne, and G. J. Bloxside (1988,

- 2016/11/11). Active control of reheat buzz. *AIAA Journal* 26(7), 783–790. (p. 13)
- Dowling, A. P. and Y. Mahmoudi (2015). Combustion noise. *Proceedings of the Combustion Institute* 35(1), 65 – 100. (p. xv, 7, 15)
- Dowling, A. P. and S. R. Stow (2003, 2016/11/11). Acoustic analysis of gas turbine combustors. *Journal of Propulsion and Power* 19(5), 751–764. (p. 12, 67)
- Dowling, A. P. and J. E. F. Williams (1983). Sound and sources of sound. *Ellis Horwood*. (p. 12)
- Duchaine, P., L. Zimmer, and T. Schuller (2009). Experimental investigation of mechanisms of sound production by partially premixed flames. *Proceedings of the Combustion Institute* 32(1), 1027 – 1034. (p. 213)
- Ducruix, S., D. Durox, and S. Candel (2000). Theoretical and experimental determinations of the transfer function of a laminar premixed flame. *Proceedings of the Combustion Institute* 28(1), 765 – 773. (p. 82)
- Ducruix, S., T. Schuller, D. Durox, and S. Candel (2003, 2016/11/11). Combustion dynamics and instabilities: Elementary coupling and driving mechanisms. *Journal of Propulsion and Power* 19(5), 722–734. (p. 3, 4, 16, 94)
- Ducruix, S., T. Schuller, D. Durox, and S. Candel (2006). Combustion instability mechanisms in premixed combustors. *AIAA Progress in Astronautics and Aeronautics, "Combustion Instabilities in Gas Turbine Engines: Operational Experience, Fundamental Mechanisms, and Modeling"*, chapter 9, edited by T. C. Lieuwen and V. Yang, AIAA. (p. 82, 83, 85, 97, 98)
- Duran, I., S. Moreau, F. Nicoud, T. Livebardon, E. Bouty, and T. Poinsot (2014). Combustion noise in modern aero-engines. *Journal AerospaceLab AL07-05*. (p. 8)
- Durox, D., T. Schuller, and S. Gandel (2002). Self-induced instability of a premixed jet flame impinging on a plate. *Proceedings of the Combustion Institute* 29(1), 69 – 75. (p. 82)
- Eckstein, J., E. Freitag, C. Hirsch, and T. Sattelmayer (2004). Experimental study on the role of entropy waves in low-frequency oscillations for a diffusion burner. *GT2004-54163*, pp. 743-751, *ASME Turbo Expo 2004: Power for Land, Sea, and Air, Vienna, Austria, June 14–17, 2004*. (p. 13)
- enHealth (2004). The health effects of environmental noise – other than hearing loss. *Technical report, Department of Health and Ageing - Australian government, 2004*. (p. 1)
- EPA, U. (2010). U. s. climate action report - fifth national communication of the united states of america. *U. S. Environmental Protection Agency, 2010*. (p. 1)
- FAA (2016). Aircraft noise issues. *Federal Aviation Administration Homepage*. (p. 4)

- Floryan, D., J. Hofferth, and W. Saric (2012). Design, assembly and calibration of a focusing schlieren system. *Texas A & M University, Project report*. (p. *xix*, 126)
- Franzelli, B., E. Riber, L. Y. M. Gicquel, and T. Poinso (2012). Large eddy simulation of combustion instabilities in a lean partially premixed swirled flame. *Combustion and Flame* 159(2), 621 – 637. (p. 14)
- Fritz, J., M. Kroner, and T. Sattelmayer (2004, 06). Flashback in a swirl burner with cylindrical premixing zone. *Journal of Engineering for Gas Turbines and Power* 126(2), 276–283. (p. 3, 4, 30)
- Giauque, A., M. Huet, and F. Clero (2012, 09). Analytical analysis of indirect combustion noise in subcritical nozzles. *Journal of Engineering for Gas Turbines and Power* 134(11), 111202–111202. (p. 17, 28, 35)
- Giauque, A., M. Huet, F. Clero, S. Ducruix, and F. Richecoeur (2013, 08). Thermoacoustic shape optimization of a subsonic nozzle. *Journal of Engineering for Gas Turbines and Power* 135(10), 102601–102601. (p. 17, 28, 35)
- Giuliani, F., T. Leitgeb, A. Lang, and J. Woisetschlager (2009, 12). Mapping the density fluctuations in a pulsed air-methane flame using laser-vibrometry. *Journal of Engineering for Gas Turbines and Power* 132(3), 031603–031603. (p. 18, 130, 182)
- GmbH, S. M. (2006). Re-06 computer module. *Technical manual for Laser Vibrometer*. (p. 181)
- Goh, C. S. and A. S. Morgans (2013). The influence of entropy waves on the thermoacoustic stability of a model combustor. *Combustion Science and Technology* 185(2), 249–268. (p. 16)
- Groenstedt, T., M. Irannezhad, X. Lei, O. Thulin, and A. Lundbladh (2013, 11). First and second law analysis of future aircraft engines. *Journal of Engineering for Gas Turbines and Power* 136(3), 031202–031202. (p. xv, 1, 2)
- Gruber, M. R., A. S. Nejad, T. H. Chen, and J. C. Dutton (1995, 2016/11/11). Mixing and penetration studies of sonic jets in a mach 2 freestream. *Journal of Propulsion and Power* 11(2), 315–323. (p. 224, 231)
- Guedel, A. and A. Ferrando (1986, 2016/11/11). Experimental study of turboshaft engine core noise. *Journal of Aircraft* 23(10), 763–767. (p. 8)
- Gupta, A., D. Lilley, and N. Syred (1984). Swirling flows. *Tunbridge Wells, Kent : Abacus Press*. (p. 64)
- Harper-Bourne, M., A. Moore, and H. Siller (2008, 2016/11/11). *A Study of Large Aero-Engine Combustor Noise*. American Institute of Aeronautics and Astronautics. (p. 8)
- Hassan, H. A. (1974, 11). Scaling of combustion-generated noise. *Journal of Fluid Mechanics* 66(3), 445–453. (p. 164)
- Hendricks, E. S. (2011). Development of an open rotor cycle model in npss using a multi-point design approach. *ASME 2011 Turbo Expo: Turbine*

- Technical Conference and Exposition*, pp. 441-450. (p. 2)
- Higgins, B., M. McQuay, F. Lacas, J. Rolon, N. Darabiha, and S. Candel (2001). Systematic measurements of {OH} chemiluminescence for fuel-lean, high-pressure, premixed, laminar flames. *Fuel* 80(1), 67 – 74. (p. 50, 171)
- Howe, M. S. (1979). On the theory of unsteady high reynolds number flow through a circular aperture. *Proceedings of the Royal Society of London. Series A, Mathematical and Physical Sciences* 366(1725), 205–223. (p. 74)
- Howe, M. S. (2003). Theory of vortex sound. (p. 10)
- Hulshoff, S. J., A. Hirschberg, and G. C. J. Hofmans (2001, 07). Sound production of vortex-nozzle interactions. *Journal of Fluid Mechanics* 439, 335–352. (p. 10)
- Jeschke, P. (2012). Manuskript zur vorlesung luftfahrtantriebe. *Institut fuer Strahlantriebe und Turboarbeitsmaschinen, Univ.-Prof. Dr.-Ing. P. Jeschke, RWTH Aachen*. (p. xv, 3, 14, 28)
- Karchmer, A. and M. Reshotko (1976). Core noise source diagnostics on a turbofan engine using correlation and coherence techniques. *The Journal of the Acoustical Society of America* 60(S1), S112–S113. (p. 7, 8)
- Keane, R. D. and R. J. Adrian (1990). Optimization of particle image velocimeters. i. double pulsed systems. *Measurement Science and Technology* 1(11), 1202. (p. 108)
- Kings, N., K. Knobloch, L. Enghardt, and F. Bake (2011). Indirect combustion noise : Experimental investigation of the vortex sound generation mechanism. *17th AIAA/CEAS Aeroacoustics Conference, Portland, OR (June)*, 5â€8. (p. 10)
- Kings, N., W. Tao, M. Mazur, P. Scouffaire, F. Richecoeur, and S. Ducruix (2015). Experimental and numerical investigation on combustion noise sources in a model gas turbine combustor. *X-NOISE Workshop 2015, La Rochelle France*. (p. xxi, xxii, 179, 180, 196)
- Kings, N., W. Tao, P. Scouffaire, F. Richecoeur, and S. Ducruix (2016). Experimental and numerical investigation of direct and indirect combustion noise contributions in a lean preamixed laboratory swirled combustor. *Proceedings of ASME Turbo Expo 2016, GT2016, June 13-17 2016, Seoul, South Korea*. (p. 179, 183)
- KISTLER (2013). Oscillations de tubulure. *Technical document*. (p. xvi, 37)
- Köberl, S., F. Fontaneto, F. Giuliani, and J. Woisetschlager (2010). Frequency-resolved interferometric measurement of local density fluctuations for turbulent combustion analysis. *Measurement Science and Technology* 21(3), 035302. (p. 182)
- Kouchi, T., C. P. Goynes, R. D. Rockwell, and J. C. McDaniel (2015). Focusing-schlieren visualization in a dual-mode scramjet. *Experiments in Fluids* 56(12), 211. (p. 130, 131, 133)
- Kovitz, A. A. and H.-M. Fu (1961). On bluff body flame stabilization. *Applied*

- Scientific Research* 10(1), 315. (p. 219)
- Lamraoui, A. (2011). Acoustique et dynamique de flamme dans un foyer turbulent prémélangé swirlé : application à l'étude du bruit de combustion dans les chambres de turbines à gaz. *PhD thesis, École Centrale Paris, 2011*. (p. xv, 17, 32, 67)
- Lamraoui, A., F. Richecoeur, T. Schuller, and S. Ducruix (2010, 09). A methodology for on the fly acoustic characterization of the feeding line impedances in a turbulent swirled combustor. *Journal of Engineering for Gas Turbines and Power* 133(1), 011504–011504. (p. xvii, 69)
- Lapeyre, C. (2015). Numerical study of flame stability, stabilization and noise in a swirl-stabilized combustor under choked conditions. *PhD Thesis, INP Toulouse*. (p. xv, 3)
- Lapeyre, C. J., M. Mazur, P. Scouffaire, F. Richecoeur, S. Ducruix, and T. Poinsot (2016). Acoustically induced flashback in a staged swirl-stabilized combustor. *Flow, Turbulence and Combustion*, 1–18. (p. 3, 30, 214)
- Law, C. (1989). Dynamics of stretched flames. *Symposium (International) on Combustion* 22(1), 1381 – 1402. (p. 83)
- Leitgeb, T., T. Schuller, D. Durox, F. Giuliani, S. Köberl, and J. Woisetschläger (2013). Interferometric determination of heat release rate in a pulsated flame. *Combustion and Flame* 160(3), 589 – 600. (p. 181, 184)
- Letty, C., B. Renou, J. Reveillon, S. Saengkaew, and G. Gréhan (2013). Experimental study of droplet temperature in a two-phase heptane/air v-flame. *Combustion and Flame* 160(9), 1803 – 1811. (p. xviii, 111, 112)
- Leyko, M. (2010). Mise en oeuvre et analyse des calculs aéroacoustiques de type sge pour la prévision du bruit de chambres de combustion aéronautiques. *PhD thesis, INP Toulouse*. (p. 6)
- Leyko, M., F. Nicoud, and T. Poinsot (2009, 2016/11/11). Comparison of direct and indirect combustion noise mechanisms in a model combustor. *AIAA Journal* 47(11), 2709–2716. (p. xv, 14, 15)
- Li, J. (2012). Development of novel diagnostic techniques to measure heat release rate perturbations in flames. *PhD thesis, Ecole Centrale Paris*. (p. xxi, 18, 180)
- Lieuwen, T. and J. H. Cho (2005). Coherent acoustic wave amplification/damping by wrinkled flames. *Journal of Sound and Vibration* 279(3&5), 669 – 686. (p. 4)
- Lieuwen, T. and B. T. Zinn (1998). The role of equivalence ratio oscillations in driving combustion instabilities in low nox gas turbines. *Symposium (International) on Combustion* 27(2), 1809 – 1816. (p. 82, 85)
- Lighthill, M. J. (1952). On sound generated aerodynamically. i. general theory. *Proceedings of the Royal Society of London A: Mathematical, Physical and Engineering Sciences* 211(1107), 564–587. (p. 11)
- Livebardon, T. (2015). Modeling of combustion noise in helicopter engines.

- PhD thesis, INP Toulouse. (p. 8, 14)*
- Marble, F. and S. Candel (1977). Acoustic disturbance from gas non-uniformities convected through a nozzle. *Journal of Sound and Vibration* 55(2), 225 – 243. (p. 14, 15, 35, 75, 146, 152, 179, 196, 197, 201, 209)
- Mayrhofer, N. and J. Woisetschläger (2001). Frequency analysis of turbulent compressible flows by laser vibrometry. *Experiments in Fluids* 31(2), 153–161. (p. 18, 181)
- Mazur, M., P. Scouffaire, F. Richecoeur, and S. Ducruix (2015). High speed piv measurements in reactive flows using a continuous wave laser. *Gordon Research Conference 2015: Laser Diagnostics in Combustion, August 2015, Waterville Valley, NH, USA. (p. 107)*
- Mazur, M., P. Scouffaire, F. Richecoeur, L. C. C. Mesquita, A. Vié, and S. Ducruix (2017). Planar velocity measurements at 100 khz in a gas turbine combustors with a continuous laser source. *Proceedings of ASME Turbo Expo 2017 : Turbine Technical Conference and Exposition, GT2017-64597, June 26-30, 2017, Charlotte, NC, USA. (p. 120, 123, 210)*
- Mazur, M., W. Tao, P. Scouffaire, F. Richecoeur, and S. Ducruix (2015). Experimental and analytical study of the acoustic properties of a gas turbine model combustor with a choked nozzle. *Proceedings of ASME Turbo Expo 2015 : Turbine Technical Conference and Exposition, GT2015-43013, June 15-19, 2015, Montréal, QC, Canada. (p. 67)*
- Melling, A. (1997). Tracer particles and seeding for particle image velocimetry. *Measurement Science and Technology* 8(12), 1406. (p. 114, 116)
- Mersinligil, M., J.-F. Brouckaert, and J. Dasset (2010). First unsteady pressure measurements with a fast response cooled total pressure probe in high temperature gas turbine environments. *Proceedings of the ASME Turbo Expo 2010 Power for Land, Sea and Air, June 14-18, 2010, Glasgow, UK. (p. 36)*
- Mersinligil, M., J. Dasset, and J. F. Brouckaert (2011). High-temperature high-frequency turbine exit flow field measurements in a military engine with a cooled unsteady total pressure probe. *Proceedings of the Institution of Mechanical Engineers, Part A: Journal of Power and Energy* 225(7), 954–963. (p. 36)
- Miller, J. D., N. Jiang, M. N. Slipchenko, J. G. Mance, T. R. Meyer, S. Roy, and J. R. Gord (2016). Spatiotemporal analysis of turbulent jets enabled by 100-khz, 100-ms burst-mode particle image velocimetry. *Experiments in Fluids* 57(12), 192. (p. 107)
- Moase, W. H., M. J. Brear, and C. Manzie (2007, 008). The forced response of choked nozzles and supersonic diffusers. *Journal of Fluid Mechanics* 585, 281–304. (p. 14)
- Morgans, A. S. and I. Duran (2016). Entropy noise: A review of theory, progress and challenges. *International Journal of Spray and Combustion*

- Dynamics*. (p. [xv](#), [7](#), [10](#), [12](#), [13](#), [14](#), [16](#))
- Muthukrishnan, M., W. C. Strahle, and D. H. Neale (1978, 2016/11/11). Separation of hydrodynamic, entropy, and combustion noise in a gas turbine combustor. *AIAA Journal* 16(4), 320–327. (p. [8](#))
- Neise, W. and L. Enghardt (2003). Technology approach to aero engine noise reduction. *Aerospace Science and Technology* 7(5), 352 – 363. (p. [xv](#), [5](#))
- Palies, P., D. Durox, T. Schuller, and S. Candel (2011, 04). Experimental study on the effect of swirler geometry and swirl number on flame describing functions. *Combustion Science and Technology* 183(7), 704–717. (p. [64](#))
- Peterleithner, J., N. V. Stadlmair, J. Woisetschlager, and T. Sattelmayer (2015, 09). Analysis of measured flame transfer functions with locally resolved density fluctuation and oh-chemiluminescence data. *Journal of Engineering for Gas Turbines and Power* 138(3), 031504–031504. (p. [182](#))
- Peterleithner, J., S. Zorobin, and J. Woitsetschlager (2016). Anaysis of combustion noise using locally resolved density fluctuations and a microphone array. *Proceedings of ASME Turbo Expo 2016 : Turbine Technical Conference and Exposition, GT2016, June 13-17, 2016, Seoul, South Korea*. (p. [224](#))
- Peters, N. (2000). Turbulent combustion. *Cambridge University Press, Cambridge, U.K.* (p. [83](#))
- Picano, F., F. Battista, G. Troiani, and C. M. Casciola (2011). Dynamics of piv seeding particles in turbulent premixed flames. *Experiments in Fluids* 50(1), 75–88. (p. [116](#))
- Pickett, G. (1975, 2016/11/11). *Core engine noise due to temperature fluctuations convecting throughturbine blade rows*. American Institute of Aeronautics and Astronautics. (p. [8](#))
- Poinsot, T. and D. Veynante (2005). Theoretical and numerical combustion. *2nd edition, Edwards, 2005*. (p. [67](#), [75](#))
- Poinsot, T. J., A. C. Trouve, D. P. Veynante, S. M. Candel, and E. J. Esposito (1987, 04). Vortex-driven acoustically coupled combustion instabilities. *Journal of Fluid Mechanics* 177, 265–292. (p. [82](#))
- Providakis, T., L. Zimmer, P. Scoufflaire, and S. Ducruix (2013). Characterization of the coherent structures in swirling flames stabilized in a two-staged multi-injection burner: Influence of the staging factor. *Comptes Rendus Mecanique* 341(1), 4 – 14. (p. [xiii](#), [111](#), [112](#), [117](#))
- Reichel, T. G., S. Terhaar, and O. Paschereit (2015, 07). Increasing flashback resistance in lean premixed swirl-stabilized hydrogen combustion by axial air injection. *Journal of Engineering for Gas Turbines and Power* 137(7), 071503–071503. (p. [4](#), [30](#))
- Richecoeur, F., T. Schuller, A. Lamraoui, and S. Ducruix (2013). Analytical and experimental investigations of gas turbine model combustor acoustics operated at atmospheric pressure. *Comptes Rendus Mecanique* 341(1), 141 – 151. (p. [67](#), [72](#), [77](#))

- Roux, S., G. Lartigue, T. Poinsot, U. Meier, and C. Bérat (2005). Studies of mean and unsteady flow in a swirled combustor using experiments, acoustic analysis, and large eddy simulations. *Combustion and Flame* 141(1&2), 40 – 54. (p. 67)
- Sattelmayer, T. (2002, 12). Influence of the combustor aerodynamics on combustion instabilities from equivalence ratio fluctuations. *Journal of Engineering for Gas Turbines and Power* 125(1), 11–19. (p. 13)
- Sattelmayer, T., C. Mayer, and J. Sangl (2015, 08). Interaction of flame flashback mechanisms in premixed hydrogen–air swirl flames. *Journal of Engineering for Gas Turbines and Power* 138(1), 011503–011503. (p. 4, 30)
- Scarpato, A. (2014). Linear and nonlinear analysis of the acoustic response of perforated plates traversed by a bias flow. *PhD Thesis, Ecole Centrale Paris*. (p. 17, 68)
- Scarpato, A., S. Ducruix, and T. Schuller (2013). Optimal and off-design operations of acoustic dampers using perforated plates backed by a cavity. *Journal of Sound and Vibration* 332(20), 4856 – 4875. (p. 30)
- Scarpato, A., N. Tran, S. Ducruix, and T. Schuller (2012). Modeling the damping properties of perforated screens traversed by a bias flow and backed by a cavity at low strouhal number. *Journal of Sound and Vibration* 331(2), 276 – 290. (p. 30)
- Schetz, J. A. and F. S. Billig (1966, 2016/11/11). Penetration of gaseous jets injected into a supersonic stream. *Journal of Spacecraft and Rockets* 3(11), 1658–1665. (p. 224)
- Schobeiri, M. T. and S. M. Ghoreyshi (2014). The ultra-high efficiency gas turbine engine with stator internal combustion, uhegt. *U.S. patent application 62/046,542*. (p. 2)
- Schobeiri, M. T. and S. M. Ghoreyshi (2015, 09). The ultrahigh efficiency gas turbine engine with stator internal combustion. *Journal of Engineering for Gas Turbines and Power* 138(2), 021506–021506. (p. 2)
- Schuller, T., S. Ducruix, D. Durox, and S. Candel (2002). Modeling tools for the prediction of premixed flame transfer functions. *Proceedings of the Combustion Institute* 29(1), 107 – 113. (p. 82)
- Schuller, T., D. Durox, and S. Candel (2002). Dynamics of and noise radiated by a perturbed impinging premixed jet flame. *Combustion and Flame* 128(1&2), 88 – 110. (p. 9, 50, 82, 89, 163, 165)
- Schulz, C. and V. Sick (2005). Tracer-lif diagnostics: quantitative measurement of fuel concentration, temperature and fuel/air ratio in practical combustion systems. *Progress in Energy and Combustion Science* 31(1), 75 – 121. (p. 171)
- Sensiau, C. (2013). Investigation of combustion noise on snecma turbofans. *Seminar on the French Research Project MAMBO about Combustion Noise-Scientific Days, October 18th, Onera*. (p. xv, 5, 6)
- Settles, G. S. (2001). Schlieren and shadowgraph techniques. *Springer-Verlag*

- Berlin Heidelberg.* (p. 126)
- Shadow, K. C., E. J. Gutmark, T. P. Parr, D. M. Parr, K. J. Wilson, and J. E. Crump (1989, 04). Large-scale coherent structures as drivers of combustion instability. *Combustion Science and Technology* 64(4-6), 167–186. (p. 82)
- Shivashankam, B. N. (1978, 2016/11/11). Gas turbine core noise source isolation by internal-to-far-field correlations. *Journal of Aircraft* 15(9), 597–600. (p. 8)
- Shivashankara, B., W. Strahle, and J. Handley (1975, 2016/11/11). Evaluation of combustion noise scaling laws by an optical technique. *AIAA Journal* 13(5), 623–627. (p. 11)
- Silva, C. F. (2010). Numerical study of combustion noise in gas turbines. *PhD thesis, Université Montpellier II.* (p. 6)
- Singh, K. K., C. Zhang, J. P. Gore, L. Mongeau, and S. H. Frankel (2005). An experimental study of partially premixed flame sound. *Proceedings of the Combustion Institute* 30(2), 1707 – 1715. (p. 213)
- Sisco, J., Y. Yu, V. Sankaran, and W. Anderson (2011). Examination of mode shapes in an unstable model combustor. *Journal of Sound and Vibration* 330(1), 61 – 74. (p. 67)
- Smith, T. J. B. and J. K. Kilham (1963). Noise generation by open turbulent flames. *The Journal of the Acoustical Society of America* 35(5), 715–724. (p. 11)
- Stöhr, M., I. Boxx, C. Carter, and W. Meier (2011). Dynamics of lean blowout of a swirl-stabilized flame in a gas turbine model combustor. *Proceedings of the Combustion Institute* 33(2), 2953 – 2960. (p. 3)
- Strahle, W. C. (1978). Combustion noise. *Progress in Energy and Combustion Science* 4(3), 157 – 176. (p. 7, 11)
- Strahle, W. C. and M. Muthukrishnan (1980, 2016/11/11). Correlation of combustor rig sound power data and theoretical basis of results. *AIAA Journal* 18(3), 269–274. (p. 8)
- Suder, K. (2012, 2016/11/11). *Overview of the NASA Environmentally Responsible Aviation Project's Propulsion Technology Portfolio.* American Institute of Aeronautics and Astronautics. (p. xv, 2, 3)
- Tao, W. (2015). Time resolved temperature and pressure based methodology for direct and indirect combustion noise separation. *PhD thesis, Centrale-Supélec.* (p. xxi, 18, 182)
- Taylor, Z. J., R. Gurka, G. A. Kopp, and A. Liberzon (2010). Long-duration time-resolved piv to study unsteady aerodynamics. *IEEE Transactions on Instrumentation and Measurement* 59(12), 3262–3269. (p. 114, 115)
- Theunissen, R. (2013). Adaptive image interrogation for piv. *PhD thesis, TU Delft and VKI.* (p. 114, 115)
- Thomas, A. and G. T. Williams (1966). Flame noise: Sound emission from spark-ignited bubbles of combustible gas. *Proceedings of the Royal Society of London A: Mathematical, Physical and Engineering Sci-*

- ences 294(1439), 449–466. (p. 11)
- Tran, N. (2009). Influence of inlet acoustic boundary condition on large amplitude combustion instabilities : design of a robust impedance control system. *PhD Tesis, Ecole Centrale Paris*. (p. 17)
- Tran, N., S. Ducruix, and T. Schuller (2009a). Damping combustion instabilities with perforates at the premixer inlet of a swirled burner. *Proceedings of the Combustion Institute* 32(2), 2917 – 2924. (p. 28, 30, 38)
- Tran, N., S. Ducruix, and T. Schuller (2009b, 06). Passive control of the inlet acoustic boundary of a swirled burner at high amplitude combustion instabilities. *Journal of Engineering for Gas Turbines and Power* 131(5), 051502–051502. (p. 30, 67)
- Tropea, C., A. L. Yarin, and J. F. Foss (2007). Springer handbook of experimental fluid mechanics. *Springer Verlag Berlin Heidelberg*. (p. 108)
- Tsien, H. S. (1952, 2016/11/11). The transfer functions of rocket nozzles. *Journal of the American Rocket Society* 22(3), 139–143. (p. 14)
- Ullrich, W. and T. Sattelmayer (2016). Numerical investigation of aero engine combustion noise. *TU Munich, Homepage*. (p. xv, 7)
- Vedantham, A. and M. Oppenheimer (1998). Long-term scenarios for aviation: Demand and emissions of {CO₂} and {NO_x}. *Energy Policy* 26(8), 625 – 641. (p. 1)
- Weinstein, L. M. (1993, 2016/11/11). Large-field high-brightness focusing schlieren system. *AIAA Journal* 31(7), 1250–1255. (p. xix, 127, 128, 129)
- Weinstein, L. M. (2010). Review and update of lens and grid schlieren and motion camera schlieren. *The European Physical Journal Special Topics* 182(1), 65–95. (p. 127, 131)
- Willert, C. E. (2015). High-speed particle image velocimetry for the efficient measurement of turbulence statistics. *Experiments in Fluids* 56(1), 17. (p. xiii, 107, 111, 112)
- Woody, M., B. H. Baek, Z. Adelman, M. Omary, Y. F. Lam, J. J. West, and S. Arunachalam (2011). An assessment of aviation’s contribution to current and future fine particulate matter in the united states. *Atmospheric Environment* 45(20), 3424 – 3433. (p. 1)
- Xue, Z., J. J. Charonko, and P. P. Vlachos (2013). Signal-to-noise ratio, error and uncertainty of piv measurement. *PIV13; 10th International Symposium on Particle Image Velocimetry, Delft, NL*. (p. 115)
- Xue, Z., J. J. Charonko, and P. P. Vlachos (2014). Particle image velocimetry correlation signal-to-noise ratio metrics and measurement uncertainty quantification. *Measurement Science and Technology* 25(11), 115301. (p. 115)
- Zeldovich, Y. B. (1946). The oxidation of nitrogen in combustion and explosions. *Acta Physicochim. URSS* 21(4), 577–628. (p. 2)
- Zukoski, E. E. and J. M. Auerbach (1976, 01). Experiments concerning the response of supersonic nozzles to fluctuating inlet conditions. *Journal of*

Engineering for Power 98(1), 60–64. (p. 9)

Titre : Etude expérimentale du bruit de combustion dans un foyer de type aéronautique

Mots clés : Bruit de combustion, bruit entropique, instabilité de combustion, diagnostics à haute cadence

Résumé : Le bruit de combustion est devenu un contributeur de plus en plus important dans le bruit total de moteur d'avion. Ce bruit global a deux composantes: Le bruit direct et le bruit indirect. Le premier est issu des fluctuations de dégagement de chaleur dans la flamme elle-même. Le deuxième a pour origine les inhomogénéités de température dans les gaz brûlés. L'objectif de ce travail est la conception d'un banc de combustion sous pression avec une flamme pauvre, prémélangée swirlée dont les paramètres d'injection permettront d'obtenir des grandes quantités de bruit indirect.

Il est nécessaire de caractériser ce banc et d'établir quelle est la part du bruit direct et de l'indirect afin d'identifier les sources de ces contributions. Pour cette caractérisation il est nécessaire d'utiliser différents diagnostics, de prendre en compte la résolution temporelle. Ces diagnostics à haute cadence permettent de caractériser les champs de vitesse et les dynamiques de flamme, les instabilités de combustion dans le système et ainsi évaluer les contributions du bruit direct et indirect.

Title : Experimental study of combustion noise in an aeronautic type combustion chamber

Keywords : Combustion noise, entropy noise, combustion instability, high-speed diagnostics

Abstract : Combustion noise has become an increasing contributor of overall aircraft engine noise. It consists of two major parts, direct and indirect combustion noise. The former is generated by the heat release fluctuations of the flame itself. The latter is generated by the temperature inhomogeneities in the burnt gases, which are accelerated in the turbine stages or nozzle following the combustion chamber. The aim of this work is to design and build a pressurized lean swirling combustor test bench, in order to quantify the two contributions.

The combustor is thus supposed to generate high quantities of indirect combustion noise. The second aim is then to determine the contributions of direct and indirect combustion noise quantitatively and to gain insight about the sources of the two contributions. These analyses are conducted by different high-speed diagnostics, which were worked on during this work. These diagnostics allow to characterize the flow fields and flame dynamics, to put forward the combustion instability in the system and finally to quantify the direct and indirect combustion noise contributions.

